




ADVERTIMENT. L'accés als continguts d'aquesta tesi queda condicionat a l'acceptació de les condicions d'ús establertes per la següent llicència Creative Commons:  http://cat.creativecommons.org/?page_id=184

ADVERTENCIA. El acceso a los contenidos de esta tesis queda condicionado a la aceptación de las condiciones de uso establecidas por la siguiente licencia Creative Commons:  <http://es.creativecommons.org/blog/licencias/>

WARNING. The access to the contents of this doctoral thesis it is limited to the acceptance of the use conditions set by the following Creative Commons license:  <https://creativecommons.org/licenses/?lang=en>



**Universitat Autònoma
de Barcelona**

Electrically conductive nanocomposites for additive manufacturing

Imran Khan

*A thesis submitted in partial fulfilment of the requirements for the degree of
Doctor of Philosophy
in
Material Science
Department of Physics
University Autonomous Barcelona.*

This doctoral work is conducted under the collaborative contribution between Politechnic Institute of Leiria (IPL), Portugal, and ALBA Synchrotron Radiation facility, Barcelona, Spain. The work is conducted using the facilities and resources from the aforementioned Institutes. The programme was carried out under joint supervision from both institutes. Professor Dr. Geoffrey R. Mitchell remain one of the two potential supervisor for this program and he belongs to the Politechnic Institute of Leiria (IPL), Portugal. He has an extensive experience in polymer science. Dr. Christina Kamma-Lorger is a beamline scientist and the supervisor from ALBA synchrotron radiation facility, Barcelona, Spain. She is the beamline scientist responsible for BL-11 (NCD- SWEET) beamline. This project was funded by these two institutes through different projects.

(Prof. Geoffrey Robert Mitchell)

(Dr. Christina Kamma-Lorger)



Author's declaration

I hereby declare that I am the sole author of this thesis. This is a final copy of the thesis, including any required suggestions, recommendations, and revisions, as accepted by my examiners.

I can understand that my thesis may be made electronically available to the public.

Executive Summary

Additive manufacturing is a process of making successive layers of material to build a three-dimensional solid object from a digital model, as opposed to subtractive manufacturing methodologies. This technology offers the freedom to design and innovation of a product so that complex parts can be obtained and revise if needed, within a small time as compared to traditional manufacturing technologies. In terms of its full utilization and widespread, the technology has limited applications. On similar grounds, nanotechnology is considered as the driving force behind a new industrial revolution. It has the ability to incorporate specific functionalities, occur due to the nanometric scale, to desired parts that offer freedom to design functional devices like electrodes for energy storage devices.

The thesis is focusing on the use of electrically conductive nanocomposites into additive manufacturing. In this scenario, two types of nanocomposites are prepared to use as raw material for printing of electrically conductive nanocomposites employing two different types of matrix material; (1) a thermoplastic polymer and (2) a thermoset resin. Carbon nanotubes were used as electrically conductive nanostructure particles. These nanostructures form complex networks into a polymer matrix such that the matrix material transforms from an insulative material into an electrically conductive material. Polycaprolactone is a semicrystalline polymer and it is considered suitable matrix material amongst the class of thermoplastic polymers as it offers excellent rheological, flow and the elastic characteristics. Strands were printed using a bio extruder and electrical conductivity was measured in these strands under the effect of uniaxial deformation. The microstructure changes under the effect of uniaxial deformation leading to alter the orientation of carbon nanotubes in the polycaprolactone matrix. As a consequence of realignment of nanotubes, conductive pathways either disrupt or organize which can increase or decrease an electrical conductivity in the nanocomposites. Synchrotron radiations are used to probe such changes in the microstructure. Two different compositions were prepared using carbon nanotubes and the printed samples are studied in terms of electrical conductivity and microstructure using synchrotron radiations. Based on the analysis, a model is proposed that can predict the orientation of carbon nanotubes under the effect of uniaxial deformation.

In terms of thermoset polymers, a simple system is introduced for the printing of thermoset polymer (epoxy) based nanocomposites. Complete detail of the printing system is provided in one of the chapters. Epoxy-based nanocomposite ink was prepared to contain carbon nanotubes as filler particles with a small portion of thermoplastic polymer, polycaprolactone. The printed samples are subject to the external bias which indicate that these are electrically conductive. In this way, the printing system offers not only to extend the range of printable materials but materials having some functionality that can be further utilized to manufacture fully functional devices. A complete methodology was provided for the preparation of nanocomposite ink. Different compositions were prepared using glycidyl bisphenol-A epoxy resin, triethylenetetramine, polycaprolactone, carbon nanotubes and issues are highlighted to acquire appropriate print quality. The printed samples were studied in terms of electrical conductivity studying alternating and direct current electrical conductivity. The material system is explored in terms of the level of crosslinking, structure and morphology and thermal behaviour. A model is presented for the nanocomposites using impedance data obtained through broadband dielectric spectroscopy. The printer will be used in future to print small scale functional devices including energy storage devices e.g. solid-state batteries, supercapacitors and electrode plates for such kind of devices.

Acknowledgements. *I appreciate and thanks to Professor Geoffrey Robert Mitchell, my supervisor for his valuable advice, suggestions and support to conduct this research work. I would like to warmly and informally thank Geoffrey for always having involved in my work through his criticism which directed me not to ignore fine details about the work. Professor Geoffrey has given me the room to explore the paths that have lured off the trail towards innovations and academic adventures. I want to thank you for reinforcing me in the choices I have taken, and the decisions that I have made. Equally, my sincere thanks go to my second supervisor and beamline scientist Dr Cristina Kamma- Loriger from ALBA synchrotron radiation facility, Barcelona, Spain. As my supervisor, you have provided me with a working environment to explore my ideas by providing me state of the art facilities. The time I spent during experimental work at ALBA synchrotron not only helped me to explore in depth my printed materials but make me a part of the vibrant scientific community. Indeed, this work is very hard to finalise if your support is not with me. I honour and thank you for the support and help you have provided to me.*

I am humbled and grateful to the directors of “Center for Rapid and Sustainable Product Development” of Polytechnic of Leiria, Portugal, Dr Nuno Alves and Dr Artur Mateus for providing me additive manufacturing systems and materials characterization facilities and unconditional financial support. On similar grounds, I am grateful to director ALBA synchrotron, Dr Caterina Biscari for the approval and initiation of this collaborative PhD programme. I am thankful to beamline scientists Dr Marc Malfois and Dr Juan Carlos Martínez regarding some in house beam-time and technical discussion. Everyone has academic sparring partners or colleagues who chat, discuss and share ideas and knowledge. Thank you are a least saying for all the time we have shared to discuss ideas and support me to formulise this thesis. I am thankful to Miguel Belbut Gaspar, Dr Saeed Daren Mohan, Dr Vidhura Mahendra, Carla Moura, Pedro Carreira, Sara Biscaia, Margarida Franco, Ana Rita Fonseca and rest of all the CDRSP team. And last but not least, people who are in the background but their contribution is immense as they work hard so that we are on time to conduct experiments or attend seminars and meetings without delay. A special thanks go to honourable Margarida Filipe and her team. Dear Margarida, you will have special respect in my heart for all the moral and administrative support you ever provided to me. A big thank to you for your time and support.

Dedicated to

*my beloved parents, brothers,
and
my cute family.*

Publications

- Khan, I., Kamma-Lorger, C.S., Mohan, S.D., Mateus, A., Mitchell, G.R., 2019. *The Exploitation of Polymer-Based Nanocomposites for Additive Manufacturing: A Prospective Review. Applied Mechanics and Materials* 890, 113–145.
- Khan, I., Mateus, A., Kamma-Lorger, C.S., Mitchell, G.R., 2017. *Part specific applications of Additive Manufacturing, Procedia Manufacturing* 12, 89 – 95.
- Khan, I., C.S., Mohan, S.D., Belbut M., Kamma-Lorger, C.S., Mateus, A., Mitchell, G.R., 2017. *Multiscale Structure Evolution in Electrically Conductive Nanocomposites Studied by SAXS, Procedia Manufacturing, 12, 79-88.*
- Khan, I., Kamma-Lorger, C.S., Mitchell, G.R., 2020. *Electrical and stress-strain behaviour in carbon nanotubes based strands printed through an additive manufacturing system (expected to publish in a journal in December 2020).*

Funding resources and support

This work is supported by the Fundação para a Ciência e a Tecnologia (FCT) and Centro 2020 through the Project references:

- UID/Multi/04044/2013 and UID/Multi/04044/2019;
- PAMI -ROTEIRO/0328/2013 (Nº 022158); (co-promoção n.º 3414),
- MecatronicaFlexivel (CMUP-ERI/TIC/0021/2014)
- Add.Additive-add additive manufacturing to Portuguese industry (projeto nº 24533) funded by FEDER – através do COMPETE 2020 – Programa Operacional Competitividade e Internacionalização.
- Additionally, besides using synchrotron radiation, ALBA Synchrotron supported the experimental research carried out in Barcelona.

Table of Contents

Chapter 1:	Introduction	1
1.1	Introduction	1
1.2	Aims and objective	3
1.3	Thesis organization.....	5
1.4	References	6
Chapter 2:	State of the art in additive manufacturing	7
2.1	Introduction	7
2.2	Nanostructure Particles.....	9
2.3	Additive Manufacturing	11
2.4	Remarks on technological merger	12
2.5	Electrically conductive nanocomposites	15
2.6	Percolation theory:	16
2.6.1	Percolation in conducting materials:	17
2.7	Quantum tunnelling:.....	18
2.8	References	19
Chapter 3:	Materials, methods and experimental techniques.....	22
3.1	Introduction:	22
3.2	Thermoplastic Polymers:.....	22
3.2.1	Acrylonitrile butadiene styrene:	24
3.2.2	Polycaprolactone.....	25
3.3	Thermoset Polymers	26
3.3.1	Polyurethane	27
3.3.2	Epoxy Thermosets	29
3.4	Carbon nanotubes	36
3.5	Dispersion solvents.....	37
3.5.1	N, N-Dimethylformamide.....	37
3.5.2	Chloroform	38

3.5.3	Dichloromethane.....	39
3.6	Triton X-100.....	40
3.7	Additive Manufacturing systems.....	41
3.8	Electronic Balance.....	42
3.9	Heating stage/Magnetic stirrer	43
3.10	Incubator shaker	44
3.11	Ultrasonication	45
3.12	Electrical conductivity calculation	48
3.12.1	Two probe method.....	48
3.12.2	Four probe method.....	49
3.12.3	Equipment Specifications	50
3.13	Extensometers	51
3.13.1	Concept and design of sample holding grips	51
3.13.2	Data acquisition systems.....	53
3.14	Broadband dielectric spectroscopy.....	54
3.14.1	System specification	56
3.15	Use of Synchrotron Radiation	57
3.15.1	Properties of synchrotron radiation	59
3.15.2	ALBA Synchrotron Light Source	59
3.15.3	Small angle X-ray scattering (SAXS).....	60
3.15.4	Wide angle X-ray scattering	67
3.16	Electron microscopy	69
3.17	Fourier-transform infrared spectroscopy (FTIR).....	70
3.17.1	Attenuated total reflectance (ATR)	71
3.17.2	Equipment specification	72
3.18	Simultaneous Thermal analysis.....	73
3.18.1	Differential scanning calorimetry	73
3.18.2	Thermogravimetry Analysis	76
3.19	Data Processing	76

3.20	References	76
 Chapter 4: Additive manufacturing of thermoplastic polymer based electrically conductive strands		
4.1	Introduction	83
4.2	Materials and Methods	83
4.2.1	Materials	83
4.2.2	Nanocomposite preparation	84
4.2.3	Additive manufacturing system	84
4.2.4	Additive manufacturing of strands	85
4.2.5	Fourier Transform Infrared Spectroscopy	86
4.2.6	Measurement of electrical conductivity.....	87
4.2.7	Mechanical characterization	88
4.2.8	Small-angle X-ray scattering	88
4.2.9	Scanning Electron microscopy	95
4.2.10	Dynamic scanning Calorimetry	95
4.3	Results	95
4.3.1	Spectroscopic analysis	95
4.3.2	Measurement of electrical conductivity.....	96
4.3.3	Uniaxial deformation experiments	98
4.3.4	Structural Characterization	101
4.3.5	Morphological analysis.....	113
4.3.6	Thermal analysis	114
4.4	Discussion	115
4.5	Model.....	121
4.6	Summary	131
4.7	References	134
 Chapter 5: Design and configuration of a 3D printer system for thermosetting polymer-based nanocomposites		
5.1	Introduction	139
5.2	Overall design and structure.....	141
5.3	Configuration of axes and 3D motion	142

5.3.1	Calibration of axes	143
5.4	Extrusion principle	144
5.5	Material deposition assembly	145
5.6	Command and Control system	147
5.7	Electronics and software	148
5.8	Model definition and input for printing.....	150
5.9	Measurement of flow rate.....	151
5.10	Process Parameters	152
5.11	Case study.....	152
5.12	Nanocomposite preparation (conductive ink)	153
5.13	Printing of samples	155
5.14	The workflow scheme	157
5.15	constraints and limitations.....	158
5.16	Future update	158
5.17	Conclusion.....	159
5.18	References	159
Chapter 6: Characterization of samples printed through newly designed printer system		161
6.1	Introduction	161
6.2	Results and discussion.....	162
6.2.1	3D printed epoxy-based nanocomposites under the effect of MWCNTs (% w/w) loading.....	162
6.2.1.1	3D printed epoxy-based nanocomposites under the effect of Polycaprolactone loading.....	193
6.2.1.2	3D printed epoxy-based nanocomposites under the effect of Triethylenetetramine loading.....	199
6.3	Discussion	207
6.3.1	Model.....	211
6.4	Conclusion.....	215
6.5	References	218
Chapter 7: Conclusion and Future work		224

7.1	Introduction	224
7.2	Overall conclusions	225
7.3	Future Perspective	229
7.4	References	229

Chapter 1: Introduction

1.1 INTRODUCTION

The chapter introduces the field of research work, aims and objectives of the study and thesis organization. Additive manufacturing is a class of technology used to process materials in a layer-by-layer fashion by depositing material. It involves the shaping of a product through the use of liquid phase which is subsequently transformed to the solid-state by cooling or through the use of chemical cross-linking reactions [1]. Physical objects are designed as Computer-Aided Design (CAD) model which are sliced as layers, pass to the additive manufacturing system leading to the desired part. The model is built by joining material volume, one cross-sectional layer at a time, in an additive way, as opposed to subtractive manufacturing methodologies [2]. The general workflow scheme for additive manufacturing is shown in Figure 1.1. The selection of an additive manufacturing process depends on nature (the type of polymer or metals) and form (filament, resin, granules) of material for the desired application. For an example, if there is a polymer material in the form of filament then a fused deposition modelling (FDM) can serve the purpose, which works on an extrusion principle while if the polymer is in the form of powder then selective laser sintering (SLS) is the process.

Additive manufacturing methods have several advantages over traditional manufacturing techniques. First, additive manufacturing offers “freedom to design”. It is possible to build complex geometries, because of its additive approach. On the other hand, conventional manufacturing methods require a long fabrication time when dealing with complex geometries. The literature supports this argument that the AM is better suited where relatively higher complexity or customisation is necessary [3]. One example of such arena is electrochemical energy storage, where unique building properties of additive manufacturing and 3D printing can be exploited for enhanced performance in batteries and supercapacitors [4][5]. AM offers reduced waste and minimal use of harmful chemicals (such as etching and cleaning solutions) when compared to traditional manufacturing techniques. However, the functional parts

manufactured through AM required assemblage to create fully-functional devices.

Additive Manufacturing work flow

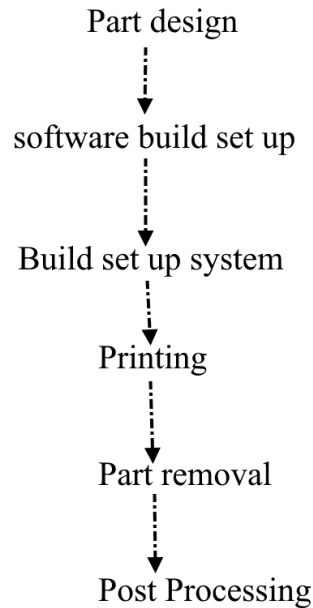


Figure 1.1. Additive manufacturing workflow.

Therefore, AM challenge is broad in application-oriented manufacturing, among many others. At this stage, the interest of research and industry lies in establishing where additive manufacturing can replace or offer new manufacturing systems [3] to process complex materials. In other words, acquiring parts having some functionality through AM. This is closely related to the choice of available materials, which are limited when desired for a particular application. Research in advanced materials is continuously driving modern technologies forward. For example, semiconductors have laid the foundation for today's electronics industry. Composite materials emerged in the middle of the 20th century as a promising class of engineering materials providing new prospects for modern technology [6]. Among many other, electrically conductive composites are attractive due to their lightweight, resistance to corrosion, flexibility and processing advantages [7]. While structural composites emphasize high strength and high modulus, electrically conductive composites emphasize low thermal expansion, low dielectric constant, high/low electrical conductivity and/or electromagnetic interference (EMI) shielding effectiveness, depending on the particular application of interest [8]. Composite materials are generally intended as structural materials for use. These materials are finding more and more electronic uses, with the rapid growth of the electronics industry. Other than

design and environmental advantages, the adoption of AM as a means for fabricating end-use components has historically been dampened by the technologies' narrow selection of available materials [9]. The majority of materials used presently by modern AM techniques are proprietary polymers. While different types of materials can be used in AM, their material properties such as strength, electrical and thermal conductivity, and optical transparency typically have inferior properties compared to conventionally manufactured counterparts due to the anisotropy caused by the layer-by-layer approach. While constantly searching for new materials, one of the important aspects is to find manufacturing systems that can address issues and limitations which are difficult to address using conventional manufacturing systems or methods. The motivations for such an inclination towards AM include cost reduction, manufacturing time reduction, and ease of handling complex materials (polymers) manufacturing. In these scenarios, additive manufacturing has the potential to address such kind of challenges.

In this work, electrically conductive nanocomposites are printed using additive manufacturing systems. A specially designed printing system is introduced in this scenario for the printing of thermoset polymer-based nanocomposites. Nanocomposites that contain either thermoplastic polymer or thermoset polymer are printed using two different AM systems. Nanostructures are described as novel materials whose size of the elemental structure has been engineered at the nanometer scale. Materials in the nanometer size range exhibit fundamentally new behaviour. Moreover, intervention in the properties of materials at the nanoscale enables the creation of materials and devices with enhanced or completely new characteristics and functionalities [10]. In this regard polymer matrices, carbon nanotubes are used as electrically conductive nanofiller structures for sample printing by additive manufacturing, providing them with the ability to pass electric current under an appropriate bias. The characteristics of printed samples are explored through electrical, mechanical, structural and morphological techniques and results are presented in the following chapters.

1.2 AIMS AND OBJECTIVE

During the current decade, the focus of the rapidly developing area of additive manufacturing is moving from rapid prototyping to rapid manufacturing of high-performance parts. In context to this, there is a need to develop simple and cost-

effective additive manufacturing system and printing methodologies for application-oriented nanocomposites. This research work is therefore aimed at developing new materials, a simple cost-effective additive manufacturing system and a material preparation methodology that offers the functionality to manufacture parts that will lead from prototype to fully functional devices or components in the future.

- The primary objective of the thesis is to study the processing of polymer-based electrically conductive nanocomposites through additive manufacturing. Polymers of both classes, thermoplastic and thermoset, will be considered as matrices for the preparation of nanocomposites, whilst carbon nanotubes will be used as electrically conductive filler particles. Nanocomposites are complex material in a context that nanostructures aggregate due to large surface to volume ratio. Carbon nanotubes based nanocomposite materials have been the focus of the scientific community for the last decades, as they have a substantial improvement in electrical conductivity even at low loadings. Their performance depends on several parameters but the MWCNTs dispersion and distribution state remains the key challenge to benefit full potential from the nanocomposites. The changes in the microstructure due to additive manufacturing process can increase/decrease carbon nanotubes networks resulting in increased or decreased electrical conductivity in the printed samples. The microstructure, morphology, electrical and thermal response of printed samples is explored through different experiments developing an understanding about the filler arrangement in a polymer matrix.
- The secondary objective of the study is the design, development and configuration of a printing system for thermoset resin-based nanocomposites. The majority of printable polymers in additive manufacturing belong to the class of thermoplastic polymers, and very few exist for thermoset resins. Thermoset polymers are a versatile class of polymer offering unique features contrary to thermoplastic polymers including high strength-to-weight ratio, outstanding dielectric strength, low thermal conductivity, microwave transparency, resistance to corrosion and water. Considering a wide range of applications using thermoset polymer, a printer is required which can print nanocomposite materials based on

thermoset polymer or a thermoset polymer. Currently, UV –curable resins are used to print parts. The systems or printers used to print such resins are expensive and with a complex control system. Therefore, a new and relatively simple system is proposed for the printing of thermoset resin-based electrically conductive nanocomposites.

- The other objective of this research work is the modelling of the electrical conductivity in the polymer-based nanocomposites. Models are presented in the study, based on experimental work, demonstrating electrical conductivity in the samples printed through additive manufacturing. In this regard, deformable (thermoplastic polymer) and non-deformable materials (thermoset polymers) are printed using carbon nanotubes and models are produced for each kind of material. For the sake of this, a material preparation methodology is provided for the printing of these materials.

1.3 THESIS ORGANIZATION

The presentation of this thesis is considered as follows:

Chapter 1 is devoted to the introductory part, the specific aims and objectives and thesis organization.

Chapter 2 Introduces the relevant background and literature related to the field of research work conducted in this thesis. Specific theoretical concepts are briefly discussed in context to electrically conductive nanocomposites.

Chapter 3 includes relevant materials, methods and characterization techniques used to conduct experimental work. Theoretical aspects are also provided for the significant techniques used in this work.

Chapter 4 unveil methodology to print polycaprolactone based nanocomposite containing carbon nanotubes. Strands were printed which were electrically conductive under the application of a suitable bias. Experimental methodology is provided explaining variation in electrical conductivity and microstructure under the effect of uniaxial deformation. Results and discussion are presented for the deformed strands.

Chapter 5 reveals information about a newly designed AM system (3D printer) for thermosets resin-based electrically conductive nanocomposites, containing carbon nanotubes. A detailed explanation of the printing system is presented with key components. In addition, the methodology is provided to prepare nanocomposites ink, based on Bisphenol A diglycidyl ether (epoxy) resin and carbon nanotubes.

Chapter 6 presents different results from printed samples of epoxy-based nanocomposites containing carbon nanotubes using the AM system mentioned in Ch.5. Such findings provide details on the characteristics of printed samples as investigated by electrical, mechanical, structural, and morphological analysis. These characteristics are found using a variety of techniques including broadband dielectric spectroscopy, small and wide angle x-ray scattering, scanning electron microscopy, Fourier-transform infrared spectroscopy and thermal analysis techniques. The results are discussed and a model is proposed to predict an electrical conductivity in the thermoset polymer-based nanocomposites.

Chapter 7 contain key conclusions drawn from the study and indicates where and how this work lead to future research work.

1.4 REFERENCES

- [1] G. R. M. A. Tojeira, S. Biscaia, T. Viana, P.J. Bártolo, “Structure development during additive manufacturing,” in *High-Value Manufacturing: Advanced Research in Virtual and Rapid Prototyping*, P.J. Bártolo, Ed. Taylor & Francis Group, 2014, pp. 211–216.
- [2] Y. Zhai, D. A. Lados, and J. L. Lagoy, “Additive Manufacturing: Making imagination the major Limitation,” *Jom*, vol. 66, no. 5, pp. 808–816, 2014.
- [3] T. Pereira, J. V. Kennedy, and J. Potgieter, “A comparison of traditional manufacturing vs additive manufacturing, the best method for the job,” *Procedia Manuf.*, vol. 30, pp. 11–18, 2019.
- [4] U. Gulzar, C. Glynn, and C. O’Dwyer, “Additive manufacturing for energy storage: Methods, designs and materials selection for customizable 3D printed batteries and supercapacitors,” pp. 1–11, 2020.
- [5] P. Chang, H. Mei, S. Zhou, K. G. Dassios, and L. Cheng, “3D printed electrochemical energy storage devices,” *J. Mater. Chem. A* vol. 7, no. 9, pp. 4230–4258, 2019.
- [6] V. Vasiliev and E. Morozov, *Advanced Mechanics of Composite Materials and Structural Elements*, 3rd ed. Elsevier Inc., 2013.
- [7] R. B. Mathur, B. P. Singh, and S. Pande, *Carbon Nanomaterials: Synthesis, Structure, Properties and Applications*. Boca Raton, FL: Taylor & Francis Group, 2016.
- [8] D. D. L. Chung, *Composite materials*. Springer, London, 2003.
- [9] Olga S. Ivanova, C. B. Williams, and T. A. Campbell, “Additive Manufacturing and Nanotechnology: Promises and challenges,” *Rapid Prototyp. J.*, vol. 19, no. 5, pp. 353–364, 2013.
- [10] M. Ramrakhiani, “Nanostructures and their applications,” *Recent Res. Sci. Technol.*, vol. 4, no. 8, pp. 14–19, 2012.

Chapter 2: State of the art in additive manufacturing

2.1 INTRODUCTION

The current chapter is compiled to briefly introduce additive manufacturing, nanocomposites, use of nanocomposites into additive manufacturing and significant theoretical concepts in context to electrically conductive nanocomposites. In this regard, additive manufacturing and exploitation of polymer-based nanocomposites into additive manufacturing are discussed in the early part of the chapter. In the middle of this chapter, information is disclosed about the polymers, polymer-based nanocomposites and their exploitation into an additive manufacturing process. Besides, success and limitations in context to the exploitation of nanocomposites into additive manufacturing are discussed that becomes the source of motivation for this research work. At the end of this chapter, relevant theoretical concepts are discussed at the end of this chapter in context to electrically conductive polymer-based nanocomposites.

Composite materials have been widely studied with examinations focused upon how the host material is influenced by the presence of one or more additional components (fillers). Nanocomposites are defined as a class of materials that contain at least one phase with constituents in the nanometer domain [1]. The literature suggests that the use of nanoparticles influence the various features of a host material making it suitable for applications ranging from drug delivery [2], corrosion prevention [3], electrical [4], electronic [5], aeronautics and automotive [6] parts to industrial equipment [7]. The development of nanocomposite materials is currently an area of great research interest due to the benefits of producing materials with enhanced features [8]. Although the advent of nanotechnology can have a huge potential impact on product development, the lack of consistent manufacturing techniques limits its wide use in different industries. A consistent and cost-effective route is the need of the hour to fully benefit from nanocomposite materials. A consistent way to achieve such a desired nano precision and resolution is the development and wide implementation of nanofabrication technologies [9]. The fast and quick delivery of nanocomposites with enhanced features can be achieved with the application of Additive

Manufacturing. Additive Manufacturing refers to a group of technologies that build physical objects directly from 3D Computer-Aided Design (CAD) data. It is defined as the process of joining materials to make objects from 3D model data, usually layer upon layer, as opposed to subtractive manufacturing methodologies.

Table 2.1. Differentiation of AM according to the nature of matrix material.

Type	AM Technologies	Host Materials
Extrusion	Fused deposition modelling (FDM)	Thermoplastics (e.g. PLA, ABS), eutectic metals
Granular	Direct metal laser sintering (DMLS)	Metal /Alloy/Polymer Powder
	Electron beam melting (EBM)	
	Selective heat sintering (SHS)	
	Selective laser sintering (SLS)	
	Powder bed and inkjet head 3d printing, Plaster-based 3D printing (PP)	
Light polymerised	Stereolithography (SL)	Photopolymer
	Digital Light Processing (DLP)	

A complex-shaped model or piece to suit a specific function can be easily manufactured using AM through CAD. Ideally, the manufactured part should have properties suited for its application, such as good mechanical, electrical or parts compatible with biological features. AM can be used in a variety of fields ranging from forming direct parts for aerospace, household appliances, automotive and biomedical applications [10] as it gives the designers an ability to design and turn concepts into 3D models or 3D prototypes. Amongst all, mechanical [11], thermal [12], electrical [13] and flame retardance [14] is the core characteristics which have attracted the interest for the incorporation of nanomaterials into the AM process. Table 2.1 distinguishes AM techniques based on feedstock or input material that after processing transform into a 3d object of desired geometry. The chapter introduces

nanocomposites, additive manufacturing and use of nanocomposites into additive manufacturing or more precisely developing trends in manufacturing with the use of nanoparticles. After the brief introduction of additive manufacturing, nanoparticles, and nanocomposites, Some conclusive remarks are presented from the literature review. The chapter ends with the presentation of relevant theoretical concepts including percolation theory and quantum tunnelling.

2.2 NANOSTRUCTURE PARTICLES

All kinds of solid particles with at least one characteristic dimension in the 100 nm range are referred to as nanoparticles. In general, the size-dependent effects may have both a classic and quantum nature. As the size of particles is reduced from macro to nano-scale a dramatic change in all its properties is observed as quantum size effects becoming more and more relevant. This leads to occur unusual physical properties of nanoparticles (NPs) below 100 nm, significantly different from their bulk particles (micro or bigger sizes), where the size of the particle appears to dictate its physical and chemical properties. For example, a nanoparticle of silver will respond to photons and electrons in ways profoundly different from a larger particle or bulk silver [15].

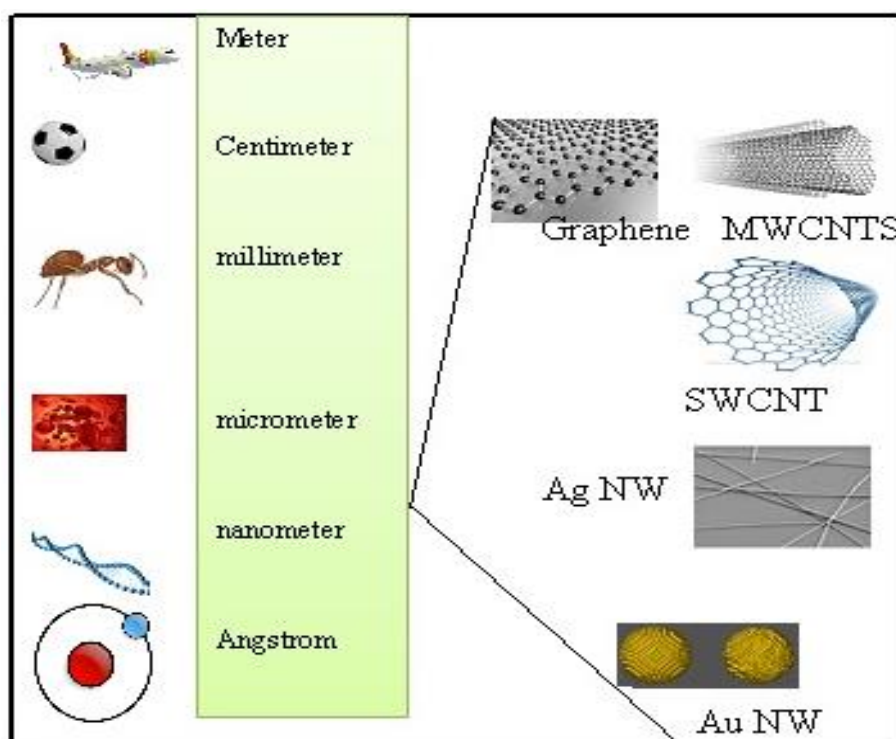


Figure 2.1. A comparative chart to compare sizes nano to macro-scale objects.

This may be attributed to the particle's surface to volume ratio at this scale, which is considerably high and is beneficial for interacting with the surrounding environment, i.e. the host material. The presence of neighbouring surfaces, containing 0-D, 1-D, and 2-D nanostructures, causes a change in the distribution of the phonon group velocities as a function of phonon wavelength which affects overall thermal conductivity. From this, it is evident that size does matter and is elaborated in a comparative chart (Figure 2.1) to highlight the importance of size scale. Numerous forms of NP can be used, from metallic to carbonaceous, clay, ceramic and semiconducting nanoparticles. Overall the choice of filler particle used will depend on the desired properties for the composite material that is to be manufactured. For example, the carbonaceous nanoparticle, carbon nanotubes are widely studied as an option for incorporation into a host material as they can improve the electrical and thermal properties of the host material without sacrificing mechanical features. Different types of commercially available nanoparticles with the prominent feature are presented in Table 2.2

Table 2.2. Some of the commercially available nanoparticles,

Acronyms	Nanoparticles	Features
SWCNT	Single wall carbon nanotubes	Electrical & Mechanical
MWCNT	Multiwall carbon nanotubes	Electrical & Mechanical
DWNT	Double-wall carbon nanotubes	Electrical & Mechanical
G or GO	Graphene or graphene oxide	Electrical & Mechanical
Ag NP	Silver nanoparticles	Electrical & Antimicrobial
AuNP	Gold nanoparticles	Electrical & Antimicrobial
(Fe ₃ O ₄) NP	Iron oxide	Electrical & Magnetic
Si NP	Silica NP	Mechanical
Pd NP	Palladium nanoparticles	Electrical & Catalytic
Rh NP	Rhodium nanoparticles	Chemical & Catalytic
NaM NP	Sodium Metatitanate	Chemical & Catalytic
BNP	Boron nitride	Electrical & Thermal
TiO NP	Titanium dioxide	Antiseptic & antibacterial
CuONP	Copper(II) oxide	Electrical & Catalytic
PbS (CdSe)	PbS (CdSe) quantum dots	biomedical & Photonic
Cts NP	Chitosan NP	Pharmaceutical

2.3 ADDITIVE MANUFACTURING

In the additive manufacturing (AM) process, the discrete slices are obtained from 3D CAD geometry. These slices are directly related to the build layers of the AM process targeted for manufacture. The continual recreation of the discrete adjacent slices, layer by layer, via the AM system, allows one to manufacture a virtual and complex geometry of a part [16]. The process involved in the AM is indicated in Figure 2.2. AM is characterized by assembling layers using only the materials required, as opposed to subtractive manufacturing which involves cutting and wasting of material not needed from larger pieces of the material. The input material is sometimes referred to as feedstock material which can be in the form of powder, pellets, liquid or filament. The selection of the AM process also depends on the type of feedstock material. For instance, fused deposition modelling (FDM) is utilizing filament kind of feedstock material to print a part in a layer by layer fashion. The competitive advantages of AM include an enormous range of shape complexity, rapid delivery of parts and deskilling of some of the manufacturing steps. These advantages had led to considerable enthusiasm for AM. Along with these encouraging signs, AM has come speculation about future benefits that are less certain. Many of AM technologies still have well-known challenges. These include slow build rate, poor surface finishing, dimensional tolerances, expensive equipment, high material costs and limited material choices [17].

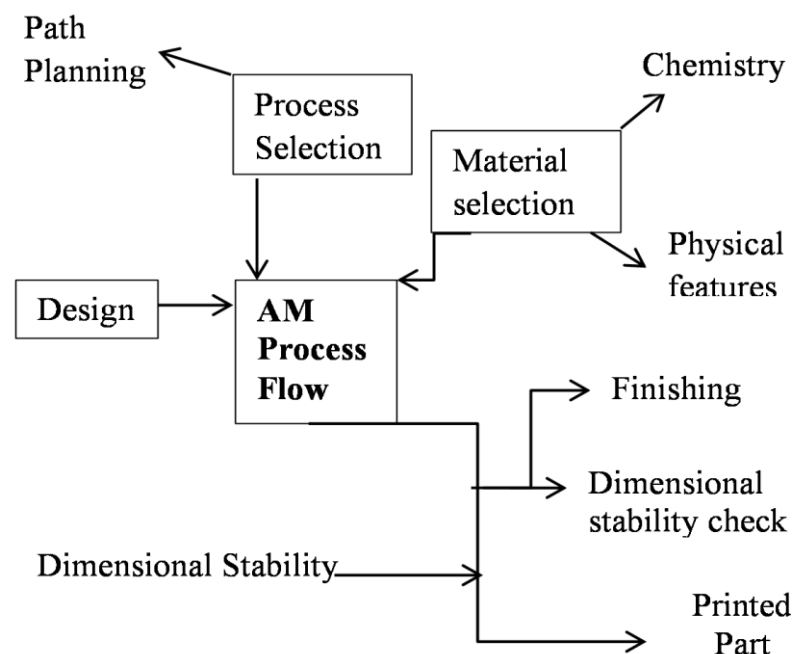


Figure 2.2. Schematic of additive manufacturing process flow.

Accuracy of the printed parts depends on functionality caused by nano additives, part design and dimensional stability compared to other fabrication methods. As an example, a comparative study related to dimensional error for the PolyJet, SLS and 3DP techniques was studied for medical models by Mika Salmi [18]. The accuracy in case of PolyJet was reported higher when compared with SLS or 3DP techniques while the repeatability of the measurements was excellent in case of 3DP as compare to the rest of the techniques [18]. These results can help clinicians/ manufacturer to choose a suitable AM technique that yield results with excellent accuracy. Cost is an important factor whenever introducing a new technology at an industrial scale. AM is a cost-effective technology on an industrial scale due to specific build-up process that leads to a significant reduction in waste materials. AM is a progressive technology which is evolving with time. With regards to the development of nanocomposite materials using AM, different systems were reported in literature fulfilling different needs.

2.4 REMARKS ON TECHNOLOGICAL MERGER

AM having the ability to fill the gap between available process techniques for nanocomposites. Their alliance could generate an additional stream to push the nano revolution into a new phase. Overall, semi-encouraging results (Figure 2.3) have been found in the application of nanocomposites into additive manufacturing, however, the integration demands a comprehensive research work to fully address the complexities and inherent potential. The following conclusions are drawn from the study:

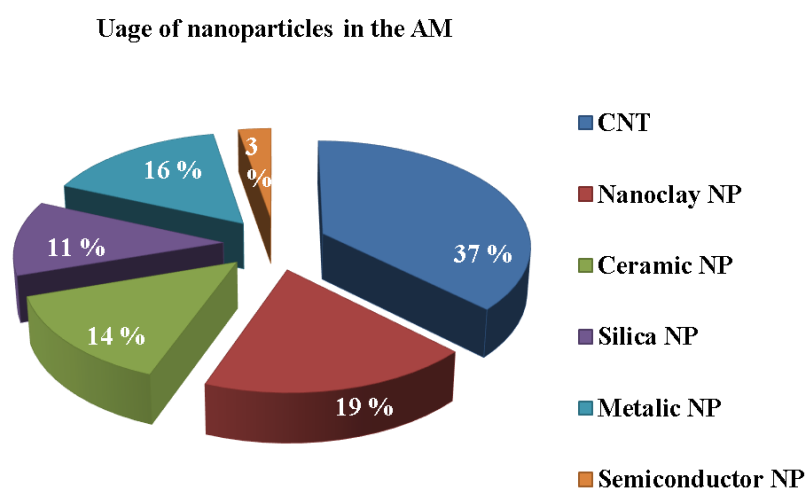


Figure 2.3. The pie chart is used to show how various nanoparticles are used in additive manufacturing. The data is collected from the published work.

1. Not much work had done in this field and it requires more attention to understand the compatibility issues between nanoparticles and host materials. The literature survey reveals that few rapid manufacturing techniques were employed in which nanocomposites used as raw material. There is a need to employ other additive manufacturing techniques to print nanocomposites as a raw material for having fully functional parts or components.
2. Enhanced mechanical and electrical properties were observed in different attempts indicating the feasibility and use of nanocomposites in rapid manufacturing techniques. Mechanical properties were investigated more as compared to other physical properties, for example, a few people investigated the enhancement in electrical conductivity of nanocomposites for rapid manufacturing applications.
3. Dispersions containing nanoparticles with high UV-vis absorption are not suitable to employ them in UV-curable resin to construct a prototype. UV-vis absorption of nanoparticles must be comparable to the intensity of UV radiations to get a good spinning, curing and hence solidification of nanocomposite fibre.
4. Suitable photopolymers are critical for the SL process. Important characteristics, such as viscosity, sensitivity, and wavelength response need to be considered for the SL application.
5. Possibly, a portion of UV energy absorbed by nanoparticles can lead towards insufficient curing of UV resin. Therefore, prior knowledge or study can help to avoid incomplete cure in the printed parts.
6. Stereolithography system optimization is required to avoid post-processing. The right choice and optimum amount of NPs can help to get fully cured parts.
7. Efficient methodologies are required to reduce viscosity rise caused by nanoparticles insertion into the UV curable resins.
8. The sintering temperature has significant effects on aggregation and caking of nanoparticles during the SLS process.
9. Nanocomposite powder with spherical shape is preferred over square-edged particles to construct 3D objects.
10. Degassing the materials' polymer and nanoparticles can help to overcome porosity and can enhance mechanical properties for the printed parts.

11. An efficient powder production method/system can produce powders with uniform morphology and facilitates sintering process to improve the mechanical properties of the printed parts.
12. Processing conditions, including laser power, scan speed, bed temperatures and chamber temperatures are equally important during the sintering process. The quality of the manufactured part depends on optimum conditions. It is advisable to carefully select optimum conditions to print parts which change from material to material.
13. Due to the stair-step effect, a rough surface finish is produced which make components less detailed due to a high processing temperature and high shrinkage and demands a comprehensive research work in future.
14. Nature of host material in most of the studies was PA whereas a different trend is observed in the case of nano additives ranging from CNTs, carbon black, clay nanoparticles in the SLS process. The reason to use carbon nanofiller is their high aspect ratio leading towards high mechanical strength and conductivity while PA is available commercially as well as naturally, besides that indicates limitations of materials in case of SLS technique as compared to the traditional manufacturing process.
15. FDM is limited by the availability of application-specific functional materials. Thermoplastic polymers with nano additives can help to delimit the choice of specific functional materials.
16. Nozzle wear during the FDM printing process can also affect print quality. It is advice able to monitor nozzle after some usage. Hardened steel nozzles can serve the purpose to overcome nozzle abrasion.
17. The homogeneous dispersion of nano additives into a polymer matrix is necessary to achieve desired functionality in the printed nanocomposites.
18. Exploiting nanostructured material characteristics and properties in AM may open a new window for markets offering rapidly manufactured functional devices.
19. Several research questions still need to be addressed for the success and implementation of the technological merger. There is a need for new materials that can fulfil requirements required for 3D printing including flow rate, crystallization and shrinking properties.

20. Theoretical models required to fully understand the behaviour of nanoparticles during part fabrication and explaining the compatibility issues between nanoparticles and matrix material during the layering process.

2.5 ELECTRICALLY CONDUCTIVE NANOCOMPOSITES

Electrically conductive nanocomposites are application-specific materials for the design and development of smart materials. These materials are obtained by structuring a network of conductive fillers/nanofillers (carbon or metallic) into an insulating polymer matrix. In such a way, these materials contribute original properties such as chemical, mechanical, electrical or thermo-sensitive into nanocomposites that allowing smart functionalities to target promising applications. Several manufacturing technologies have been developed to prepare nanocomposites acquiring electrical conductivity for diverse and application-oriented requirements. For the sake of this, nanocomposites are prepared by adding a variety of conductive nanofillers in a polymeric matrix with various mixing ratios for tuning the electrical properties. Different schemes of preparation were exercised and reported in literature describing the influencing parameters on the electrical conductivity in nanocomposites. These include filler volume/weight fraction, filler nature, polymer matrix, crystalline and amorphous polymers etc. Besides the effect of the aforementioned parameters, the processing and dispersion techniques [19], surfactants and the dispersion medium are also critical to acquire the desired electrical conductivity in the nanocomposite [20]. The choice of appropriate dispersion technique is critical and it greatly influences the orientation, homogeneity and distribution of nanofillers within the polymer matrix. For example, it was reported in numerous studies that the electrical conductivity increases with the loading of fillers [21] used to prepare nanocomposites and based on experimental data, model was produced to predict electrical conductivity in the nanocomposites [22]. Electrical conductivity was modelled using significant factors including volume fraction, shape and size, aspect ratio, critical value, and orientation of filler particles [23]. Controlling the filler orientations in the nanocomposites and understanding its consequent effect on the electrical conductivity is important as the level of orientation can affect the conductive pathways that ultimately can promote or demote the electrical conductivity in the composite. Conductive nanocomposites based on various percolation and non-percolation mechanisms [24] have been investigated for more than two decades to meet the requirements of applications, such as battery

electrodes, display devices, fuel cells, sensors, electronic whiskers, etc. Percolation is one of the widely accepted theories used to study conductive composites and is briefly discussed in the coming section.

Nevertheless, to synthesize conductive polymer nanocomposites with reliable, durable, and reproducible characteristics, it is necessary to pay attention to the construction steps of the 3D conducting architectures, to their formulation, and their characterization at different scales of observation from the nano- to the microscale [25]. Among various other challenges, the suitable materials, their effective integration and utilization remain at the core of this flourishing field [26]. For electronic components with these features, there are a need to investigate new materials, new preparation and processing methods, which allow the required degree of stretchability, without sacrificing the electronic performance [27].

2.6 PERCOLATION THEORY:

The percolation theory is a part of probability theory and it has multiple applications in natural and engineering sciences [28]. The use of percolation model was first effectively considered by chemist Paul Flory in the early 1940s in his study of gelation in polymers [29]. It accounts as a fundamental step in dealing with complex systems, models and even dynamical processes occurring on the networks. The theory deals with the special features of the appearance, critical phenomena and evolution as well as the properties of clusters arising in stochastic processes. For the sake of understanding, considering the example of water infiltration into the sand particles. The sand particles in a cubical sample of sand seem closely packed but there are gaps in between particles. When water is poured on top of a cubical sample of sand (Figure 2.4 (a)), will it be able to make its way from gap to gap and reach the bottom? This physical question is modelled mathematically as a three-dimensional network of $n \times n \times n$ vertices, usually called "sites", in which the edges are "bonds" between every two neighbours. The sites may be open (allowing the water through) with probability p or closed with probability $1 - p$. Therefore, for a given p , there is a probability that an open path exists from the top to the bottom through which water percolates through the sand particles and vice versa. The probable path exists from top to bottom is referred to as a giant network. The minimum quantity of water used to make such a giant network is referred, as critical water quantity (p_c) required for water percolation and commonly called a percolation threshold. Two models are commonly used to

study percolation problems, the bond percolation model (Figure 2.4 (b)) and site percolation model (Figure 2.4 (c)). The bond percolation model is introduced in the mathematics literature by [30]. and is studied using a regular point lattice $L=L^d$ in d -dimensional Euclidean space, which considers the lattice graph edges as the relevant entities.

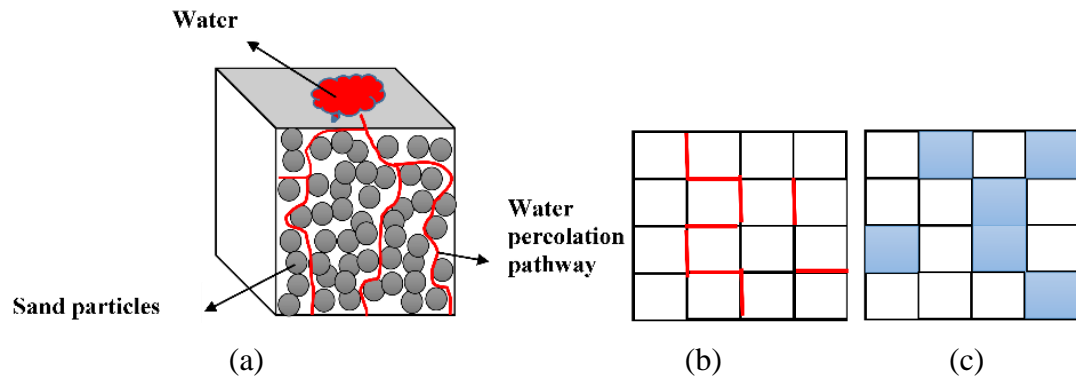


Figure 2.4. (a) Water percolation into the sand, (b) Bond percolation and (c) Site percolation.

In a slightly different mathematical notion, a site is occupied with a probability p or empty with a probability $(1 - p)$, using a regular point lattice $L=L^d$ in d -dimensional Euclidean space, for obtaining a random graph and is termed as a site percolation model. These two models, “site percolation” and “bond percolation” are referred to as classical percolation models in the literature. In general, the percolation theory represents adequate mathematical tools and the possibility of a physical description of phenomena, caused by the appearance of linked (quasi-linked) domains having typical body dimensions, i.e., percolation clusters of arbitrary nature: phases, defects, interfaces, etc [28].

2.6.1 Percolation in conducting materials:

Percolation is the simplest and fundamental model in statistical mechanics that exhibits phase transitions signalled by the emergence of a giant connected component [31]. In context to electrical characteristics and phase transition in materials, in particular to nanocomposites, the percolation of carbon nanotubes or another sort of nanoparticles has gained special attention within the previous two decades. Percolation theory is the simplest model displaying a phase transition. Due to the large aspect ratio of carbon nanotubes, even a small amount of doping (at a level of $0.01 \pm 0.1\%$) is enough to increase the conductivity of the material by more than ten orders of magnitude, thus changing it from an insulator to a conductor. At low doping, charge

transfer is of a percolation nature in the sense that nanotubes that are in contact with each other form conducting channels in the material [32]. Importantly, the conductivity has a threshold nature, so that the conduction jump occurs upon an arbitrarily small increase in a doping level above the critical value (V_c) (Figure 2.5 (a)) and can be described by a power-law expression shown in Eq.2.1 [33]

$$\sigma \propto (V - V_p)^\alpha \quad (2.1)$$

where V_p is the percolation threshold, V is the volume fraction of the dispersed inclusions, and σ and s are the electrical conductivity and a critical exponent respectively. Parameters in the above equation are determined through experimental electrical conductivity data fitting, which is obtained using the measured resistance along with the sample and sample dimension under test (Figure 2.5 (b)).

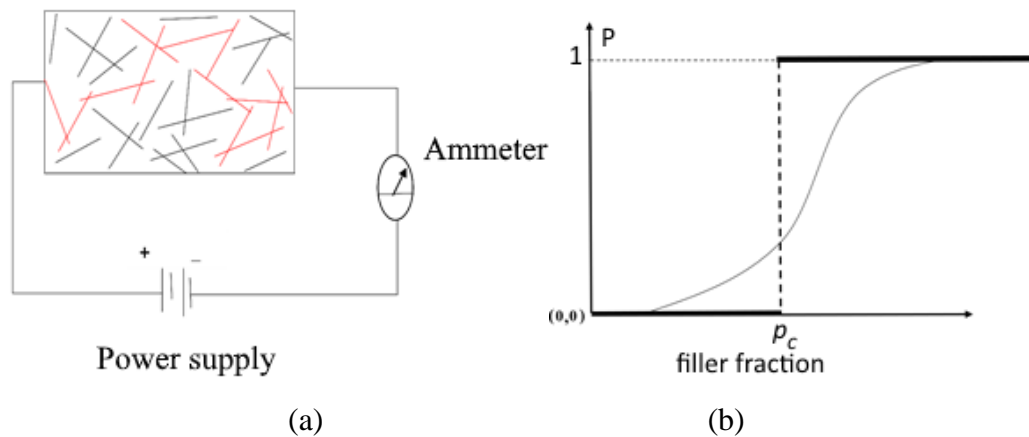


Figure 2.5. (a) Percolation network of carbon nanotubes in a polymer matrix. The red colour indicates nanotubes for giant network causing to happen phase transition while black colour tubes are used to represent tubes, not in the giant network. (b) The phase transition from insulator to conductor behaviour with a probability distribution and critical concentration.

2.7 QUANTUM TUNNELLING:

Quantum tunnelling or tunnelling is the quantum mechanical phenomenon where a subatomic particle (e.g. electron) passes through a potential barrier that it cannot surmount under the provision of classical mechanics. Quantum mechanics is a physical science dealing with the behaviour of matter and energy on the scale of atoms and subatomic particles/waves. The tunnel diode, quantum computing, and in scanning tunnelling microscope are prominent applications of quantum tunnelling [34]. Tunnelling is often explained in terms of the Heisenberg uncertainty principle that the quantum object can be known as a wave or as a particle in general. In terms of polymer-based nanocomposites, it is considered that electrical conductivity of a nanocomposite

can be governed by the electron tunnelling between neighbouring nanotubes besides being interconnected physically (ohmic contact). It is considered that polymer–CNTs exhibit the nature of a conducting polymer in such a way that the tunnelling of electrons occurs one by one from the first CNT electrode to the next-nearest neighbouring CNT electrode through a thin polymer barrier [35]. This kind of arrangement between CNT/polymer/CNT forms a conductive pathway. Multiple conductive pathways, when considered on the scale corresponding to the sample under test, constitute a conductive network. Such kind of networks is desired to achieve an electrical conductivity in a nanocomposite. The current distribution in nanocomposites is chaotic due to the random distribution of carbon nanotubes within the polymer matrix. Besides, there are many more conducting paths than the simple tip to tip paths [36]. Many of these paths carry current that is two orders of magnitude higher than that of conventional paths [36]. In contrary, some paths carry negligible current despite the tunnelling distance between CNTs remains within the (1-2 nm) range. In real material systems, physical parameters, such as the tunnelling resistance, can have large variations as a function of the junction configuration and materials properties of nanotubes and polymer. In addition to the tunnelling resistance, there is also the resistance of the conducting nanotube segments [37]. These two types of resistance form the resistor network for electron conductance. Nanocomposites with reasonable dispersion of carbon nanotubes, individual tubes are separated by polymer molecules and the resulted tunnelling resistance can be several orders larger in magnitude than the resistance of individual tubes. Considering the two types of resistors are always linked in alternating order in the resistor network, the much larger tunnelling resistance plays the determinant role in the electrical resistance of nanocomposites [37].

2.8 REFERENCES

- [1] S. Seal, S. C. Kuiry, P. Georgieva, and A. Agarwal, "Manufacturing nanocomposite parts: Present status and future challenges," *MRS Bull.*, vol. 29, no. 1, pp. 16–21, 2004.
- [2] M. De, P. S. Ghosh, and V. M. Rotello, "Applications of nanoparticles in biology," *Adv. Mater.*, vol. 20, no. 22, pp. 4225–4241, 2008.
- [3] A. Agrawal and J. P. Cronin, "(12) United States Patent," US 8,749,869 B2, 2014.
- [4] I. Khan, S. D. Mohan, M. Belbut, C. S. Kamma-Lorger, A. Mateus, and G. R. Mitchell, "Multiscale Structure Evolution in Electrically Conductive Nanocomposites Studied by SAXS," *Procedia Manuf.*, vol. 12, no. December 2016, pp. 79–88, 2017.

- [5] G. Matzeu, A. Pucci, S. Savi, M. Romanelli, and F. Di Francesco, "A temperature sensor based on a MWCNT/SEBS nanocomposite," *Sensors Actuators, A Phys.*, vol. 178, pp. 94–99, 2012.
- [6] A. Ashori, S. Sheshmani, and F. Farhani, "Preparation and characterization of bagasse/HDPE composites using multi-walled carbon nanotubes," *Carbohydr. Polym.*, vol. 92, no. 1, pp. 865–871, 2013.
- [7] G. Tegart, "Nanotechnology: The technology for the twenty-first century," *Foresight*, vol. 6, no. 6, pp. 364–370, 2004.
- [8] D. Lukkassen and A. Meidell, "Advanced materials and structures and their fabrication processes," 3ed., Narvik Univ. Coll., vol. 2, pp. 1–14, 2007.
- [9] L. Li et al., "Laser nano-manufacturing - State of the art and challenges," *CIRP Ann. - Manuf. Technol.*, vol. 60, no. 2, pp. 735–755, 2011.
- [10] Y. Yan et al., "Rapid Prototyping and Manufacturing Technology: Principle, Representative Technics, Applications, and Development Trends," *Tsinghua Sci. Technol.*, vol. 14, no. SUPPL. 1, pp. 1–12, 2009.
- [11] J. Kim and T. S. Creasy, "Selective laser sintering characteristics of nylon 6/clay-reinforced nanocomposite," *Polym. Test.*, vol. 23, no. 6, pp. 629–636, 2004.
- [12] J. Bai, R. D. Goodridge, R. J. Hague†, and M. Song, "Carbon nanotube reinforced Polyamide 12 nanocomposites for laser sintering," *Ecol. Econ.*, vol. 1, no. 1, pp. 1–7, 2012.
- [13] S. G. Kim, W. S. Chu, W. K. Jung, and S. H. Ahn, "Evaluation of mechanical and electrical properties of nanocomposite parts fabricated by nanocomposite deposition system (NCDS)," *J. Mater. Process. Technol.*, vol. 187–188, pp. 331–334, 2007.
- [14] H. Khalil, H. J. Gläsel, and M. R. Buchmeiser, "High-mechanical-strength flame-retardant nanocomposites based on novel Al(III)- and Zr(IV)-melamine phosphates and sulfates," *Macromol. Mater. Eng.*, vol. 298, no. 6, pp. 690–698, 2013.
- [15] J. A. Scholl, A. L. Koh, and J. A. Dionne, "Quantum plasmon resonances of individual metallic nanoparticles," *Nature*, vol. 483, no. 7390, pp. 421–427, 2012.
- [16] R. Hague, I. Campbell, and P. Dickens, "Implications on design of rapid manufacturing Proceedings of the Institution of Mechanical Engineers," in *Instn Mech. Engrs*, 2003, vol. 217, pp. 25–30.
- [17] T. Gutowski et al., "Note on the Rate and Energy Efficiency Limits for Additive Manufacturing," *J. Ind. Ecol.*, vol. 21, no. 0, pp. S69–S79, 2017.
- [18] M. Salmi, K. S. Paloheimo, J. Tuomi, J. Wolff, and A. Mäkitie, "Accuracy of medical models made by additive manufacturing (rapid manufacturing)," *J. Cranio-Maxillofacial Surg.*, vol. 41, no. 7, pp. 603–609, 2013.
- [19] H. Warren, R. D. Gately, H. N. Moffat, and M. In Het Panhuis, "Conducting carbon nanofibre networks: Dispersion optimisation, evaporative casting and direct writing," *RSC Adv.*, vol. 3, no. 44, pp. 21936–21942, 2013.
- [20] Y. Feng, H. Zou, M. Tian, L. Zhang, and J. Mi, "Relationship between dispersion and conductivity of polymer nanocomposites: A molecular dynamics study," *J. Phys. Chem. B*, vol. 116, no. 43, pp. 13081–13088, 2012.
- [21] S. Stassi, V. Cauda, G. Canavese, and C. F. Pirri, "Flexible tactile sensing based on piezoresistive composites: A review," *Sensors (Switzerland)*, vol. 14, no. 3, pp. 5296–5332, 2014.
- [22] R. Taherian, M. J. Hadianfard, and A. N. Golikand, "A new equation for

- predicting electrical conductivity of carbon-filled polymer composites used for bipolar plates of fuel cells,*” *J. Appl. Polym. Sci.*, vol. 128, no. 3, pp. 1497–1509, 2013.
- [23] N. A. Mohd Radzuan, A. B. Sulong, and J. Sahari, “A review of electrical conductivity models for conductive polymer composite,” *Int. J. Hydrogen Energy*, vol. 42, no. 14, pp. 9262–9273, 2017.
 - [24] M. Weber and M. R. Kamal, “Estimation of the volume resistivity of electrically conductive composites,” *Polym. Compos.*, vol. 18, no. 6, pp. 711–725, 1997.
 - [25] T. Peijs, “Nanocomposites and Multifunctional Materials,” in *Comprehensive Composite Materials II - 2nd Edition*, II., 2017.
 - [26] J. Lewis, “Material challenge for Outside of the active device layers ,there are a variety of requisite device flexibility.,” vol. 9, no. 4, pp. 38–45, 2006.
 - [27] S. Khan and L. Lorenzelli, “Recent advances of conductive nanocomposites in printed and flexible electronics,” *Smart Mater. Struct.*, vol. 26, no. 8, p. 083001, 2017.
 - [28] Alexander Herega, “Some Applications of the Percolation Theory: Review of the Century Beginning,” *J. Mater. Sci. Eng. A*, vol. 5, no. 12, pp. 409–414, 2015.
 - [29] P. J. Flory, “Molecular Size Distribution in Three Dimensional Polymers. I. Gelation,” *J. Am. Chem. Soc.*, vol. 63, no. 11, pp. 3083–3090, 1941.
 - [30] S. R. Broadbent and J. M. Hammersley, “Percolation processes: I. Crystals and mazes,” *Math. Proc. Cambridge Philos. Soc.*, vol. 53, no. 3, pp. 629–641, 1957.
 - [31] A. A. Saberi, “Recent advances in percolation theory and its applications,” *Phys. Rep.*, vol. 578, pp. 1–32, 2015.
 - [32] A. V. Eletskii, A. A. Knizhnik, B. V. Potapkin, and J. M. Kenny, “Electrical characteristics of carbon nanotube-doped composites,” *Physics-Uspekhi*, vol. 58, no. 3, pp. 209–251, 2015.
 - [33] A. A. Dietrich Stauffer, *Introduction to Percolation Theory*, 2nd ed. London: Taylor & Francis, 1991.
 - [34] G. R. Feng, Y. Lu, L. Hao, F. H. Zhang, and G. L. Long, “Experimental simulation of quantum tunnelling in small systems,” *Sci. Rep.*, vol. 3, pp. 1–7, 2013.
 - [35] C. Gau, C. Y. Kuo, and H. S. Ko, “Electron tunnelling in carbon nanotube composites,” *Nanotechnology*, vol. 20, no. 39, 2009.
 - [36] M. S. Tsagarakis and J. P. Xanthakis, “Tunneling currents between carbon nanotubes inside the 3-dimensional potential of a dielectric matrix,” *AIP Adv.*, vol. 7, no. 7, 2017.
 - [37] Y. Yu, G. Song, and L. Sun, “Determinant role of tunnelling resistance in electrical conductivity of polymer composites reinforced by well-dispersed carbon nanotubes,” *J. Appl. Phys.*, vol. 108, no. 8, 2010.

Chapter 3: Materials, methods and experimental techniques

3.1 INTRODUCTION:

This chapter offers an introduction to the materials, instruments and experimental techniques used in the thesis by outlining their relevant significance. This begins with a brief introduction of the materials and the characterization techniques used to characterise these materials. A brief theoretical background is provided wherever it is necessary. The key experimental techniques are discussed in the framework of this thesis such as electrical conductivity, spectroscopic, thermal analysis and microstructure characterization techniques. Electrical conductivity techniques include Two - probe method (direct current), Four - probe method (direct current) and broadband dielectric spectroscopy (alternating current) techniques. Synchrotron radiation, namely small angle X-ray scattering and wide-angle X-ray scattering are used as the key microstructure characterization techniques studying morphology and structure of the prepared nanocomposites. Fourier transform infrared spectroscopy technique is used to confirm crosslinking in the thermoset polymer-based nanocomposites. The behaviour of the 3 - D printed nanocomposites under the effect of heat is studied using simultaneous thermal analysis technique.

3.2 THERMOPLASTIC POLYMERS:

A polymer that softens upon application of elevated temperature and solidifies upon cooling is referred to as a thermoplastic polymer [1]. Such type of polymers has high molecular weight with long polymer chains, held together by relatively weak Van der Waals forces, having strong chemical valence bond along the chain [2]. They derive their features from their monomer units. These polymers can have either amorphous or semi-crystalline (or semi-amorphous) structure. An amorphous structure evolves from the random spatial arrangement of polymer chains while an ordered arrangement of polymer chains is referred to as crystalline structure. Crystalline polymers often show a significant portion of the amorphous phase in the structure depending on the preparation method. Literature suggests that this usually makes up 40-70% of the polymer sample [3]. Amorphous polymers are less resistant to chemical

attack and environmental stress than semi-crystalline polymers as they lack a crystalline structure. The physical properties of a thermoplastic polymer change drastically between the glass transition (T_g) temperature and the melting temperature (T_m) without the phase change. On the basis of this, some of the thermoplastic polymers are used above their T_g while others are used below [4]. Hard and rigid plastics, for example, polystyrene and poly (methyl methacrylate) are used below their glass transition temperatures for a variety of applications including automotive and home appliances. Their T_g is well above room temperature, both at around 100 °C. Elastomers or polymers with elastic properties like polyisoprene, polyisobutylene, and polycaprolactone are used above their T_g where they are soft and flexible. Such kind of polymers is used in applications such as sealants and insulations for high voltage cables. Thermoplastics above T_g are either amorphous or semi-crystalline depending on their molecular weight and crystallization temperature. Thermoplastic polymers are not 100% crystalline; rather exhibit a semi-crystalline morphology (Figure 3.1). Ordered lamellae consist of folded, composed and packed chains of the crystalline domains, which are surrounded by the randomly entangled polymer coils of the amorphous regions. Amorphous and crystalline domains are connected by tie molecules [5] as shown in Figure 3.1.

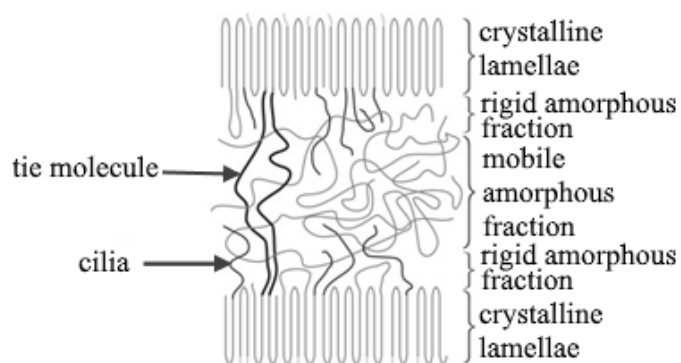


Figure 3.1. Complex phase structure of a semicrystalline polymer, where amorphous and crystalline regions are intimately connected [5].

Further, these molecules are linked to nearby crystalline domains through loose loops. Such molecules originate from the crystalline phase and protrude into the amorphous fraction [6]. Depending on the system temperature, the amorphous domains can be subdivided into the mobile amorphous and the rigid amorphous fraction [7]. The rigid amorphous fraction is the part of the amorphous domains adjacent to the crystalline lamellae, forming a constrained nanophase subsystem which

comprises 20 % to 30 % of the polymer [5]. The amorphous thermoplastic polymers are characterised by the presence of only the T_g but do not exhibit the T_m . On the other hand, semi-crystalline thermoplastics exhibit both T_g and T_m .

In this thesis, two thermoplastic polymers are used namely Acrylonitrile Butadiene Styrene (ABS) and Polycaprolactone (PCL). ABS is used for the printing of specially designed grips mounting on an extensometer. These grips serve a sample holding two ends of it under the effect of uniaxial deformation. PCL is used to prepare electrically conductive strands using additive manufacturing technology. These thermoplastics polymers are briefly discussed in the next sections.

3.2.1 Acrylonitrile butadiene styrene:

The ABS is an amorphous thermoplastic polymer and a dominant processing-material in industrial-grade fused deposition modelling (FDM) process. In the current work, it is used to print specially designed grips facilitating to calculate electrical conductivity by measuring the resistance across the samples under uniaxial deformation. It is obtained from Stratasys, Ltd (USA), in the form of a filament with a diameter 1.75 mm. ABS is a terpolymer and it is prepared through the polymerisation of styrene and acrylonitrile in the presence of polybutadiene. This results in a long chain of polybutadiene criss-crossed with shorter chains of poly (styrene-co-acrylonitrile). The proportions can vary from 15 - 35% acrylonitrile, 5 - 30% butadiene and 40 - 60% styrene [8]. Since the nitrile groups are naturally polar, their neighbouring chains attract each other and bind them together making ABS stronger than the ordinary Polystyrene. The structure of ABS and its constituting monomers are shown in Figure 3.2.

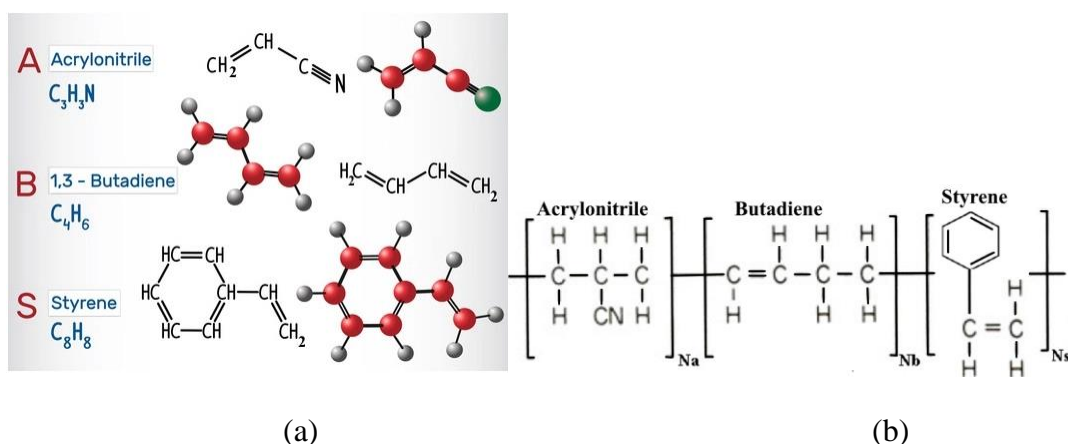


Figure 3.2. (a) Monomers of ABS. (b) Molecular structure of ABS [9].

The Styrene unit gives the plastic a glossy, impermeable surface. The Polybutadiene by nature is a rubbery substance providing toughness even at low temperatures. Its glass transition temperature is approximately 105 °C but it does not show a clear melting point being amorphous in nature. ABS plastics have electrical properties that are constant over a wide range of frequencies besides having prominent mechanical features [10]. Moreover, the electrical conductivity of the pure ABS remained under the magnitude of 10^{-15} S/m, which met the needs of a material as an insulator [11].

3.2.2 Polycaprolactone

Polycaprolactone (PCL) is a biodegradable polyester with a glass transition temperature around - 60 °C and a melting point of about 60 °C [12]. It is a semi-crystalline polymer and its crystallinity tends to decrease with increasing molecular weight [13]. Properties of PCL like solubility, low melting point (59 – 64 °C) and exceptional blend-compatibility has encouraged extensive research into its potential application in the biomedical field [14] [15]. Also, it is used mainly in thermoplastic polyurethanes resins for surface coatings and adhesives for synthetic leather and fabrics. It is used as an additive for resins to improve their processing characteristics and their end-use properties for an example impact resistance.

PCL is prepared by the ring-opening polymerisation of the cyclic monomer ϵ -caprolactone and was studied as early as 1930 [16]. Stannous Octoate, a compound of tin, is used as a catalyst for the polymerisation besides using low molecular weight alcohols to control the molecular weight of the polymer [17]. The reaction is given in Figure 3.3

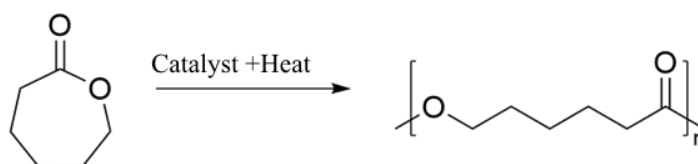


Figure 3.3 Ring-opening polymerisation of ϵ -caprolactone to Polycaprolactone.

PCL can form compatible blends with other polymers [13] due to which it can affect the degradation kinetics of those polymers. The advantages of PCL for numerous applications include tailorable degradation kinetics and mechanical properties such as ease of shaping and manufacture enabling appropriate pore sizes

conductive to tissue in-growth, and the controlled delivery of drugs contained within their matrix [13].

For the current study, PCL was supplied by Perstorp, Warrington, UK, which was a high molecular weight linear polyester derived from the ϵ -caprolactone monomer. The molecular weight of this PCL grade was 50000 mole/g. It was provided in granular form with approximately 3 mm pellet size. PCL is used to prepare electrically conductive nanocomposite films containing carbon nanotubes. Further, a bio extruder is employed to print strands using the prepared films. These strands were used to study the variation in the electrical conductivity under the effect of uniaxial deformation. PCL is also used to prepare epoxy-based nanocomposites.

3.3 THERMOSET POLYMERS

A polymer irreversibly hardened by curing of a soft viscous liquid (resin) is known as a thermosetting polymer. Curing is a chemical process employed in polymer chemistry that produces irreversibly a solid, insoluble, and infusible three-dimensional network of low molecular weight oligomers of a polymer resin [18]. A 3D network forms due to cross-linking of polymer chains through the application of heat, radiation, electron beams, or chemical additives. Characteristically, curing entails an increase in viscosity or hardness [19]. During cure reaction, thermoset resin transforms from a viscous liquid to a cross-linked gel or rubber that is regarded as a gel point. This is the point where thermoset resin sets due to chemical reactions or cross-linking between resin monomers and hardener component. In other words, gelation is the primary formation of a cross-linked network, and it is the most distinguishing characteristic of a thermoset [20]. For example, a thermoset loses its ability to flow above the gel point. Therefore, it is no longer processable and, hence defining the upper limit of the work-life.

Curing may or may not require a curing agent. Thus, two broad classes exist; i) curing induced by chemical additives (curing reagents or hardeners) and ii) curing in the absence of additives (self-curing) [21]. Moreover, crosslink density varies depending on the monomer or polymer resin and the process of crosslinking. Once cured, a thermoset polymer cannot be melted for reshaping, in contrast to thermoplastic polymers, which are easily reprocess-able with the application of heat, extrusion or injection moulding. Typical thermoset resins include, but not limited to, epoxies, phenolic, unsaturated polyesters, vinyl esters and bismaleimides. Such kind of

polymers is generally more durable than thermoplastic polymer in terms of mechanical properties including. These are designed to solve a variety of challenges and offers resistance to corrosive chemicals, superior adhesion and excellent mechanical properties. In this work, two types of thermosets are used as a matrix material to prepare nanocomposites that can conduct electrically under the effect of an external bias. These are polyurethane and epoxy thermoset polymers. These thermosets are briefly discussed in the approaching sections of this chapter.

3.3.1 Polyurethane

Polyurethane is one of the widely used thermoset polymers. Polyurethane was found by Otto Bayer in 1947 through a step-growth polymerisation of polyester polyols and diisocyanates without by-products [22]. A polyol is an organic compound containing multiple hydroxyl groups while isocyanates are a family of highly reactive, low molecular weight chemicals. These are sometimes referred to as part A and part B, respectively. In a general definition, polyurethanes are obtained by the reaction of polyisocyanates with polyhydroxy compounds including polyether, polyesters, castor oil and glycols. Thus, a typical polyurethane may contain aliphatic and aromatic hydrocarbon residues, ester, ether, and amide and urea group besides urethane linkages [23]. The reaction of an organic diisocyanate with a diol compound, leading to urethane linkages in the backbone ($-\text{NH}-\text{C}(=\text{O})-\text{O}-$), is indicated in Figure 3.4 [24]. The properties of a thermosetting polyurethane include ductility and low T_g . Polyurethanes can be classified into several different groups based on desired properties such as rigid, flexible, waterborne, binders, coating, adhesives, sealants and elastomers and the sources from which they are synthesized [25].

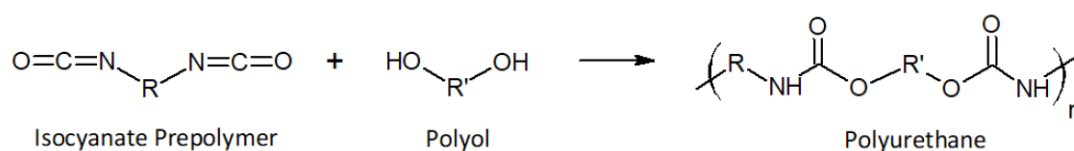


Figure 3.4. The general reaction between an isocyanate and Polyol.

Applications for Polyurethane materials have increased significantly over other kinds of thermosetting polymer materials. The significant characteristics of polyurethane including durability and toughness near to metals and the elasticity comparable to the rubber making them suitable to replace metals, plastics and rubber

in several engineered products [26]. They have also applied in biomedical, building and construction (adhesives and coatings), automotive, textiles and several other industries due to their superior properties such as hardness, elongation, strength and modulus.

In this study, electrically conductive nanocomposites are prepared using thermoset polyurethane as a matrix material containing multiwall carbon nanotubes as filler particles. It was a two-part thermoset polyurethane (TSPU) and was obtained from Huntsman group, Germany.

Polyol

There are two main types of polyols used to synthesise thermoset polyurethane: Polyetherols and Polyesterols. The Polyether polyols contain ether groups in the backbone and are the largest group of polyol used in thermoset polyurethanes while polyesters are used mainly in high-performance elastomers as the extra carbonyl groups allow for a more polar matrix with higher intermolecular forces [27]. Polyetherols are preferred for most applications as polyesters are more susceptible to hydrolysis [28]. The structures of ether and ester are illustrated in Figure 3.5.



Figure 3.5. (a) The general structure of an ether group. R and R' represent any alkyl or aryl substituent. (b) The general structure of an ester group. R and R' represent any alkyl or aryl substituent.

Most of the polyols had been used in the past to prepare polyurethanes were obtained from petroleum sources, but the high energy demands of the production process as well as environmental concerns have increased the necessity for more suitable and environment-friendly substitutes. This has recently drawn enormous commercial and academic attention to renewable resources, such as vegetable oils but these polyols are capable to partially replace petroleum-derived polyols [29]. Polyols are sometimes referred to as Part A for the sake of convenience. An industrial-grade polyol, containing the blend of hydroxyl groups from light hydrotreated petroleum distillates, is used in this study. It was a polyether polyol and was obtained from Huntsman group, Germany.

Isocyanates

Isocyanates are molecules containing the $\text{N}=\text{C}=\text{O}$ functional group, the carbon atom is highly electron-deficient due to delocalisation of electrons onto the electronegative heteroatoms. Isocyanates can react with any molecule containing an 'active' hydrogen atom [30] including amines, alcohols and carboxylic acids. There are four popular isocyanates (diisocyanates) used on an industrial scale and all are petroleum-derived. These are diphenylmethane diisocyanate (MDI), toluene diisocyanate (TDI), Hexamethyl diisocyanate (HDI) and isophorone diisocyanate (IPDI). Compared to other organic cyanates, MDI has relatively low human toxicity. The positions of the isocyanate groups influence their reactivity. In 4, 4' - MDI, the two isocyanate groups are equivalent but the two groups appear at different positions in 2, 4' - MDI which leads to differing in reactivities. The group at the 4 - position is approximately four times more reactive than the group at the 2 - position due to steric hindrance [31]. Steric hindrance at a given atom in a molecule is the congestion caused by the physical presence of the surrounding. They are referred to as a hard part or Part B.



Figure 3.6. Structures and the positions of the isocyanate groups in MDI isocyanate.

In this work, the MDI is used to crosslink polyol resin. This is an aromatic diisocyanate and contains two phenyl rings to an alkyl carbon atom as shown in Figure 3.6. It was obtained from Huntsman group, Germany.

3.3.2 Epoxy Thermosets

Thermosetting polymers are widely used within the engineering fields because of their versatility in tailoring the desired properties and performances in terms of strength, durability, thermal and chemical resistances as provided by the high cross-linked structure [32]. Epoxy is a member of a class of thermosetting polymers built up

from monomers, with an ether group, which takes the form of a three-membered epoxide ring. This three-membered epoxide ring is also known as oxirane group and is shown in Figure 3.7. Epoxy thermosets are high molecular weight polymers and encompass a wide range of properties depending on the curing agents, proportions, curing cycles and additives that can be added during their formulation [33]. The process by which chemical bonding is achieved is called curing, during which the fluid resin changes to a solid plastic [34]. Such kind of plastics is obtained through reacting a hardener with an epoxy resin or by reacting the resins with themselves. The reaction between an epoxy resin and hardener is exothermic. The hardener breaks the epoxide groups during the reaction linking together with several other molecules to produce a polymer with a three-dimensional structure offering the resultant material strength. In principle, any molecule containing reactive hydrogen may react with the epoxide groups of the epoxy resin [35]. Common classes of hardeners for epoxy resins include amines, acids, acid anhydrides, phenols, alcohols and thiols. It is possible to cure epoxy resin without using a hardener and the process is known as catalytic homopolymerisation. Epoxies are the attractive polymeric materials being used in fibre-reinforced composites and in many structural parts. In this way, epoxies are versatile with adhesive strength and hardness, impact resistance, electrical insulation and chemical and heat resistance [36].

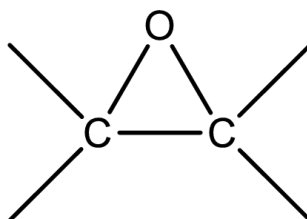


Figure 3.7. Structures of the epoxide group.

Aside from the aforementioned properties, epoxy resins have two main drawbacks that are their brittleness and moisture sensitivity. Like metals, many of these materials, and in particular fibre-reinforced composites, are notch-sensitive and lose much of their structural integrity when damaged. Damage can occur either at the time of manufacture or during service. Generally, it initiates from pre-existing defects (such as those due to fabrication processes) or stress concentrators (such as holes, corners or free edges) [34]. As a result, tremendous efforts had been focused on toughness improvement during the past three decades. The addition of a second phase,

either rigid or soft, offers a solution to this problem by improving the fracture toughness of brittle epoxies [34]. In addition, rigid particles, either inorganic or organic particles, have the potential to improve the fracture toughness of the epoxies [37].

In this work, diglycidyl ether of bisphenol-A (DGEBA) resin and Triethylenetetramine (TETA) hardener is used to prepare epoxy-based nanocomposites containing carbon nanotubes. The compositions were prepared to explore the possibility to 3D print epoxy-based electrically conductive materials.

Epoxy resins

Epoxy resins are low molecular weight pre-polymers that contain more than one oxirane group per molecule in their structure on average. A wide range of epoxy resins is produced on an industrial scale to fulfil industrial desires and requirements. These resins are quite stable at room temperature and gain their ultimate performance characteristics only when reacting with an appropriate proportion and curing agent. Epoxy resins can be crosslinked through a polymerisation reaction with hardener at room temperature or elevated temperatures. In general, resins cured at high temperature have improved properties such as higher glass transition temperature, strength and stiffness, compared to those cured at room temperature [38]. Epoxy resins include diglycidyl ether of bisphenol A (DGEBA), cycloaliphatic epoxy resins, trifunctional and tetrafunctional epoxy resins and Novolacs epoxy resins [39]. The epoxy resins are available in either liquid or solid states. Many epoxy resin precursors require to be heated to allow a sufficiently low level of viscosity for optimum mixing or dispersion of filler particles. The raw materials for epoxy resin production are today largely petroleum derived; although some plant-derived sources are now becoming commercially available examples including plant-derived glycerol used to make epichlorohydrin. Most common epoxy resins are produced from a reaction between epichlorohydrin (ECH) and bisphenol - A (BPA), though the latter may be replaced by other raw materials (such as aliphatic glycols, phenol and o-cresol novolacs) to produce speciality resins [40]. In terms of synthesis, ECH and BPA are charged into a reactor vessel where a solution of caustic soda is added (20 - 40 %) to the reaction as the solution approaches boiling point. After the evaporation of unreacted ECH, the two phases are separated by adding an inert solvent such as methylisobutylketone (MIBK). The resin is then washed with water and the solvent is removed by vacuum distillation [40]. The producers add specific additives to create special formulations that lend

special properties such as flexibility, viscosity, colour, adhesiveness, and faster curing, for a particular application.

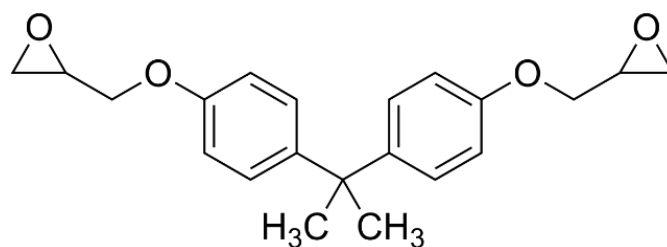


Figure 3.8. Structures of the epoxy resin used in this study for the preparation of electrically conductive nanocomposite for additive manufacturing.

In this work, a low molecular weight resin, with the two-oxirane ring in its structure, is used as a prepolymer to prepare thermoset epoxy plastic. Currently, DGEBA based resins are the most widely used resins on a commercial scale. It was obtained from Sigma Aldrich, Portugal and the structure is indicated in Figure 3.8. It has a density of 1.16 g/ml at 25 °C and having the molecular weight 340.41 g/mol.

Epoxy hardeners

Epoxy resin has a linear structure which may be cross-linked by curing agent into a macromolecular network structure and becomes insoluble and non-melting cured solid product [41]. This implies that epoxy resin solidification depends on the curing agent, commonly referred to as a hardener. There are various types of hardeners, which can be used in the hardening of epoxy resin. The epoxy resin curing reaction has been controlled or promoted by the type and concentration of epoxy hardening agents. The selection of these hardeners plays an important role in determining the properties of hardened epoxy (dry time, pot life, wetting ability, and penetration) [42]. Epoxy resin curing agents can be divided into three technologically important classes; (1) active hydrogen compounds (which cure by polyaddition reactions), (2) ionic initiators which can be further divided into anionic and cationic initiators, (3) cross-linkers which couple through the hydroxyl functionality of higher molecular weight Bisphenol A-type epoxy resin [43]. The chemistry of the first class of hardeners is based on polyaddition reactions that result in coupling as well as crosslinking with epoxy resin. The most widely used resins are based on active hydrogen compounds (polyamines, polyamides, polyacids, polymercaptans, polyphenols, etc.) undergo polyaddition via the compound containing the active hydrogen and the terminal carbon of the epoxide group, with a stabilization of the epoxide into a hydroxyl group.

In this research work, polyamines are briefly discussed as rest is beyond the scope of this study. Amine hardeners are further divided into three categories (i) aliphatic, (ii) aromatic, and (iii) cycloaliphatic amines as shown in Figure 3.9. The polyamines (primary, mixed primary and secondary, and combinations of these with tertiary amines) are useful and representative types of this class of hardeners. However, variations on the polyamines are numerous due to either resin characteristics or the necessity to improve specific properties or applications such as pot life, flexibility, speed of cure, lower toxicity, and lower exotherm in large castings. At room temperature, aliphatic amine does not react with cycloaliphatic resin. Aliphatic amines require accelerators such as tertiary amines or bisphenol-A and high temperature [44]. The amine hardeners in the absence of reactive hydrogen are called as blocked amines as they do not react with epoxy resin. These hardeners are relatively expensive and carcinogenic due to the amine group.

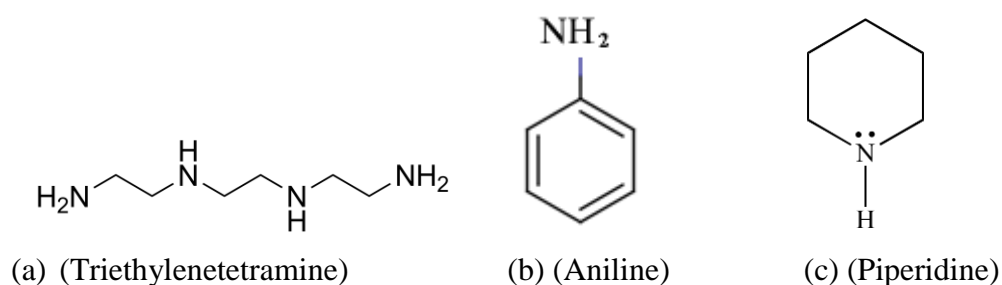


Figure 3.9. Example structure of (a) aliphatic, (b) aromatic and (c) cycloaliphatic amines.

The stoichiometry, variables affecting cure, mechanisms, and the chemistry of aromatic polyamine curing agents are similar to those of the aliphatic polyamines. However, aromatic polyamines also exhibit several basic differences; notably, a rapid reaction with cycloaliphatic epoxides. The most widely used aromatic polyamine curing agents are m-phenylenediamine, p, p'-diaminodiphenylmethane, and p, p'-diaminodiphenylsulfone. Aromatic polyamines are slower in the rate of reaction than aliphatic polyamines and do not cure at room temperature but require elevated - temperature for curing. This is because aromatic amines are more stable than aliphatic amines, being relatively less nucleophilic, hence need higher energy to destabilise them, therefore making slower to react [45]. The cycloaliphatic polyamine hardeners contain a ring structure that provides enhanced impact resistance. Cycloaliphatic curing agents generally provide better water/moisture resistance, weather ability and resistance to chemicals. The main cycloaliphatic polyamine hardeners are N-

aminoethylpiperazine (AEP), isophorone diamine, and 1, 2-diaminocyclohexane (MXDA) [46]. In general, amine hardeners are generally longer lasting and chemically resistant than amides [42]. In moist conditions, the tendency of blushing has also been observed in most of the amines. A waxy surface film is generally produced by the reaction of moisture in the air to that with hardener [42].

Polymerisation using Lewis bases, Lewis acids, salts or complex initiators is termed as ionic polymerisation. With Lewis bases, anionic polymerisation occurs whereas Lewis acids lead to the cationic polymerisation. Although both Lewis type bases and acids result in the same cured polymer, i.e., a polyether structure, their modes of initiation, propagation, and termination are different. Tertiary amines are the general class of anionic initiators most accepted commercially as curing agents for epoxy resins. Anionic initiators Pyridine, 2, 4, 6-tris (dimethylaminomethyl) phenol, benzyldimethylamine, and triethylamine are typical of the useful tertiary amines. A wide variety of compounds -notably the halides of tin, aluminium, zinc, boron, silicon, iron, titanium, magnesium, and antimony, as well as the fluoroborates of many of these metals-are cationic initiators for epoxy resins. The most important member of this class, in terms of commercial utilization, is the boron trifluoride (BF₃).

Several curing agents do not fit into the categories outlined above, however; some have achieved technological importance. A new family of curing agents appeared at the end of the 1960s because of the trend towards user-friendly systems, restricting the use of odorous and hazardous solvents, for ambient cure waterborne epoxies. The major portion of these is based on a water-reducible amine functional acrylic copolymer. Waterborne systems have a high level of mechanical properties, corrosion protection and chemical resistance regardless of their ability to cure slowly. Ambient curing relies on conditions that are available in an ambient environment such as moderate temperature, moisture, natural light and air. There is a class of crosslinker known as waterborne the hydroxyl reactive materials. Literature survey suggests that waterborne epoxy has immense potential, significance, and applications in the field of surface coatings [47], [48]. It is reported in the literature that curing agent, for some of the waterborne epoxy systems, serves a dual role i.e. as an emulsifying and as a crosslinking agent for the liquid epoxy resin [49]. There are three generic types of curing agents, all based on polyethyleneimine, which have been in common use in traditional solvent-borne epoxy coatings and have the basic amphiphilic structure. The first of these are amides prepared by the reaction of the amine with a fatty acid, III,

which are commonly referred to as amidoamine. The second is similar condensates prepared from dimer fatty acids, IV, known as polyamides. The final type, V, are prepared by the reaction of the amine with an epoxy resin and have come to be called amine adducts [49]. It should be noted that III - V is highly idealized structures. The polyethyleneamines themselves are mixtures of linear, branched, and cyclic structures [49].

DGEBA and TETA based epoxy thermoset

In this work, a low molecular weight resin is used as a prepolymer to prepare thermoset epoxy plastic. The DGEBA resin contains a two-oxirane ring in its structure. It was obtained from Sigma Aldrich, Portugal. The molecular structure of DGEBA and TETA is shown in Figures 8 and 9(a). Epoxy amine reaction is one of the most important reactions in the field of thermoset processing. The stoichiometry information regarding the reactivity of the DGEBA-based epoxy resin with amine type hardeners indicates that it progresses by the reaction of its epoxide groups through blocking, coupling, branching, and bonding reactions with the amine groups [50].

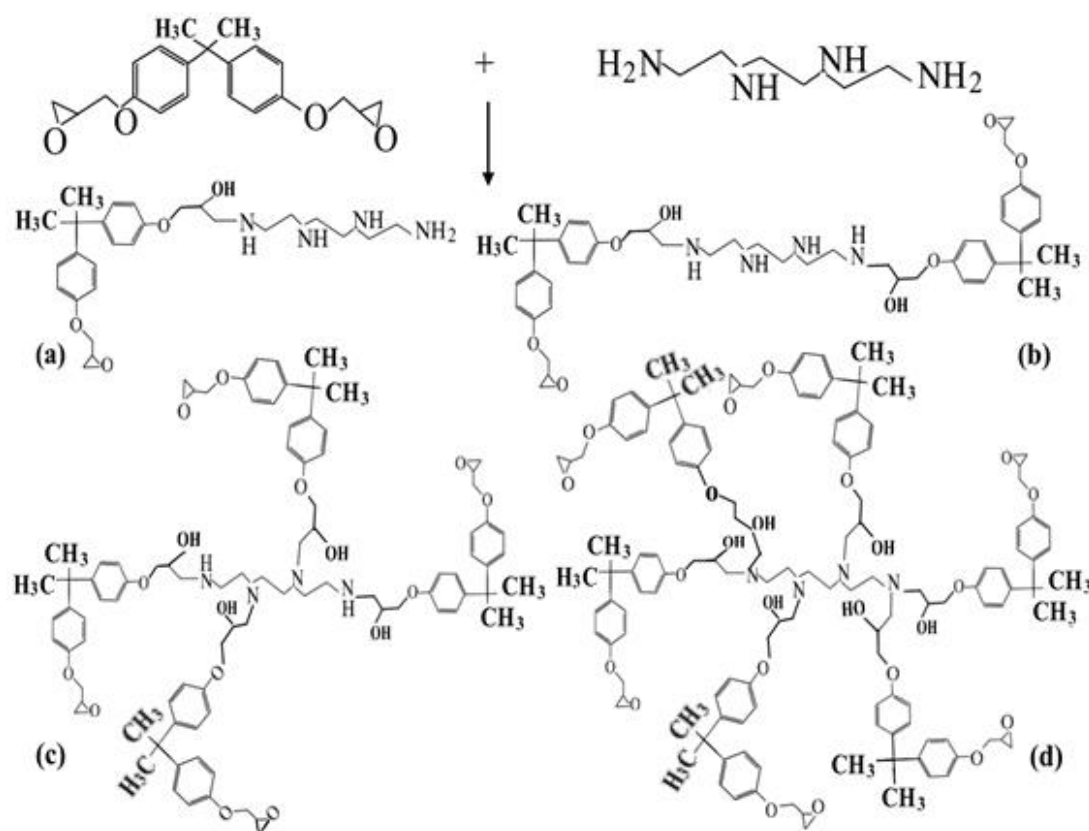


Figure 3.10. Schematic shows how TETA and DGEBA resin react [50].

The opening of oxirane rings of epoxy occurs via the transformation of the hydrogen atom of the amine functionality by nucleophilic addition, thus, joining the copolymer chains. The TETA molecule can link as many as six DGEBA molecules depending on the surrounding chemical environment [50]. The crosslinking reaction progresses through the initial steps of coupling and branching reactions. The final network structure and density depend greatly on the conversion process of coupling and branching into crosslinking, which in turn depends on the overall curing reaction conditions [50]. The reaction of TETA with DGEBA is given in Figure 3.10.

3.4 CARBON NANOTUBES

In 1990, Richard Smalley postulated the concept of buckyballs. But it wasn't until 1991 that Sumio Iijima, a researcher at NEC's Fundamental Research Lab, discovered needle-shaped structures during the acquisition of photographs of buckyballs in an electron microscope [51]. It turned out that these needle shapes were cylinders of carbon atoms that were formed at the same time that the buckyballs were formed [52]. Like buckyballs, these cylinders are called carbon nanotubes, which are a rolled lattice of carbon atoms covalently bonded to three other carbon atoms. Carbon nanotubes are buckyballs, but the end never closes into a sphere when they are formed. Instead of forming the shape of a sphere, the lattice forms the shape of a cylinder, as illustrated in Figure 11 below. The carbon nanotubes reported in the first report were composed of multi-wall tubes nesting concentrically [51].

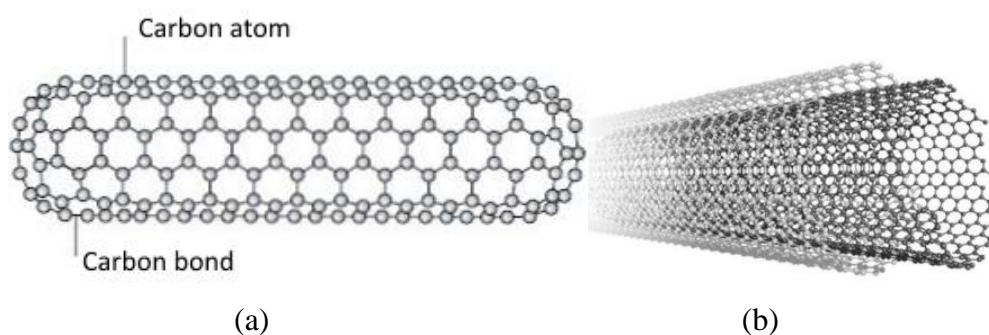


Figure 3.11. (a) Structure of single-wall carbon nanotube and (b) multiwall carbon nanotubes.

The geometrical structure of single-wall carbon nanotube and multiwall carbon nanotube is shown in Figure 3.11. The characteristic of carbon nanotubes, concerning conventional crystalline materials, is their size. The nanotubes have diameters in a range of a few nanometres and their lengths are typically a few micrometres. The

diameter of a nanotube is almost comparable to the size of an individual molecule, and therefore the carbon nanotube could be considered as a single molecule. Due to their size, carbon nanotubes behave as both molecule and solid, or their hybrid, and exhibit unique physical and chemical properties [52]. The other important factor, controlling the unique properties, comes from a variation of tubule structures that is caused by the rolling up of a honeycomb sheet of carbon atoms. There are many possible ways to do this, depending upon the direction of rolling. This could result in many chiral arrangements (spiral arrangement of carbon atoms) of the nanotube structures and a variety of diameters.

Variety of methods have been developed to produce carbon nanotubes in laboratory scale to industrial-scale quantities. These methods are chemical vapour deposition (CVD) [53], laser ablation [54], arc discharge [55], and high-pressure carbon monoxide disproportionation [56]. Most of these processes take place in a vacuum or with process gases. CVD growth of nanotubes can occur in a vacuum or at atmospheric pressure. Large quantities of nanotubes can be synthesized by these methods; advances in catalysis and continuous growth are making CNTs more commercially viable [57].

The intrinsic properties of CNTs make them the preferred material for use as electrodes in capacitors and batteries [58], transistors, electron emitter source with high current density, highly conductive electrical wire, the high thermal conductor for the heat radiator, the probe needle for scanning probe microscopes, molecular-sieves, gas adsorbers, and carriers for drug delivery systems in nano-bio medicine, etc. These possible applications play an important role in nanotechnology and are currently being investigated worldwide [52].

In the current study, multiwall carbon nanotubes (MWCNTs), having 3 to 6 walls, were purchased from Sigma-Aldrich, Portugal. The density of MWCNTs is 2.14 g/cm³. These were produced using the CVD method.

3.5 DISPERSION SOLVENTS

3.5.1 N, N-Dimethylformamide

N, N-Dimethylformamide (DMF) is a volatile solvent, albeit with a low evaporation rate. DMF is a member of the class of formamides, which is a formamide in which the amino hydrogens are replaced by methyl groups. DMF is prepared by combining methyl formate and dimethylamine or by the reaction of dimethylamine

with carbon monoxide [59]. It has a molecular formula and molecular weight as $[\text{HCON}(\text{CH}_3)_2]$ and 73.09 g/mole, respectively. It is a colourless liquid with a faint fishy odour and is slightly less dense than water. Its density is 0.94 g/cm^3 at 20°C and its vapours are heavier than air. It has the boiling point around 154°C , melting point -61°C and a flashpoint 58°C .

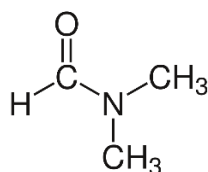


Figure 3.12. Structure of the DMF.

DMF is a high production volume chemical, primarily used as an industrial solvent. DMF solutions are used to process polymer fibres, films, and surface coatings; to permit easy spinning of acrylic fibres; to produce wire enamels, and as a crystallization medium in the pharmaceutical industry. It is also used to disperse filler particles into the polymer matrices through adsorption on the surface of the filler particles by a hydrophobic or $\pi - \pi$ bond interaction [60]. It has also been used in leather tanning, the production of pesticides and plastics, and the manufacture of adhesives, synthetic leathers, and surface coatings [61]. It is evidenced by experimental studies that DMF is carcinogenic [62]. For the current study, DMF (N, N Dimethylformamide) is obtained from Merck, Germany. It is used to acquire dispersion of carbon nanotubes into the polymer matrix. The structure of the DMF is shown in Figure 3.12.

3.5.2 Chloroform

Chloroform (also known as trichloromethane) is an organic polar compound. The very first use of chloroform was an anaesthetic in the medical field [63]. Later, it is used in other fields for an example in the production of the refrigerant R - 22, commonly used in the air conditioning business. It is one of the intermediate substance that occurs in the production of Polytetrafluoroethylene and commonly known as Teflon. In industry, chloroform is produced by heating a mixture of the chlorine with either methane (Eq. 3.1) or chloromethane [64]



Chloroform is used as a solvent. Chloroform is a colourless liquid with an ethereal odour. It has density 1.489 g ml^{-1} , melting point -63.5°C and boiling point 61.15°C . In this work, chloroform is used to disperse carbon nanotubes into the polymer matrix [65]. The structure of chloroform is given in Figure 3.13. The chloroform used in this work was obtained from Scharlau Chemie and it was 99% pure.

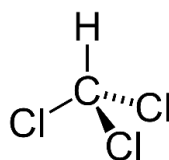


Figure 3.13. Structure of chloroform.

3.5.3 Dichloromethane

Dichloromethane or methylene chloride (DCM) is a geminal organic compound with the formula CH_2Cl_2 . This colourless, volatile liquid with a moderately sweet aroma is widely used as a solvent. Although it is not miscible with water, it is polar and miscible with many organic solvents [64]. It has a density of 1.32 g/cm^3 at 20°C . DCM has a melting point -96.7°C and boiling point around 39.6°C . It is produced (Eq. 3.2. and Eq.3.3) by treating either chloromethane or methane with chlorine gas at $400 - 500^\circ\text{C}$ [64].



Since DCM is a polar solvent, it can facilitate dispersing carbon nanotubes into the polymer matrix [66]. The structure of the DCM is given in Figure 3.14. DCM used in this study was obtained from Honeywell reagents with 99.9 % purity.

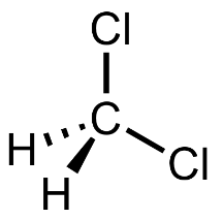


Figure 3.14. The structure of DCM.

3.6 TRITON X-100

Surfactants are compounds that lower the surface tension (or interfacial tension) between a polymer matrix and the filler particles when used to prepare composites. A surfactant is a substance that has the property of adsorbing onto the surfaces or interfaces of the system and of altering to a marked degree the surface or interfacial free energies of those surfaces (or interfaces) [67]. The use of a non-ionic surfactant Triton X - 100 was suggested in other studies [68] to treat the surface of carbon nanotubes for the nanocomposite fabrication, which can serve as a bridge between nanotubes and epoxy matrix without disturbing a structure or introducing defects into the nanotubes. The hydrophobic octyl group of the surfactant interacts with nanotube through adsorption, while the hydrophilic segment interacts with the polymer matrix through hydrogen bonding [69].

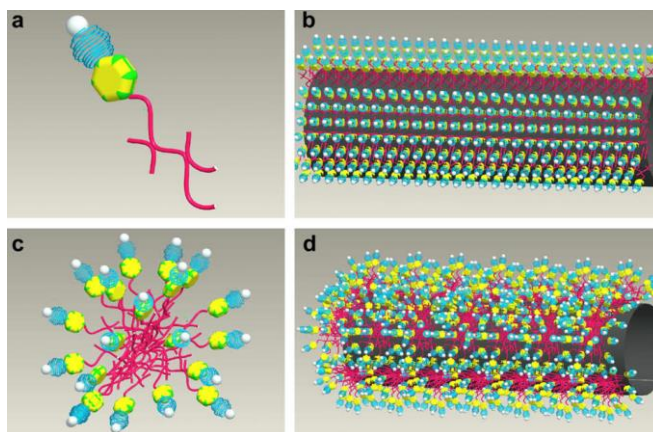


Figure 3.15. Schematics of (a) single Triton X-100 molecule; (b) a CNT wrapped by Triton X-100 molecules (1 CMC); (c) a Triton X-100 micelle; (d) a CNT wrapped by Triton X-100 micelles (10 CMC) [68].

The long tail (red colour) is a hydrophobic part, while the other end corresponds to the hydrophilic head (Figure 3.15 (a)). At a critical micelle concentration (CMC), the interface becomes saturated (Figure 3.15 (b)), and above the CMC, the molecules start to form aggregates or micelles (Figure 3.15 (c)). Because the larger the micelle size, the stronger the steric repulsive force introduced by micelles (Figure 3.15 (d)), it is expected that the surfactant with a higher concentration can disentangle more effectively large CNT agglomerates [68]. It can be said that the dispersion of nanotubes is caused by the steric repulsion occurred between hydrophilic heads of surfactant molecules attached to different nanotubes.

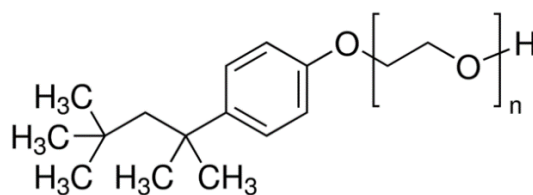
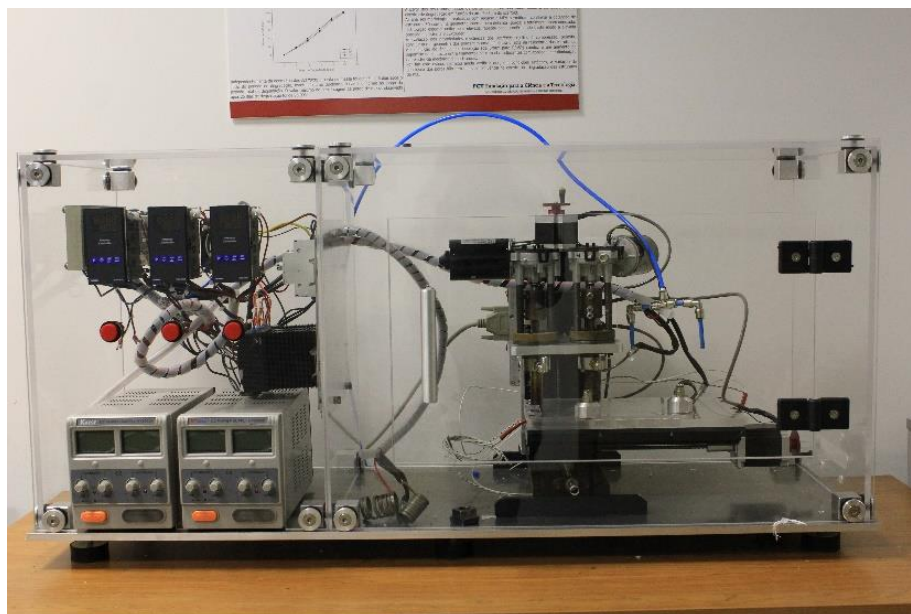


Figure 3.16. Chemical structure of Triton X-100 ($n = 9-10$).

Triton X - 100 was used in this study as a surfactant to improve the dispersion of carbon nanotubes into the polymer matrix. It was obtained from Sigma Aldrich. Triton X - 100 is a non-ionic surfactant that has a hydrophilic polyethene oxide chain and an aromatic hydrocarbon hydrophobic group. The chemical structure of Triton X - 100 is shown in Figure 3.16. It was received as a colourless to light yellow liquid with a density of 1.06 g/ml at 25 °C.

3.7 ADDITIVE MANUFACTURING SYSTEMS

In this study, two printers are used to print nanocomposites based on the matrix material containing carbon nanotubes. In this section, only a brief introduction of these printers is provided and a thorough description is provided in respective chapters. The first printer was a home built bio - extruder [70]. It is used to print thermoplastic polymer-based nanocomposites. The system takes information in the form of G - codes using a CNC- machines controlling software package. G-code is a numerical control programming language, which has many variants. There is a temperature control system to melt the polymer at the desired temperature due to which polymer flows towards the nozzle for printing. The screw rotation velocity is controlled by the voltage applied through a power supply. The bio - extruder can print material using a variety of nozzle diameter that has an impact on print quality. A compressed air line is attached to push the material downward that restrict material to stick against the walls of the reservoir. The reservoir has a capacity of around 10 ± 1 g. The deposition speed or print speed can be varied around 300 ± 100 mm/min. The second printer was a newly designed printer used for printing of thermoset polymer-based nanocomposites containing carbon nanotubes. It is an extrusion-based system works on the principle of a piston system. It has a syringe (10 ml) as a reservoir where material needs to load for printing. A special support system was also printed to hold syringe during printing. These two systems are shown in Figure 3.17.



(a)



(b)

Figure 3.17. Additive manufacturing systems used in this thesis to print electrically conductive nanocomposites using an (a) thermoplastic polymer-based matrix, (b) thermoset polymer-based matrix.

3.8 ELECTRONIC BALANCE

An electronic balance from Kern & Sohn, Germany, is used to measure the weight of nanoparticles and the polymers used in this study. The body dimensions (W x D x H) of this electronic balance are 225 mm x 315 mm x 330 mm having a net weight of 7 Kg. It can read 0.1 mg to 220 g weight of the material. The response time for the balance is 3 sec. It operates with 12 - volt power supply. The weighting plate

is made of steel having a diameter 80 mm. The balance is shown in Figure 3.18. The balance works on the principle of measuring the force that acts downward on the pan when the mass is placed on it. Such a force is equal to the product of the sample's mass and its acceleration due to gravity. This force strains the film, which causes to change resistance in it. The resistance is recorded by a strain gauge. A Strain gauge is a kind of sensor whose resistance varies under the effect of applied force. The load cells return to their original shape after removal of the load, and so do the strain gauges. Finally, the change in the electrical resistance is converted to a digital signal, which is then processed to look readable on the display.



Figure 3.18. The electronic balance used in the current study to prepare different compositions.

3.9 HEATING STAGE/MAGNETIC STIRRER

Heating stage coupled with a magnetic stirrer is used in this study acquiring mixing and dispersion of MWCNTs into the polymer matrix. A heating stage is used to remove unnecessary solvent from the composition that is used for the dispersion of the MWCNTs into the polymer matrix. The system used is an E- series, from Selecta, Spain. The unit has dimensions of 17 x 16 x 25 cm and a mass 3.5 kg. It has an upper temperature limit of 390 °C with a resolution of 1 °C. It comes with an upper rotational speed/ frequency 1600 rpm. The system is shown in Figure 3.19. The hot plate works on the principle of induction heating. In induction heating, an electrically conducting object (usually a metal) is heated by electromagnetic induction. The heat is generated in the object by the eddy currents. Eddy currents are the electric currents generated inside the conductor due to rapid penetration of alternating magnetic field into the object. The eddy currents flowing through the resistance of the material and heat it by Joule heating. Proportional integral derivative (PID) controller is used in induction

heating hot plate to control the temperature [71]. A PID controller continuously calculates an error value as the difference between the desired setpoint and a measured variable point and applies a correction based on proportional, integral, and derivative terms. The controller attempts to minimize the error over time by adjustment of a control variable, such as the opening of a control valve, to a new value determined by a weighted sum of the control terms [72]. A magnetic stirrer or magnetic mixer is a laboratory device that employs a rotating magnetic field to cause a stir magnetic bar immersed in a liquid to spin at a certain specified frequency. The rotating field may be created by a rotating magnet or a set of stationary electromagnets, placed beneath the vessel with the liquid. The magnetic coil technology is based on the inductive principle with alternative current (AC) as its driving force. The generated moving magnetic field drives the spinning of the stir bar in the vessel.



Figure 3.19. A hot plate used in this work.

3.10 INCUBATOR SHAKER

An incubator shaker is also used as a mechanical mixer besides using ultrasonic waves for the removal of organic solvent and the dispersion of MWCNTs. An incubator facilitates to protect material due to changes in temperature, humidity, CO₂ and O₂. Temperature can be regulated by water or air jackets. The incubator used in this study is purchased from IKA (KS 4000i control) and is shown in Figure 3.20. Its innovative design, having an LED display for speed (rpm) and time (0-999 hrs) settings, allowing unattended operation in a temperature-controlled environment. It has an integrated proportional–integral – derivative (PID) temperature controller maintaining temperature to the desired level. It has an adjustable speed (10 – 500) rpm and can shake weight up to 20 kg. The temperature can be set in the range of 5 °C to 80 °C.



Figure 3.20. Incubator used in the preparation of epoxy-based nanocomposites.

3.11 ULTRASONICATION

Nanoparticles come in the sub-class of ultrafine particles that are characterized by dimensions in the nanoscale, within the limits between 1 and 100 nm, with the recognition that these particles exhibit novel size-dependent properties. A discrete and identifiable nanoparticle in an engineered/ environmental system is sometimes referred to as primary nanoparticle and in this context, an ensemble of such nanoparticles is a larger structure commonly referred to as an aggregate of particles. Formally, an aggregate is a discrete assemblage of primary particles strongly bonded together through fusion, sintering, or metallicity bonded, which require energy to break and get apart [73]. While the distinction is often blurred, aggregates might also be differentiated from agglomerates, which are assemblages of particles (including primary particles and/or smaller aggregates) held together by relatively weak forces (e.g., Van der Waals, capillary, or electrostatic), that may break apart into smaller particles upon processing using sonication, high-intensity mixing or mechanical mixing [73]. Similarly, agglomeration and aggregation refer, respectively, to the process by which agglomerates or aggregates form and grow. It should be noted that, although here we define them as distinct entities, the terms aggregate and agglomerate are often used interchangeably to denote particle assemblies. Significant literature is available revealing the fact that properties of nanocomposites containing a polymer matrix with carbon nanotubes are significantly affected by the quality of dispersion of carbon nanotubes/nanoparticles [74] [75]. For the sake of this purpose, a variety of organic solvents, stabilisers and surfactants are used to achieve optimum dispersion of

carbon nanotubes into polymer matrix [76]. Besides the use of chemicals, considerable efforts were made towards mechanical methods including mechanical mixers and ultrasonicators [77]. Sonication is considered as an appropriate method amongst different mechanical methods as the energy required to break aggregates of carbon is comparable to that due to which nanotubes form an aggregate in a particular polymer system.

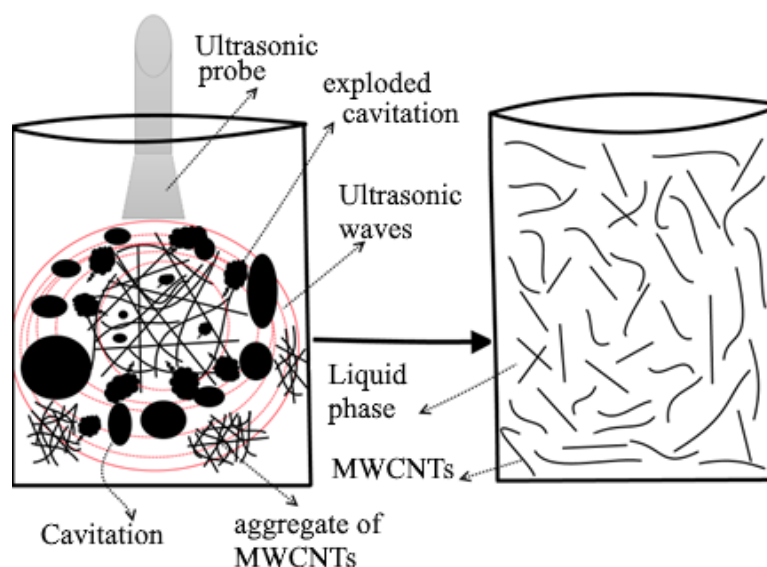


Figure 3.21. Schematic of ultrasonic wave generation using a probe sonicator leading to cavitation and hence facilitates in dispersing MWCNTs.

Sonication is the application of sound energy (higher than $\gg 20$ kHz) to agitate/disperse particles or fibres in aggregate or agglomerate through a process known as cavitation [68] as shown in Figure 3.21. In other words, through the process of sonication aggregate or agglomerates of carbon nanotubes are brought to breakdown and thereby facilitating to acquire a uniform dispersion of carbon nanotubes. In this process, ultrasonic frequencies >20 kHz are usually used, hence, the process is also known as Ultrasonication [73]. Ultrasonic waves can be applied using either an ultrasonic bath or an ultrasonic probe (sonicator). Both systems are shown in Figure 3.22.

When sonicating liquids at high intensities, the sound waves that propagate into the liquid medium result in alternating high-pressure (compression) and low-pressure (rarefaction) cycles, with rates depending on the frequency. During the low-pressure cycle, high-intensity ultrasonic waves create small vacuum bubbles or voids in the liquid. When the bubbles attain a volume at which they can no longer absorb energy,

they collapse violently during a high-pressure cycle. This phenomenon is termed cavitation. Cavitation is the collective effect of formation, growth, and implosive collapse of bubbles in a liquid leading to shock waves. Cavitation collapse produces intense local heating (~ 5000 K), high pressures (~ 1000 atm), and enormous heating and cooling rates ($> 10^9$ K/sec) and liquid jet streams (~ 400 km/h) [78]. Cavitation can be produced in different ways: e.g. by high-pressure nozzles, rotor-stator mixers, or ultrasonic processors. In all those systems, the input energy is transformed into friction, turbulence, waves and cavitation.

The rapid vibration of sound waves generates cavitation, formation and violent collapse of microscopic bubbles in a liquid, containing carbon nanotubes in the form of aggregates. The collapse of thousands of cavitation bubbles releases a tremendous amount of energy in the cavitation field within the liquid. Aggregates, agglomerates, and their surfaces within the cavitation field are strongly affected by this energy, which leads to disperse carbon nanotubes depending on the particular concentration of MWCNTs.



Figure 3.22. (a) Ultrasonic bath and (b) ultrasonic probe used in the current study to disperse MWCNTs.

In the current work, carbon nanotubes were dispersed in the polymer matrix using either an ultrasonic cleaning bath (Figure 22 (a)) or an ultrasonic probe sonicator (Figure 22 (b)). An ultrasonic cleaning bath is a high-quality unit with outer case and cleaner tank manufactured from rigid stainless steel also having a lid, made of Acrylonitrile butadiene styrene (ABS). It is from Langford Ultrasonic, UK. The outer and inner body dimensions (length x width x height) are 20 cm x 32 cm x 16.2 cm, and 10 cm x 13.5 cm x 24 cm, respectively. The tank capacity is 2.3 lit. It generates a

frequency of 40 kHz. through the power consumption of 100 Watt. Power source uses double half-wave high-frequency generators resulting in extremely efficient dispersing of particles/MWCNTs. The ultrasonic cycle time is fixed at 15 minutes that is not alterable and for less/longer duration need to use manual separate stopwatch/ repeat the cycle. The other sonicator used in this study is an ultrasonic probe sonicator that is a handheld ultrasonic homogenizer (UP200Ht), with 200 watts, from Hielscher, Germany. It has a digital control system with a touch screen to operate it. Generally, it is used for the sonication of sample volumes from 0.1 to 1000 ml. The device can be used as a handheld or stand-mounted ultrasonic lab device. It is possible to use probe sonicator in a pulsed mode or continuous mode depending on the requirement. The bath sonicator operates with low frequency and therefore agitates particles less vigorously and takes a relatively long time as compare to probe sonicator for the dispersion of carbon nanotubes into a polymer matrix.

3.12 ELECTRICAL CONDUCTIVITY CALCULATION

Electrical conductivity is the measure of a material's ability to allow the transport of an electric charge and it is the reciprocal value of the magnitude of the electrical resistivity. It is important to mention at this stage that electrical conductivity studied, in the current work, is bulk DC (direct current) electrical conductivity. Therefore, in the whole of this thesis wherever electrical conductivity mentioned, the reader should consider it as a bulk DC electrical conductivity of the material under study. The AC (alternating current) electrical conductivity will be particularly mentioned if stated somewhere. Two methods were used to measure the electrical conductivity in the printed/ unprinted samples, namely, the two-probe method and four-probe method. In the two-probe method, the contact resistance is ignored in comparison to bulk resistance of the samples under the assumption that composite samples have electrical conductivity intermediate in magnitude between that of a conductor and an insulator. The four-probe method is free from such kind of errors, as it does not include contact resistance when measured across the samples [79].

3.12.1 Two probe method

Two - probe method is used for measuring the electrical conductivity in the nanocomposites. The contact resistance is ignored in this experimental set-up as it is admitted that it will be much lower than the resistance of the sample under test. The

resistance (R) of a conductor, at a constant temperature, is proportional to its length L and inversely proportional to its area of cross-section A [80]. Mathematically, the above is represented in the form of Eq. 3.4.

$$R = (1/\sigma)(L/A) \quad (3.4)$$

Where,

$$A = wx t$$

$$\sigma = \frac{1}{R} (L/A) \quad (3.5)$$

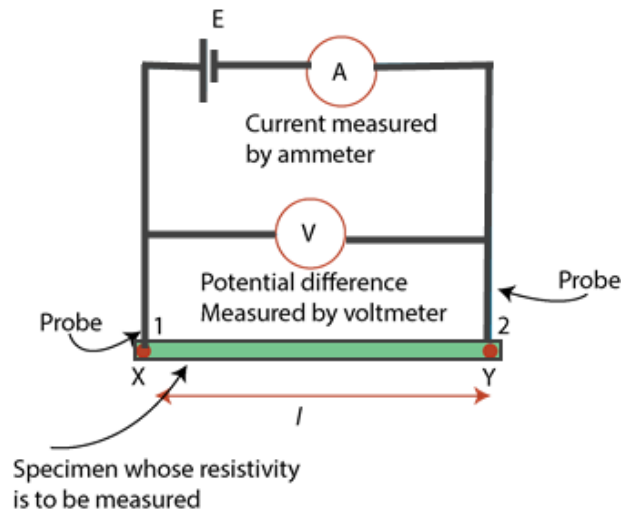


Figure 3.23. Schematic of the two probes experimental setup used to measure the electrical conductivity in 3D printed specimen.

Where σ is a proportionality constant and represent the electrical conductivity of the sample under test. The parameters L and A represent the length and the area of cross-section of the sample under test. The resistance is measured in the unit of an ohmmeter. Hence, the electrical conductivity of the sample is measured by measuring the voltage drop across the sample due to passage of a known current supplied by the source of current through the probes at the two ends of the sample as shown in Figure 3.23. The potential difference (V) between the two contacts at the ends of the sample can be measured by a voltmeter. In this work, electrical conductivity is measured with the help of Eq. 3.5.

3.12.2 Four probe method

Four-probe set-up is one of the standard and most widely used set-up for the measurement of electrical conductivity in materials. In the four-probe method, the experimental set up consists of four probes arrangement, a sample, a constant current source, and digital multimeters for the sake of current and voltage measurements.

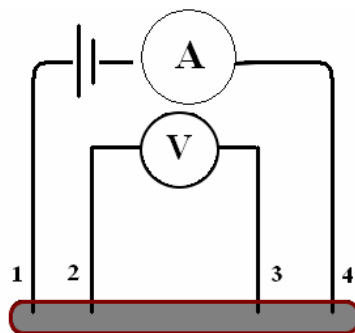


Figure 3.24. A four-probe set- up for measuring the electrical conductivity in samples used in the current study.

It consists of four probes placed on the sample in such a way that outer two probes are used to feed electric current into the sample while inner two probes are used to sense the corresponding voltage drop due to passage of electric current. The experimental configuration is shown in Figure 3.24. The amount of current passes through the specimen depends on the electrical conductivity of the specimen under test [81]. A constant source of current is used for this purpose. If the potential drop measured across the middle two probes is V when a constant current I passes through the outer two probes, then the electrical conductivity of the specimen can be given with the help of Eq. (3.6),

$$\sigma = \frac{\ln 2}{\pi \cdot T} (I/V) \quad (3.6)$$

Where I and V , indicate electric current and corresponding voltage drop in the sample and T is the thickness of the sample under test.

3.12.3 Equipment Specifications

Electric current and corresponding voltage drop are measured by two digital multi-meters, both from Thurlby Thandar, model TT - 1906. In this thesis, “voltmeter” refers to a voltage mode while “ammeter” refers to the electric current mode of TT - 1906 multi-meters. The constant current sources used in this thesis were tuneable in the range $1 \mu A - 5 mA$. A blade is used to scratch a specific surface point on the samples to achieve reasonable contact and to avoid the surface layer of the polymer. Two types of extensometers are used acquiring uniaxial deformation in the samples. One of the extensometers is home (CDRSP) built system for custom-designed experiments e.g. deformation study under the effect of temperature and performing simultaneous scattering experiments. The other system belongs to NCD-SWEET beamline, ALBA Synchrotron, Barcelona, Spain.

3.13 EXTENSOMETERS

Two systems are used to deform 3 D- printed electrically conductive strands. One of the systems is used for the simultaneous measurement of electrical conductivity under the effect of uniaxial deformation (Figure 3.25 (a)). Specially designed 3 D printed grips are used in this set up for holding the sample under uniaxial deformation. The other system is used to deform the sample in such a way that electrical conductivity was measured before and after deformation (Figure 3.25(b)). In this setup, the simultaneous measurement of electrical conductivity under the effect of uniaxial deformation is not possible due to the design and metallic sample holding grips.

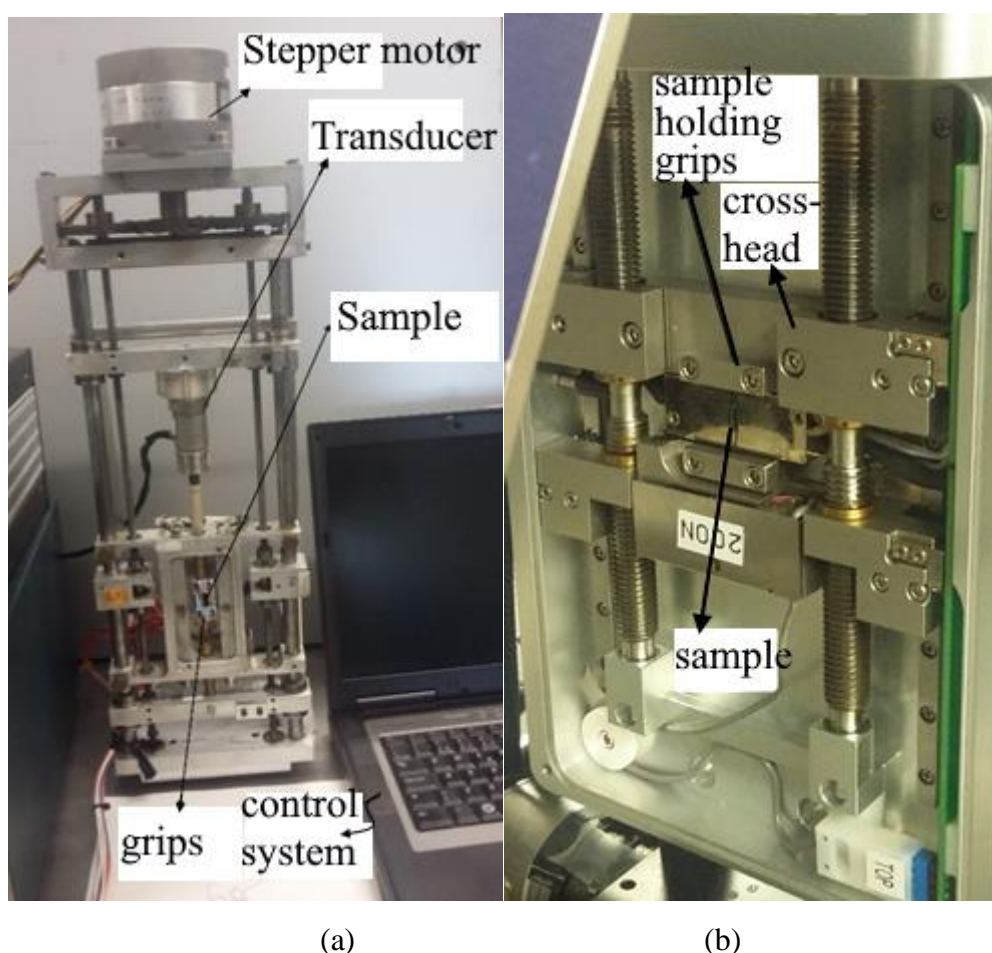


Figure 3.25. Extensometers used at ALBA synchrotron for; (a) the simultaneous and (b) non-simultaneous measurement of the electrical conductivity under the effect of uniaxial deformation.

3.13.1 Concept and design of sample holding grips

In this thesis, besides concentration effects of carbon nanotubes, electrical conductivity and microstructure (SAXS and WAXS) are studied simultaneously under the effect of uniaxial deformation. For this purpose, special grips were designed for

holding the samples during uniaxial deformation and thereby facilitating current and voltage measurement without sample slipping, fracture and misalignment. Additionally, these grips isolate the current and voltage measuring circuit to avoid short circuit during the data acquisition. These experiments were performed at the ALBA Synchrotron facility, Barcelona, Spain using BL11-NCD (SWEET) beamline. Solidworks from 3D CAD software was used to design the grips. Afterwards, the CAD drawing is converted to an STL format file. The object is ready to manufacture after generating the STL file. Figure 3.26 shows the top and bottom of the designed grips generated using Solidwork software.

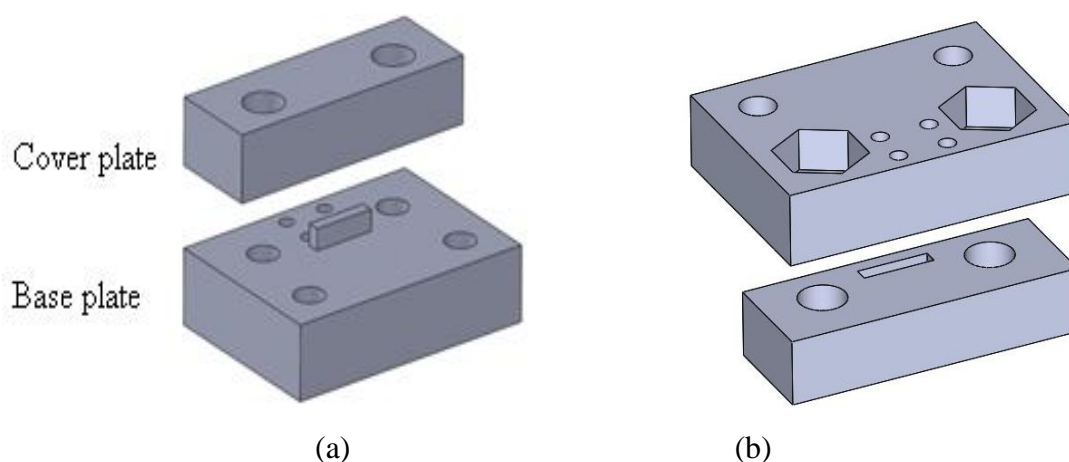
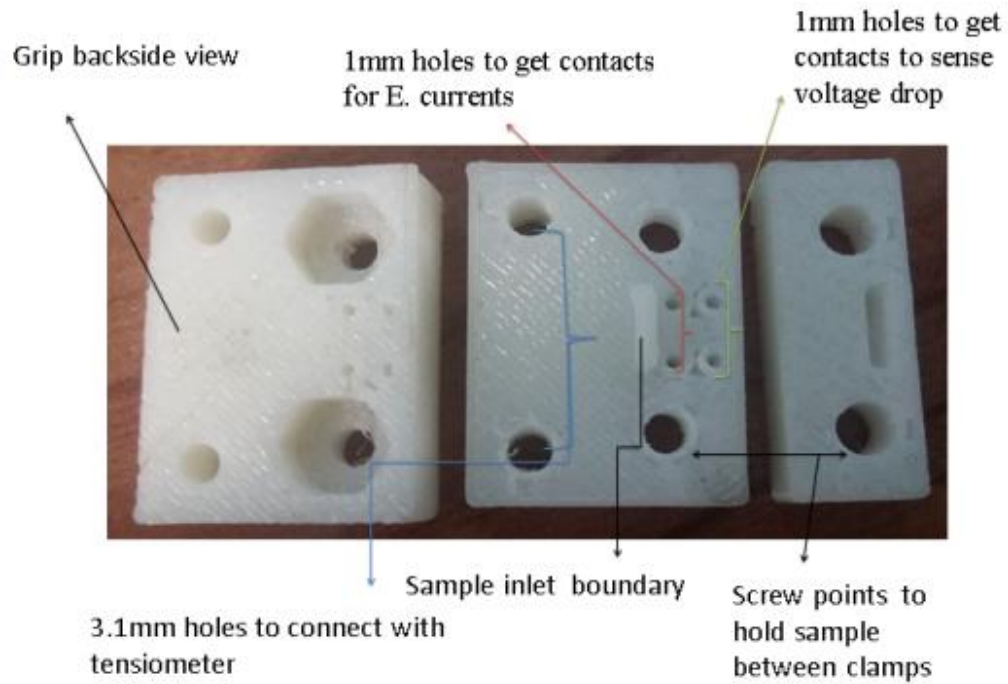
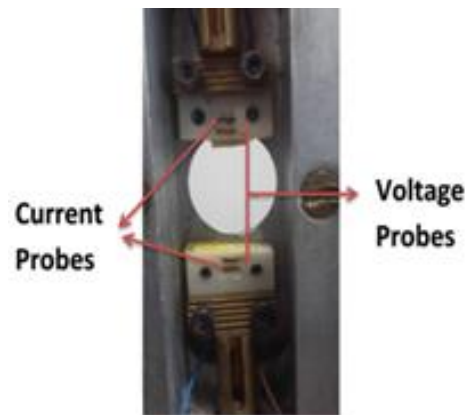


Figure 3.26. A CAD model of the designed grips. (a) Top view; (b) bottom view.

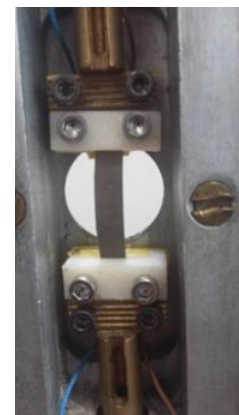
An amorphous thermoplastic polymer acrylonitrile butadiene styrene (ABS) is used to print these grips having an electrical conductivity far below than the material under test. These grips prove to be useful as several experiments can be performed with one set of these grips. The grips fracture after testing around 25 ± 5 samples. Figure 3.27 depicts a full description of the printed grips concerning designated points for the electrical connections, sample mounting and the mounting of grips on the extensometer.



(a)



(b)



(c)

Figure 3.27. The final 3D printed grips, with specific points where wires make physical contact with sample under test for electric current and corresponding potential. (a) 3D printed grips with designated locations for electrical contacts to the sample when mounted between grips. (b) Grips mounted on the extensometer with designated connections for measuring electrical current and corresponding voltage drop in the sample under test. (c) A test sample is mounted for simultaneous measurement of electric current (I) and the corresponding voltage drop (V) under the effect of uniaxial deformation.

3.13.2 Data acquisition systems

Two computer systems are used to record the data. One of the systems is a Toshiba laptop with window XP. It is used to record electric current, corresponding voltage drop and the uniaxial deformation data. The microstructure changes, under the

effect of uniaxial deformation, in the form of small angle and wide-angle x-ray images that are recoding to the second system belonging to NCD - SWEET, ALBA Synchrotron facility. The experiment is conducted in such a way that the variations in the electrical conductivity, variation in the microstructure (SAXS and WAXS) and the uniaxial deformation effects of the sample under test are recorded for a specific interval of time. This is achieved using different need based on written programs. A home written programme is used to record data from the electric current (I), and the voltage drop (V). The information about the programme is supplied as supplementary information at the end of the thesis. This programme allows recording three data points per second. The data is saved in an ASCII file.

3.14 BROADBAND DIELECTRIC SPECTROSCOPY

The broadband dielectric spectroscopy (BDS) deals with the frequency response of the materials. It is an experimental technique and performed in the frequency domain by varying the frequency of the applied alternating current (AC) field to carry out a variety of measurements [82]. These measurements include but not limited to dielectric properties, energy storage and dissipation properties and impedance of the material under test. The acquisition and reliability of these measurements depend on the choice of appropriate configuration depending on the frequency range. It is possible to investigate the microscopic dynamic behaviour of the molecules in a broad range of frequency (10^{-6} Hz to 10^{12} Hz). The intensive complex dielectric quantities including dielectric permittivity $\epsilon^*(\omega)$, electrical modulus $M^*(\omega)$, electrical conductivity $\sigma^*(\omega)$ and resistivity $\rho^*(\omega)$ are immediately derivable from $Z^*(\omega)$. It is important to mention here that

$$\omega = 2\pi f, \text{ where } f \text{ is the measuring frequency in Hz} \quad (3.7)$$

BDS data is expressed in terms of the aforementioned quantities to study materials. Dipole relaxation behaviour is normally represented in terms of ϵ^* and electric conduction behaviour in terms of σ^* , Z^* , M^* or ρ^* depending on the particular problem involved to study material under test.

The 3D printed sample (minimum diameter ≈ 7 mm and thickness ≈ 1 mm) is mounted between external electrodes connected to the appropriate analyser for measuring the complex impedance of the sample. The inter-electrode distance was the thickness of the 3D printed sample. In the simplest configuration of the technique, a

small amplitude of a sinusoidal (AC) signal $V(\omega)$ is applied to the sample under test to perturb the system and the frequency response recorded as impedance and phase angle [83].

$$V(\omega) = V_o \exp(i\omega t) \quad (3.8)$$

The output current of the system is represented as

$$I(\omega) = I_o \exp(i\omega t + \varphi) \quad (3.9)$$

Where $\omega = 2\pi f$. The complex impedance (Z^*) of the circuit at any frequency f can be presented by Ohm's law

$$Z^* = V(\omega) / I(\omega) = (V_o / I_o) \exp^{-i\varphi} = Z_o \exp^{-i\varphi} \quad (3.10)$$

$$Z^* = Z_o \cos\varphi - Z_o \sin\varphi \quad (3.11)$$

$$Z^* = Z' - iZ'' \quad (3.12)$$

Where Z' and Z'' are real and imaginary parts of the complex impedance Z^* , respectively. The modulus, phase angle and parts of the complex impedance are given as the following:

$$Z' = Z_o \cos\varphi \quad (3.13)$$

$$Z'' = Z_o \sin\varphi \quad (3.14)$$

$$|Z| = \sqrt{(Z')^2 + (Z'')^2} \quad (3.15)$$

$$\varphi = \tan^{-1} (Z'' / Z') \quad (3.16)$$

Impedance spectroscopy is used to characterize the dielectric behaviour of the material in terms of the complex impedance (Z^*), complex permittivity or dielectric constant (ϵ^*) and complex modulus (M^*). The representations of complex permittivity and modulus are used in analysing the dielectric response of the test sample. The complex permittivity is expressed as:

$$\epsilon^* = \epsilon' - i\epsilon'' \quad (3.17)$$

where (ϵ') is the real part of the complex permittivity often referred to as the dielectric constant, and (ϵ'') is the imaginary part of the complex permittivity referred to the dielectric loss. The dielectric constant is a measure of the amount of energy stored, and the dielectric loss is a measure of the amount of energy dissipated in the dielectric material under an applied electric field. The complex dielectric function contains information about polarization, conduction, and molecular dynamic processes

in the sample [84]. The dielectric constant (ϵ') and dielectric loss (ϵ'') can be presented as:

$$\epsilon' = Z''/2\pi f C_o Z^2 \quad (3.18)$$

$$\epsilon'' = Z'/2\pi f C_o Z^2 \quad (3.19)$$

where C_o is the geometrical capacitance in the vacuum of the same dimension defined as

$$C_o = \epsilon_o A/d \quad (3.20)$$

A is the area, d is the thickness of the samples and ϵ_o is the permittivity of free space having a defined value 8.854×10^{-12} F/ m. It is obvious from Eq. 3.20 that capacitance of a material depends on the geometry of the material and the dielectric constant. Moreover, the AC electrical conductivity (σ_{AC}) can be calculated using the following relation [83],

$$\sigma_{AC} = 2\pi f \epsilon'' \epsilon_o \quad (3.21)$$

The setup consists of the sample holder, cryostat, a liquid nitrogen Dewar with pressure sensor, two heating units (Dewar and gas heaters) three temperature controllers (for the Dewar, gas and sample temperature) and a vacuum pump. The sample holder is placed inside the cryostat where the temperature of the sample is varied by the flow of cold nitrogen gas, which passes through the gas heaters inserted between the Dewar and the cryostat. A PT-100 platinum resistor sensor was used to measure the sample temperature, by placing it in thermal contact with one of the capacitor plates. The temperature range of the system can vary between 293 °K and 333 °K with a precision of 0.1°K.

3.14.1 System specification

The broadband dielectric and impedance spectroscopy experiments were conducted in the laboratory of “Group of Characterization of Materials (GCM)” of the Polytechnic University of Catalonia (UPC), Barcelona, Spain. The epoxy-based 3D printed samples are used to measure the electric and dielectric response of the samples using two-electrode spectroscopic measurements. An “Alpha Analyzer”, from Novocontrol Technologies GmbH & Co., Germany (Figure 3.28), was used to study

electric and dielectric behaviour of nanocomposites containing carbon nanotubes as filler particles.

The frequency range used for the experiments is 1×10^{-2} Hz – 10×10^6 Hz while the samples scanned under the effect of temperature using the -60 °C – 50 °C. The electrodes used for the experiment have a 2.0 cm diameter. The alternating current voltage (V_{rms}) used for the experiment is 1.0 V. The data is measured for alternating current electrical conductivity under the effect of frequency. Besides, the data is collected for the real and the imaginary parts of dielectric constant and impedance of the material.



Figure 3.28. The system used to conduct broadband dielectric spectroscopic experiments.

3.15 USE OF SYNCHROTRON RADIATION

Synchrotron radiation is electromagnetic radiation emitted by charged particles (e.g., electrons and ions) that are moving at speeds close to that of light when their paths are altered using a magnetic field (bending magnets, wigglers or undulators) [85]. If the particle is non-relativistic, then the emission is termed as cyclotron emission, contrary to that if the particles are relativistic, the emission is referred to as synchrotron emission. Synchrotron radiation may be achieved artificially in synchrotrons or storage rings, or naturally by fast electrons moving through magnetic fields. These synchrotrons are ring-shaped machines that are often very large. The radiation produced in this way has a characteristic polarization and the frequencies generated ranging over the entire electromagnetic spectrum. The bending magnets,

undulators or wigglers are used to change the direction of the beam [85]. The bending magnets are placed at many locations on the ring to guide the beam along the reference path. Undulators consists of a periodic structure of dipole magnets (permanent magnets or superconducting magnets). The static magnetic field alternates along the length of the undulator with a wavelength (λ). Electrons traversing the periodic magnet structure are forced to undergo oscillations and thus to radiate energy. The radiation produced in an undulator is very intense and concentrated in narrow energy bands in the spectrum. The radiation is guided through beamlines for experiments in various scientific areas. The undulator strength parameter is defined in Eq. 3.22 [86].

$$K = \frac{eB\mu}{2\pi c m_e} \quad (3.22)$$

Where e is the electron charge, B is the magnetic field, μ is the spatial period of the undulator magnets, m_e is the electron rest mass, and c is the speed of light. There have been over 70 synchrotron light sources constructed for scientific and technical purposes all over the world, mostly in the USA, Europe, and East Asia [87]. Two types of experiments can be performed using synchrotron radiation.

First-generation synchrotron light sources were beamlines built onto existing facilities designed for particle physics studies. Second-generation synchrotron light sources were dedicated to the production of synchrotron radiation and employed electron storage rings to harness the synchrotron light [88]. Current (third-generation) synchrotron light sources optimise the intensity of the light by incorporating long straight sections into the storage ring for ‘insertion devices’ such as undulator and wiggler magnets. Wigglers create a broad but intense beam of incoherent light. Undulators create a narrower and significantly more intense beam of coherent light, with selected wavelengths, or ‘harmonics’, which can be ‘tuned’ by manipulating the magnetic field in the device. Consequently, third-generation light sources typically have much brighter photon beams than previous ones [87]. The third-generation light sources can accommodate as many undulator beamlines as possible [89]. These include the scattering of light by atoms and the absorption of light by atoms. Almost all the uses of synchrotron radiation fit into one or other category. When photons interact with matter, the probability of absorption or scattering depends on the photon energy and the type of atom involved. In general, with increasing photon energy the absorption probability goes down and the scattering probability goes up [90]. The work covered in this thesis is based on scattering experiments.

3.15.1 Properties of synchrotron radiation

Synchrotron radiation is preferred over the laboratory sources due to the following advantages [87].

- o Broad Spectrum: the users can select the wavelength required for the particular experiment configuration.
- o High Flux: high-intensity photon beam allows rapid experiments
- o High Brilliance: highly collimated photon beam generated by a small divergence and small size source (spatial coherence).
- o High Stability: submicron source stability.
- o Polarization: both linear and circular.
- o Pulsed Time Structure: pulsed length down to tens of picoseconds allows the resolution of process on the same time scale.
- o Simultaneously small and wide angle X-ray scattering experiments (Figure 3.29) constitute a unique tool to obtain a broad range of data for qualitative and quantitative investigation of material that is useful to understand macroscopic properties of materials.

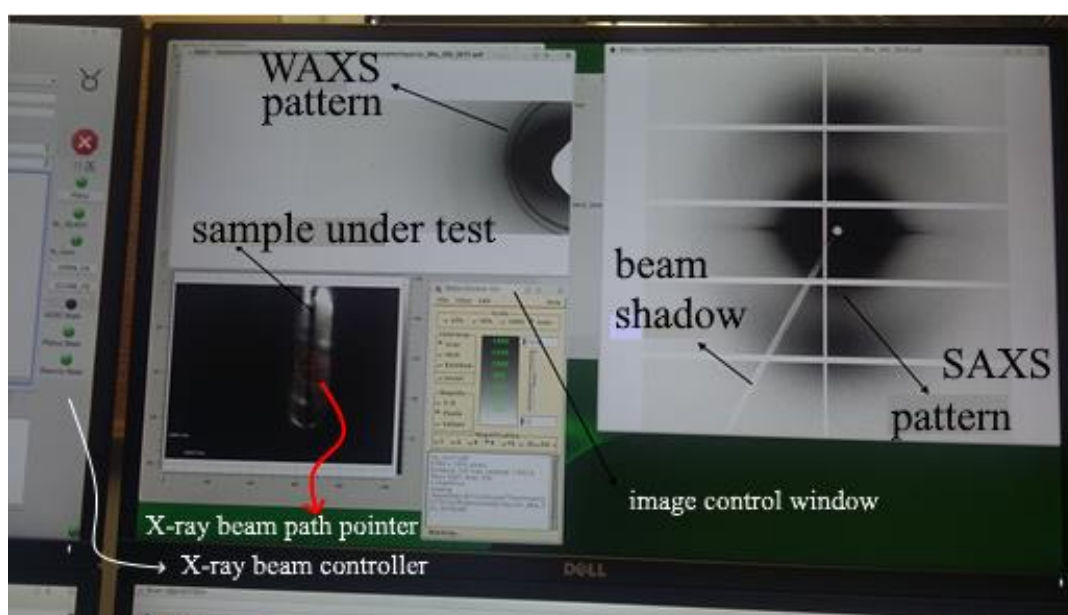


Figure 3.29. A screenshot obtained at BL 11 (NCD-SWEET) during simultaneous SAXS and WAXS experiment performed on the electrically conductive 3D printed strand.

3.15.2 ALBA Synchrotron Light Source

A significant portion of experimental work is conducted at ALBA Synchrotron radiation facility (Figure 3.30) studying the microstructure of the nanocomposites.

ALBA Synchrotron is a 3rd generation Synchrotron Light facility located in Cerdanyola Del Valles, (Barcelona, Spain). It is a complex of electron accelerators for producing synchrotron light, using a 3 GeV electron beam energy achieved by combining a Linear Accelerator (LINAC) and a low-emittance, full-energy booster placed in the same tunnel as the storage ring [91]. It has a 270 m perimeter with 17 straight sections all of which are available for the installation of insertion devices.

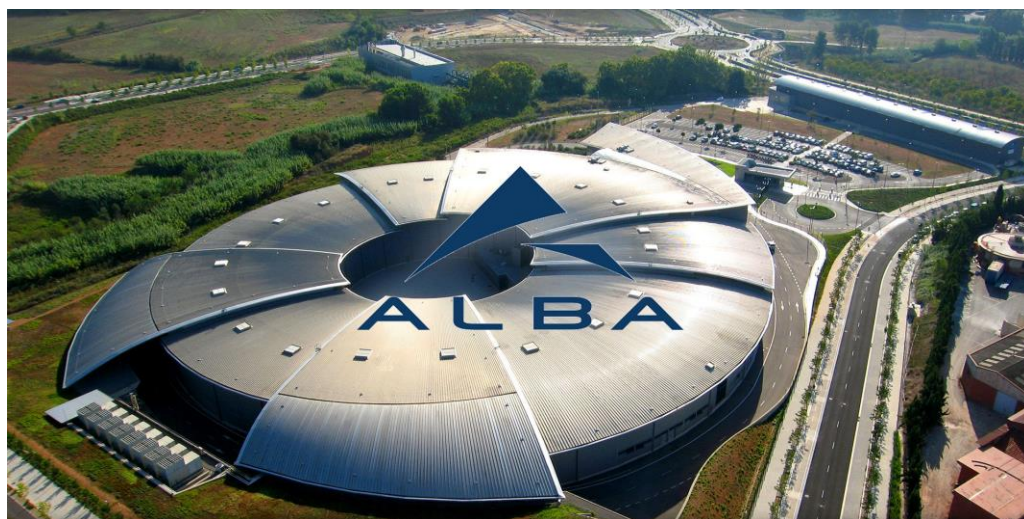


Figure 3.30. ALBA Synchrotron facility located in Cerdanyola del Valles, (Barcelona, Spain).

ALBA currently has eight operational state-of-the-art beamlines, comprising soft and hard X-rays, which are devoted mainly to biosciences, condensed matter (magnetic and electronic properties, nanoscience), chemistry and materials science. Additionally, four beamlines are in construction (low-energy ultra-high-resolution angular photoemission for complex materials, microfocus for macromolecular crystallography, absorption and diffraction and fast X-ray tomography & radioscopy). The facility has a large scientific infrastructure providing more than 6000 hours of beam time per year to the academic and the industrial sector, serving more than 2.000 researchers every year.

3.15.3 Small angle X-ray scattering (SAXS)

X-ray scattering is a non- invasive method of characterization of materials. When X-rays are directed at a material of interest, they scatter in predictable patterns based on the internal structure of the material. SAXS is a technique where the elastic scattering of x-rays by a sample is recorded at very low angles. In this technique, electron density differences in a sample are quantified which are used to determine

nanoparticle size distributions, resolve the size and shape of macromolecules, pore sizes and characteristic distances of partially ordered materials [92]. The principles and first uses of the SAXS method started in the middle of the 20th century. The Guinier [93] used SAXS for studying the nanostructure of metallic alloys while Kratky [92] applied SAXS for the characterization of (biological) macromolecules in solution. Each SAXS system consists of an X-ray source, a collimation system, a sample stage, and a detector. Appropriate software are used to process and evaluate the parameters of interest from scattering data. A typical SAXS setup up is shown in Figure 3.31.

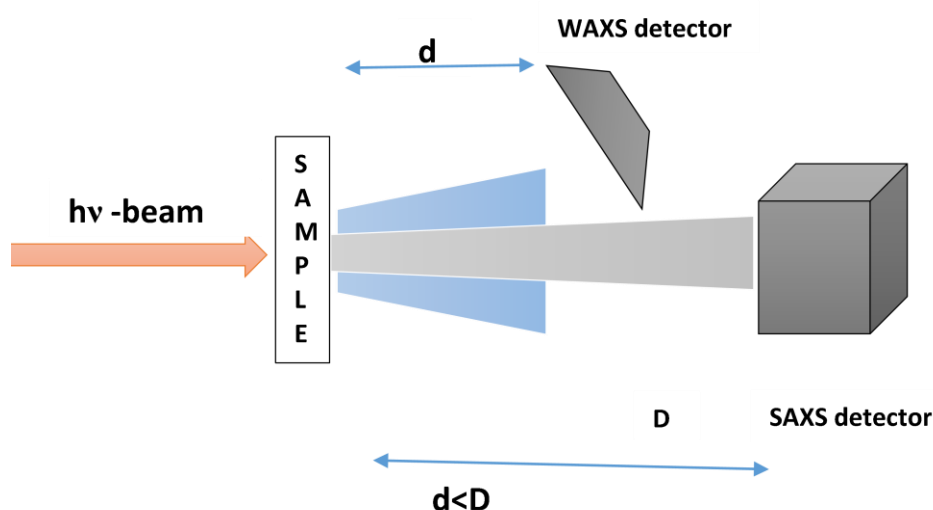


Figure 3.31. A simple experimental set up used to study materials using X-ray scattering.

Theory of SAXS

To understand small angle X-ray scattering, it is suitable to start assuming a fixed entity (or particle), with an arbitrary structure that is represented by an electronic density function $\rho(\vec{r})$. Assuming that a monochromatic radiation beam, with vector \vec{k}_0 as wave vector, hits a particle, the scattered wave direction will be defined by wave vector, \vec{k} , as shown in Figure 3.32.

In the elastic scattering, the scattered wave has the same modulus as that of the incident wave with absolute value $2\pi/\lambda$, where λ is the wavelength of the incident radiation. This helps to establish the difference between the incident and scattered beams, which is given by the following relation:

$$\vec{q} = \vec{k} - \vec{k}_0 \quad (3.23)$$

where, \vec{q} is the scattering vector. The scattering vector in terms of magnitude and direction can be defined as:

$$q = 2\pi/\lambda (\vec{v} - \vec{v}_0) \quad (3.24)$$

\vec{v} and \vec{v}_0 in the above relation are unitary vectors for the incident and scatter beam directions, respectively. Since 2θ is the angle formed by the incident and scattered beams, then the magnitude of the scattering vector is [95]

$$q = 4\pi (\sin \theta) / \lambda \quad (3.25)$$

It is important to mention that Eq. 3.25 is defined for wavelength $n = 1$. The scattering amplitude is related to the electron density distribution, $\rho(r)$, of the scatterer using a Fourier transformation. The $\rho(r)$ represents the number of electrons per unit volume at the position r . A volume element dV at r contains $\rho(r) dV$ number of electrons. Then the scattering amplitude of the entire irradiated volume V can be given as

$$A(\vec{q}) = A_e \int_V \rho(\vec{r}) e^{-iq\vec{r}} d\vec{r} \quad (3.26)$$

Where A_e denotes the scattering amplitude of one electron.

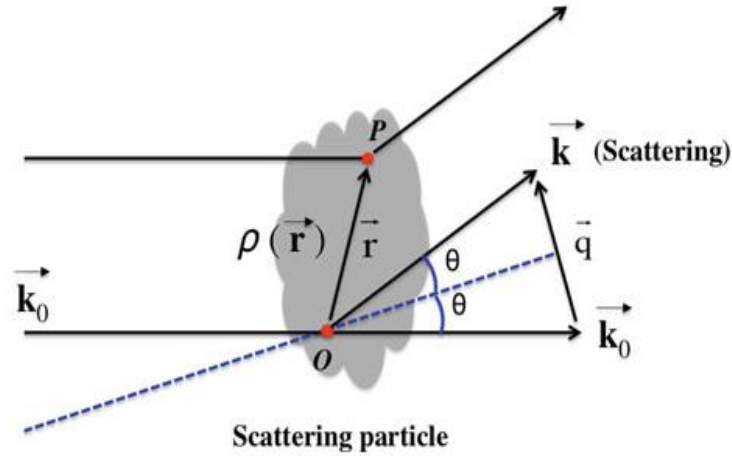


Figure 3.32. Representation of the small angle scattering process by a fixed particle [94].

The scattering intensity $I(q)$ of a single particle $I_0(q)$ is the absolute square given by the product of the amplitude and its complex conjugate $A(r)^*$.

$$I_0(\vec{q}) = A(\vec{q}) \cdot A(\vec{q})^* = I_e \int_V \int_V \rho(\vec{r}) \rho(\vec{r}') e^{-iq(\vec{r}-\vec{r}')} d\vec{r} d\vec{r}' \quad (3.27)$$

The scattering electron intensity $I_e(q)$ has been given by the Thomson formula.

$$I(\theta)_e = I_p (7.9 * 10^{-26}) \frac{1}{d^2} \frac{1+(\cos\theta)^2}{2} \quad (3.28)$$

Where I_p denotes the primary intensity and the distance between the sample and detector. The numerical factor is the square of the so-called classical electron radius. The intensity depends only on the scattering angle θ by the polarization factor, which is practically equal to one for the small angles. As the electron scattering intensity I_e applies to all formulae to follow, it will be omitted for brevity, i.e., the SAXS scattering intensity is expressed in units of the scattering intensity of a single electron (e.u. or electron units). The above expression referred to the scattering process of a particle in a fixed orientation in a vacuum. The following situations can exist in the majority of SAXS experiments [96]:

- o The particles are statistically isotropic and no long-range order exists, i.e., there is no correlation between particles at great spatial distances.
- o The filler particles are embedded in a matrix. The matrix is considered a homogeneous medium with the electron density ρ_0 . The examples include particles in a solution or a polymer. The electron density in equations (26 - 27) is replaced by the difference in electron density $\Delta \rho = \rho - \rho_0$, which can take a positive or negative value. The positive electron density difference indicates that the electron density of particles is higher than the matrix while a negative value is an indication that the electron density of the matrix is higher than filler particles.

In such a case, the average overall orientations lead to the fundamental formula of Debye [95]

$$e^{-iq \cdot r} = \frac{\sin(q \cdot r)}{(q \cdot r)} \quad (3.29)$$

$$I_o(q) = 4\pi \int_0^\infty \gamma(r) \frac{\sin qr}{qr} r^2 dr \quad (3.30)$$

Eq. (2.6) is the general formula for the scattering pattern of any systems, which obey the above two restrictions. $\gamma(r)$ is the so-called correlation function or characteristic function[95]. It can be obtained by the inverse Fourier transform with

$$\gamma(r) = \left(\frac{1}{2\pi^2}\right) \int_0^\infty I_o(q) q^2 \frac{\sin qr}{qr} dq \quad (3.31)$$

For $q = 0$ and $r = 0$, as the Debye factor equals to unity, Eq. (2.6) and (2.7) reduce to

$$I_o(0) = \int_0^\infty \gamma(r) (4\pi r^2) dr \quad (3.32)$$

$$\gamma(0) = \left(\frac{1}{2\pi^2}\right) \int_0^\infty I_o(q) q^2 dq = V_p \overline{(\Delta\rho)^2} \quad (3.33)$$

For Eq. (2.8), at $q = 0$ exactly, all secondary waves are in phase, so that $I_o(0)$ may be expected to be equal to the square of the total number of electrons in the irradiated volume V_p (volume of one single particle). However, this quantity is experimentally not available. Therefore, it is extrapolated as a value through Guinier approximation or Zimm plot [96], which will be discussed in the next section. Equation (2.9) shows that the integral of the intensity over all the reciprocal space is directly related to the mean square fluctuation of excess electron density, irrespective of special features of the structure. From this point, an important quantity “invariant” Q is produced as

$$Q = \int_0^\infty I(q) q^2 dq = (2\pi^2) V_p \overline{(\Delta\rho)^2} \quad (3.34)$$

Equation 3.34 plays an important role in the analysis of the scattering pattern.

Guinier's Law

Regardless of particle shape, at low q region, i.e., for $qr \ll 1$ the Debye factor becomes [92]

$$\frac{\sin(qr)}{qr} \cong 1 - \frac{(qr)^2}{6} + \dots \dots \dots \quad (3.35)$$

Eq. (2.6) reduces to

$$I_o(q) = (4\pi) \int \gamma(r) \left(1 - \frac{(qr)^2}{6} + \dots\right) r^2 dr = I_o(0) \left(1 - \frac{(q)^2 (R_g)^2}{3}\right) \quad (3.36)$$

Where R_g is the radius of gyration given by

$$R_g^2 = \frac{(\frac{1}{2}) \int \gamma(r) r^4 dr}{\int \gamma(r) r^2 dr} \quad (3.37)$$

Which is related to the electron density $\rho(r)$ of the particle, can also be represented as

$$R_g^2 = \frac{\int \rho(s) s^2 ds}{\int \rho(s) ds} \quad (3.38)$$

With defining s as the vector taken from the centre of gravity of $\rho(s)$. For homogeneous particles, the radius of gyration is only related to the geometrical parameters of simple triaxial bodies [96], for example, spheres with radius R .

$$R_g = R(\sqrt{3/5}) \quad (3.39)$$

and, for cylindrical particles with length H and radius R in cross-section

$$R_g = R[\frac{R^2}{2} + \frac{L^2}{12}]^{1/2} \quad (3.40)$$

Within the approximation, $e^{-x} \cong 1-x$, for $qr \ll 1$ Eq. (2.11) can be also expressed as

$$I_0(q) \cong I_0(0) \exp(-\frac{q^2 R_g^2}{3}) \quad (3.41)$$

Equation 3.41 is known as Guinier's law. It is useful relation in SAXS data analysis since it allows to obtain R_g^2 and $I_0(0)$ from scattering data in the region of smallest angles without any prior assumption on the shape and internal structure of the particles under study.

Porod's Law

Günther Porod gives Porod's law after examining the sequence of a SAXS signal. Porod observed that in number the data follow an asymptotic behaviour with a fourth power-law decay. This behaviour is expected for a two-phase system with the electron density (ρ) can assume only two values zero and 1. Moreover, it is concerned with scattering vector (q) that is small compared to the scale of usual Bragg diffraction; typically ($q \leq 1\text{nm}^{-1}$). In this range, the sample is not described at an atomistic level, rather uses a continuum description in terms of scattering electron density. Porod's q is relatively large compared to the usual scale of SAXS. In this regime, correlations between remote surface segments and inter-particle correlations are so random that they average out. Therefore, one sees only the local interface roughness. Since the advent of fractal mathematics, it has become clear that Porod's law requires adaptation for rough interfaces as the value of the surface S may be a function of q (the yardstick by which it is measured). In the case of a fractal rough surface with a dimensionality d between 2-3 Porod's law states [95] [96]

$$\lim_{q \rightarrow \infty} I(q) \propto S q^{-(6-d)} \quad (3.42)$$

Thus if plotted logarithmically the slope of $\ln(I)$ versus $\ln(q)$ would vary between -4 and -3 for such a surface fractal. If the interface is flat, then Porod's law predicts the scattering intensity

$$I(q) = S q^{-4} \quad (3.43)$$

Where S is the surface area of the particles, which can be experimentally determined when the acquired data is in absolute units.

Kratky Law

The Kratky interpretation originates from Debye's scattering formulation mentioned in Eq. (3.34). A plot of $I.q^2$ vs q is sensitive to the morphology of particles and known as Kratky plot. It is used to deduce information about the compactness of aggregates of carbon nanotubes in the polymer matrix.

SAXS facility

The SAXS experiments were performed using NCD-SWEET beamline at ALBA synchrotron radiation facility, Barcelona, Spain. Two types of detectors are used to collect SAXS data, namely, the Quantum 210r CCD detector from ADSC and the Pilatus 1M from Dectris, the latter is shown in Figure 3.33.

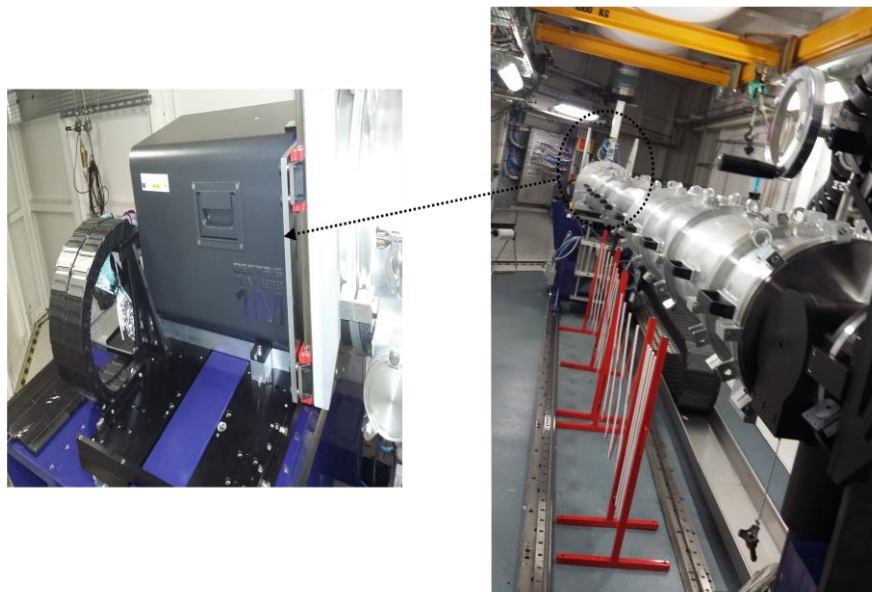


Figure 3.33. The detector used for small angle x-ray scattering at BL11 (NCD – SWEET) beamline, ALBA Synchrotron, Barcelona, Spain, studying morphology in 3 D printed nanocomposites.

Different q - ranges are used to perform experiments which are limited by the photon energy, sample-to-detector distance (SDD), the pixel size and geometry of the X-ray detector, and size of the beam stopper [97]. The beamline is tunable over a wavelength range of 0.62 Å - 1.90 Å and delivers a high-photon flux onto the sample. All experiments were performed using a wavelength of 0.99 Å. The beam has excellent

beam collimation and is highly stable. For this purpose, the photon source of this beamline is an undulator, placed in a medium 4 m straight section. The beam has an approximate size at the sample position $\approx 349 \mu\text{m} \times 379 \mu\text{m}$ (h x v). It is possible to use different sample environment depending on the desired experiment. The experiments were performed in different time slots and experimental configurations. Each experimental configuration is further explained in relevant chapters.

3.15.4 Wide angle X-ray scattering

Wide-angle X-ray scattering (WAXS) is an X-ray diffraction technique to study Bragg peaks scattered to wide angles, which (by Bragg's law) are caused by sub-nanometre-sized structures [98]. WAXS refers to X-ray diffraction with a diffraction angle $2\theta > 1^\circ$. It is often used to determine the crystalline structure and the degree of crystallinity of polymer or polymer-based composite materials. More specifically, the diffraction pattern can be used to determine the chemical composition, preferred alignment of the crystallites and the crystallite size. The scattering intensity can be plotted as a function scattering angle 2θ , d spacing between planes or scattering vector q . The basic difference between WAXS and SAXS is the distance from the sample to the detector. A shorter distance is used in the WAXS experiment relative to the SAXS experiment and thus diffraction maxima are observed at larger angles.

Principle of WAXS

WAXS is considered an appropriate technique determining the microstructure in materials including crystalline (metals), non-crystalline and semi-crystalline materials (polymers). WAXS is particularly useful for the characterisation of the structure and morphology in semicrystalline or mixture of polymers.

A diffraction pattern from a polymeric material can be related to its structure through Bragg's equation:

$$n\lambda = 2d\sin\theta \quad (3.44)$$

Where d is the Bragg spacing, λ is the wavelength of the radiation, n is an integer and 2θ is the angle between the diffraction radiation and incident radiation. Often, it is written in terms of the scattering vector q as:

$$q = 4\pi \sin\theta / \lambda \quad (3.45)$$

For the first order reflection, i.e. $n = 1$,

$$q = 4\pi \sin\theta / \lambda = 2\pi / d \quad (3.46)$$

For polymeric materials, their enormous length and irregularity in long-chain molecules hinder the three-dimensional long-range order for a macroscopic crystal structure [99]. Thus, polymer samples are either amorphous or semi-crystalline, which shows a halo ring for amorphous or sharp crystalline peaks (more or less) accompanied by various amorphous halos [100]. Moreover, imperfections in the crystalline regions of polymers result in broadening of the diffraction peaks. Therefore, the imperfection of the crystallinity can be quantified by the correlation length [101] following Equation (47).

$$\Delta L = 2\pi / \Delta q = D_{hkl} \quad (3.47)$$

ΔL is measured through the line broadening of diffraction peaks i.e. Δq is obtained by measuring the half-height width of the corresponding diffraction peak. It can be seen that in the case of an ideal or perfect crystal (without imperfections), ΔL is nearly equal to the crystal size D_{hkl} [100]. Therefore, the correlation length is a measure for the dimension of the corresponding order in the structure. The shorter the correlation length, the less order in the molecular organization.

WAXS facility

The WAXS experiments were performed using NCD-SWEET beamline at ALBA synchrotron radiation facility, Barcelona, Spain. The experiments were performed in different time slots and experimental configurations. The WAXS detector used in this study is Rayonix. It has 1920 pixels x 5760 pixels (h x v) and single-pixel size is 44 x 44 μm^2 . It is possible to acquire 10-140 frames /sec using this detector. For the sake of this reasoning, WAXS detector is placed always near to sample acquiring maximum diffracted radiation. The sample to detector distance is used is 0.2 ± 0.1 m. The detector used at BL11 (NCD –SWEET) beamline at ALBA Synchrotron, Barcelona, Spain studying structure in 3 D printed electrically conductive nanocomposites is shown in Figure 3.34.

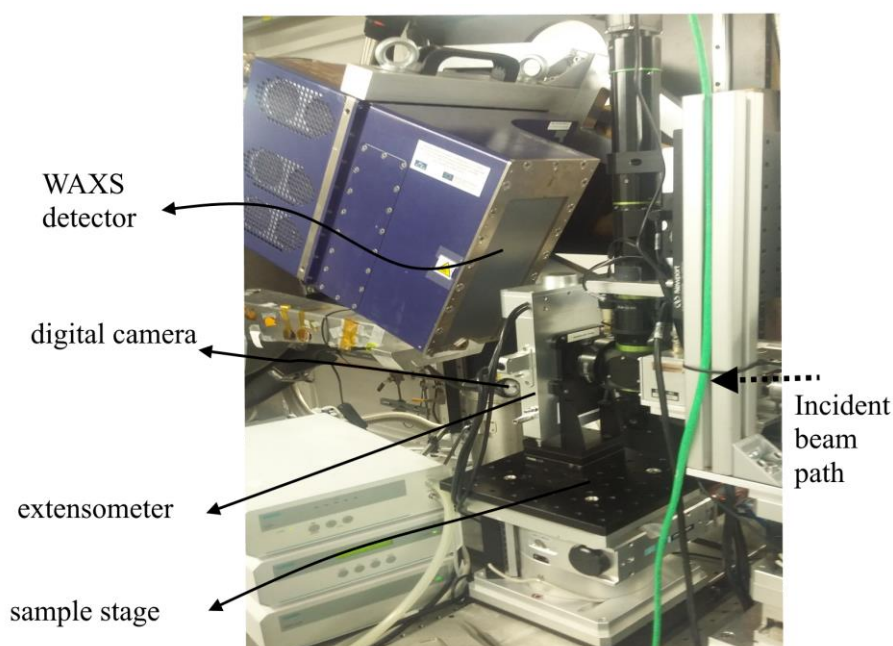


Figure 3.34. WAXS Rayonix LX255-HS detector used to study structure in the 3 D printed nanocomposites samples at BL11 (NCD–SWEET) beamline, ALBA Synchrotron, Barcelona, Spain.

3.16 ELECTRON MICROSCOPY

Advanced microscopic techniques are used to get information for the visual inspection of carbon nanotubes into a polymer matrix. In this work, a high-resolution scanning electron microscope (HR-SEM) is used for the acquisition of images from the pure nanotubes and its nanocomposites. The HR-SEM microscope is used from ICN2, Barcelona, Spain. The Magellan 400L is a Field Emission Scanning Electron Microscope (FESEM) equipped with a newly developed electron column with a monochromator, (Unicolor) Technology. The microscope features excellent capabilities in the traditional high energy (15-30 kV) as well as low beam energies with a sub-nanometre resolution for unmatched surface-sensitive imaging. It works using a beam current of 0.6 pA – 22 nA. It has a specimen stage 100 mm x 100 mm with piezo control.

A FESEM is used to visualize very small topographic details on the surface or fractioned objects. A FESEM microscope works with electrons (particles with a negative charge) instead of light. These electrons are liberated by a field emission source. A field emission source is a type of electron gun in which a sharply pointed Müller-type emitter is held at several kilovolts negative potential relative to a nearby electrode so that there is sufficient potential gradient at the emitter surface to cause

field electron emission [102]. Emitters are either of cold-cathode type, usually made of single-crystal tungsten sharpened to a tip radius of about 100 nm, or of the Schottky type [103] in which thermionic emission is enhanced by barrier lowering in the presence of a high electric field. Electrons are liberated from a field emission source and accelerated in a high electrical field gradient. Within the high vacuum column, these so-called primary electrons are focussed and deflected by electronic lenses to produce a narrow scan beam that bombards the object. As a result, secondary electrons are emitted from each spot on the object. The angle and the velocity of these secondary electrons relate to the surface structure of the object. A detector catches the secondary electrons and produces an electronic signal. This signal is amplified and transformed into a video scan-image that appears on a monitor. These images can be saved into the system and further processed for the relevant information using image analysis software.

3.17 FOURIER-TRANSFORM INFRARED SPECTROSCOPY (FTIR)

The Fourier transform (FT) is a tool that breaks a function or signal into an alternate representation, characterized by sine and cosines. In other words, the Fourier transform is a mathematical operation used to reverse a function. The Fourier transform of a function $f(x)$ can be expressed as [104],

$$f(w) = 1/\sqrt{m} \int_{-\infty}^{+\infty} \exp(\sigma q i w x) f(x) dx \quad (3.48)$$

Fourier-transform infrared spectroscopy (FTIR) originates from the fact that a beam containing several frequencies of light shines at once and measures the amount of absorption within the material. Further, the beam is modified to contain a different combination of frequencies, providing a second data point. The process is repeated number of times. Afterwards, a computer takes all this data and works backwards to infer the amount of absorption at each wavelength. The beam described above is generated by starting with a broadband light source. The raw data is commonly referred to as an interferogram with inverse dimension, so the Fourier Transform of the interferogram possesses in the reciprocal length dimension (L^{-1}), which is the dimension of the wavenumber. An FTIR spectrometer simultaneously collects high-spectral-resolution data over a wide spectral range. The use of FTIR spectrometer is depended on the region of interest (mid or near IR) used for a particular analysis. For the mid-IR region, $2 - 25 \mu m$ ($5000 - 550 \text{ cm}^{-1}$), the source is the Germanium (Ge)

crystal. Shorter wavelengths of the near-IR, $1 - 2.5 \mu m$ ($10000 - 4000 \text{ cm}^{-1}$), require a higher temperature source, typically a tungsten-halogen lamp.

Fourier transform infrared (FTIR) spectroscopy measures the fundamental vibrations and associated overtones of the chemical species present in a sample using the infrared radiation (IR). Frequencies of electromagnetic waves in the infrared tend to couple effectively to oscillating charge distributions due to the vibrations set up in the molecular structures. When the frequency of IR radiation matches the resonance frequency of the oscillating charge, coupling gets strong [105]. Frequencies of molecular vibrations are determined by the masses in motion and the binding force between them. Analogous to a weight suspended on a spring, frequencies of molecular vibration are directly related to molecular composition (the atoms making up the molecule) and the molecular structure (how the atoms are disposed of in the molecule).

The Beer-Lambert law states that the absorbance (A) is the logarithm of the ratio of the intensity of transmitted light (I_t) to that of incident light (I_0). Further, this is proportional to molar concentration c ($\text{mol}\cdot\text{l}^{-1}$), path distance of the light through the sample l (cm), and the molar absorptivity of the sample which is a constant, ϵ ($\text{l}\cdot\text{mol}^{-1}\cdot\text{cm}^{-1}$), [106]

$$A = -\log(I/I_0) = \epsilon \cdot t \cdot c \quad (3.49)$$

Absorbance, therefore, is dimensionless, t is in cm , ϵ is in $\text{l}\cdot\text{mol}^{-1}\cdot\text{cm}^{-1}$, and concentration expressed as the molar concentration $\text{mol}\cdot\text{l}^{-1}$.

3.17.1 Attenuated total reflectance (ATR)

Attenuated total reflection (ATR) is a sampling technique used in conjunction with infrared spectroscopy enabling the qualitative and quantitative determination of components in a sample without using special preparation methods [107] ATR uses a property of total internal reflection resulting in an evanescent wave. A beam of infrared light is passed through the ATR crystal (Platinum diamond) in such a way it reflects at least once off the internal surface in contact with the sample. This reflection forms the evanescent wave that extends into the sample. The penetration depth into the sample is typically between 0.5 and 2 micrometres, with the exact value being determined by the wavelength of the light, the angle of incidence and the indices of refraction for the ATR crystal and the medium being probed [108]. The number of reflections may be varied by varying the angle of incidence. The beam is then collected by a detector as it exits the crystal. Most modern infrared spectrometers can be

converted to characterise samples via ATR by mounting the ATR accessory in the spectrometer's sample compartment. The accessibility of ATR-FTIR has led to substantial use by the scientific community. The evanescent effect only works if the crystal is made of an optical material with a higher refractive index than the sample being studied [109]. Otherwise, light is lost to the sample. In the case of a liquid sample, pouring a shallow amount over the surface of the crystal is sufficient. In case of a solid sample, it is firmly clamped against the ATR crystal. This helps the evanescent wave improving into the solid sample through intimate and subtle contact. In this way, trapped air is not the medium through which the evanescent wave travels, as that would distort the results. The signal to noise ratio obtained depends on the number of reflections but also on the total length of the optical light path, which dampens the intensity. Therefore, a general claim that more reflections give better sensitivity cannot be made.

Typical materials for ATR crystals include germanium, diamond and zinc selenide, while silicon is ideal for the use in the Far-IR region of the electromagnetic spectrum. The excellent mechanical properties of diamond make it an ideal material for ATR, particularly when studying very hard solids, but due to its higher cost, less widely applicable.

3.17.2 Equipment specification

The ATR-FTIR equipment used in this study belongs to the material characterization laboratory of the Centre for the rapid and sustainable product (CDRSp); institute polytechnic Leiria (IPL), Portugal. The system is from an Alpha series manufactured by the Bruker optics, GmbH, and is shown in Figure 3.35. It includes the following key components:

- ALPHA spectrometer: This is further composed on the measurement module and a crystal plate with ATR crystal.
- Power cable with a mains adapter.
- Data cable (crossover cable for 10 Base-T Ethernet).
- A computer system, at least Pentium processor, equipped with windows XP professional.

In this study, the samples were scanned 64 times in a single run and the average data is used for further analysis. The OPUS software package, version 6.5, is used for

the measurement of the FTIR spectra (qualitative/quantitative) for the extraction of the data.



Figure 3.35. The ATR-FTIR equipment used, in this study, for the quantitative analysis of nanocomposites.

3.18 SIMULTANEOUS THERMAL ANALYSIS

Simultaneous thermal analysis (STA) refers to the simultaneous application of differential scanning calorimetry (DSC) and thermogravimetry (TGA) to a sample in a single instrument. In this work, STA6000, from PerkinElmer, is used to study the thermal behaviour of the nanocomposite samples. The test conditions are considered identical for the TGA and DSC signals including the atmosphere, gas flow rate, and heating rate.

3.18.1 Differential scanning calorimetry

In the DSC mode of the STA, thermal transitions of a polymer/composite are studied under the effect of heat transfer, for example, the melting of a crystalline polymer. The heat flow at a given temperature yield information about the sample that can be used for further studies. The heat flow is given in units of heat (Q) supplied per unit time, t.

$$\text{heat flow} = \frac{\text{heat}}{\text{time}} = Q/t \quad (3.50)$$

$$\text{heating rate} = \frac{\text{Temperature increase}}{\text{time}} = \Delta T/t \quad (3.51)$$

The division of the heat flow (Q/t) by the heart rate ($\Delta T/t$) defines the heat capacity of the sample under test

$$\text{heat capacity} = C_p = \frac{Q/t}{\Delta T/t} = Q/\Delta T \quad (3.52)$$

Above the glass transition, polymers have a lot of mobility. They wiggle and squirm and mobile for a very long time. They gain an ordered arrangement after reaching a thermal equilibrium, which is referred to as crystal temperature. When chains are, in the crystalline arrangements, they release heat and an exothermic peak can be seen in the DSC curve. The temperature at the lowest point of this exothermic dip is called the crystallization temperature (T_c) and it is an indication that the material may crystallize [110]. Further application of the heat to the sample under test, eventually, reaching another thermal transition called a melting point. At this stage, polymer crystals begin to fall apart, that is they melt. The chains come out of their ordered arrangements, and begin to move around freely. When the polymer crystals melt, Polymers must absorb heat to melt crystals. At the melting temperature, the polymer's temperature will not rise until all the crystals have melted due to the first-order transition. This means that the little heater under the sample pan is required to supply a lot of heat into the polymer to both melts the crystals and keep the temperature rising at the same rate. This extra heat flow during melting shows up a big peak in the DSC plot. The above-mentioned transitions, under the effect of heat transformation, is shown in Figure 3.36.

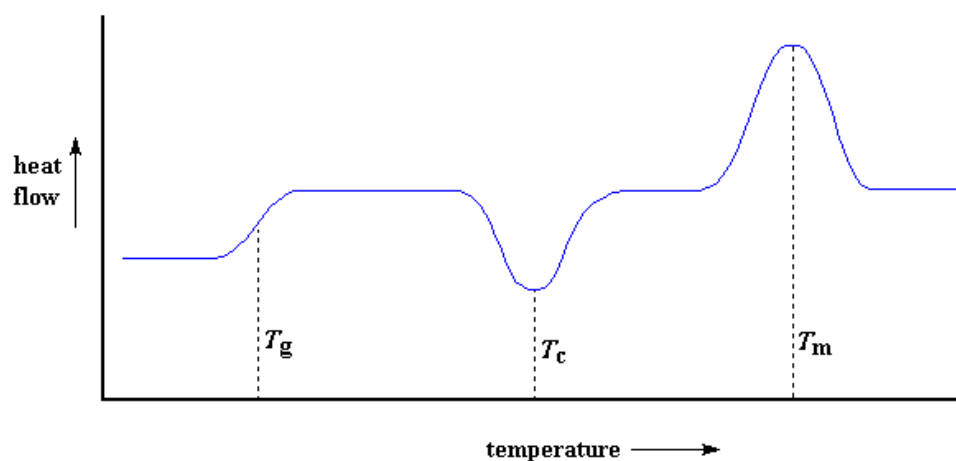


Figure 3.36. A typical thermal analysis curve indicating transition points when subject to heat-treatment in the DSC system.

DSC can be used to determine the amount of amorphous and/or crystalline phase and the per cent crystallinity in a polymer sample through calculating the latent heat of melting (ΔH_m) comparing to the 100% crystalline same polymer. The ΔH_m is measured using the area under the endothermic peak in a standard DSC plot for a polymer sample.

$$area = \frac{heat \times temperature}{time \times mass} = J.K/s.g \quad (3.53)$$

Since the polymer sample is heated using a particular heating rate, this follows Eq. (3.54)

$$\Delta H_m = area / heating\ rate = \frac{J.K/s.g}{K/s} = J/g \quad (3.54)$$

The latent heat of melting of polymer sample was measured using, approximately, 8 ± 1 mg of a sample from the test specimen using the test conditions mentioned in Table1.

Table 3.1. Conditions used to scan sample using a PerkinElmer system for STA

Initial temperature	28 °C
Final temperature	600 °C
Heating rate	10 °C/min
Purge gas	Approximately 3 mg
Sample pan	Ceramic pan

The heats of melting, ΔH_m , and cold crystallization, ΔH_c , are determined by integrating the area (J/g) under the peaks. Depending upon the sample's given the thermal history, a cold crystallization exothermic peak may or may not be observed during the DSC experiment. The % crystallinity is then determined using the following Eq. (3.55)

$$\% Crystallinity = \left[\frac{\Delta H_m - \Delta H_c}{\Delta H_{m^0}} \right] \times 100 \quad (3.55)$$

where ΔH_m and ΔH_c are enthalpies of fusion measured experimentally from the heat of melting and the heat of cold crystallization. The normalization term ΔH_{m^0} is a reference value and represents the heat of melting when the polymer was 100 % crystalline. ΔH_{m^0} used in this work considered from literature. The Pyris software (thermal analysis manager), from the Perkin - Elmer, is used to process the DSC data.

3.18.2 Thermogravimetry Analysis

Thermogravimetry analysis or thermal gravimetric analysis (TGA) is a method of thermal analysis in which the mass of a substance is monitored as a function of temperature or time as the sample specimen is subjected to a controlled temperature program in a controlled atmosphere. This measurement provides information about the physical phenomena, such as phase transitions, absorption, adsorption and desorption; as well as the chemical phenomena including chemisorption, thermal decomposition, and solid-gas reactions (e.g., oxidation or reduction) [111]. TGA data is often represented to as a 2 D curve with time or temperature along abscissa while weight (mg) or weight per cent (%) along the ordinate. The onset temperature defines the temperature at which the sample under test starts to decompose or lose weight. This temperature is obtained from the extrapolation of the TGA curve. Further, the peak of the first derivative indicates the point of the greatest rate of change on the weight loss curve. This is also known as the inflexion point. For the present study, the TGA scan rate is the same as mentioned for DSC.

3.19 DATA PROCESSING

MS Excel 2016 and Matlab 2014 are used to prepare different plots for the compilation of the chapter. The image [112], open-source image processing software, is used for the acquisition and processing of X-ray scattering data using YAX macro [113]. In particular, SasView, version 4.0, is used to process and model SAXS data [114].

3.20 REFERENCES

- [1] S. A. Baeurle, A. Hotta, and A. A. Gusev, "On the glassy state of multiphase and pure polymer materials," *Polymer (Guildf)*, vol. 47, no. 17, pp. 6243–6253, 2006.
- [2] L. (Leonard) Hollaway and P. R. (Peter R. Head, *Advanced polymer composites and polymers in the civil infrastructure*. Elsevier Science, 2001.
- [3] M. R. Kessler, *Advanced topics in characterization of composites*. Trafford, 2004.
- [4] Mostofa S.R., "Design for Usability: Understanding Tg and Tm in Plastic Products," 2016. [Online]. Available: <https://www.ecnmag.com/article/2016/05/design-usability-understanding-tg-and-tm-plastic-products>. [Accessed: 05-Jun-2019].
- [5] S. Wietzke et al., "Thermomorphological study of the terahertz lattice modes in polyvinylidene fluoride and high-density polyethylene," *Appl. Phys. Lett.*, vol. 97, no. 2, 2010.
- [6] M. L. Di Lorenzo and M. C. Righetti, "Crystallization-induced formation of

- rigid amorphous fraction," *Polym. Cryst.*, vol. 1, no. 2, p. e10023, 2018.
- [7] B. WUNDERLICH, "Thermodynamics and Kinetics of Crystallization of Flexible Molecules," *J. Polym. Sci. Part B Polym. Physics*, Vol. 46, 2647–2659, vol. 46, pp. 26467–2659, 2008.
- [8] L. W. McKeen, "Styrenic Plastics," in *The Effect of Long Term Thermal Exposure on Plastics and Elastomers*, Elsevier, 2014, pp. 73–84.
- [9] "Acrylonitrile Butadiene Styrene (ABS) and its Features." [Online]. Available: <https://omnexus.specialchem.com/selection-guide/acrylonitrile-butadiene-styrene-abs-plastic>. [Accessed: 05-Jun-2019].
- [10] C. A. Harper, *Handbook of Plastics and Elastomers*. McGraw-Hill, Maidenhead and New York, 1975., vol. 8, no. 3. John Wiley & Sons, Ltd, 1976.
- [11] G. Li et al., "Surface modification of boron nitride via poly (dopamine) coating and preparation of acrylonitrile-butadiene-styrene copolymer/boron nitride composites with enhanced thermal conductivity," *Polym. Adv. Technol.*, vol. 29, no. 1, pp. 337–346, 2018.
- [12] L. W. McKeen, *The effect of sterilization on plastics and elastomers*. William Andrew, 2012.
- [13] M. A. Woodruff and D. W. Hutmacher, "The return of a forgotten polymer - Polycaprolactone in the 21st century," *Prog. Polym. Sci.*, vol. 35, no. 10, pp. 1217–1256, 2010.
- [14] G. R. Mitchell, M. Domingos, and P. J. Bartolo, "Polymers, Biomanufacturing and Regenerative Medicine," *Adv. Mater. Res.*, vol. 506, pp. 11–14, 2012.
- [15] J. C. Silva, C. S. Moura, N. Alves, J. M. S. Cabral, and F. C. Ferreira, "Effects of Different Fibre Alignments and Bioactive Coatings on Mesenchymal Stem/Stromal Cell Adhesion and Proliferation in Poly (ϵ -caprolactone) Scaffolds towards Cartilage Repair," *Procedia Manuf.*, vol. 12, no. December 2016, pp. 132–140, 2017.
- [16] W. H. C. Frank J. van Natta, Julian W. Hill, "Studies of Polymerization and Ring Formation. XXIII.1 ϵ -Caprolactone and its Polymers," *J. Am. Chem. Soc.*, vol. 56, no. 2, pp. 455–457, 1934.
- [17] R. F. Storey and A. E. Taylor, "Effect of Stannous Octoate on the Composition, Molecular Weight, and Molecular Weight Distribution of Ethylene Glycol-Initiated Poly (ϵ -Caprolactone)," *J. Macromol. Sci. Part A Pure Appl. Chem.*, vol. 35, no. 5, pp. 723–750, 1998.
- [18] "thermosetting polymer," in *IUPAC Compendium of Chemical Terminology*, Research Triangle Park, NC: IUPAC.
- [19] H. Q. Pham and M. J. Marks, "Epoxy Resins," in *Ullmann's Encyclopedia of Industrial Chemistry*, Weinheim, Germany: Wiley-VCH Verlag GmbH & Co. KGaA, 2005.
- [20] "Thermoset Characterization Part 4: Introduction to Gelation - Polymer Innovation Blog." [Online]. Available: <https://polymerinnovationblog.com/thermoset-characterization-part-4-introduction-gelation/>. [Accessed: 05-Jun-2019].
- [21] G. Tang, K. Zhang, Z. Yan, L. Ma, and X. Huang, "A self-curing, thermosetting resin based on epoxy and organic titanium chelate as an anticorrosive coating matrix for heat exchangers: Preparation and properties," *Prog. Org. Coatings*, vol. 102, pp. 225–230, 2017.
- [22] O. Bayer, "Das Di-Isocyanat-Polyadditionsverfahren (Polyurethane)," *Angew. Chemie*, vol. 59, no. 9, pp. 257–272, Sep. 1947.
- [23] M. H. Irfan, "Introduction," in *Chemistry and Technology of Thermosetting*

- Polymers in Construction Applications*, Dordrecht: Springer Netherlands, 1998, pp. 1–7.
- [24] “Polymer Properties Database.” [Online]. Available: <https://polymerdatabase.com/polymer-classes/Polyurethane-type.html>. [Accessed: 05-Jun-2019].
- [25] M. (Michael) Szycher, *Szycher’s handbook of polyurethanes*. CRC Press, 2013.
- [26] K. M. Zia, S. Anjum, M. Zuber, M. Mujahid, and T. Jamil, “Synthesis and molecular characterization of chitosan-based polyurethane elastomers using aromatic diisocyanate,” *Int. J. Biol. Macromol.*, vol. 66, pp. 26–32, 2014.
- [27] L. K. Williams, *Polyurethanes from renewable resources*, University of Sheffield, UK, 2013.
- [28] Z. P. LIANG, “WO2015124476A1_patent.pdf,” 2015.
- [29] J. O. Akindoyo, M. D. H. Beg, S. Ghazali, M. R. Islam, N. Jeyaratnam, and A. R. Yuvaraj, “Polyurethane types, synthesis and applications-a review,” *RSC Adv.*, vol. 6, no. 115, pp. 114453–114482, 2016.
- [30] A. Shokuhi Rad and M. Ardjmand, “Chemical Technology an Indian journal,” *Chem. Technol. an Indian J.*, vol. 3, no. 1, pp. 60–71, 2008.
- [31] D. Randall and S. Lee, *The polyurethanes book*. [Huntsman Polyurethanes], 2002.
- [32] J. Pascault, H. Sautereau, J. Verdu, and R. J. J. Williams, *Thermosetting polymers*. 2002.
- [33] A. Kausar, “Role of Thermosetting Polymer in Structural Composite,” *Am. J. Polym. Sci. Eng.*, vol. 5, no. 1, pp. 1–12, 2017.
- [34] A. C. Garg and Y. W. Mai, “Failure mechanisms in toughened epoxy resins-A review,” *Compos. Sci. Technol.*, vol. 31, no. 3, pp. 179–223, 1988.
- [35] J. M. Madhava Rao. B, Lokesh. H, Kosaraju Srinivas, Murthy KSN, “Development and characterization of Flame retardant epoxy resin for battery terminal sealing application,” *Am. J. Eng. Res.*, vol. 8, no. 1, pp. 260–266, 2019.
- [36] X. M. Chen and B. Ellis, “Coatings and other applications of epoxy resins,” in *Chemistry and Technology of Epoxy Resins*, Dordrecht: Springer Netherlands, 1993, pp. 303–325.
- [37] R. Bagheri, B. T. Marouf, and R. A. Pearson, “Rubber-toughened epoxies: A critical review,” *Polym. Rev.*, vol. 49, no. 3, pp. 201–225, 2009.
- [38] R. J. C. Carbas, E. A. S. Marques, L. F. M. Da Silva, and A. M. Lopes, “Effect of cure temperature on the glass transition temperature and mechanical properties of epoxy adhesives,” *J. Adhes.*, vol. 90, no. 1, pp. 104–119, 2014.
- [39] F. L. Jin, X. Li, and S. J. Park, “Synthesis and application of epoxy resins: A review,” *J. Ind. Eng. Chem.*, vol. 29, pp. 1–11, 2015.
- [40] “Epoxy resins – Manufacturing process of Epoxy resins :” [Online]. Available: <https://guichon-valves.com/faqs/epoxy-resins-manufacturing-process-of-epoxy-resins/>. [Accessed: 06-Jun-2019].
- [41] Z. Yang, H. Peng, W. Wang, and T. Liu, “Crystallization behaviour of poly(ϵ -caprolactone)/layered double hydroxide nanocomposites,” *J. Appl. Polym. Sci.*, vol. 116, no. 5, pp. 2658–2667, 2010.
- [42] I. Rafique, A. Kausar, Z. Anwar, and B. Muhammad, “Exploration of Epoxy Resins, Hardening Systems, and Epoxy/Carbon Nanotube Composite Designed for High-Performance Materials: A Review,” *Polym. - Plast. Technol. Eng.*, vol. 55, no. 3, pp. 312–333, 2016.
- [43] Thomas F. Mika and Ronald S. Bauer, *Epoxy Resins: Chemistry and*

- Technology, Second Edition,* 2nd ed., May Clayton A, Ed. Taylor & Francis, 1988, p. 1288.
- [44] F. Ferdosian, M. Ebrahimi, and A. Jannesari, "Curing kinetics of solid epoxy/DDM/nano clay: Isoconversional model versus fitting model," *Thermochim. Acta*, vol. 568, pp. 67–73, 2013.
 - [45] Stuart M. Lee, Ed., *Reference Book for Composites Technology*. Pennsylvania: Technomic Publishing Company, Inc., 1989.
 - [46] D. Hanna and S. H. Goodman, *Handbook of Thermoset Plastics*. Elsevier Science, 2013.
 - [47] D. H. Klein and K. Jörg, "Two-component aqueous epoxy binders free of volatile organic content (VOC)," *Prog. Org. Coatings*, vol. 32, no. 1–4, pp. 119–125, 1997.
 - [48] S. Zafar, "Waterborne Epoxy Based Coating Materials," *Am. Sci. Res. J. Eng. Technol. Sci.*, vol. 50, no. 1, pp. 133–154, 2018.
 - [49] F. H. Walker and M. I. Cook, "Two-Component Waterborne Epoxy Coatings," in *Technology for Waterborne Coatings*, J. E. Glass, Ed. Washington DC: American Chemical Society, 1997, pp. 71–93.
 - [50] F. Awaja, M. Gilbert, B. Fox, G. Kelly, and P. J. Pigram, "Investigation of the post-cure reaction and surface energy of epoxy resins using time-of-flight secondary ion mass spectrometry and contact-angle measurements," *J. Appl. Polym. Sci.*, vol. 113, no. 5, pp. 2755–2764, Sep. 2009.
 - [51] Sumo Iijima, "Helical microtubules of graphitic carbon," *Nature*, vol. 354, no. 354, pp. 56–58, 1991.
 - [52] Iijima Sumio, "The Discovery of Carbon Nanotubes - Basle, 22.11.2007." [Online]. Available: <https://www.balzan.org/en/prizewinners/sumio-ijima/the-discovery-of-carbon-nanotubes-ijima>. [Accessed: 06-Jun-2019].
 - [53] S. S. Xie et al., "Large-Scale Synthesis of Aligned Carbon Nanotubes," *Science* (80-.), vol. 274, no. 5293, pp. 1701–1703, 1996.
 - [54] P. Collins and P. Avouris, "Nanotubes Electronics," *Sci. Am.*, vol. 283, no. 6, pp. 62–69, 2017.
 - [55] T. W. Ebbesen and P. M. Ajayan, "Large-scale synthesis of carbon nanotubes," *Nature*, vol. 358, no. 6383, pp. 220–222, Jul. 1992.
 - [56] P. Nikolaev et al., "Gas-phase catalytic growth of single-walled carbon nanotubes from carbon monoxide," *Chem. Phys. Lett.*, vol. 313, no. 1–2, pp. 91–97, 1999.
 - [57] K. Takeuchi, T. Hayashi, Y. A. Kim, K. Fujisawa, and M. Endo, "the State-of-the-Art Science and Applications of Carbon Nanotubes," *Nanosyst. Physics, Chem. Math.*, vol. 5, no. 1, pp. 15–24, 2014.
 - [58] C. T. Inc., "Carbon Nanotube Applications and the Properties of Carbon Nanotubes," *Azo Nano*. [Online]. Available: <https://www.azonano.com/article.aspx?ArticleID=2176&azosrc=downloadpdfcopyemail>. [Accessed: 29-Aug-2019].
 - [59] K. Weissert and H.-J. Arpe, *Industrial organic chemistry*. Wiley-VCH, 2003.
 - [60] T. T. Nguyen, S. U. Nguyen, D. T. Phuong, D. C. Nguyen, and A. T. Mai, "Dispersion of denatured carbon nanotubes by using a dimethylformamide solution," *Adv. Nat. Sci. Nanosci. Nanotechnol.*, vol. 2, no. 3, 2011.
 - [61] M. M. Heravi, M. Ghavidel, and L. Mohammadkhani, "Beyond a solvent: Triple roles of dimethylformamide in organic chemistry," *RSC Adv.*, vol. 8, no. 49, pp. 27832–27862, 2018.
 - [62] M. T. Smith et al., "Key characteristics of carcinogens as a basis for organizing

- data on mechanisms of carcinogenesis," *Environ. Health Perspect.*, vol. 124, no. 6, pp. 713–721, 2016.
- [63] "Chloroform - used, first, anaesthetic, blood, body, Anesthetic Chloroform, Simpson Discovers Chloroforms Potency." [Online]. Available: <http://www.discoveriesinmedicine.com/Bar-Cod/Chloroform.html>. [Accessed: 06-Jun-2019].
- [64] M. H. Lumpkin, "Chlorinated Hydrocarbons," *Hamilt. Hardy's Ind. Toxicol. Sixth Ed.*, pp. 541–566, 2015.
- [65] C.-X. Liu and J.-W. Choi, "Improved Dispersion of Carbon Nanotubes in Polymers at High Concentrations," *Nanomaterials*, vol. 2, no. 4, pp. 329–347, 2012.
- [66] M. Gupta, S. Malhotra, S. Chopra, and R. Maheshwari, "CVD grown single-walled carbon nanotubes (SWNTs) in organic solvents," *AIP Conf. Proc.*, vol. 1324, pp. 394–398, 2010.
- [67] Rosen J. Milton and Kunjappu T. Joy, "Characteristic Features of Surfactants," in *Surfactants and Interfacial Phenomena*, 4th ed., R. J. M. and K. T. Joy, Ed. Hoboken, NJ, USA: John Wiley & Sons, Inc., 2012, pp. 1–38.
- [68] Y. Geng, M. Y. Liu, J. Li, X. M. Shi, and J. K. Kim, "Effects of surfactant treatment on mechanical and electrical properties of CNT/epoxy nanocomposites," *Compos. Part A Appl. Sci. Manuf.*, vol. 39, no. 12, pp. 1876–1883, 2008.
- [69] X. Gong, J. Liu, S. Baskaran, R. D. Voise, and J. S. Young, "Surfactant-Assisted Processing of Carbon Nanotube / Polymer Composites," *Chem. Mater.*, vol. 12, pp. 1049–1052, 2000.
- [70] G. Rodriguez, J. Dias, M. A. D'Ávila, and P. Bártolo, "Influence of hydroxyapatite on extruded 3D scaffolds," *Procedia Eng.*, vol. 59, pp. 263–269, 2013.
- [71] Y. Wang and F. Cao, "Induction heating power supply temperature control based on a novel fuzzy controller," *Proc. 2008 Int. Conf. Comput. Electr. Eng. ICCEE 2008*, pp. 615–618, 2008.
- [72] T. O. Naoyuki Kubota, Kazuo Kiguchi, Honghai Liu, Ed., *Intelligent robotics and applications : 9th International Conference, ICIRA 2016, Tokyo, Japan, August 22-24, 2016, Proceedings. Part I*. Springer Switzerland, 2016.
- [73] J. S. Taurozzi, V. A. Hackley, and M. R. Wiesner, "Ultrasonic dispersion of nanoparticles for environmental, health and safety assessment issues and recommendations," *Nanotoxicology*, vol. 5, no. 4, pp. 711–729, 2011.
- [74] Q. Y. Tang, I. Shafiq, Y. C. Chan, N. B. Wong, and R. Cheung, "Study of the Dispersion and Electrical Properties of Carbon Nanotubes Treated by Surfactants in Dimethylacetamide," *J. Nanosci. Nanotechnol.*, vol. 10, no. 8, pp. 4967–4974, 2010.
- [75] A. Poorsolhjoui and M. Hassan Naei, "Effects of carbon nanotubesTM dispersion on effective mechanical properties of nanocomposites: A finite element study," *J. Reinf. Plast. Compos.*, vol. 34, no. 16, pp. 1315–1328, 2015.
- [76] O. K. Park, T. Jeevananda, N. H. Kim, S. il Kim, and J. H. Lee, "Effects of surface modification on the dispersion and electrical conductivity of carbon nanotube/polyaniline composites," *Scr. Mater.*, vol. 60, no. 7, pp. 551–554, 2009.
- [77] S. Grishchuk and R. Schledjewski, "Mechanical Dispersion Methods for Carbon Nanotubes in Aerospace Composite Matrix Systems," in *Carbon Nanotube Enhanced Aerospace Composite Materials, Solid Mechanics and Its*

- Applications*, vol. 188, A. S. P. and V. Kostopoulos, Ed. Dordrecht: Springer Science+Business Media, 2013, pp. 99–154.
- [78] Kirk-Othmer, “Kirk-Othmer Encyclopedia of Chemical Technology - Vol 8,” *Journal of the American Chemical Society*, vol. 5. pp. 455–456, 1998.
- [79] Y. SINGH, “Electrical Resistivity Measurements: a Review,” *Int. J. Mod. Phys. Conf. Ser.*, vol. 22, no. January 2013, pp. 745–756, 2013.
- [80] A. T. Caballo and L. A. Acebron, “Implementation of the Two Probe Method: A Technique in Measuring Electrical Properties,” vol. 14, no. 3, pp. 1–5, 2017.
- [81] I. Miccoli, F. Edler, H. Pfnür, and C. Tegenkamp, “The 100th anniversary of the four-point probe technique: the role of probe geometries in isotropic and anisotropic systems,” *J. Phys. Condens. Matter*, vol. 27, no. 22, p. 223201, May 2015.
- [82] A. . A. . V. and A. . S. . Prokhorov, “Broadband Dielectric Spectroscopy of solids,” *Radiophys. Quantum Electron.*, vol. 46, no. 8–9, pp. 657–665, 2003.
- [83] Z. M. Elimat, “AC-impedance and dielectric properties of hybrid polymer composites,” *J. Compos. Mater.*, vol. 49, no. 1, pp. 3–15, 2013.
- [84] F. Kremer and A. Schönhals, Eds., *Broadband Dielectric Spectroscopy*. Berlin, Heidelberg: Springer Berlin Heidelberg, 2011.
- [85] H. Winick, G. Brown, K. Halbach, and J. Harris, “Wiggler and undulator magnets,” *Phys. Today*, vol. 34, no. 5, pp. 50–63, 1981.
- [86] M. Quattromini, M. Artioli, E. Di Palma, A. Petralia, and L. Giannessi, “Focusing properties of linear undulators,” *Phys. Rev. Spec. Top. - Accel. Beams*, vol. 15, no. 8, pp. 1–9, 2012.
- [87] C. Fan, J. Hu, and Z. Zhao, “Synchrotron Light for Materials Science,” *Adv. Mater.*, vol. 26, no. 46, pp. 7685–7687, 2014.
- [88] “Development of synchrotron light sources.” [Online]. Available: <http://archive.synchrotron.org.au/about-us/our-facilities/accelerator-physics/development-of-synchrotron-light-sources>. [Accessed: 06-Jun-2019].
- [89] F. J. Wuilleumier, “An experimental comparison of first, second and third generation synchrotron - radiation sources for gas phase photoelectron spectrometry,” in *Sincrotrone Trieste Third Users’ Meeting*, 1995.
- [90] G. P. Williams, “A general review of synchrotron radiation, its uses and special technologies,” *Vacuum*, vol. 32, no. 6, pp. 333–345, 1982.
- [91] “About ALBA.” [Online]. Available: <https://www.cells.es/en/about/welcome>. [Accessed: 06-Jun-2019].
- [92] O. Glatter, O., Kratky, Ed., *Small angle X-ray Scattering.pdf*. London: Academic press Inc., 1982.
- [93] Andere Guinier and Gerard Fornet, *Small-angle scattering of X-rays*. John Wiley & Sons, Ltd, 1955.
- [94] O. M. Londoño, P. Tancredi, P. Rivas, D. Muraca, L. M. Socolovsky, and M. Knobel, “Small-Angle X-Ray Scattering to Analyze the Morphological Properties of Nanoparticulated Systems,” in *Handbook of Materials Characterization*, Pablo Leite Bernardo and Helio Salim de Amorim, Ed. Cham: Springer International Publishing, 2018, pp. 37–75.
- [95] L. Boldon, F. Laliberte, and L. Liu, “Review of the fundamental theories behind small angle X-ray scattering, molecular dynamics simulations, and relevant integrated application,” *Nano Rev.*, vol. 6, no. 1, p. 25661, 2015.
- [96] L. Li, “Structural Analysis of Cylindrical Particles by Small Angle X-ray Scattering,” *University of Bayreuth*, 2005.
- [97] A. F. Craievich, “Small-Angle X-ray Scattering by Nanostructured Materials,”

- in *Handbook of Sol-Gel Science and Technology*, 2nd ed., L. Klein, M. Aparicio, and A. Jitianu, Eds. Cham: Springer International Publishing, 2018, pp. 118–1230.
- [98] D. Lamba, “Wide-Angle X-Ray Scattering (WAXS),” in *Encyclopedia of Membranes*, E. Drioli, Ed. Berlin, Heidelberg: Springer Berlin Heidelberg, 2016, pp. 2040–2042.
- [99] Z. He, “Structural modification in rigid and semi-flexible Polymers,” University of Reading, Uk, 1993.
- [100] F. J. Baltá-Calleja and C. G. Vonk, *X-ray scattering of synthetic polymers*. Elsevier, 1989.
- [101] Bernard Dennis Cullity, *Elements of x-ray diffraction*, 1st ed. Addison-Wesley Publishing Company, Inc., 1959.
- [102] J. Cazaux, *Understanding solid state physics : problems and solutions*. Taylor & Francis Group, 2016.
- [103] L. W. Swanson and G. A. Schwind, “Review of ZrO/W Schottky Cathode,” in *Handbook of Charged Particle Optics*, CRC Press, 2017, pp. 1–28.
- [104] “The Power of the Fourier Transform for Spectroscopists - Chemistry LibreTexts.” [Online]. Available: [https://chem.libretexts.org/Bookshelves/Physical_and_Theoretical_Chemistry_Textbook_Maps/Supplemental_Modules_\(Physical_and_Theoretical_Chemistry\)/Spectroscopy/Fundamentals_of_Spectroscopy/The_Power_of_the_Fourier_Transform_for_Spectroscopists](https://chem.libretexts.org/Bookshelves/Physical_and_Theoretical_Chemistry_Textbook_Maps/Supplemental_Modules_(Physical_and_Theoretical_Chemistry)/Spectroscopy/Fundamentals_of_Spectroscopy/The_Power_of_the_Fourier_Transform_for_Spectroscopists). [Accessed: 07-Jun-2019].
- [105] Peter J. Larkin, *IR and Raman Spectroscopy: principles and spectral interpretation*. Oxford: Elsevier Inc., 2011.
- [106] A. E. Krauklis, A. I. Gagani, and A. T. Echtermeyer, “Near-Infrared Spectroscopic Method for Monitoring Water Content in Epoxy Resins and Fiber-Reinforced Composites,” *Mater. (Basel, Switzerland)*, vol. 11, no. 4, Apr. 2018.
- [107] “FT-IR Spectroscopy—Attenuated Total Reflectance (ATR)” . Perkin Elmer Life and Analytical Sciences.” *PerkinElmer Life and Analytical Sciences*, p. 5, 2005.
- [108] F. M. Mirabella, *Internal reflection spectroscopy: theory and applications*. New York: Marcel Dekker, 1993.
- [109] David A. Woods and Colin D. Bain, “Total internal reflection spectroscopy for studying soft matter,” *Soft Matter*, vol. 10, no. 8, pp. 1071–96, 2014.
- [110] A. Saleem, L. Frormann, and A. Iqbal, “High performance thermoplastic composites: Study on the mechanical, thermal, and electrical resistivity properties of carbon fiber-reinforced polyetheretherketone and polyethersulphone,” *Polym. Compos.*, vol. 28, no. 6, pp. 785–796, Dec. 2007.
- [111] A. W. Coats and J. P. Redfern, “Thermogravimetric Analysis: A Review,” *Analyst*, vol. 88, no. 1053, pp. 906–924, 1963.
- [112] C. A. Schneider, W. S. Rasband, and K. W. Eliceiri, “NIH Image to ImageJ: 25 years of image analysis,” *Nat. Methods*, vol. 9, no. 7, pp. 671–675, 2012.
- [113] S. L. Gras and A. M. Squires, “Dried and Hydrated X-Ray Scattering Analysis of Amyloid Fibrils,” *Methods Mol. Biol.*, vol. 752, pp. 147–163, 2011.
- [114] “SasView - Small Angle Scattering Analysis.” [Online]. Available: <https://www.sasview.org/>. [Accessed: 22-Sep-2019].

Chapter 4: Additive manufacturing of thermoplastic polymer based electrically conductive strands

4.1 INTRODUCTION

The chapter describes the printing of electrically conductive strands and a methodology of the novel experiments performed at the synchrotron facility with the record of data offering a simultaneous structure-property relationship. Electrically conductive strands were printed, containing carbon nanotubes dispersed in a polycaprolactone matrix, using a digitally controlled bio-extruder. Polycaprolactone is a semicrystalline polymer offering promising 3D print qualities such as rheology, layer adherence, excellent impact strength and durability. The 3D printed strands were studied under the effect of uniaxial deformation probing the deformation effects on the network of carbon nanotubes. For the sake of understanding, the study is conducted into two experimental schemes. In one of the scheme, strands are printed and studied against the bulk film. Electrical conductivity is calculated in these samples before and after deformation. In the other scheme, electric current and corresponding voltage drop are measured along the length of 3D printed strand, for electrical conductivity calculation, simultaneously during uniaxial deformation. Small-angle x-ray scattering is used as a key technique to probe structural variation under the effect of uniaxial deformation. A 1D-correlation function is used to find structural parameters namely long period, crystalline lamellae and amorphous phase. The dynamic calorimetric data is used to elucidate the crystallinity of the nanocomposite material with the inclusion of carbon nanotubes. A predictive strain-dependent electrical conductivity model is presented based on the experimental work.

4.2 MATERIALS AND METHODS

4.2.1 Materials

Multiwall carbon nanotubes (MWCNTs) were purchased from Sigma Aldrich, Portugal with diameter 6-9 nm and 5.0- μ m length. Poly (ϵ -caprolactone) (PCL) is used as a matrix material for the preparation of nanocomposite. PCL is a semi-crystalline biocompatible and biodegradable linear aliphatic polyester with a low melting point

and glass transition temperature [1]. It was obtained from Perstorp, the UK with trade name Capa 6500, having a molecular weight (M_w) 50,000 g/mol . It was supplied in pellets form with approximate size 3 mm . The solvents used to disperse MWCNTs include dichloromethane (DCM) and chloroform. These were obtained from Scharlau Chemie and Honeywell, respectively. Triton X-100 was used as a surfactant to improve the dispersion of MWCNTs into the PCL matrix and obtained from Sigma Aldrich. These materials are discussed in detail in Ch.3, section 3.5. Polycaprolactone is preferred due to its low melting point and elasticity as desired for uniaxial deformation while carbon nanotubes preferred over other conductive nanostructures due to relatively lower density.

4.2.2 Nanocomposite preparation

Two different schemes have been used to prepare nanocomposites. In the first scheme, MWCNTs were dispersed in DCM in the presence of Triton X-100 (2.0 % w/w) using a probe sonicator, (Ch.3, section 3.11), for 5 min . MWCNTs are used in the study with loadings of 0.5 % w/w. Subsequently, PCL was added to the sonicated solution and the composition was left in the incubator Ch. 3, section 10) set for 18 hrs with 100 rpm at 25 °C. PCL was dissolved in DCM after 18 hours. Further, the sonication process was repeated to achieve appropriate dispersion of MWCNTs. The solution kept in the incubator at 25 °C for 2.5 hrs to observe stable dispersion of MWCNTs in the PCL matrix. The composition was then transferred into a Petri dish and left for 72 hrs into the incubator at 25 °C to remove the DCM. The composite films were ready to use as input material for the bio extruder. In the second scheme of composite preparation, 1.0 % w/w MWCNTs were dispersed in chloroform with the help of a Triton X-100, using the same preparation procedure as explained before.

4.2.3 Additive manufacturing system

A dual bio-extruder [2] is used to print conductive strands containing PCL based nanocomposite containing MWCNTs. The major characteristic of this system is the possibility of extruding materials having either high, medium or low viscosity and with the application of low or high temperatures. The system is shown in Figure 4.1. The key components include a temperature controller, a screw rotation controller, a printing stage, a reservoir for feedstock material, a printing nozzle, a compressed air system, three motors controlling motion along three axes, and a computer system for

control and command of the extruder. A large number of nozzle diameters can be used ranging from 0.1 to 1mm.

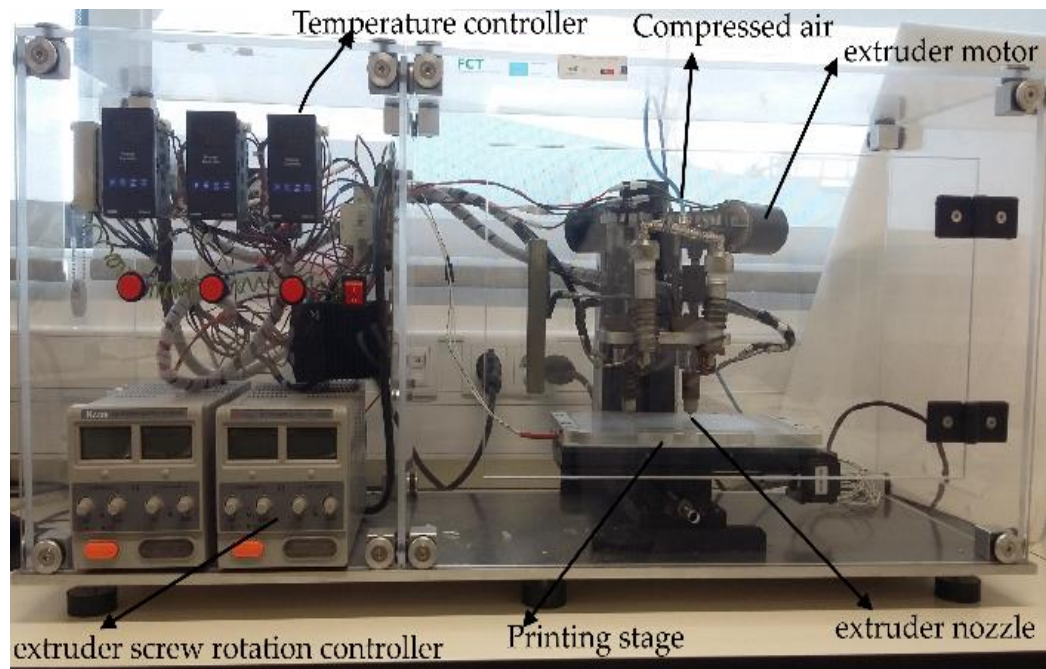


Figure 4.1. The description of an additive manufacturing system is presented that is used to print an electrically conductive MWCNT /PCL nanocomposites strands.

The screw rotation velocity and melt temperature can be tuned through the knobs provided for robust control. Induction coils are used to melt nanocomposite material and a temperature controller is used to control the temperature for melting of material in the reservoir. There are three induction coils such that one for reservoir and others for rest of assembly connecting between a printing nozzle and the reservoir. The temperature controller has a temperature range of $25 \pm 5^\circ\text{C}$ to $350 \pm 5^\circ\text{C}$. The screw rotation speed of the extruder is controlled through the application of voltage. The printable material is pushed from the reservoir towards extruder using a compressed air having a pressure of 5.0 bar. The extruder takes commands (input information) from a Matlab based programme and acts accordingly. The printable part information is provided through a .txt file. The stage is made of acrylic and it is removable from the printing platform.

4.2.4 Additive manufacturing of strands

Nanocomposite films are prepared with different loadings of MWCNTs using the preparation schemes as mentioned in section 4.2.2. The prepared films are cut into small flakes. This helps to fill the reservoir of the bio-extruder that is cylindrical as

indicated in Figure 4.2. The reservoir has an internal diameter of 18.0 ± 0.1 mm from the top side (material insertion side) and an outlet inner diameter 4.0 ± 0.1 mm. The cylinder has a length of 90.0 mm. The nanocomposite bulk films, prepared through the process mentioned in section 4.2.2, were cut into small flakes. The size of flakes was 3-4 times smaller than the diameter of the reservoir.

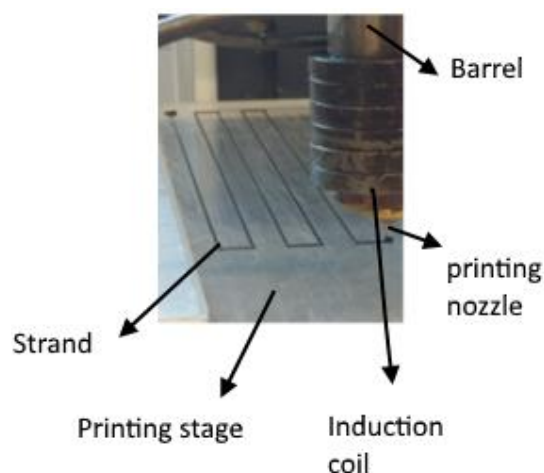


Figure 4.2. An electrically conductive strand is Printed using MWCNT/PCL nanocomposite having diameter 200-300 μ m. The printing is achieved using the system described in Figure 4.1.

Rectangular samples (21x1.98 x 0.18 in mm) were taken out from the nanocomposite film containing 0.5 % w/w MWCNTs to compare with its 3D printed strands having dimension 21 x 0.38 x 0.48 in mm. The bio-extruder is shown in Figure 4.1 for the printing of an electrically conductive strand from nanocomposite flakes obtained through nanocomposite film. The 3D printed strands are indicated in Figure 4.2. Electrically conductive strands were printed using 0.5 % (w/w) and 1.0 % (w/w) MWCNTs. Both compositions were 3D printed under similar conditions (extrusion temperature, screw rotation speed) except deposition velocity. The strands contained 0.5 % w/w of MWCNTs were printed at 140 °C with the screw rotation velocity 25 rpm and the deposition velocity 400 mm/min. The other composition (1.0 % w/w MWCNTs) were printed using the same conditions except for the deposition velocity, which was 300 mm/min. The overall length of the 3D printed strand was around 550 mm.

4.2.5 Fourier Transform Infrared Spectroscopy

Fourier Transform Infrared spectroscopy (FTIR) was used to determine the presence of significant functional groups in PCL and its nanocomposite containing

MWCNTs. The presence of functional groups is determined from the spectra recorded using the system described in Ch.3, section 3.17. The samples are scanned 64 times using the mid-infrared range from 400 cm^{-1} to 4000 cm^{-1} in the absorption mode.

4.2.6 Measurement of electrical conductivity

A four-probe method is used for the calculation of direct current (DC) electrical conductivity in 3D printed strands and the samples from bulk film under the effect of uniaxial deformation. During uniaxial deformation, the current and voltage data recorded non-simultaneously/simultaneously for samples containing MWCNTs with 0.5 % (w/w) and 1.0 % (w/w), respectively. Special grips, described elsewhere [3] and discussed briefly in Ch.3, section 3.13.1, are used for the simultaneous acquisition of current (I), and voltage (V) data during uniaxial deformation. These grips provide a specific space for holding the sample when attached with the crossheads of the extensometer. A set of two grips is required for holding the sample during uniaxial deformation. One grip contains two parts that hold one end of the sample when placed in between two parts, where preconfigured current and voltage measuring probes sensing the variations due to uniaxial deformation. A similar kind of grip with respective probes holding another end of the sample and thereby completing the circuit. In this way, the grips isolate the sample under test from the rest of the extensometer assembly and thereby avoiding the possible interference. The length of the samples used for uniaxial deformation was 10 mm while a length 6-7 mm was used for clamping on each end of the sample. Preliminary measurements and calculations were conducted for the electrical conductivity enabling to select reasonable samples for deformation experiments. The electrical conductivity is calculated with the help of Eq. (4.1) [4] using the sample dimension and recorded data (I , V).

$$\sigma = \left(\frac{I}{V}\right)\left(\frac{l}{w.t}\right)\lambda^2, \text{ where } \lambda = (1 + \varepsilon) \quad (4.1)$$

Where λ , ε , l , w and t represents the extension ratio, engineering strain, length, width and thickness of the sample, respectively, while I and V represent the amount of the current and the corresponding voltage drop measured across the sample under uniaxial deformation. The systems were used to measure current, voltage and deformation are described in Ch.3, section 3.12.2 and 3.13.2, respectively.

4.2.7 Mechanical characterization

Electrically conductive nanocomposite strands with an initial length of 10 mm were strained along the length of the sample using two different extensometers, discussed separately in Ch.3, section 3.13. A TST350 tensile stress testing system, from ALBA synchrotron, was used to deform samples with two precision ground stainless steel lead screws to maintain a perfect and uniform vertical and horizontal alignment. Sample jaws move in opposite directions to maintain the sample in position as desired for SAXS experiments. Samples were deformed using three different strain rates 0.064 s^{-1} , 0.032 s^{-1} and 0.016 s^{-1} . The strain rate is defined through the expression in Eq. (4.2)

$$\begin{aligned}\varepsilon(t) &= \frac{l(t) - l_o}{l_o} \\ \dot{\varepsilon}(t) &= \frac{d}{dt} \left(\frac{l(t) - l_o}{l_o} \right) \\ \dot{\varepsilon}(t) &= \frac{1}{l_o} \cdot \frac{d}{dt} l(t) = v(t)/l_o\end{aligned}\quad (4.2)$$

Where $\dot{\varepsilon}(t)$ is the strain rate, $v(t)$ is the speed at which the cross-heads of the extensometer are moving away from each other and l_o is the length of the sample before deformation. These strain rates were considered so that reasonable x-ray scattering, electrical and mechanical data was acquired during the experiments. The other extensometer used was an in house built system with the possibility to use sample holder grips of choice. A rate of 0.1 s^{-1} was used for uniaxial deformation. Both the systems were remotely controlled from outside the experimental hutch to collect the experimental data. The measurement systems are described in Ch. 3, sections 3.12 and 3.13 concerning the record of data for electrical conductivity and mechanical deformation, respectively.

4.2.8 Small-angle X-ray scattering

SAXS experiments performed at the beamline BL11-NCD (SWEET), ALBA Synchrotron facility in Barcelona, Spain. Two separate experimental small-angle X-ray scattering (SAXS) setups were used to study morphology and the structure of the nanocomposites. In one of the two experimental setups, time-resolved SAXS patterns

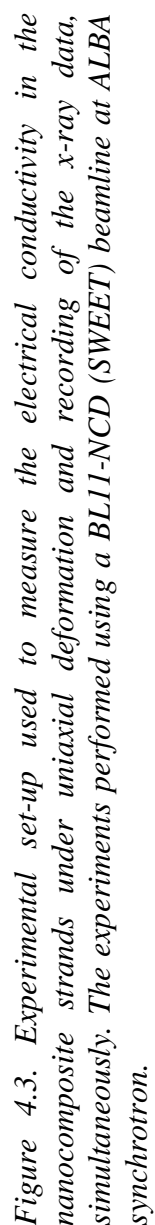


Figure 4.3. Experimental set-up used to measure the electrical conductivity in the nanocomposite strands under uniaxial deformation and recording of the x-ray data, simultaneously. The experiments performed using a BL11-NCD (SWEET) beamline at ALBA synchrotron.

of two seconds. The experimental set up for the simultaneous acquisition of data is shown in Figure 4.3. The SAXS patterns were recorded with a Pilatus 1M detector having a resolution of 981 x 1043 pixels and pixel size of $172 \mu m^2$. The 2D X-ray patterns were recorded using a sample-to-detector distance of 6480 mm. The intensity profile showed the plot of the scattering intensity as a function of the scattering vector, $q = 4\pi (\sin \theta/\lambda)$, where λ is the X-ray wavelength ($\lambda = 1.0 \text{ \AA}^{-1}$) and 2θ is the scattering angle. The scattering vector q lies in the range $(0.002-0.12) \text{ \AA}^{-1}$. The scattering vector was calibrated using rat-tail collagen by the beamline scientist. In the second experimental configuration, SAXS patterns obtained during uniaxial deformation along the length of samples (3D printed strands) containing 1.0 % w/w MWCNTs with an exposure time of 1.0 sec. The sample to detector (ADSC Q210r CCD detector) distance was 6310 mm with a resolution of 3072 x 3072 pixels, a pixel size of $102 \mu m^2$. In this experimental arrangement, the effective scattering vector q lies in the range $(0.005-0.12) \text{ \AA}^{-1}$. The scattering vector was calibrated using silver behenate. The 2D SAXS patterns were integrated to 1-D data using Image J, a public domain Java image-processing program [5], employing YAX macro [6]. Further, 1D SAXS data was background corrected using the in house written Matlab codes. For the extraction of the characteristic parameter (degree of crystallinity, long period and lamellar thickness) from the SAXS profiles (after radial integration), the autocorrelation function of the one-dimensional electron density distribution $\gamma(R)$ is calculated by Fourier transformation of $I(q).q^2$ [7]. For a two-phase layered system, a periodic correlation function is expected, where $\gamma(R)$ at $R = 0$ is related to crystallinity. For an ideally ordered lamellae $\gamma(0) = R_{max}$ holds for all maxima at higher R-values. A difference between $\gamma(0)$ and the first maximum γ_{max} at $R > 0$ reflects a deviation from an ideal two-phase layered system. The position of the first maximum at $R > 0$ of the electron density correlation function (R_{max}) corresponds to the long period $L = 2\pi/q_{max}$ of the lamella stack. The position can be estimated from the third zero crossings of $d\gamma(R)/dR$ as mentioned in Eq. (4.3)

$$\gamma(R) = \int_0^\infty q^2 I(q) \cos(qR) dq / \int_0^\infty q^2 I(q) dq \quad (4.3)$$

Where $I(q)$ is the intensity at each value of the scattering vector ($q = 2\pi/L_b$, where L_b is the Bragg spacing). The shape and properties of the $\gamma(R)$ are discussed thoroughly in the case of a strictly periodic two-phase system [7].

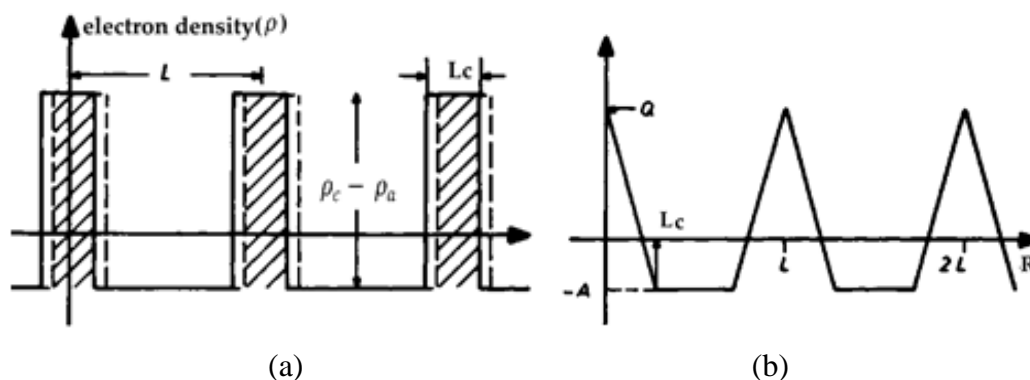


Figure 4.4. (a) Electron density distribution $\eta(R)$ and (b) the related correlation function $\gamma(R)$ for an ideal periodic two-phase structure (semicrystalline polymer) as mentioned in equation 3 [7].

The periodic structure shows an electron density distribution, $\eta(R)$, as indicated in Figure 4.4 (a). It can be described by specifying the long-period (L), the crystallite thickness L_c , and the electron density difference ($\eta_c - \eta_a$), under the condition, where the crystallinity $X_c = L_c/L < 0.5$. For the definition of L_c and L , the reader is directed to consider Figure 4.4. The different correlation functions differ only by a constant. The “self-correlation triangle” centred at the origin is of principal importance and it is defined as a sequence of triangles, centered at $z = 0, L, 2L, \dots$, which reflect the correlations within a lamella, between next neighbours and second neighbours and so on. Hence, it is used to determine autocorrelation function and the relevant parameters of interest. The “self-correlation triangle” has several characteristic properties. The value at $z = 0$ is referred to as the invariant (Q) and can be deduced as

$$\gamma(R = 0) = q = X_c (1 - X_c)(\eta_c - \eta_a)^2 \quad (4.4)$$

The slope $(\gamma)/dR$ is

$$\frac{d(\gamma)}{dR} = -\frac{1}{L}(\eta_c - \eta_a)^2 \frac{d(\gamma)}{dR} = -\frac{1}{L}(\eta_c - \eta_a)^2 \quad (4.5)$$

The horizontal line between the triangles is called the “baseline” with coordinate (negative) given as

$$A = (X_c)^2 (\eta_c - \eta_a)^2 \quad (4.6)$$

The height of the triangle is defined as

$$A + q = X_c (\eta_c - \eta_a)^2 \quad (4.7)$$

The purpose of referencing above relations is to show that the application of these relations are not restricted to the highly regular system but can be extended, with slight modifications, to real systems. The reader is referred to consider [8] for the detailed explanation of the above relations. The Herman's orientation factor, $\langle P_2 \rangle$, was determined from azimuthal integration of 2D SAXS patterns [9] and it is defined in Eq. (4.8)

$$f = \langle P_2 \rangle = \frac{3\langle \cos^2 \varphi \rangle - 1}{2} \quad (4.8)$$

$$\text{Where} \quad \langle \cos^2 \varphi \rangle = \frac{\sum_{i=0}^{i=90} I_i \cos^2 \varphi \sin \varphi_i}{\sum_{i=0}^{i=90} I_i \sin \varphi_i} \quad (4.9)$$

In the above equations, I_i and φ are the intensity and angle at the i th position along the diffraction ring. The limiting values of Herman's parameter $\langle P_2 \rangle$ are in the range of $-0.5 \leq \langle P_2 \rangle \leq 1.0$. For $\langle P_2 \rangle = 1.0$ the CNTs perfectly aligned parallel to the deformation direction while $\langle P_2 \rangle = 0$ denotes a random orientation and $\langle P_2 \rangle = -0.5$ for alignment perpendicular to the deformation direction.

A different approach is adopted for the decomposition of anisotropic x-ray scattering patterns from oriented multi-component samples into the scattering from each component. The method [10] is based on the representation of an anisotropic scattering pattern by an orthogonal series of spherical harmonic functions. For the sake of this, a two-phase system containing a fraction (x) of "a" and $(1-x)$ of "b" is considered to present the approach. For a system in which the length scale of the phase-separated structure is large compared with the length scale-giving rise to the scattering, the total scattering $I(|q|, \alpha)$ can be written as the algebraic sum of the scattering from the two components:

$$I(|q|, \alpha) = x.I^a(|q|, \alpha) + (1-x).I^b(|q|, \alpha) \quad (4.10)$$

Here $|q|$ and α represents the scattering vector and the angle between the scattering vector $|q|$ and the symmetry axis of the sample. The scattering for a sample exhibiting a partial level of preferred orientation can be written as the convolution of the scattering for a perfectly aligned system $I^0(|q|, \alpha)$ with the orientation distribution function $D(\alpha)$:

$$I(|q|, \alpha) = I^0(|q|, \alpha) * D(\alpha) \quad (4.11)$$

The function $D(\alpha)$ describes the distribution of the structural units to the symmetry axis of the sample. The intensity functions and the orientation distribution

function can be expressed in terms of a series of spherical harmonics, $I_{2n}(|q|)$, $I_{2n}^0(|q|)$ and D_{2n} . The convolution of this is written as [11]

$$I_{2n}(|q|) = \frac{2\pi}{(4n+1)} I_{2n}^0(|q|, \alpha) D_{2n} \quad (4.12)$$

where $n = 0, 1, 2, 3, \dots, \infty$. Only the even terms of each series are required due to the inversion centre intrinsic to an X-ray scattering pattern for a non-absorbing sample. The components of each series can be obtained by:

$$I_{2n}(|q|) = (4n+1) \int_0^{\pi/2} I(|q|, \alpha) P_{2n}(\cos \alpha) \sin \alpha d\alpha \quad (4.13)$$

where $P_{2n}(\cos \alpha)$ are Legendre polynomials; only the even number terms are required due to the inversion symmetry inherent in an X-ray diffraction pattern for a non-absorbing sample. Few even order Legendre polynomials are provided in Table 4.1. The complete scattering pattern may be recovered by:

$$I(|q|, \alpha) = \sum_{2n=0}^{2n=\infty} I_{2n}(|q|) P_{2n}(\cos \alpha) \quad (4.14)$$

The first five spherical harmonic components (P_0 , P_2 , P_4 and P_6) are shown in Figure 4.5. The I_0 component represents the scattering from an equivalent macroscopically unoriented sample, while I_2 , I_4 , I_6 , I_8, \dots, I_{2n} arise from the anisotropic scattering, which may well include scattering from crystalline, amorphous and filler phase.

Table 4.1. First few even-order Legendre polynomials.

n=0	$P_0(\cos \theta) = 1$
n=1	$P_2(\cos \theta) = \frac{1}{4}(1 + 3 \cos 2\theta)$
n=2	$P_4(\cos \theta) = \frac{1}{64}(9 + 20 \cos 2\theta + 35 \cos 4\theta)$
n=3	$P_6(\cos \theta) = \frac{1}{512}(50 + 105 \cos 2\theta + 126 \cos 4\theta + 231 \cos 6\theta)$

The value of this representation is that the effects of preferred orientation are separated from the dependence of the scattering on the spatial correlations. Eq. 4.12 underlines the fact that for samples with the same structure, the variation of the amplitudes of the spherical harmonics $I_{2n}(|q|)$ with $|q|$ are essentially the same, with a simple constant multiplier dependent on the level of preferred orientation [8].

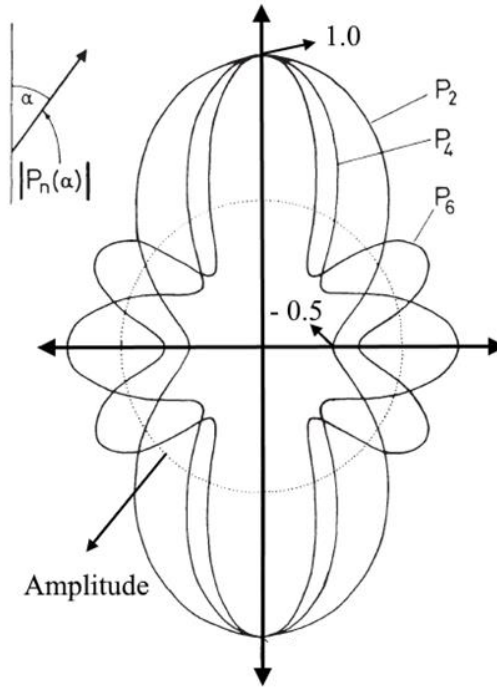


Figure 4.5. Sections through the even-ordered spherical harmonic functions, P_0 , P_2 , P_4 and P_6 , which represent orientation distributions [12].

The orthogonal nature of the spherical harmonics in Eq. 4.13 means that for a multiple-phase structure in which the scattering is additive, the resultant spherical harmonics will also be linear combinations of the harmonic functions for each phase. We can write:

$$I_{2n}(|q|) = x \cdot I_{2n}^a(|q|) + (1 - x) \cdot I_{2n}^b(|q|) \quad (4.15)$$

where $I_{2n}^a(|q|)$ are the spherical harmonics for the pure phase. Combining Eq. 4.12 with 4.15 results:

$$I_{2n}(|q|) = x \cdot I_{2n}^{0a}(|q|) D_{2n}^a(2\pi/4n + 1) + (1 - x) \cdot I_{2n}^{0b}(|q|) D_{2n}^b(2\pi/4n + 1) \quad (4.16)$$

where $I_{2n}^{0a}(|q|)$ are the functions for the pure perfectly aligned phase. For a particular experimentally observed harmonic Eq. 4.16 reduces to:

$$I_{2n}(|q|) = I_{2n}^{0a}(|q|) k_{2n}^a + k_{2n}^b I_{2n}^{0b}(|q|) \quad (4.17)$$

where k^a and k^b are scaling constants with k^a given by

$$k_{2n}^a = x \cdot D_{2n}^a \cdot (2\pi/4n + 1) \quad (4.18)$$

and k^b by a similar expression. Eq. 4.17 provides a route to the separation of the scattering into the contributions from each phase. We simply need a mechanism to

identify the components within each 1-d function. There is a considerable advantage in using information from the scattering patterns of the pure phases where this is available. Although such scattering patterns need to arise from samples with the same structure, it is not necessary to be the same for the level of preferred orientation. As emphasised above the variation of the harmonic function with $|q|$ does not depend, other than through a simple constant, on the orientation.

4.2.9 Scanning Electron microscopy

The morphology of MWCNTs in 3D printed strand is studied using Field Emission Scanning Electron Microscope (FESEM). The sample surface before and after deformation is scanned using a low voltage (1Kv). In FESEM, the detector gets information from secondary electrons emitted because of the primary beam directed on the desired surface. The principle of FESEM and the description of the microscope is provided in Ch.3, section 3.16.

4.2.10 Dynamic scanning Calorimetry

Differential scanning calorimetry (DSC) analysis was used for the measurement of the crystallinity of the pure polycaprolactone (PCL) and its nanocomposite containing MWCNTs. A STA6000 from Perkin Elmer was used to serve the purpose. An explanation about the system used and theoretical concepts using DSC is provided in Ch. 3, section 3.18. The samples with a weight of about 7.0 ± 1 mg placed into a ceramic pan and thermally scanned from 30 °C to 90 °C, at a rate of 5 °C/m. All the experiments were conducted under nitrogen with a flow rate of 20 ml/m, to prevent oxidation. The degree of crystallization for the pure PCL and its nanocomposites was measured employing an equilibrium melting enthalpy for a 100 % crystalline PCL sample of 139.5 J/g [13].

4.3 RESULTS

4.3.1 Spectroscopic analysis

FTIR experiments were performed for the identification of vibrational modes in PCL and its nanocomposite containing MWCNTs 1.0 % (w/w). Following peaks are detected from the PCL spectra presented in Figure 4.6. These include 1723 cm^{-1} for C = O stretching vibrations, 2850 cm^{-1} for symmetric C – H₂ stretching vibrations, 2930 cm^{-1} asymmetric C – H₂ stretching vibrations, 1292 cm^{-1} for C – O and C – C stretching in the crystalline phase and 1162 cm^{-1} for C – O and C – C stretching vibrations. The

literature suggests similar bands for the aforementioned peaks with a slight variation in the PCL spectrum [14].

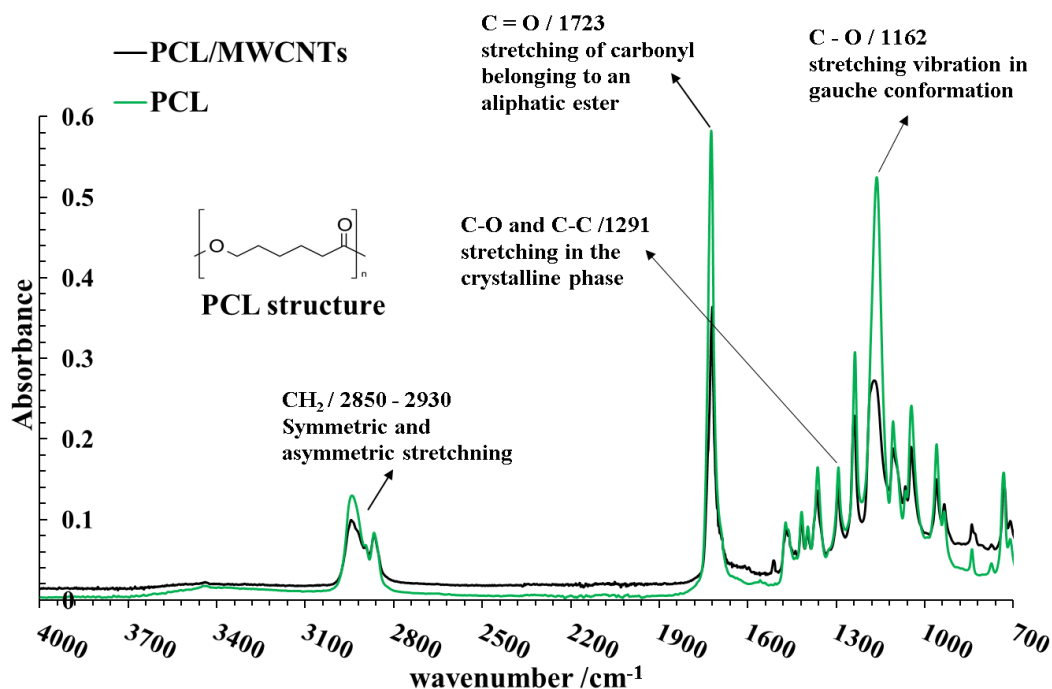


Figure 4.6. FTIR spectra of PCL and its nanocomposite containing MWCNTs (1.0 % w/w).

4.3.2 Measurement of electrical conductivity

Results are presented in this section for the experiments primarily concerned with the electrical conductivity response under the effect of uniaxial deformation. It is interesting to explore the deformation effects in nanocomposites prepared under controlled processing conditions, using additive manufacturing, against samples prepared under uncontrolled conditions. The deformation in these nanocomposites consequence to altering electrical conductivity in the nanocomposites. The relative increase or decrease signifies the importance of a processing methodology for an electrically conductive nanocomposite.

Deformation effects are studied in context to electrical conductivity in 3D printed samples before and after uniaxial deformation and simultaneously during uniaxial deformation. Also, electrical conductivity is calculated in the bulk film (BF) and it is presented in comparison with the conductive strands. The DC electrical conductivities are calculated in 3D printed strands and bulk film (BF) before deformation that are well above the electrical conductivity of pure PCL, as reported in the literature (1×10^{-10} S/m). In the first type of experiments, electrical conductivity is

calculated before and after uniaxial deformation for conductive strands and the bulk film containing 0.5 % *w/w* MWCNTs. An electrical conductivity $5.0 \times 10^{-2} \text{ S/m}$ is calculated in 3D printed strands before uniaxial deformation and without significant conduction after deformation. In contrast to 3D printed strand, an electrical conductivity $8.4 \times 10^{-1} \text{ S/m}$ and $1 \times 10^{-7} \text{ S/m}$ are calculated in the BF before and after uniaxial deformation, respectively. Two aspects are revealed from these experiments; the electrical conductivity in 3D printed strands is lower than the BF and it decreases for both kind of samples under the effect of uniaxial deformation. Before deformation, a decrease in electrical conductivity in 3D printed strand compare to the bulk film is an indication that the extrusion process significantly affected the networks of MWCNTs. Secondly, Bulk film is prepared from solution cast methodology which takes longer to solidify compare to the melt extrusion process. The molten material quickly solidifies [12] as compared to solution cast BF. In this way, carbon nanotubes do not have sufficient time for networking comparing to bulk film. Variety of parameters are affected through uniaxial deformation, which directly or indirectly alters electrical conductivity of the nanocomposite. For example, the decrease in the electrical conductivity is attributed to MWCNTs network failure due to uniaxial stress [15]. The other parameter is tunnelling resistance that plays a dominant role in electronic conduction when the material is subjected to deformation [16]. Also, when MWCNTs are subjected to mechanical strain a change in their chirality leads to modulation of the conductance [17]. There is no literature available to the best of author's knowledge for the sake of comparison considering the PCL based nanocomposite-containing MWCNTs. However, the work of [18] suggests a semi-similar kind of trend in electrical conductivity using nanocomposite containing styrene-butadiene rubber, polycaprolactone (PCL) and carbon black as conductive inclusion. In the second type of experiments, electrical conductivity is calculated in the nanocomposites containing 1.0 % (*w/w*) MWCNTs simultaneously during uniaxial deformation. The results are indicated in Figure 4.7 from these simultaneous measurements, indicating an increase in the electrical conductivity under the effect of uniaxial deformation. The increase in electrical conductivity is attributed to two factors. One of the factors is the improvement in conductive pathways due to the formation of physical paths of nanotubes. The other factor is a rearrangement of nanotubes under intermediate deformation with loadings above the percolation threshold.

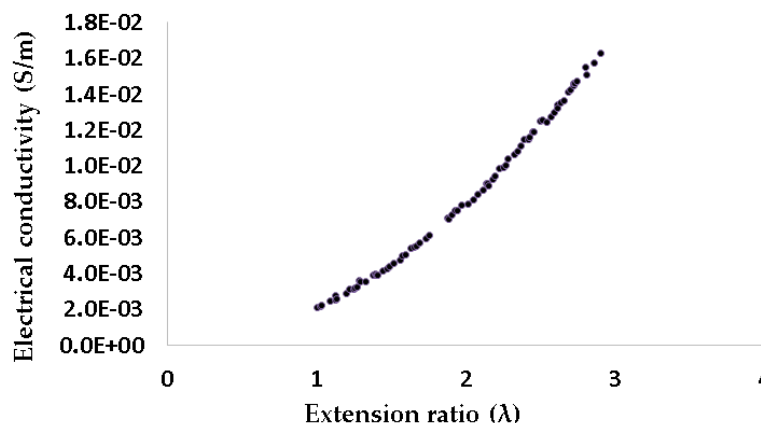


Figure 4.7. The plot shows a variation in the electrical conductivity under uniaxial deformation in 3D printed strand containing 1.0 % MWCNTs, while λ represents an extension ratio.

During 3D printing of the nanocomposites, it becomes obvious that 3D printed strands with concentrations of MWCNTs less than 0.5 % (w/w) are not been able to pass an appreciable amount of current and voltage drop. This implies that the amount of current and the corresponding voltage drop is far below than the minimum resolution of the measuring units. Besides, the transition will occur from insulator to conductor below 0.5 % (w/w) through the formation of conducting pathways when subject to a suitable external bias. This is commonly referred to as the percolation threshold for the compositions. The literature suggests a significant variation in the percolation threshold which ranges 0.08 – 3 % (w/w). [19]–[21].

4.3.3 Uniaxial deformation experiments

Uniaxial deformation in 3D printed strands versus bulk film

Solution cast nanocomposite films, containing 0.5 % w/w MWCNTs and its 3D printed strands were deformed uniaxial along the length of the sample. The study is conducted to find the effect of the print process on its tensile properties. Both samples are strained with the same uniaxial strain rate of 0.032 S^{-1} . The experiments are concerned with Young's modulus, yield strength, and fracture modes due to uniaxial deformation. Plots are presented in Figure 4.8 for a stress-strain behaviour for BF and its 3D printed strand. It is obvious from the stress-strain plot that the elastic modulus increases in the case of the bulk film compared to 3D printed strands.

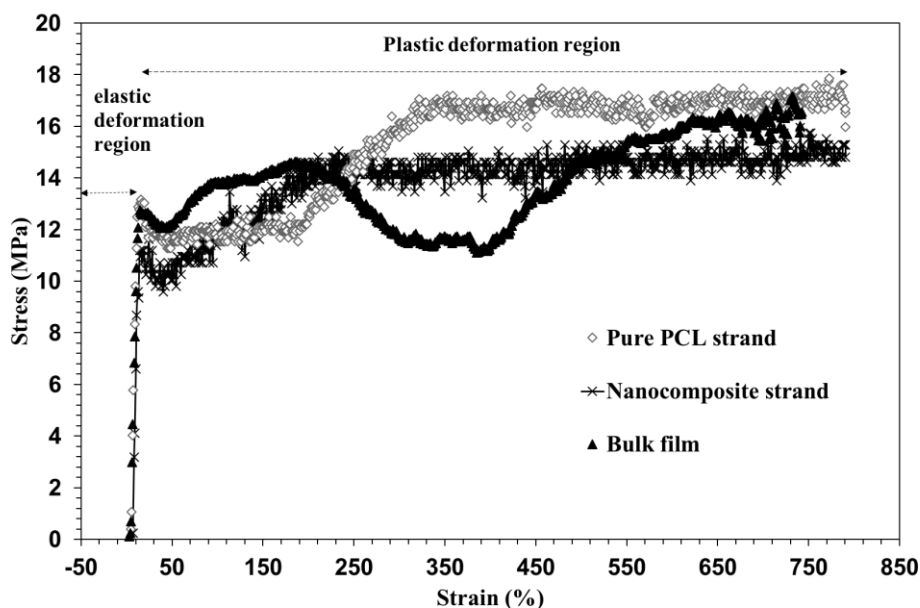


Figure 4.8. Stress-strain plots are presented for the 3D printed strands of pure PCL, nanocomposite bulk film sample and the 3D printed conductive strands printed using bulk film. These samples are deformed with 0.032 s^{-1} .

Moreover, it is obvious from Figure 4.8 that Young's modulus, yield strength, and fracture modes are slightly higher in bulk film relative to 3D printed strands. The yield strength and fracture modes are 12.7 N/mm^2 and 16 N/mm^2 measured in the bulk film, which decreases to 10 N/mm^2 and 14 N/mm^2 in 3D printed conductive strands. The blue circle indicates partial collapsing of the PCL phase and shifting of the load to MWCNTs during plastic deformation. The BF sample is fractured before extensometer reaches its limits while the strand is stretched without attaining a fracture point.

Effect of strain rate

Effect of strain rate (deformation rate) was studied in the electrically conductive samples (bulk film and 3D printed strands) containing MWCNT (0.5 % w/w). Stress-strain plots are presented in Figure 4.9 with different strain rates (0.064 S^{-1} , 0.032 S^{-1} , and 0.016 S^{-1}) for the bulk film and 3D printed strands. The elastic region, yield point and fracture point are decreased at a relatively high strain rate. The plastic deformation region is prolonged at relatively high deformation rate. In the case of 3D printed strands, less profound effects are observed with different strain rates comparing to bulk film. The elastic regions are linear in both kinds of samples. A variation in yield point is observed in BF while it remains constant in case of 3D printed strands under the effect of different strain rates. Different plastic deformation region and hence fracture

point are observed in BF samples under the effect of different strain rates. The plastic deformation region shrinks with strain rates. The fracture mode remains the same in all 3D printed strands.

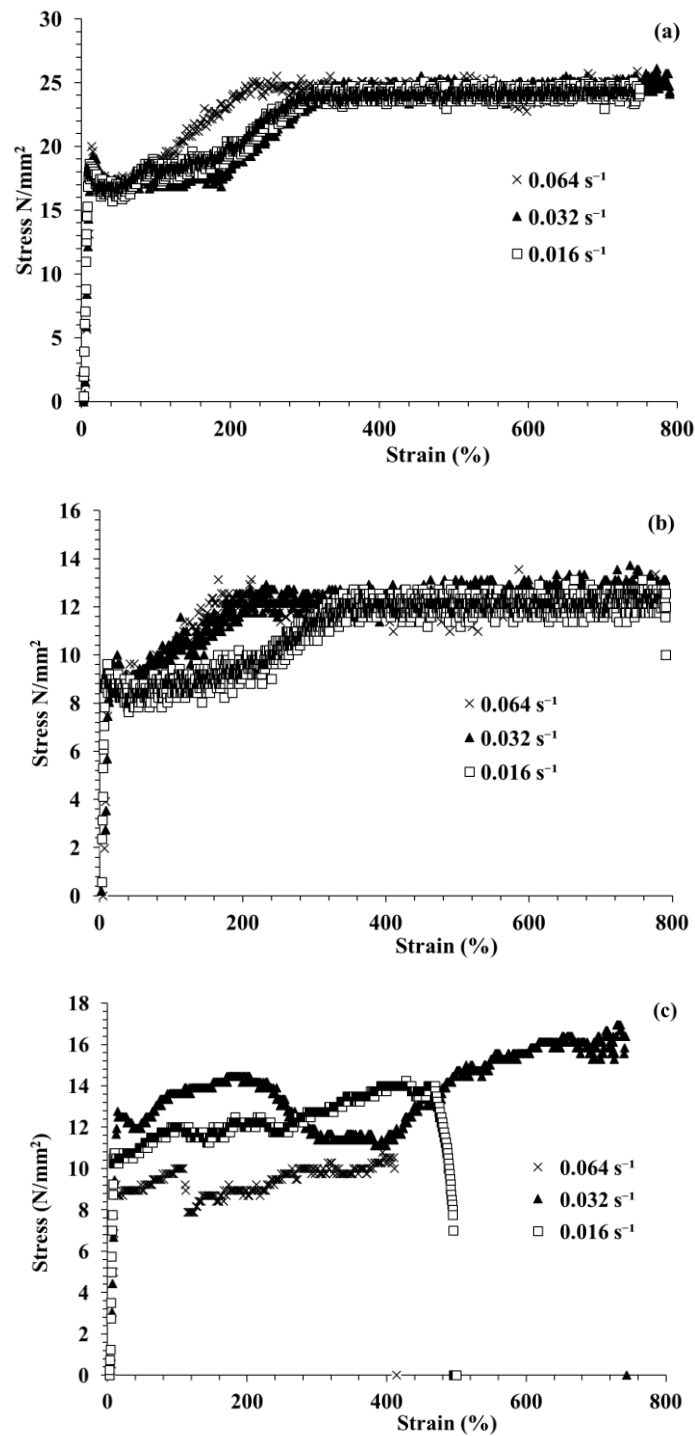


Figure 4.9. Stress-strain plots with different deformation rates for the (a) 3D printed strands of pure PCL, (b) strands of nanocomposites (PCL/MWCNTs) and (c) nanocomposite bulk film.

4.3.4 Structural Characterization

An electrically conductive nanocomposite can be visualized as a network of carbon nanotubes in a semicrystalline polymer. PCL is a semicrystalline polymer, which crystallizes upon cooling from melting, mechanical stretching or solvent evaporation. Predominantly, carbon nanotubes settle in the amorphous phase of the PCL matrix. In this way, the network properties of carbon nanotubes predominantly affected through variations in the microstructure of the PCL matrix under uniaxial deformation. A double logarithmic plot is obtained from 2D SAXS patterns for the 3D printed strand of pure PCL and its nanocomposites (bulk film and its 3D printed strand) during uniaxial deformation, as shown in Figure 4.10 (a-c). From the plots, the gradients are determined, suggesting a fractal morphology. A gradient -3 is measured from the double logarithmic plot of 3D printed strands of PCL yielding a surface fractal dimension 3.

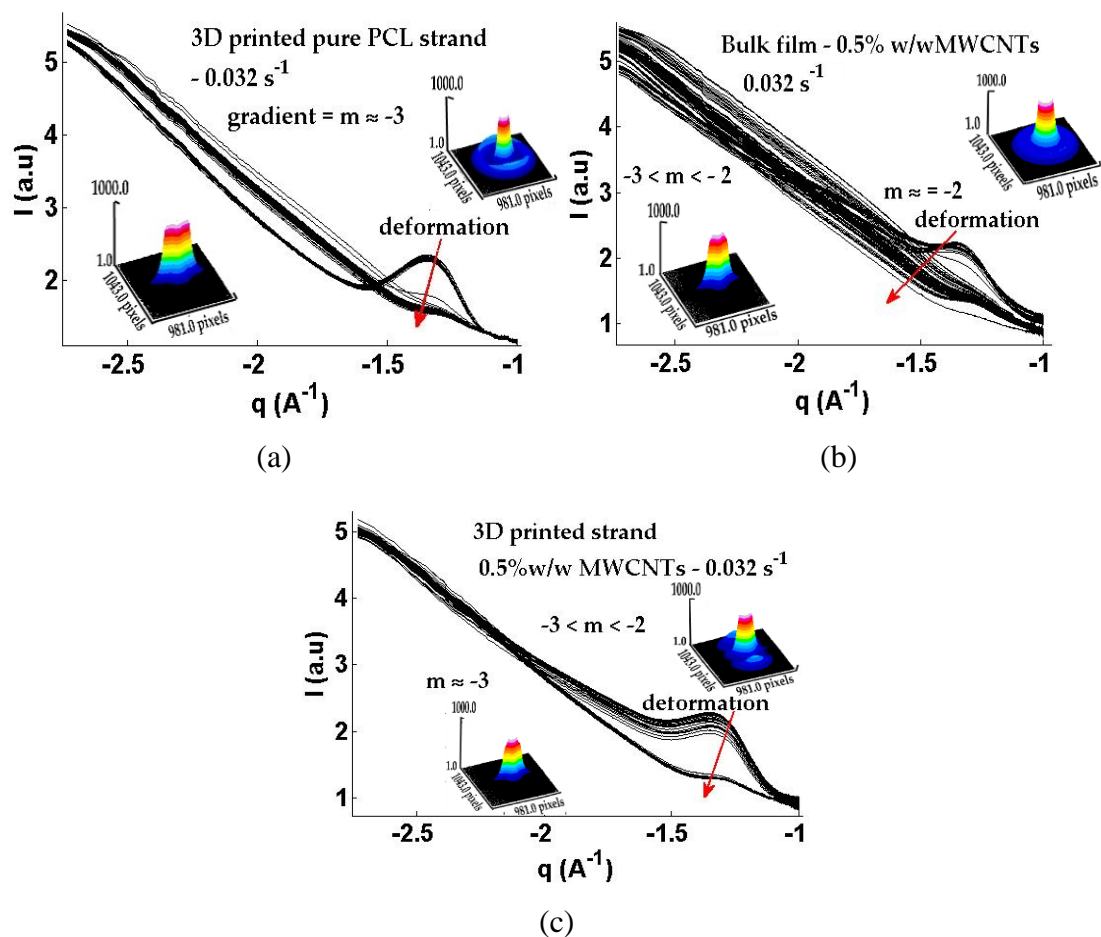


Figure 4.10. Double logarithm plot of 1D scattering intensity (I) against scattering vector for (a) 3D printed strand of pure PCL. (b) The composite film and (c) its 3D printed strand under the effect of uniaxial deformation with a strain rate of 0.032 s^{-1} . Insets show surface scattering profiles before and after uniaxial deformation.

This kind of surface fractal is a sign of rough surface [22]. This indicates that 3D printed strands of pure PCL contain microspores due to which a sharp interface exist between two. These surface fractals do not alter under the effect of the applied load. The prominent effect is diminishing the crystalline peak under the effect of deformation. Contrary to this, a gradient nearly -2 is measured from samples of BF, without deformation. This gradient changes to $-3 < m < -2$ when the sample is deformed uniaxially. These gradients belong to mass fractal morphology. A mass fractal is a structure containing branches to form a 3D network [23].

In case of the 3D printed nanocomposite, a mass fractal dimension $-3 < m < -2$ is measured before deformation which changes to -3 under the effect of uniaxial loading. This indicates that the branch structure of MWCNTs exist after deformation in BF while these branches break in 3D printed strands after deformation. A crystalline peak is observed at relatively high- q ($\approx 0.044 \text{ \AA}^{-1}$) in all type of samples (Figure 4.10), which is near to diminish gradually with the applied load. This is obvious from the surface scattering plots in the inset of Figure 10(a, c). Further, this is discussed in Figure 4.11 using a 2D scattering data from uniaxial deformation, electrical conductivity and 2D SAXS patterns.

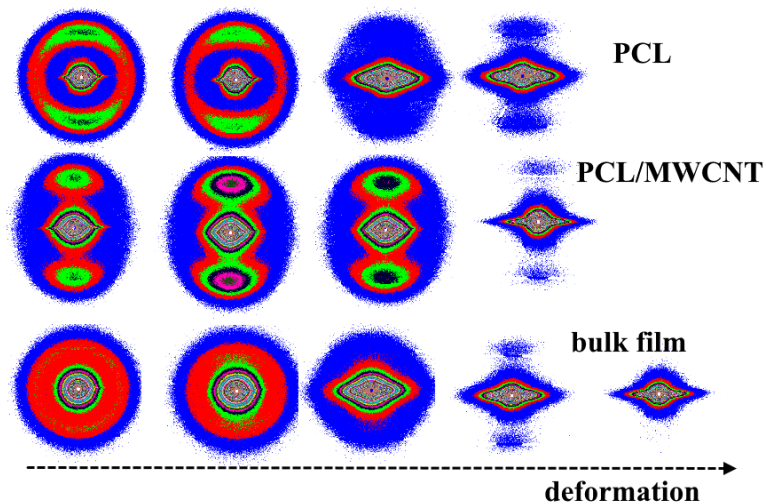


Figure 4.11. The SAXS 2D patterns for the bulk film in comparison to its 3D printed conductive strands printed using bulk film and pure PCL strands.

Symmetrical scattering is obvious in case of BF while anisotropic scattering is evidenced in 3D printed strand before deformation. After deformation, a streak appears along the meridian axis in the bulk film while a butterfly pattern appears in 3D printed strand having a streak along the meridian axis and wings along the equatorial axis.

This shows some level of anisotropy in the samples due to uniaxial deformation leading to reorganisation of amorphous phase or crystalline lamellae or MWCNTs. The level of anisotropy is explored through the azimuthal integration of 2D SAXS patterns for the q – range indicated in Figure 4.12.

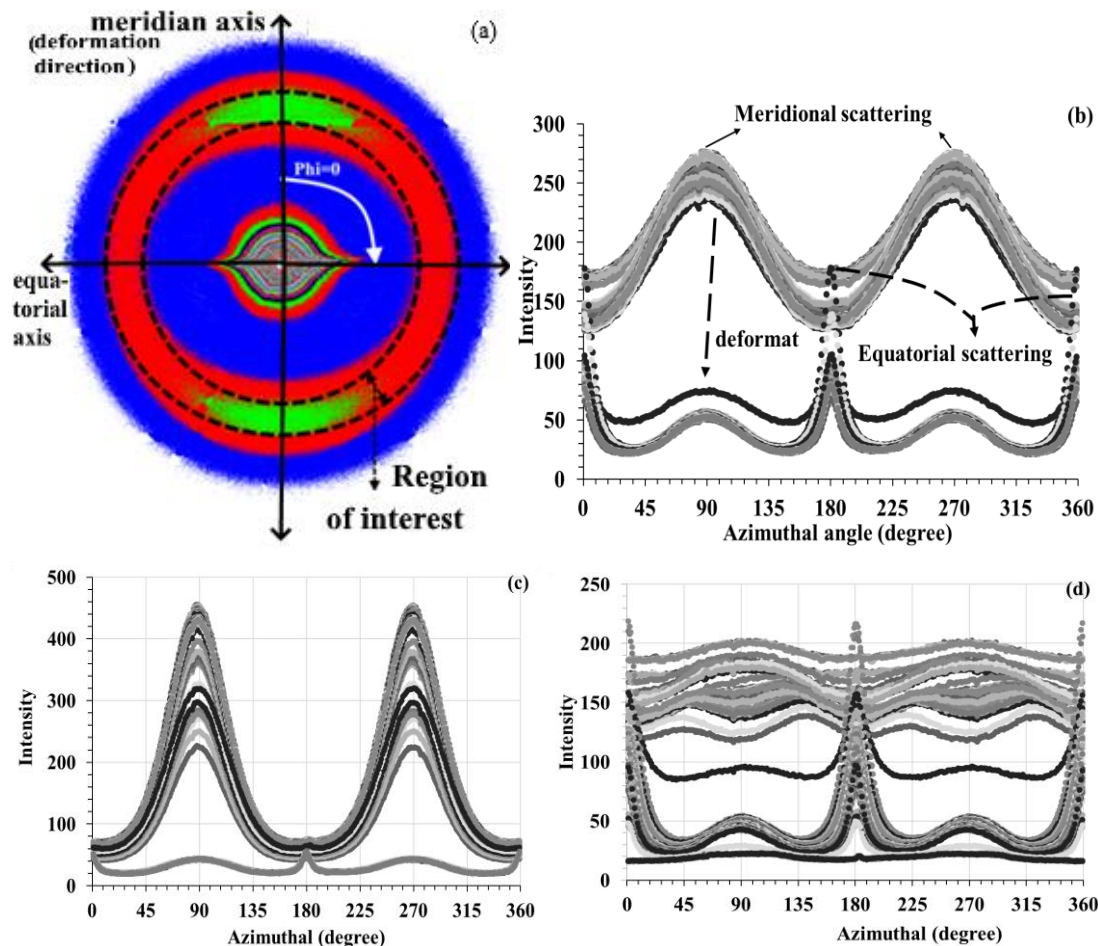


Figure 4.12. (a) A 2D SAXS profile of pure PCL is presented with reference direction for calculation of Herman orientation factor. Azimuthal profiles are presented of 2D SAXS patterns of 3D printed strand of (b) pure PCL, (c) PCL/MWCNTs, and (d) and the nanocomposite bulk film. The q – range used for azimuthal integration is 0.04-0.047 \AA^{-1} . These samples were deformed with 0.032 strain rate.

Herman's orientation factor is calculated from azimuthal profiles and results are presented in Figure 4.13. These plots indicate that the Herman orientation factor is relatively higher in 3D printed strands compare to bulk film samples. Also, the Herman orientation factor is increased further in a strand containing MWCNTs. This implies that some of the nanotubes are aligned along the print direction. The Herman orientation factor indicates a random distribution of lamellar organization in the bulk film. It increases slightly until 400 % strain and then decreases suddenly in the case of

3D printed strands. In the case of a bulk film, the behaviour is similar, except that a sudden decrease appears earlier ($\approx 300\%$) than 3D printed strands.

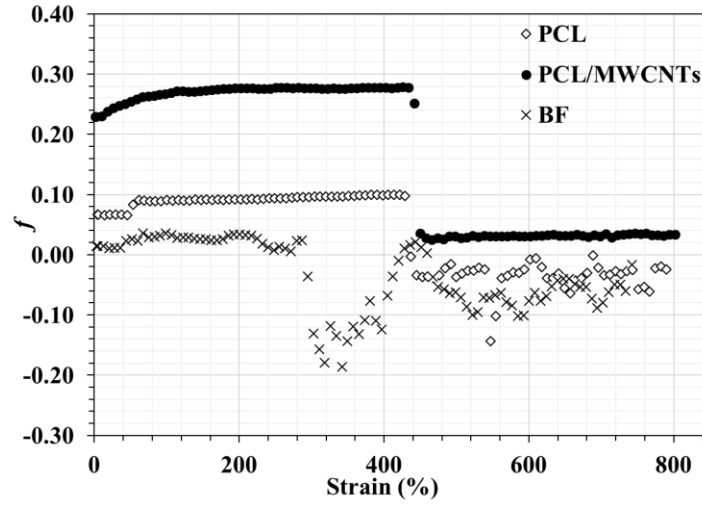


Figure 4.13. The variation in Herman's orientation factor is presented in 3D printed strands of pure PCL and its nanocomposite containing MWCNTs under the effect of uniaxial deformation. The q -range used for azimuthal integration is $0.04\text{--}0.047\text{ \AA}^{-1}$.

The contribution from MWCNTs appears in the range $0.012 < q\text{ (\AA}^{-1}\text{)} < 0.022$ as evidenced by the analysis of $1D$ log-log plots in Figure 4.14(a). In this q -range, the scattering intensity enhances significantly relative to pure PCL. This methodology is used as carbon nanotubes aggregates, suggested from numerous other studies [24].

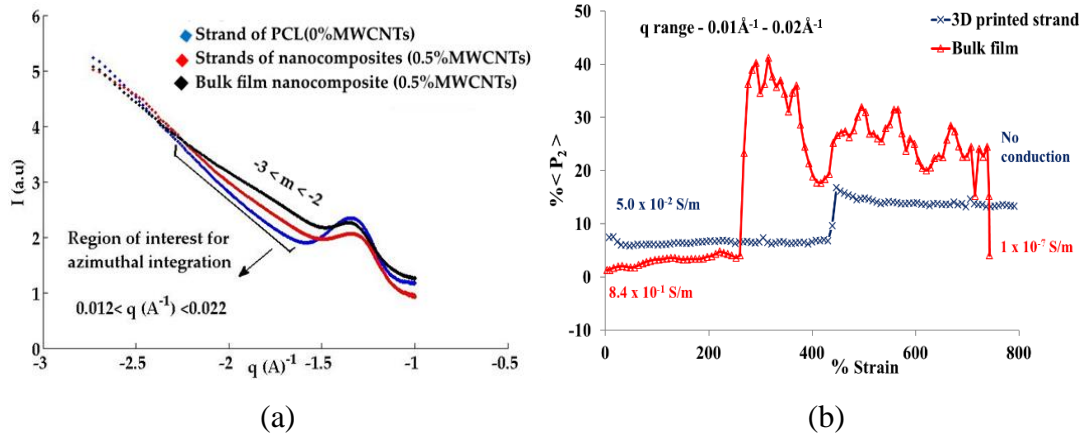


Figure 4.14. (a) Comparative double logarithmic in which the scattering intensity enhance relative to pure PCL. plots of scattering intensity (I) against scattering vector are shown for the samples mentioned in Figure 10(a-c), indicating q – the range where scattering contribution from MWCNTs is prominent relative to scattering in the low and high q regions. (b) $\langle P_2 \rangle$ is the Herman orientation factor that is measured from the azimuthal integration of 2D SAXS patterns for samples mentioned in Figure 10(b, c).

Several factors are responsible for such an aggregation of nanotubes, including entangling of MWCNTs during the growth process and attraction by van der Waals force between individual MWCNTs [24]. The $\langle P_2 \rangle$ measured from azimuthal integration of 2D SAXS patterns are presented against uniaxial strain, as in Figure 4.14 (b). It minimally increases in the elastic limit under uniaxial deformation with a sudden jump (beyond Yield point) which gradually decreases and attains a constant value.

The BF sample fractured before reaching limits of extensometer while 3D printed strand was not fractured during the experiment. This is an indication that MWCNTs are non-uniformly distributed in the PCL matrix as compared to 3D printed strand. The non – uniform distribution causes to generate non- uniform stress distribution leading to fracture point [25]. It is obvious from the plot that less profound change happened in the $\langle P_2 \rangle$ in the elastic region as compared to the plastic deformation region. It is obvious from plots in Figure 4.14(b) that there is anisotropy in 3D printed strands before deformation while BF is isotropic. After deformation, anisotropy increases in BF more than two times at relatively low strain. This is attributed to the free volume available in the vicinity of MWCNTs where their movement is not restricted under the effect of deformation, which is the case for 3D printed strands.

Nanostructure fillers aggregate in the polymer matrix and their aggregate size varies depending on the dispersion process. Consequently, consideration of the whole q -range for data analysis is essential. This can be evaluated from the anisotropy in the scattering patterns by considering the azimuthal variation of the intensity for the whole $|q|$ range. This is achieved by representing scattering intensity in terms of spherical harmonics [11][10]. Therefore, the experimental scattering intensity data, $I(|q|, \alpha)$, of diffraction patterns of 3D printed strands of pure PCL and its nanocomposites are expressed as a series of spherical harmonics, $I_{2n}(|q|)$, [10] and these are shown in Figure 4.15 and Figure 4.16 for unstrained and strained samples, respectively. These plots are presented on a vertical scale for the sake of visual inspection. Three features are visible from the plots in Figure 4.15; first, the amplitude of different orders of the spherical harmonics $\langle P_{2n}(\cos\phi) \rangle$ decrease for both pure PCL and its nanocomposite strands. Secondly, the relatively high scattering intensity is observed in the low $-q$ region in strands containing carbon nanotubes compare to pure PCL strand. Thirdly, the broad peak appears around 0.045\AA^{-1} in pure PCL strand is diminished in the strand containing nanotubes. It is important to mention that the zero-order curve is the

scattering function which would correspond to an assembly of unoriented and uncorrelated units [26]. The curves for $n=1$, that is $\langle P_2(\cos\varphi) \rangle$ is positive for values

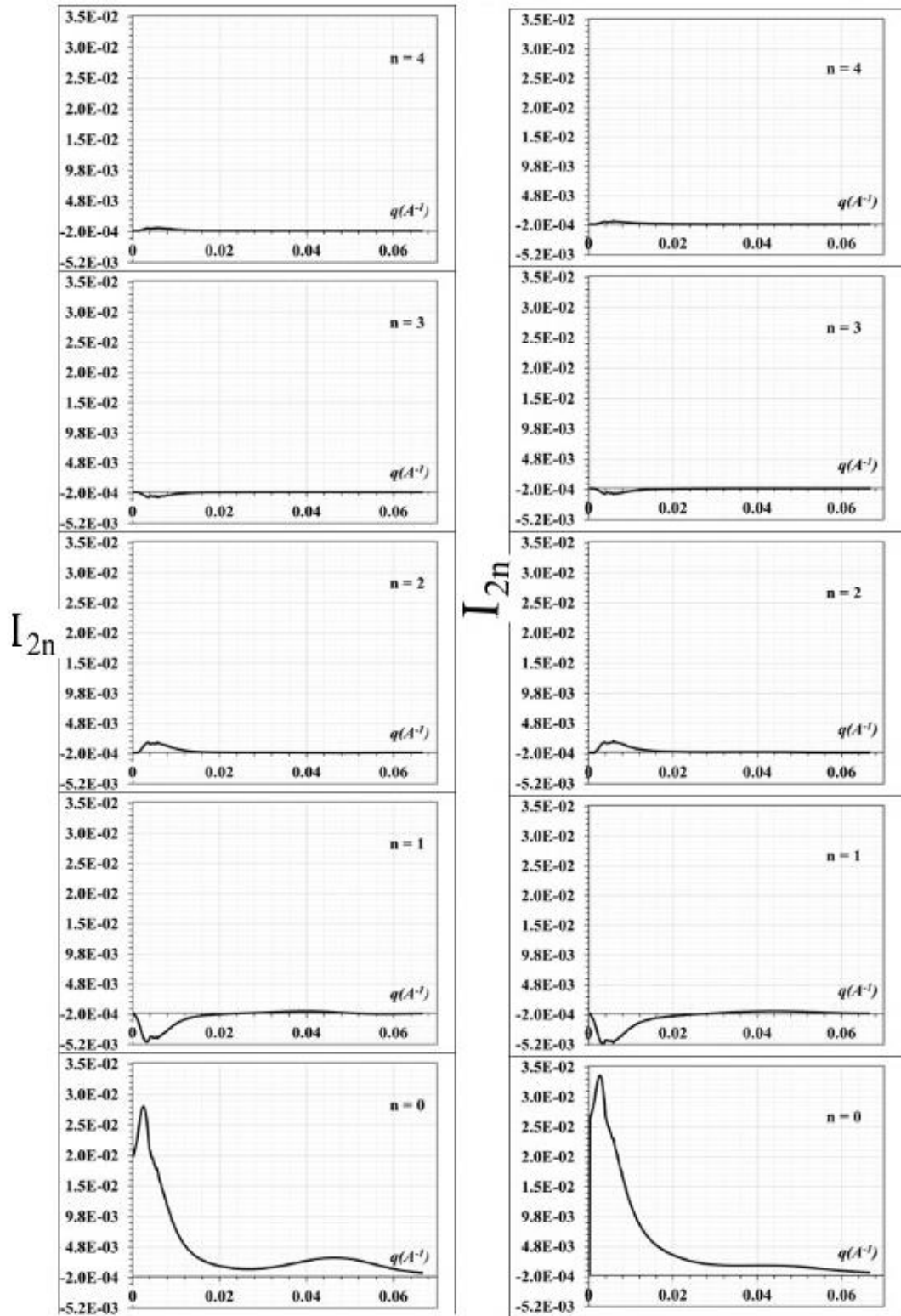


Figure 4.15. Plots of the amplitudes of spherical harmonics of the calculated intensity are presented for 3D printed strands of (Left) pure PCL and (Right) PCL/MWCNTs before deformation. The vertical scale is the same for each component.

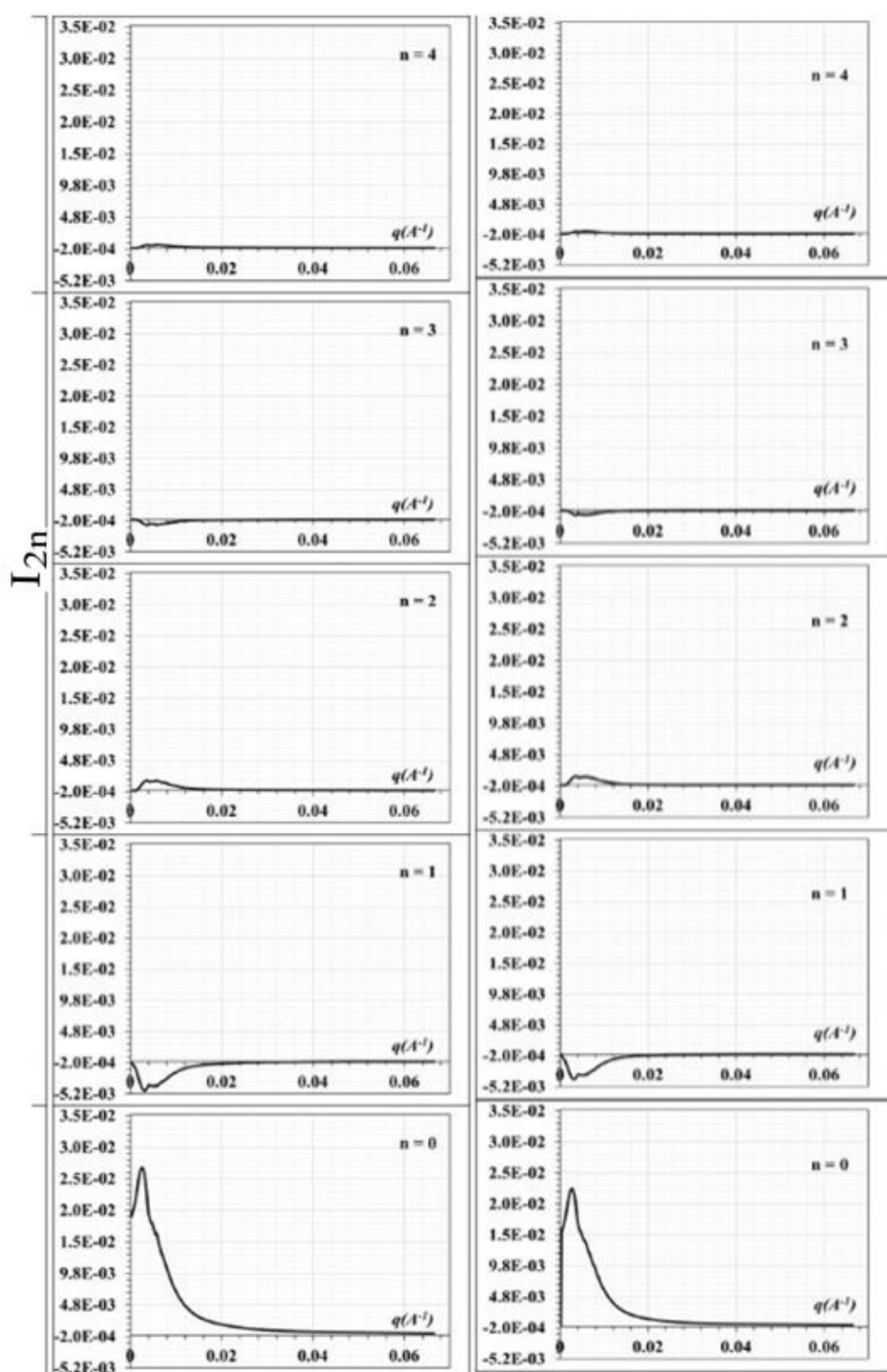


Figure 4.16. Plots of the amplitudes of spherical harmonics of the calculated intensity are presented for 3D printed strands of (Left) pure PCL and (Right) PCL/MWCNTs after deformation.

of q where the intensity is concentrated on the meridian. The peak at $q = 0.045 \text{ \AA}^{-1}$ confirms the meridional character of the maxima which disappear in the higher harmonics. The fact that it is positive in the region of the interchain peak in the experimental scattering results from the omission of interchain correlations in the scattering calculations. Such correlations lead to equatorial scattering and hence negative values for $\langle P_2(\cos\phi) \rangle$ in the lower q range [26]. The levels of anisotropy of the polymer matrix (crystal and amorphous components) and fillers (carbon nanotubes) will impact differently on the mechanical [26] and electrical properties [27] and it is reasonable to separate the contributions. The fraction of aligned nanotubes due to the extrusion process and uniaxial deformation can be obtained from spherical harmonic plots. If I_{2_PCL} is considered as the total contribution from the matrix and $I_{2_PCL/MWCNTs}$ from the nanocomposite strand, then the fraction of the oriented MWCNTs can be calculated from the following relation:

$$f_{PCL} = \frac{\int_{q_{min}}^{q_{max}} I_{2_PCL}(|q|) dq}{\int_{q_{min}}^{q_{max}} I_{2_PCL/MWCNTs}(|q|) dq} \quad (4.19)$$

$$f_{MWCNTs} = 1 - f_{PCL} \quad (4.20)$$

The result of this analysis is presented in Figure 4.17 in the form of a plot indicating the fraction (normalised) of aligned nanotubes under the effect of the strain. From this analysis, it is clear that around 40 % of nanotubes are affected by a strain of 400 %. Besides, only 5.0 % of nanotubes are affected by the strain beyond 400 %.

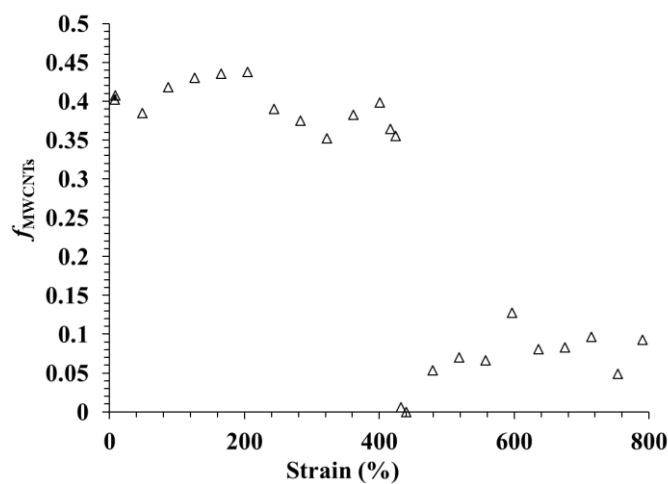


Figure 4.17. The fraction of oriented MWCNTs is presented from the Spherical harmonic plots for the whole q -range.

This indicates that significant contribution comes from the elastic region of the polymer matrix compare to plastically deformation region. It can be concluded that nanotubes network failure or formation significantly affected in the elastic region. Less number of tubes are affected in the plastic deformation region indicating that a significant portion of nanotubes is not in-network due to which electrical conductivity decreases appreciably.

The long period (L_p), amorphous phase (L_a) and crystalline phase (L_c) were calculated from the $1D$ correlation plots as shown in Figure 4.18 (a-c). All of these parameters decreased, in all samples, under the effect of uniaxial deformation. Similar kind of results was reported in other studies, in which melt-crystallized nanocomposite was studied, using $1D$ correlation function [27]. The long period decreases to nearly half under uniaxial deformation in the bulk film and $3D$ printed strands (composite and pure PCL samples). The amorphous and crystalline lamellae are decreased accordingly as measured from $1D$ -correlation plots and the numerical values are shown in the inset of Figure 4.18 (a-c).

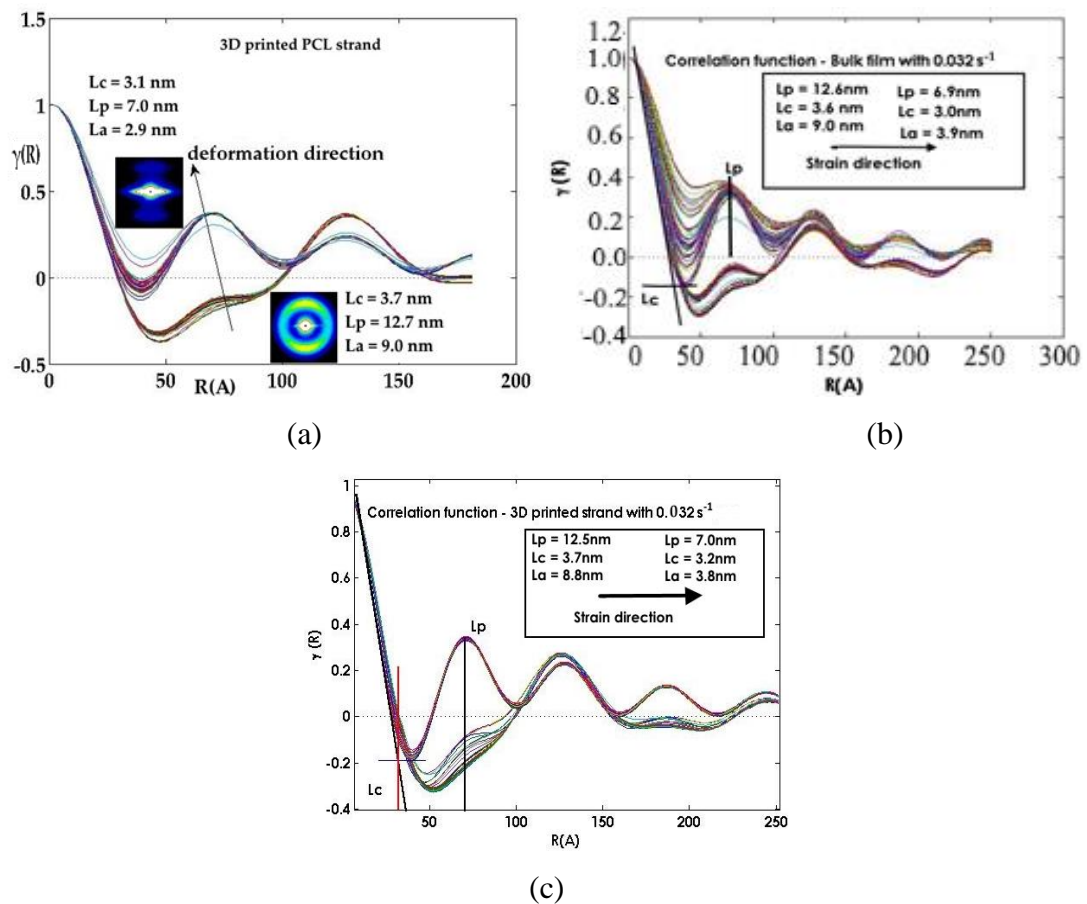


Figure 4.18. (a, b, c) $1D$ correlation plots obtained from the samples mentioned in Figure 10(a-c), respectively. Insets show parameters extracted using $1D$ correlation

plots. These parameters are L_c , L_a and L_p and these represent the thickness of crystalline lamellae amorphous layers and long period, respectively of the PCL matrix.

In the second scheme of experiments, 2D SAXS patterns were obtained during uniaxial deformation besides measuring electric current and voltage drop simultaneously for electrical conductivity in 3D printed strand containing MWCNTs (1.0 % w/w). These patterns are presented in Figure 4.19 showing scattering intensity along the meridian and the equatorial directions with variations in the extension ratio. The scattering intensity is symmetrical in these patterns before deformation and it indicates a random distribution of MWCNT into the PCL matrix. However, patterns change into elliptical anisotropic patterns with the applied load. The development of the anisotropy in the patterns due to uniaxial deformation attributed to the alignment of the MWCNTs.

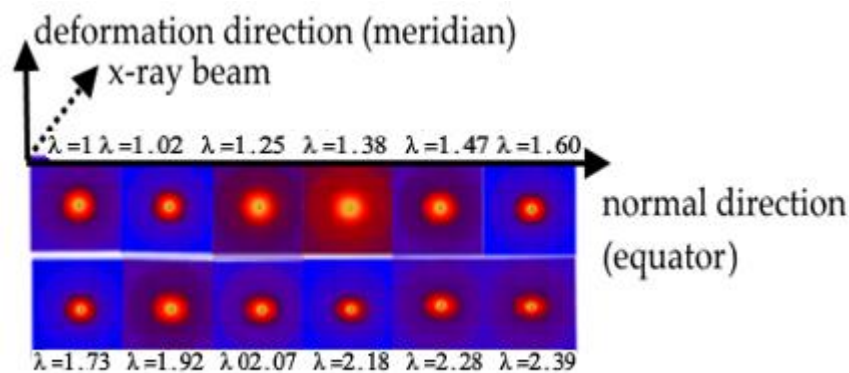


Figure 4.19. Anisotropic 2D SAXS patterns obtained during uniaxial deformation when measuring the electrical conductivity in 3D printed nanocomposite strand with 1.0 % w/w MWCNTs. The strands were stretched along the meridian – axis, the X-ray beam is directed normal to the central axis of the strand and λ represents the extension ratio.

Further, 2D scattering intensity patterns are radially integrated; yielding a 1-D scattering intensity (I) as a function of the scattering vector (q) and these are plotted on a double logarithmic plot against the λ as shown in Figure 4.20. In a low q -region, a mass fractal morphology is revealed in the printed strand as evident from gradients, which lie between -3 and -1. The absence of a q -region with slopes close to ≈ -1 is an indication of nanotube aggregation. Considering together, a mass fractal morphology with an absence of a tubular morphology indicates branches of aggregates of MWCNTs into PCL matrix. These branches form conductive pathways for electronic conduction in the nanocomposite. Towards a high- q region, a gradient ≈ -4 is

measured in relatively high q region indicating surface fractal morphology. Such kind of morphology belongs to a smooth interface between polymer and MWCNTs [28]. A common shoulder is appeared between these q regions, within the log-log plot. The shoulder position is moved towards the high q region under uniaxial deformation. It indicates the occurrence of variation in long-range order under the effect of uniaxial deformation and thereby the branched structure becomes smaller. A comparison with data in Figure 4.10 (a) indicates that the shoulder appears due to counterbalancing the scattering from the crystalline peak from the PCL matrix to that of MWCNTs. The net scattering appears as a shoulder or plateau in between these regions. Also, the literature suggests that such a shoulder is a signature of an aggregation of MWCNTs [29][30].

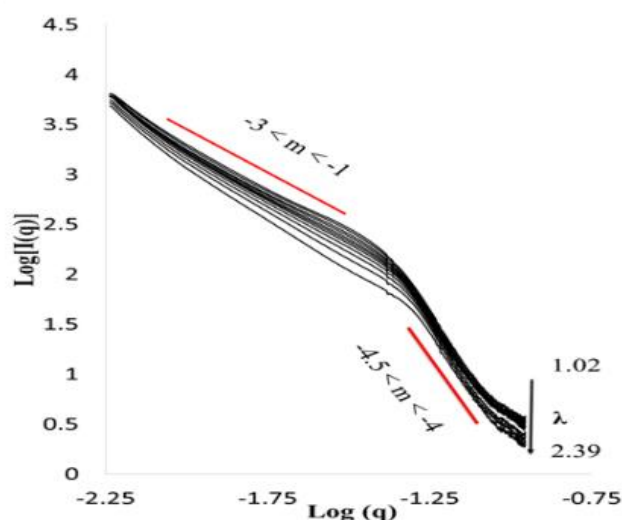


Figure 4.20. Double logarithmic plots of I versus q are presented against λ for 3D printed strand containing PCL/MWCNTs (1.0 % w/w). The λ represents the extension ratio of the deformed 3D printed strand. These plots indicate fractal morphology in the conductive strands.

It is useful to multiply the scattering intensity by an extra factor q^2 (Kratky-plot) [29], to study variation in aggregate of MWCNTs under the effect of uniaxial deformation. Figure 4.21 shows the reduced scattering intensity using Kratky-representation. It is obvious from the Kratky plots that the height of the aggregate peak decreases and shifts towards higher q -values with an extension ratio. Before deformation of the sample, a broad peak is observed in the Kratky plot. The peak becomes broader further gradually under the effect of deformation. From this analysis, it can be deduced that the aggregate size of MWCNTs is decreased with the increase in λ . The aggregate size is measured from peak position and these are indicated with

red dotted arrows in Figure 4.21. The aggregate size is decreased around $\approx 18\%$ under the effect of uniaxial deformation.

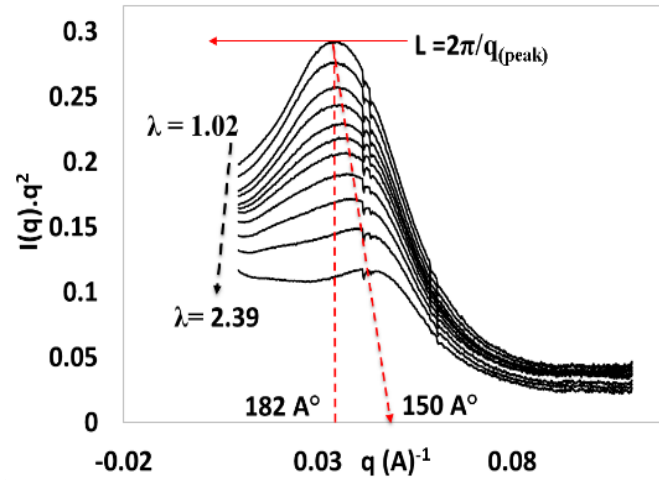


Figure 4.21. Kratky plots are provided to measure the aggregate size of MWCNTs in 3D printed strand containing 1.0 % (w/w) MWCNTs during deformation. The λ represents the extension ratio while L represents the size of scatterers in real space.

The 1D-correlation plots are obtained from scattering intensity along the meridian and the equatorial direction before and after deformation to deduce microstructure features. There is a clear difference in the 1D-correlation plots along the meridian and equatorial direction, as shown in Figure 4.22. On the other hand, not a significant difference is observed in the plots with deformation. This is due to the presence of MWCNTs that provide support to the matrix material through bearing and resisting against the applied load.

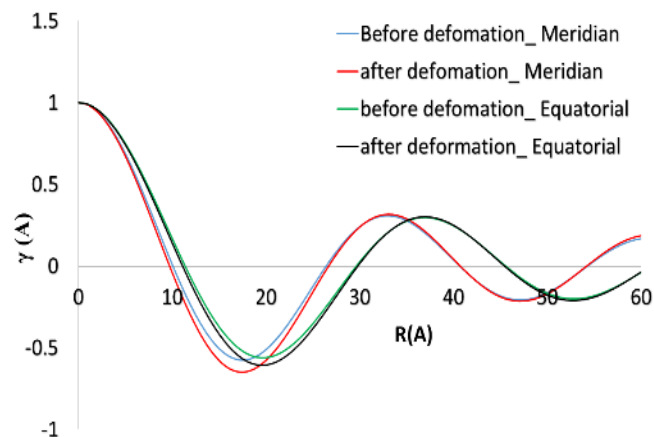


Figure 4.22. The 1D-correlation plots along the meridian and the equatorial direction obtained from 1.0% w/w MWCNT/PCL nanocomposite strand before and after deformation.

The microstructure parameters deduced from the 1D-correlation plots are tabulated in Table 4.2. The results indicate that there is no change in the long period while crystalline lamellae are increased slightly with deformation of the strand. On a similar way, the crystallinity of the strand is increased around $\approx 7.0\%$ after uniaxial deformation. The increase in crystallinity is attributed to the ordering of the amorphous layer.

Table 4.2. Parameters extracted from 1D-correlation plots for 3D printed strands contained MWCNTs 1.0 % w/w before and after deformation along the meridian and equatorial scattering.

Samples	L_p (Å)	L_c (Å)	L_a (Å)	Crystallinity %
Before deformation _Meridian	33	14	19	42
After deformation _ Meridian	33	15	18	45
Before deformation _Equator	37	15	22	40
After deformation _ Equator	37	16	21	43

4.3.5 Morphological analysis

The morphology of MWCNTs in 3D printed strand, containing 1.0 % w/w MWCNTs, is studied using scanning electron microscopy (SEM). A tubular morphology is revealed from the nanocomposite strand that indicates the presence of MWCNTs. Curled and entangled MWCNTs are present in the form of aggregates in 3D printed as revealed from the SEM image in Figure 4.23 (a). It is considered that these entanglement caused by the van der Waals interaction that further lead to agglomerates of carbon nanotubes [31]. MWCNTs are disentangled under the effect of uniaxial deformation as shown in Figure 4.23 (b). It is evident from SEM images that carbon nanotubes have wavy structure even after stretching. It is evident through measurement that the length of carbon nanotubes decreased near to half as compared to the one provided from the supplier ($5.0\ \mu m$). The shortening of nanotubes length is an indication that nanotubes have broken due to ultrasonic waves during the dispersion process.

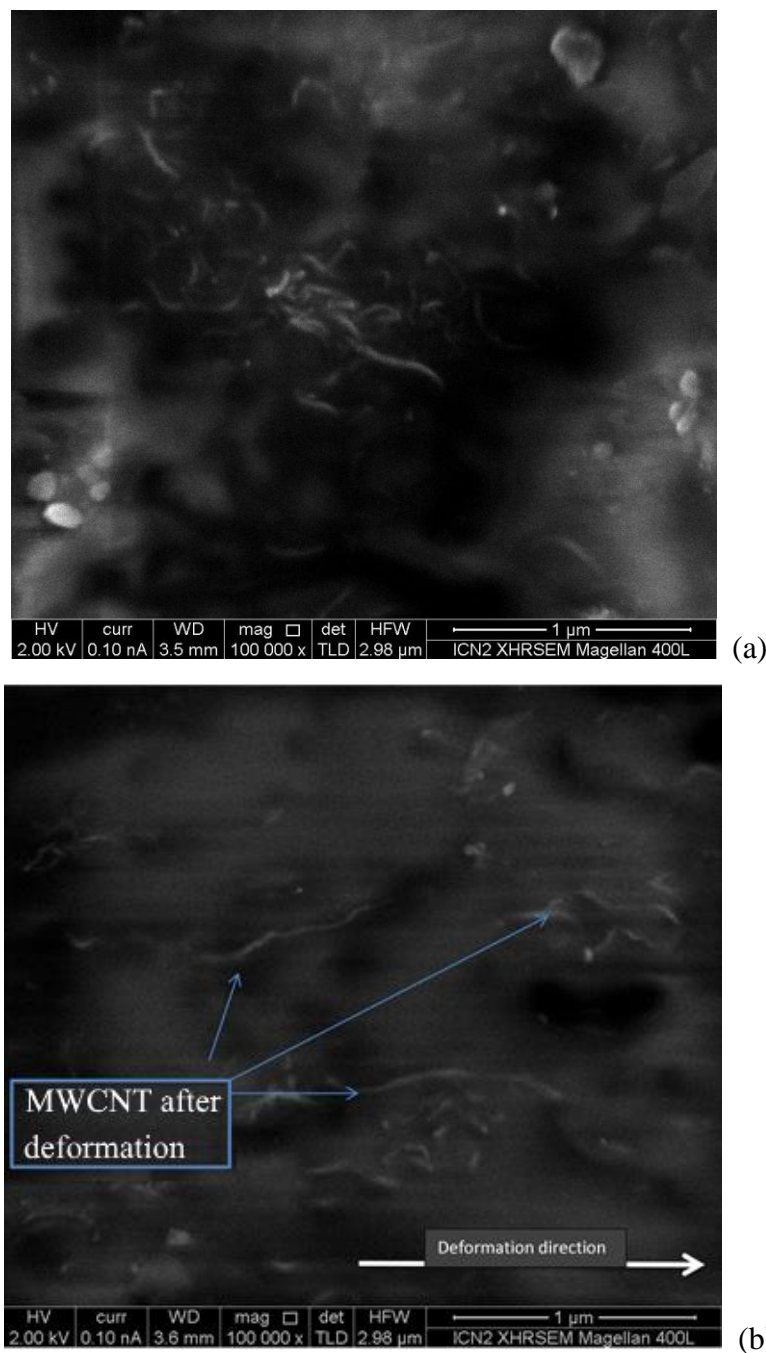


Figure 4.23. SEM images are presented from 1.0 % w/w MWCNT/PCL nanocomposite strand. (a) Before deformation and (b) After deformation.

4.3.6 Thermal analysis

The assessment of the degree of crystallinity ($\% X_c$) of the nanocomposites was performed using differential scanning calorimetry (DSC) in the heat flow into the sample. Figure 4.24 illustrates a typical DSC scan registered during the heat flow into the PCL and its nanocomposites strands constrained with scan rate at $5^\circ\text{C}/\text{m}$. The onset of melting temperature (T_m), enthalpy of fusion, (ΔH_f) and the degree of crystallinity ($\% X_c$) have decreased for samples containing MWCNTs as shown in Table 4.3.

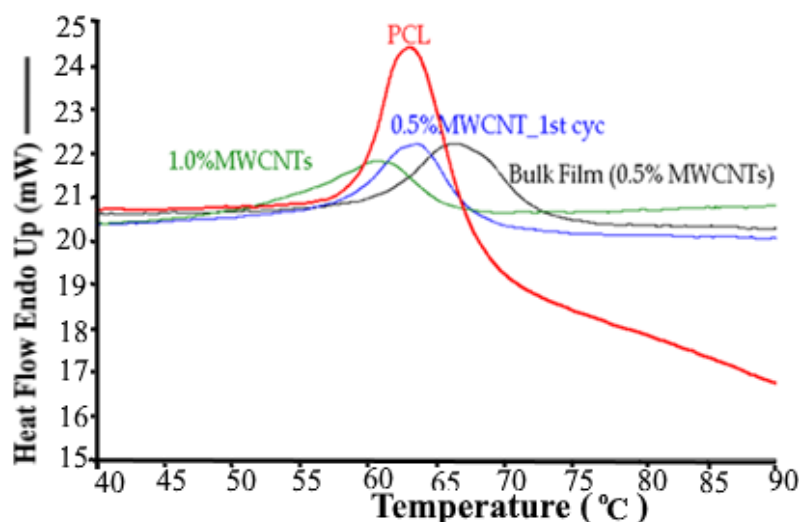


Figure 4.24. DSC curves of 3D printed strands of pure PCL, PCL/MWCNTs (0.5 % w/w), PCL/MWCNTs (1.0 % w/w) and bulk film of PCL/MWCNTs (PCL/MWCNTs (0.5 % w/w)).

The decrease in crystallinity was also reported in other studies [32]. This is caused by several factors including the interaction between the PCL and the MWCNTs surface hindering polymer chain mobility in the amorphous phase, the quality of the dispersion, and the steric hindrance between the polymer chains and the MWCNTs which limits chain diffusion during crystallization [33]. Fundamentally, this phenomenon is not well-understood requiring further investigation [34].

Table 4.3. The onset of crystallization temperature (T_m), enthalpy of fusion (ΔH_f) and the degree of crystallinity (% X_c) obtained through DSC plots shown in Figure 4.25.

Sample	Onset T_m °C	ΔH_f J/g	X_c %
PC	59.2	53.2	38.1
BF (0.5 % MWCNT/PCL)	61.4	17.4	12.5
Strand (0.5 % MWCNT/PCL)	58.9	15.7	11.3
Strand (1.0 % MWCNT/PCL)	54.7	13.5	9.8

4.4 DISCUSSION

For the sake of electrical conductivity, the main contribution is the existence of MWCNTs networks in a PCL matrix. It is found that DC electrical conductivity is decreased after deformation of the nanocomposite samples (bulk film and 3D printed strands) containing 0.5 % w/w MWCNTs. No significant amount of current is detected in the 3D printed strand while there is an electric current in the BF sample after

deformation. A reduced amount of current in the printed samples is attributed to a decreased number of multiple paths or breaking of the junction between nanotubes. Besides, an increase in DC electrical conductivity is calculated in 3D printed strands with 1.0 % w/w MWCNTs during uniaxial deformation. Overall, contrary results are found from the two compositions under the effect of deformation. This is because of the huge difference in % strain for the two compositions. Strands with 0.5 % (w/w) are stretched more than 3 times compare to strands with 1.0 % w/w MWCNTs due to apparatus limitations. A relatively higher strain lead to complete network failure or an enhancement in the tunnelling resistance [35]. Secondly, MWCNTs are higher in number in strands printed with 1.0 % w/w resulting in an increased number of neighbours in the PCL matrix. The deformation of strand causes to break MWCNTs networks. This is a new arrangement that develops an increased number of conductive pathways because of an increased number of neighbours. The stress-strain curves of PCL/MWCNTs (strand and BF) exhibit distinct regions of elastic, yield and plastic deformation regions, whereas continued deformation after the yield point results in necking along the sample length. There are appreciable differences in the tensile properties (Tensile modulus, fracture point) with strain rate in the bulk film compare to 3D printed strand which is attributed to non-uniform distribution of MWCNTs into PCL. Relatively higher strain rate results in higher stress/strain curves, and increased susceptibility to the formation of upper yield strength behaviour. In case of 3D printed strand, the dispersion of the MWCNTs in the polycaprolactone matrix results to a uniform stress distribution. This minimizes the presence of stress-concentration centres leading to increase the interfacial area for stress transfer from the polymer matrix to the MWCNTs [36], [32] and thereby facilitate to increase tensile properties in 3D printed strands. Besides, carbon nanotubes form percolative networks, which are responsible for the development of yield point and solid-like behaviour [37]. However, it is considered that a combined network built by nanotubes and the connecting polymer chains enhance the mechanical properties of nanocomposite [38]. This is supported through numerous other studies suggesting an enhancement in the tensile properties of the nanocomposites with the addition of MWCNTs [39]. The interface region is of significance for the sake of acquiring enhanced properties. This is because the interfacial regions surrounding the MWCNTs are in the nanometric scale due to the nanoscale dimensions of the MWCNTs and this leads to transfer applied stress easily from PCL to MWCNTs [40]. This is supported from exceptionally high Young's

modulus of MWCNTs (~1 TPA) [41]. In terms of interface, there are three synergizing aspects of interaction in carbon nanotube-based nanocomposites, i.e., polymer – nanotube, nanotube – nanotube and intra-polymer interactions. It was reported that continuous nanotubes most effectively enhance the buckling resistance of the composites [42]. The continuity happens due to entanglement of MWCNTs, confirmed through SEM images, as shown in Figure 4.23. It is considered that these entanglements caused by the van der Waals interactions that further lead to agglomerates of carbon nanotubes [31]. In terms of electrical conductivity, the literature suggests that some level of aggregation favours enhancing electronic conduction in the composites [43]. The crystallinity is directly related to the many of the key properties of a semi-crystalline polymer including brittleness, toughness, Young's modulus, and long-term stability. The onset of melt temperature in a PCL matrix is decreased with the presence of MWCNTs with loadings 1.0 % (w/w) while it increased with 0.5 % (w/w). The decrease is attributed to aggregation of MWCNTs, which restricted long-range crystalline order while an increase is a result of an increased crystallinity due to nucleation effect of MWCNTs. On contrary, the crystallinity is decreased in the presence of MWCNTs, which is due to reduced mobility of the amorphous phase caused by MWCNTs. The length of nanotubes is significantly higher than the amorphous layer, which restricts the mobility of the amorphous phase. DSC measurements demonstrated an increase in T_m with increasing MWCNT content. This is due to the nucleation effect caused by the presence of MWCNTs. Despite the nucleating effect of MWCNTs, a reduction in the percentage crystallinity is observed in the PCL/MWCNTs nanocomposites [39]. Filling of polymer matrix with carbon nanotubes can result not only change in the crystallization temperature and the degree of crystallinity but also crystallite sizes [44]. In terms of the polymer phase, the reason for less crystallinity could be the kinetic hindrance caused by entanglements among the polymer chains. This could not be abolished and, possibly, leading to the formation of amorphous layers during solidification from the melt in 3D printed strands. The process of solidification from the melt leaves the stacked lamellar crystals and entangled amorphous polymeric chains in between lamellae, forming a semi-crystalline state [45]. Incorporation of carbon nanotubes had a significant influence on both melting and crystallization processes. The influence of MWCNTs on the melting temperature of 3D printed strands is prominent which can be due to different molecular arrangements caused by

the processing method [27]. This can further results in more imperfect crystals in the nanocomposites. The mechanical properties of PCL depend largely on microstructure and morphology [37] [46]. The fractal morphology is an indication of MWCNTs network into PCL. The degree of crystallinity, long period and lamellar thickness decrease with the application of uniaxial load, which also possibly affects the MWCNTs networks. The 2D SAXS patterns were symmetrical in the bulk film compared to the 3D printed strand with the two-point pattern before stretching and transform into a kind of four-point pattern under uniaxial strain for both kinds of samples. The registry of the lamellae gives rise to two-point or four-point SAXS patterns was also reported in other studies [46]. The origin of the two-point and four-point patterns is controversial and unclear. In one model, a four-point pattern was obtained when the lamellae were arranged in a lattice that resembles a checkerboard, and a two-point pattern is obtained when the lamellae are arranged in columns, and positions of the lamellae in the neighbouring columns are uncorrelated. In another model, tilting of the lamellar surface is described as a progressive shear between the crystalline stems within the lamellae [47]. Another study was described by [48] in which four-point pattern was attributed to tilted lamellae in an elliptical shape of the scattering patterns, which was attributed to an affine deformation of a lattice. The tilt is considered as an indicator of the internal strain in the amorphous regions that link the crystalline lamellae [48]. In a 3D printed strand with 1.0 % MWCNTs, the symmetrical pattern obtained which gradually transform into an oblate 2D SAXS pattern. This strand strained relatively less in comparison to strands with 0.5 % w/w MWCNTs, due to instrumental limitations. All these patterns show that there is a prominent effect of uniaxial strain on microstructure. In the elastic limit before yield point, the SAXS patterns minimally change for all samples. In the elastic limit, amorphous lamellae orient in the stretching direction and without any noticeable change in the crystalline lamellae as the scattering along the meridian did not vary appreciably, thereby any stress on crystalline phase. MWCNTs are favourably settle in the amorphous phase due to pressures originate from crystalline lamellar organization. In addition, length of MWCNTs is significantly higher than crystalline lamellae. Clear variation is observed in the 2D SAXS patterns at the yield point along the equator. This is the point where amorphous lamellae stretched to its fullest. This lead to force MWCNTs to reorient along with amorphous phase. There will be variation in the conductivity, either it will decrease or fluctuate depending on

MWCNTs content in the vicinity. In failure of nanocomposites, the main energy consuming process is plastic deformation of the matrix, which modified by the presence of the MWCNTs. The 2D SAXS patterns slightly change in the plastic deformation region and gradually keep on changing with a slow pace until fracture point where patterns appear to be four-point scattering pattern. The stress energy utilizes to crystalline phase reorientation due to which networks of MWCNTs alters.

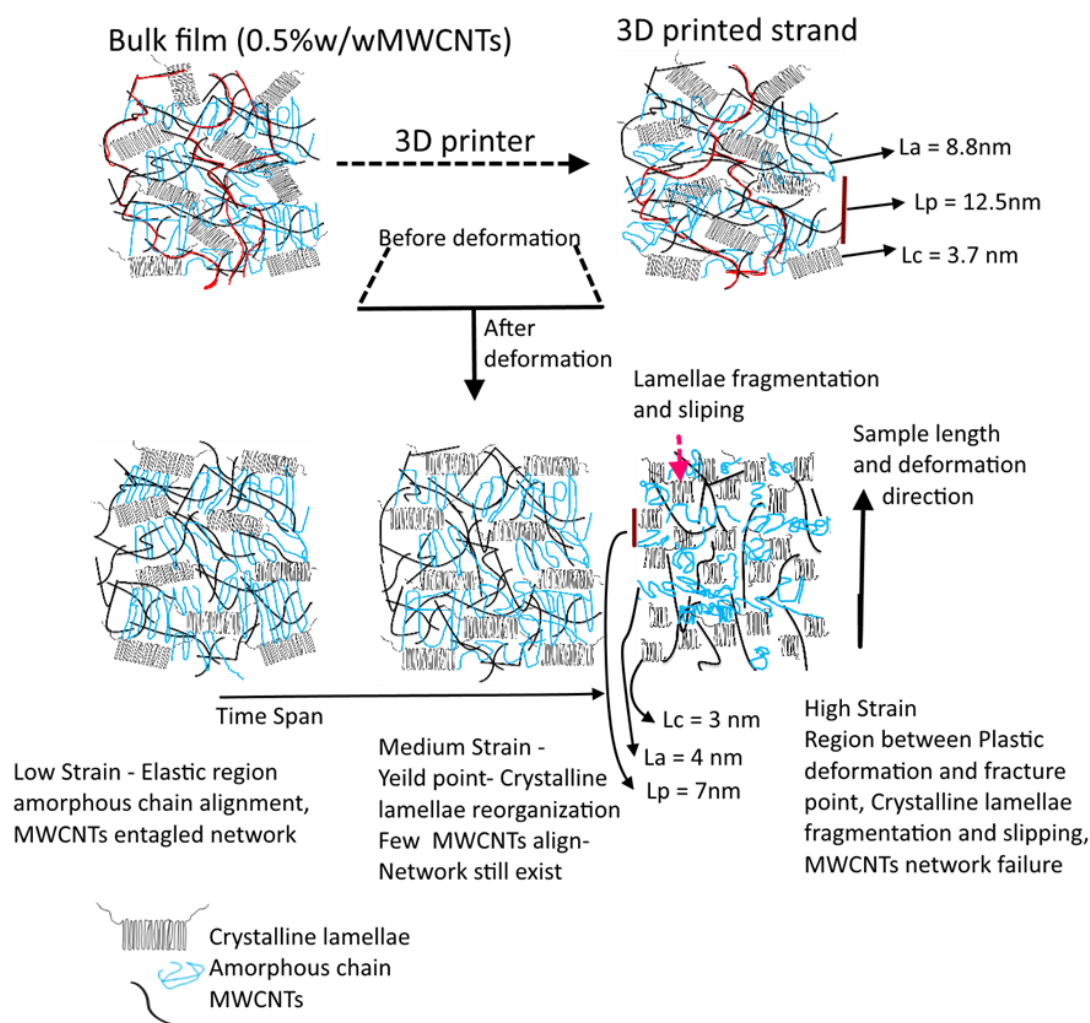


Figure 4.25. The model used to explain reorganization of crystalline and amorphous lamellae in 3D printed strands under uniaxial deformation and the consequent effects on the network failure in carbon nanotubes leading to a decrease in the electrical conductivity.

A variation in electrical conductivity is occurred because of such network alteration. It is important to emphasize that electrical conductivity decreases under uniaxial deformation if network alteration happens at low strain with low loadings of MWCNTs, while it increases if network alteration happens at low strain with high loadings of MWCNTs. However, the rearrangement of MWCNTs due to uniaxial

strain in the plastic region suppressed the crystalline lamellae leading to decrease (thin) long period and crystalline lamellae. The MWCNTs networks no more connected randomly but only crystalline lamellae's orientation-dependent networks exist, causing electrical conductivity in the nanocomposite. With the consideration that MWCNTs are settled in the amorphous phase of 3D printed strand, variations in the microstructure under uniaxial deformation are explained in Figure 4.25.

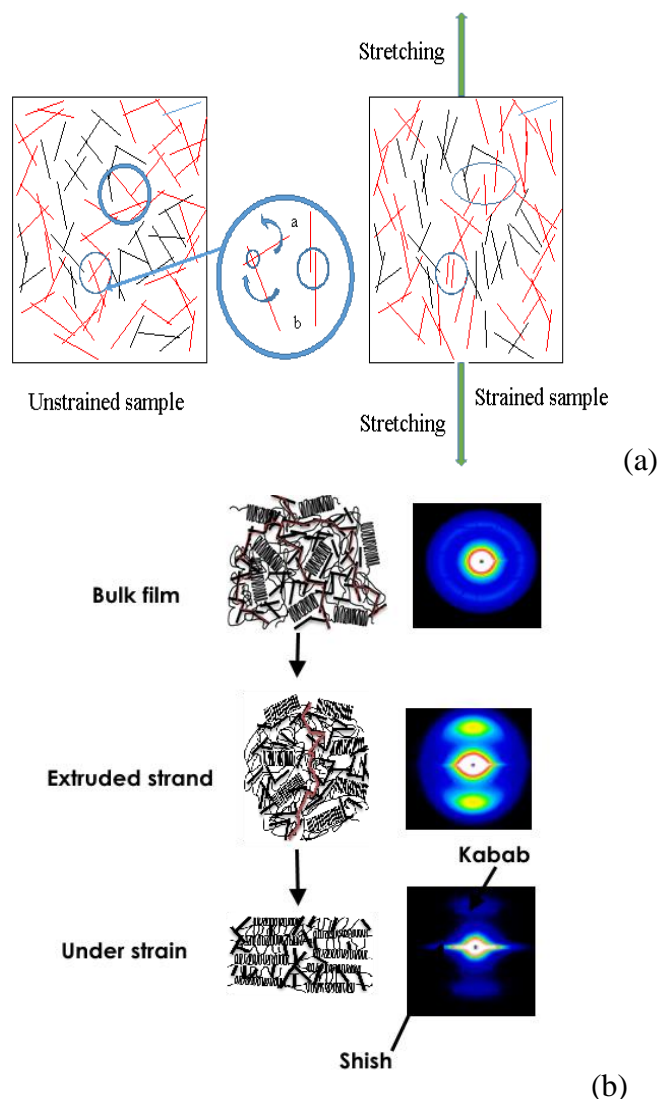


Figure 4.26. (a) Possible MWCNT-MWCNT junction breaking and alignment along with uniaxial deformation trapped between crystalline lamellae leading to develop a shish kebab morphology. The red and black colours are indicative of percolative and non-percolative pathways. (b) A shish kebab morphological development is presented in 3D printed nanocomposite (PCL/MWCNTs) strand under the effect of uniaxial strain.

The decrease of the long period during the growth of a lamellar structure has been widely observed in semi-crystalline polymers. The decrease is generally attributed to

a rearrangement of bent lamellae appearing at the beginning of the crystallization [49] or a thinning of lamellae during crystallization [50] [51]. Nevertheless, in our case, the PCL/MWCNTs nanocomposites, the reduction in the amorphous layer thickness (L_a) is much more evident than that of the crystalline thickness (L_c). The decrease of a long period is attributed to the squeezing of the amorphous phase due to crystalline lamellae slipping. This forced to alter MWCNTs network, at low to medium strain, without breaking due to entanglement. At relatively high strain, there is a crystal slipping that forced the MWCNTs to reorganize within the amorphous layer [46]. The reorganization of the MWCNTs could be due to reorientation and/or translational motion or involves both of them at the same time. The overall impact of such an organization of MWCNTs leads to breaking and formation of new networks. The net network formation is directed network due to significantly larger length of nanotubes comparing to L_c . In this way, nanotubes are present in the amorphous phase and passing around the corners of L_c . The possible MWCNT-MWCNT contact breaks mechanism during reorganization is shown in Figure 4.26 (a). The lamellae slipping is occurred at high strain, which develops a Shish kebab morphology in which an MWCNT act as “shish” while folded lamellae crystal is considered as “kebab”. The shish kebab morphology in PCL based nanocomposites, containing MWCNTs, has previously been observed in other studies [52][53]. In such kind of morphology, MWCNTs are like long rods passing over folded lamellar crystals (kebab) 4.26 (b).

4.5 MODEL

One of the objectives of the current study is to model the electrical conductivity response under the effect of uniaxial deformation. For the sake of this, it is considered that there are networks of carbon nanotubes in the polycaprolactone matrix due to which 3D printed strands behave as an electrically conductive material. The magnitude of electrical conductivity in the printed strand depends upon the density of such networks. These networks can be considered as conductive pathways through which electric current flows under the effect of a suitable bias. Any kind of variation in the density of such networks alters the electrical conductivity in the sample under test. Therefore, to model the electrical conductivity response under the effect of uniaxial strain in 3D printed strand, it is important to find an expression for the network density of MWCNTs in conjunction to the bulk electrical conductivity of strand. Two mechanisms are considered due to the density of MWCNTs networks alter under the

effect of uniaxial deformation: (1) linear translational motion and (2) rotational motion of MWCNTs. These motions are caused by the volume change of the sample, as shown in Figure 4.27. Considering the linear translational motion, the strand not only gets longer but it also gets thinner under the effect of uniaxial strain. This thinning, one-way, can be considered as equivalent to compressing the nanotubes. Due to which, possibly, nanotubes can come close to each other and contribute to increasing the network density while due to elongation nanotubes getting further apart from each other which can decrease the network density either through MWCNT- MWCNT junction breaking or through enhancement in the tunnelling distance. The reorientation of tubes can also alter the MWCNT – MWCNT junction, which can affect either way the network density in the printed strand. Hence, the overall network density of nanotubes will depend on the two modes of translational motion accompanied by rotational motion. An orientation distribution function (ODF) can be used for the rotational motion of the nanotubes under the effect of deformation.

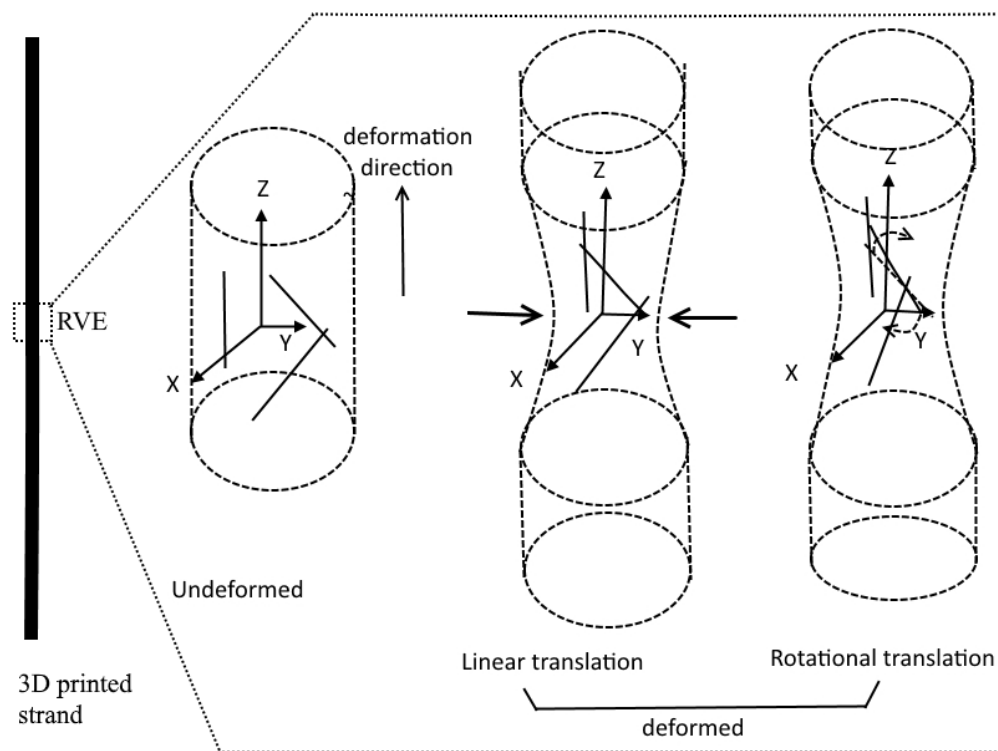


Figure 4.27. Cartoon representation of the translational and rotational motion of carbon nanotubes in a 3D printed strand under un-deformed and deformed states.

It is considered that deformation effects along the length (deformation direction) and lateral direction are different from each other. This is evident from the Poisson ratio of the composite strand. The measured Poisson ratio for the composite strand is

≈ 0.25 . It is considered that the carbon nanotubes are distributed randomly into the polymer matrix. Percolation theory is used in different field of science to study such kind of disorder in materials. Considering such an approach, it is considered that carbon nanotubes follow a stick percolation model [54]. According to the stick percolation model, the conductance of carbon nanotube`s networks is dependent on the density in MWCNTs networks. The following power-law relation holds for such a dependence [55].

$$\sigma = \sigma_o(N - N_c)^\alpha \quad (4.21)$$

Where σ and σ_o represent the conductivity of MWCNTs networks within the polymer matrix and the intrinsic electrical conductivity of nanotubes, N refers to the density of MWCNTs networks above the percolation threshold, N_c to the critical density of MWCNTs networks and α is the critical exponent which depends on the dimensionality of the system [56]. The critical exponent governs the scaling law near percolation and it has been associated with the dimensionality of the system, although its physical meaning is still controversial [56].

The critical exponent is 1.33 in a two-dimensional region and 1.94 in a three-dimensional region [55]. Now, there is a need to find the effect of uniaxial deformation on the network density of MWCNTs above the critical network density of MWCNTs. For the sake of this, If N_i represents the density of MWCNTs networks before deformation then Eq. (4.21) becomes

$$\sigma_i = \sigma_o(N_i - N_c)^\alpha \quad (4.22)$$

It is evident from SAXS data (plot of scattering intensity (I) versus scattering vector (q) analysis that these networks are mass fractals and fractals are scale-invariant [57] i.e.

$$f(\mu \cdot x) = (\mu \cdot x)^n = \mu^n \cdot f(x) \quad (4.23)$$

This implies that the nature of power-law will not be affected under the effect of uniaxial deformation but it scales up or down depending on the magnitude of applied strain. Then the above relation (Eq.4.22)) becomes

$$\sigma_d = \sigma_o(N_d - N_c)^\alpha \quad (4.24)$$

Where N_d is the density of networks under the effect of uniaxial deformation. Rearrangement and logarithm of Eq. (4.22) and Eq. (4.24) lead to the following relation

$$(\sigma_d/\sigma_i) = (N_d - N_c/N_i - N_c)^\alpha \quad (4.25)$$

As the composite was deformed above the percolation threshold, the division of numerator and denominator by N_c leads to

$$(\sigma_d/\sigma_i) = \left[\frac{\frac{N_d}{N_c} - 1}{\frac{N_i}{N_c} - 1} \right]^\alpha \quad (4.26)$$

The numerator term in the above equation indicates that the composite will be no more conducting under the effect of uniaxial deformation when the network density of MWCNTs, approaches the critical density of MWCNTs. However, under the approximation that $N_d/N_c \gg 1$ and $N_i/N_c \gg 1$, the above relation can be written as

$$(\sigma_d/\sigma_i) = \left[\frac{\frac{N_d}{N_c}}{\frac{N_i}{N_c}} \right]^\alpha \quad (4.27)$$

$$\sigma_d = \sigma_i \left(\frac{N_d}{N_i} \right)^\alpha \quad (4.28)$$

Where σ_i represents electrical conductivity before deformation and σ_d after deformation. It is considered that carbon nanotubes reorient along with the uniaxial deformation without breaking due to relatively high young's modulus and stiffness. Assuming that carbon nanotubes are distributed uniformly in the composite strand before deformation. The variations in the networks of MWCNTs along the axial direction will be different from the lateral direction. The effective area of MWCNTs networks decreases due to a reduction in the cross-sectional area of 3D printed strand under the effect of uniaxial deformation.

$$A_o - \Delta A = L_x(1 - v_{xz}\epsilon).L_y(1 - v_{yz}\epsilon) \quad (4.29)$$

$$\begin{aligned} &= L_x(1 - v_{xz}\epsilon).L_y(1 - v_{yz}\epsilon) \\ &= L_x.L_y (1 + \epsilon)^{-2\nu} \end{aligned} \quad (4.30)$$

Where A_o refers to the original area of strand without deformation and ΔA is the area change under the effect of uniaxial deformation, L_x and L_y are the thickness (t), width (w), ϵ is the strain along deformation direction (z -axis), and ν is Poisson's ratio of composites strand. The area change leading to alter the density (N_{d_area}) of carbon nanotubes networks. Such a variation in the density (N_{d_area}) of carbon nanotube's networks under the effect of an element of area change can be described as [55],

$$N_{d_area} = N_i A_o / (A_o - \Delta A) \quad (4.31)$$

$$N_{d_area} = N_i / (1 - \Delta A / A_o)$$

$$N_{d_area} = N_i / (1 + \epsilon)^{-2\nu} \quad (4.32)$$

In contrary to area change, the change in the density (N_{d_length}) of carbon nanotubes networks along the deformed element of length can be given as

$$N_{d_length} = N_i / (1 + \epsilon) \quad (4.33)$$

The net variation in density (N_d) of carbon nanotubes networks in the volume of the sample after deformation can be given using Eq. (4.32) and (4.33) as

$$N_d = N_i / (1 + \epsilon)^{1-2\nu} \quad (4.34)$$

It is clear from Eqs. (4.32) - (4.33) that network density of carbon nanotubes affected in a different way under the effect of uniaxial deformation along the lateral and axial direction, respectively. The collective effect from both contributions represents variation in density (N_d) of carbon nanotubes networks in the representative volume element (RVE). Simulation results are obtained using Eq. (4.34) and these are presented in Figure 4.28 using an initial networks number 1000.

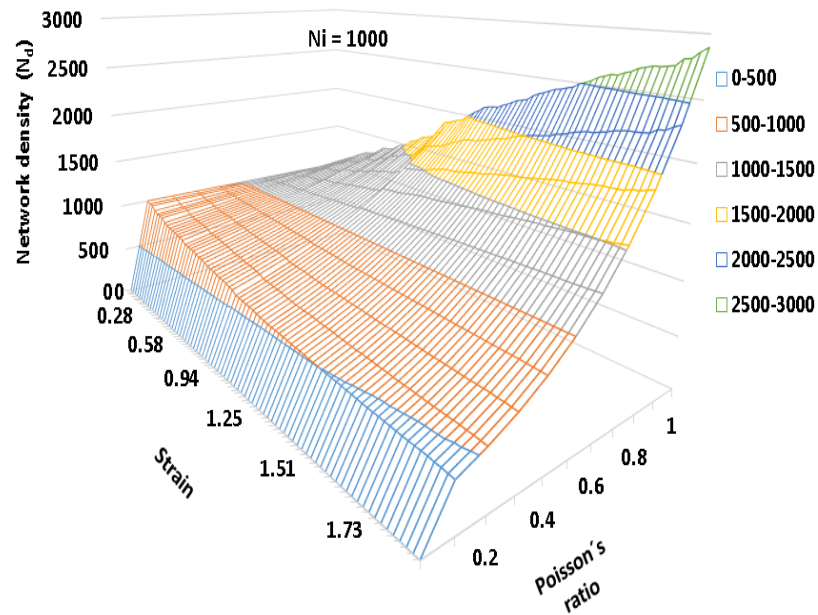


Figure 4.28. Variation of network density of carbon nanotubes under the effect of uniaxial strain and Poisson's ratio, using equation (29).

When the strand is stretched along the length of the sample, area of strand decreases due to which carbon nanotubes come close to each other leading to an increase in the network density of MWCNTs while nanotubes get far apart along the length of the sample resulting to decrease the network density in the sample. Besides,

as explained in the beginning, the deformation also causes the spatial orientation of MWCNT within the polymer matrix [58]. As nanotubes are the building blocks of the networks and any alteration in spatial orientation, under the effect of uniaxial deformation, will lead to altering network density of MWCNTs in the polymer matrix. In this way, the spatial orientation of MWCNTs has significant effects on the mechanical and electrical properties of the nanocomposites. To contribute to the orientation of the MWCNTs, an ODF is required to introduce into the model Eq. (4.34).

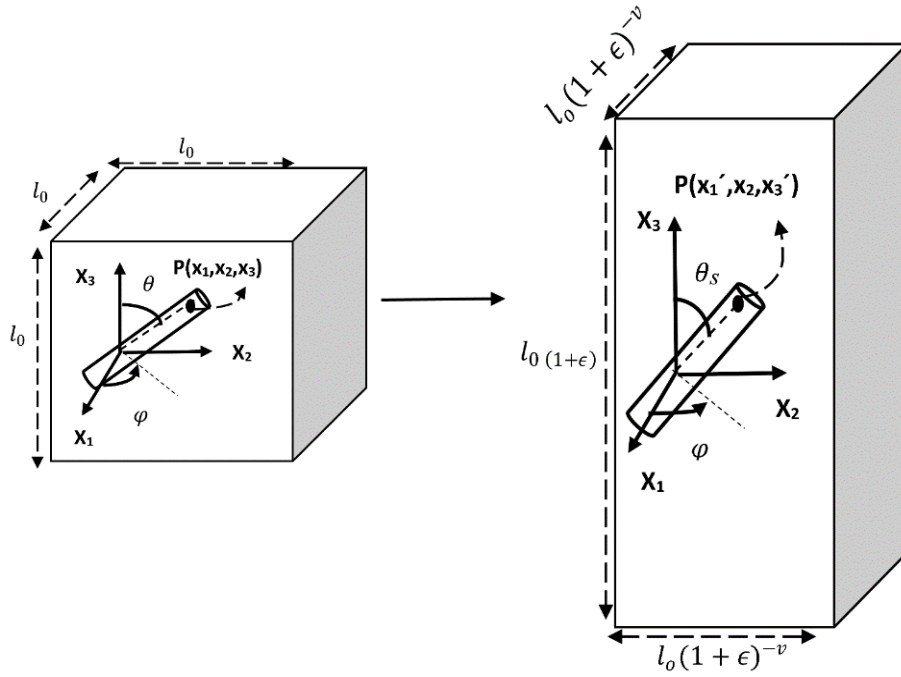


Figure 4.29. Reorientation of an MWCNT in a cell subjected to uniaxial stretching.

For the sake of this purpose, an ODF is considered from the work of [49] in terms of stretching strain and polar angle (θ). The ODF is based on the assumption that, when the strand is uniaxially deformed, dispersed MWCNTs in the PCL matrix will reorient due to the load transferred from the matrix to MWCNTs. This will result in variations of the nanotube's orientation angles, φ and θ . Figure 4.29 shows an RVE containing MWCNTs before and after a uniaxial stretching strain (ϵ) in X_3 direction. After stretching, the infinitesimal strains in the three dimensions can be written as [59],

$$\left. \begin{aligned} l &= l_o(1 + \epsilon) \\ w &= w_o(1 + \epsilon)^{-\nu} \\ h &= h_o(1 + \epsilon)^{-\nu} \end{aligned} \right\} \quad (4.35)$$

where l_0 , w_0 and h_0 are the original lengths of the RVE before stretching, and ν is Poisson's ratio of the nanocomposite containing MWCNTs. The literature suggests that the Poisson's ratio depends on both, the orientation and concentration of MWCNTs [59].

For nanocomposites with a random distribution of MWCNTs, the Poisson's ratio is calculated by measuring its physical dimensions. There was no significant work found from literature, as per the author's knowledge, for the measurement of Poisson's ratio of MWCNT. However, Poisson's ratio was reported in the literature as 0.14 ± 0.02 for single-wall carbon nanotubes [60]. It is considered that Poisson's ratio of the nanocomposite is expected to fall within the range of the values of MWCNT and the PCL (0.4) [61], regardless of the composition of the nanocomposites and the orientation of the reinforcements. Therefore, the dependence of Poisson's ratio on nanotube's concentration and orientation is neglected for the sake of simplifying the model.

Under the assumption of perfect bonding without slip between the MWCNT and the polymer matrix, the MWCNT inside the RVE tends to realign along the stretching direction under the uniaxial stretching, which results in an increase in the polar angle from θ to θ_s . For the sake of simplicity, the variation of the azimuth angle, φ , is neglected in this work [62] [58]. The updated polar angle θ_d can be derived in terms of the initial polar angle θ as

$$\theta_d = \tan^{-1} [(1 + \varepsilon)^{-(1+\nu)} \cdot \tan \theta] \quad (4.36)$$

The change of the polar angle after stretching indicates that MWCNTs tend to realign along the stretching direction, leading to a variation in ODF. For a limiting case, the MWCNTs in the polymer matrix would be perfectly aligned along the stretching direction under the effect of the large strain. To determine the ODF after stretching, it is assumed that there is a G number of nanotubes distributed in the RVE. The total number of MWCNTs dispersed in the range of $(\theta, \theta + d\theta)$ and $(\varphi, \varphi + d\varphi)$ in the RVE can be written [62] as

$$dn_{\theta, \theta+d\theta} = \frac{1}{4\pi} G \rho(\varphi, \theta) \sin \theta d\theta d\varphi \quad (4.37)$$

These fillers will be re-oriented within the ranges of $(\theta_d, \theta_d + d\theta_d)$ and $(\varphi, \varphi + d\varphi)$ after the stretching, i.e.

$$dn_{\theta_d, \theta_d + d\theta_d} = \frac{1}{4\pi} G \rho(\varphi, \theta_d) \sin \theta_d d\theta_d d\varphi = dn_{\theta, \theta + d\theta} \quad (4.38)$$

Substituting Eq. (4.36) into Eq. (4.38), the ODF $\rho(\varphi, \theta_d)$ is obtained as

$$\rho_d(\varphi, \theta_d) = (1 + \epsilon)^{(1+\nu)/2} / [(1 + \epsilon)^{-(1+\nu)} \cdot \cos^2 \theta_d + \sin^2 \theta_d (1 + \epsilon)^{(1+\nu)}]^{3/2} \quad (4.39)$$

Particularly, this ODF is unity in case of random and uniform distribution. However, ODF describes the distribution of the MWCNTs in the PCL matrix and when subjected to uniaxial deformation, it will no longer be constant under the applied stretching strain. Regardless of the MWCNTs orientation, the ODF is required to satisfy the following conditions [63][64].

$$\rho(\varphi, \theta) \geq 0 \text{ and } \frac{1}{4\pi} \int_0^{2\pi} \int_0^\pi \rho(\varphi, \theta) \sin \theta d\theta d\varphi = 1 \quad (4.40)$$

The ODF $\rho(\varphi, \theta_d)$ in Equation (4.39) reduces to unity in the absence of deformation, that is $\epsilon = 0$, and varies with an increase in strain. Figure 4.30 demonstrates the variation in the ODF with the polar angle for different Poisson's ratios and stretching strains. From Figure 4.30, it is seen that more MWCNTs tend to reorient along the stretching direction as the strain increases, which is indicated by the increasing peaks at $\theta_s = 90^\circ$.

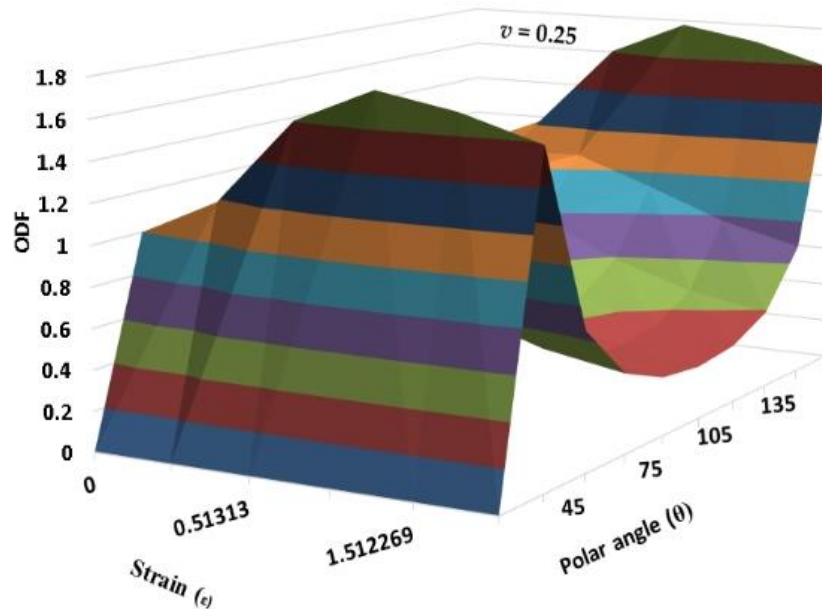


Figure 4.30. Variation of ODF (Eq. (4.39)) with strain and polar angle θ .

Hence, considering the spatial orientation of MWCNTs Eq. (4.34) becomes

$$N_d = [N_i/(1 + \epsilon)^{(1-2\nu)}] \times [\rho(\varphi, \theta)_i / \rho(\varphi, \theta)_d] \quad (4.41)$$

Where $\rho(\varphi, \theta)_i$ is ODF of nanotubes before deformation and $\rho(\varphi, \theta)_d$ after deformation. Before deformation, the ODF is considered unity due to random distribution of nanotubes while the ODF mentioned in Eq. (4.39) under the effect of uniaxial deformation. The use of ODF (Eq. 4.39) into Eq. (4.34) leads to the following expression

$$N_d = [(1 + \epsilon)^{-(1+\nu)} \cdot \cos^2\theta + \sin^2\theta(1 + \epsilon)^{(1+\nu)}]^{\frac{3}{2}} \cdot N_i / (1 + \epsilon)^{(1-2\nu)} \cdot (1 + \epsilon)^{\frac{1+\nu}{2}}$$

For the sake of simplicity θ_d is replaced as θ in the above expression.

$$N_d = [(1 + \epsilon)^{-(1+\nu)} \cdot \cos^2\theta + \sin^2\theta(1 + \epsilon)^{(1+\nu)}]^{\frac{3}{2}} \cdot N_i / (1 + \epsilon)^{\frac{3(1-\nu)}{2}}$$

$$N_d = [(1 + \epsilon)^{-2} \cdot \cos^2\theta + \sin^2\theta(1 + \epsilon)^{2\nu}]^{\frac{3}{2}} \cdot N_i \quad (4.42)$$

Hence, the expression for the electrical conductivity in Eq. (4.28) becomes

$$\sigma_d = \sigma_i [(1 + \epsilon)^{-2} \cdot \cos^2\theta + \sin^2\theta(1 + \epsilon)^{2\nu}]^{\left(\frac{3\alpha}{2}\right)} \quad (4.43)$$

$$\sigma_d = \sigma_i [\lambda^{-2} \cdot \cos^2\theta + \sin^2\theta \lambda^{2\nu}]^{\left(\frac{3\alpha}{2}\right)} \quad (4.44)$$

The expression in Eq. (4.44) is a model which correlates electrical conductivity, extension ratio, Poisson's ratio, orientation parameter and the critical exponent for the percolation of nanotubes. Simulated results from this model are presented in Figure 4.31. Besides, σ_i and ν are experimentally measurable parameters while θ and α can be deduced from the fitting of experimental data to Eq. (4.44). It is obvious from data analysis that a relatively higher level of alignment under the effect of uniaxial deformation leading to decrease electrical conductivity. On the other hand, materials having higher Poisson ratio and higher power exponent, under the effect of deformation, will lead to increase electrical conductivity in the nanocomposites.

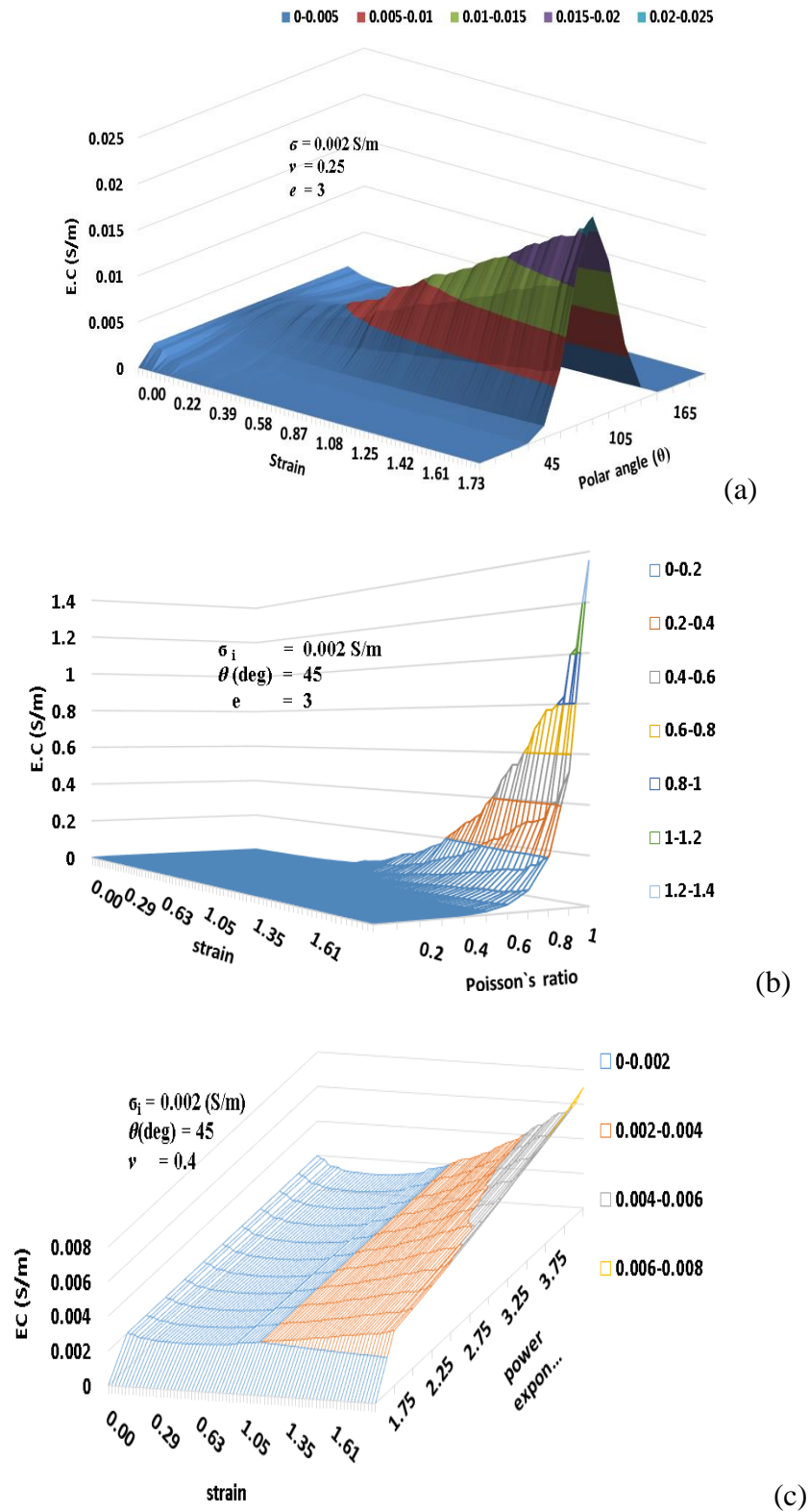


Figure 4.31. Simulation results are presented from Equation 4.44 indicating variation in electrical conductivity under the effect of (a) polar angle, (b) Poisson's ratio and (c) power exponent.

The model is validated with the help of fitting model to an experimental data. An orientation angle for MWCNTs and critical exponent for percolation are used as

fitting parameters while values measured experimentally for an electrical conductivity before deformation and Poisson's ratio are used input parameters. The later parameters are used as input parameters as can found through direct measurement. The results indicate that MWCNTs are aligned at $81^\circ \pm 2^\circ$ as shown in the inset of Figure 4.32. The critical exponent is obtained from fitting is 2.76 which is in the range reported in the literature [56]. The data obtained from the model suggests that polar angle and Poisson's ratio has a relatively profound effect on the electrical conductivity of the nanocomposite compare to power exponent when subject to uniaxial deformation. The fitting was performed in Matlab curve fitting toolbox [65]. The model is fitted using prior information for parameters including polar angle and critical exponent for the percolation threshold, which are 45° and a magnitude of 2.0, respectively. The fitting was based on the least square error using a trust-region algorithm [66].

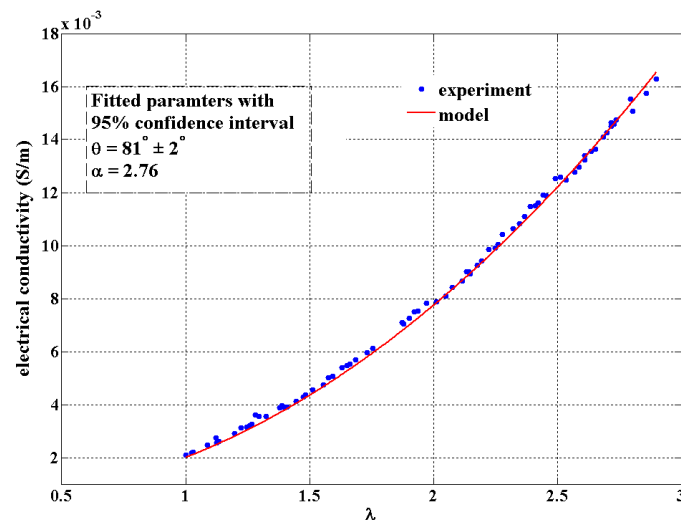


Figure 4.32. Model fitting to experimental data to extract parameters of interest (θ and t).

4.6 SUMMARY

Polycaprolactone polymer-based nanocomposite strands are 3D printed containing MWCNTs (0.5 % w/w and 1.0 % w/w) using a digitally controlled bio-extruder system. An electrical conductivity variation is studied in the strands before and after uniaxial deformation and the results are compared with the bulk film that is used as feedstock material for printing of strands. Following conclusions are drawn from the study:

- With the inclusion of MWCNTs in PCL, DC electrical conductivity in 3D printed strands and bulk films are significantly increased compared to pure PCL. An increase in electrical conductivity is attributed to the formation of conductive pathways due to the percolation of carbon nanotubes.
- Little variation in electrical conductivity ($<2.0\%$) was calculated in 3D printed strands using the same composition and print conditions compare to bulk film (7.0%). This is an indication that additive manufacturing can print parts with nearly similar properties.
- It is found that DC electrical conductivity in the 3D printed strands is relatively lower than bulk film. This is attributed to the rapid solidification of nanocomposite material right after printing which becomes a source of decrease in an electrical conductivity relative to electrical conductivity in the bulk film. Besides, the formation of crystalline lamellae from melt and solvent cast film is different. The percolation pathways of nanotubes are affected by these factors. Based on this, it is concluded that relatively higher conductive pathways exist in the bulk film as compared to 3D printed strand. In other words, the print process affects percolation pathways and hence electrical conductivity.
- The electrical conductivity is decreased after deformation in both samples i.e. a bulk films and 3D printed strands. There is a measurable electric current and voltage drop in the bulk films while no electric current and voltage drop is detected in 3D printed strands after deformation. This is attributed to either network breaking or enhancement in tunnelling resistance caused by the straining of the sample. The 3D printed Strands, containing 1.0% (w/w) MWCNTs, are strained nearly 200% under the effect of uniaxial stress without breaking.
- It is revealed that electrical conductivity increases under the effect of low uniaxial deformation ($<200\%$) while it decreases when samples are strained relatively higher than 200% . This suggests that a low level of strain or deformation causes to reorient carbon nanotubes to a certain extent. Such an orientation increases the probability of conductive pathways due to which conductivity increase in the sample. At strain higher than 200% , nanotubes reorient to such an extent that conductive pathways breaking is relatively

higher than formation. This leads to a decrease in electrical conductivity in the sample.

- The study suggests that Young's modulus, yield strength, and fracture modes are slightly higher in bulk film relative to 3D printed strands. The yield strength and fracture modes are measured 12.7 N/mm² and 16 N/mm², respectively, in case of a bulk film, which decreases to 10 N/mm² and 12 N/mm² for 3D printed conductive strands. The elastic region, yield point and fracture point are decreased at a relatively high strain rate. Also, the plastic deformation region is prolonged at a relatively high strain rate.
- FTIR spectra did not show significant differences in vibrational modes of PCL with the presence of MWCNTs. However, some of the vibrational modes are shifted (< 1.0 %) in the nanocomposite comparing to PCL, with the dispersion of MWCNTs into PCL.
- Small-angle X-ray scattering data is acquired simultaneously revealing information about the microstructure during uniaxial deformation. As an electrical conductivity is calculated before and after deformation, limited information is available from these experiments. Hence, strands are printed containing similar polymer containing relatively higher MWCNTs (1.0 % w/w) and electrical conductivity is calculated simultaneously during deformation. In this set up electric current corresponding voltage drop, SAXS, and stress-strain data are acquired simultaneously from 3D printed strands during uniaxial deformation.
- SAXS data analysis reveals a mass fractal morphology in 3D printed strands and bulk film, prepared using nanocomposite containing MWCNTs, comparing to pure PCL. The mass fractal dimension between -3 and -2 are measured from SAXS data while surface fractal dimension -3 is measured in case of pure PCL. The absence of morphology corresponding to -1 is an indication that MWCNTs form aggregates structure. Besides, 1D – correlation plots suggest that a long period decreases significantly under the effect of uniaxial strain for bulk film and 3D printed strands of pure PCL and nanocomposite strands (0.5 % w/w). In the case of strands printed with 1.0 % (w/w), the long period did not alter significantly. However, there is a difference in 1D – correlation plots along the meridian and equatorial direction that suggests relatively higher (12.0 %) long period along

equatorial direction compare to the meridian in 3D printed strands with 1.0 % (w/w) MWCNTs. However, a long period did not alter under the effect of uniaxial strain. The Kratky analysis indicates that the aggregate size of MWCNTs decreases under the effect of uniaxial strain in 3D printed strands.

- It can be concluded from the spherical harmonic analysis that nanotubes network failure or formation significantly affected in the elastic region while less number of tubes are affected in the plastic deformation region. This indicates that a significant portion of nanotubes is not in-network at relatively higher strain due to which electrical conductivity decreases appreciably.
- Scanning electron microscopy images indicate MWCNTs have a wavy structure. After dispersion in polycaprolactone, MWCNTs aggregate into the polycaprolactone matrix. Nanotubes are entangled into such aggregates.
- DSC data indicates that the crystallinity of the PCL matrix is decreased significantly with the dispersion of MWCNTs. This is attributed to an enhanced dispersion of MWCNTs hindering the nucleation of crystalline lamellae.
- Based on the study conducted, a model is presented describing variation in an electrical conductivity under the effect of uniaxial strain in polymer-based nanocomposites containing MWCNTs. The model parameters include electrical conductivity before deformation, Poisson's ratio, percolation exponent, extension ratio and orientation of carbon nanotubes. Simulation results obtained from the model suggest that polar angle and Poisson's ratio has a relatively profound effect on the electrical conductivity of the nanocomposite compare to power exponent when subject to uniaxial deformation.

4.7 REFERENCES

- [1] M. A. Woodruff and D. W. Hutmacher, "The return of a forgotten polymer - Polycaprolactone in the 21st century," *Prog. Polym. Sci.*, vol. 35, no. 10, pp. 1217–1256, 2010.
- [2] M. Domingos, D. Dinucci, S. Cometa, M. Alderighi, P. J. Bártolo, and F. Chiellini, "Polycaprolactone Scaffolds Fabricated via Bioextrusion for Tissue Engineering Applications," *Int. J. Biomater.*, vol. 2009, pp. 1–9, 2009.
- [3] I. Khan, A. Mateus, C. S. K. Lorger, and G. R. Mitchell, "Part Specific Applications of Additive Manufacturing," *Procedia Manuf.*, vol. 12, no.

- December 2016, pp. 89–95, 2017.
- [4] L. Bokobza, “Multiwall carbon nanotube elastomeric composites: A review,” *Polymer (Guildf)*, vol. 48, no. 17, pp. 4907–4920, 2007.
 - [5] T. Ferreira and W. Rasband, “ImageJ User Guide User Guide ImageJ,” *Image J user Guid.*, vol. 1.46r, 2012.
 - [6] S. L. Gras and A. M. Squires, “Dried and Hydrated X-Ray Scattering Analysis of Amyloid Fibrils,” *Methods Mol. Biol.*, vol. 752, pp. 147–163, 2011.
 - [7] G. R. Strobl and M. Schneider, “Direct evaluation of the electron density correlation function of partially crystalline polymers,” *J. Polym. Sci. Polym. Phys. Ed.*, vol. 18, no. 6, pp. 1343–1359, 2003.
 - [8] G. R. Strobl and M. Schneider, “Direct Evaluation of the Electron Density Correlation Function of Partially Crystalline Polymers.,” *J. Polym. Sci. Part A-2, Polym. Phys.*, vol. 18, no. 6, pp. 1343–1359, 1980.
 - [9] Z. W. Wilchinsky, “Measurement of orientation in polypropylene film,” *J. Appl. Phys.*, vol. 31, no. 11, pp. 1969–1972, 1960.
 - [10] G. R. Mitchell, S. Saengsuwan, and S. Bualek-Limcharoen, “Evaluation of preferred orientation in multi-component polymer systems using x-ray scattering procedures,” *Prog. Colloid Polym. Sci.*, vol. 130, no. June, pp. 149–158, 2005.
 - [11] G. R. Mitchell and R. Lovell, “Molecular orientation distribution derived,” vol. 2, pp. 5–7, 1981.
 - [12] G. R. MITCHELL and A. H. WINDLE, “Orientation in Liquid Crystal Polymers,” in *Developments in Crystalline Polymers-2, 1st ed.*, Bassett, D. C., Ed. London: Elsevier Applied Sciences Publisher Ltd, 1988.
 - [13] V. Crescenzi, G. Manzini, G. Calzolari, and C. Borri, “Thermodynamics of fusion of poly- β -propiolactone and poly- ϵ -caprolactone. comparative analysis of the melting of aliphatic polylactone and polyester chains,” *Eur. Polym. J.*, vol. 8, no. 3, pp. 449–463, 1972.
 - [14] A. Hudecki et al., “Composite nanofibers containing multiwall carbon nanotubes as biodegradable membranes in reconstructive medicine,” *Nanomaterials*, vol. 9, no. 1, 2019.
 - [15] B. Xie, Y. Liu, Y. Ding, Q. Zheng, and Z. Xu, “Mechanics of carbon nanotube networks: Microstructural evolution and optimal design,” *Soft Matter*, vol. 7, no. 21, pp. 10039–10047, 2011.
 - [16] B. De Vivo, P. Lamberti, G. Spinelli, V. Tucci, L. Vertuccio, and V. Vittoria, “Simulation and experimental characterization of polymer/carbon nanotubes composites for strain sensor applications,” *J. Appl. Phys.*, vol. 116, no. 5, 2014.
 - [17] A. Grozdanov, A. Buzarovska, M. Avella, M. E. Errico, and G. Gentile, “PCL/MWCNT Nanocomposites as Nanosensors,” in *Nanotechnological Basis for Advanced Sensors*, J. Peter Reithmaier, P. Paunovic, W. Kulisch, C. Popov, and P. Petkov, Eds. Springer Science+Business Media, 2011.
 - [18] J. Krajči, Z. Špitálský, and I. Chodák, “Relationship between conductivity and stress-strain curve of electroconductive composite with SBR or polycaprolactone matrices,” *Eur. Polym. J.*, vol. 55, no. 1, pp. 135–143, 2014.
 - [19] A. Bello et al., “Universality and percolation in biodegradable poly(ϵ -caprolactone)/multiwalled carbon nanotube nanocomposites from broad band alternating and direct current conductivity at various temperatures,” *Macromolecules*, vol. 44, no. 8, pp. 2819–2828, 2011.
 - [20] W. Defeng, W. Liang, S. Yurong, and Z. Ming, “Rheological Properties and Crystallization Behavior of Multi-Walled Carbon Nanotube/Poly(e-

- caprolactone) Composites," *J. Polym. Sci. Part B Polym. Phys.*, vol. 45, pp. 3137–3147, 2007.
- [21] J. M. Thomassin et al., "Multiwalled carbon nanotube/poly(ϵ -caprolactone) nanocomposites with exceptional electromagnetic interference shielding properties," *J. Phys. Chem. C*, vol. 111, no. 30, pp. 11186–11192, 2007.
- [22] A. Conde, C. F. Conde, and M. Millan, Eds., *Trends In Non-crystalline Solids - Proceedings of the Third International Workshop on Non-Crystalline Solids*. World Scientific, 1991.
- [23] S. K. Sharma, D. S. Verma, L. U. Khan, S. Kumar, and S. B. Khan, "Handbook of Materials Characterization," in *Handbook of Materials Characterization*, no. October, 2018, pp. 1–613.
- [24] J. H. Du, J. Bai, and H. M. Cheng, "The present status and key problems of carbon nanotube based polymer composites," *Express Polym. Lett.*, vol. 1, no. 5, pp. 253–273, 2007.
- [25] R. Zhang, J. Y. S. Li-Mayer, and M. N. Charalambides, "Development of an image-based numerical model for predicting the microstructure–property relationship in alumina trihydrate (ATH) filled poly(methyl methacrylate) (PMMA)," *Int. J. Fract.*, vol. 211, no. 1–2, pp. 125–148, 2018.
- [26] G. R. Mitchell and A. H. Windle, "The determination of molecular orientation in uniaxially compressed PMMA by X-ray scattering," *Polymer (Guildf.)*, vol. 24, no. 3, pp. 285–290, 1983.
- [27] C. Olmo et al., "Preparation of nanocomposites of poly("caprolactone) and multi-walled carbon nanotubes by ultrasound micro-molding. influence of nanotubes on melting and crystallization," *Polymers (Basel)*, vol. 9, no. 8, pp. 1–18, 2017.
- [28] I. Khan, S. D. Mohan, M. Belbut, C. S. Kamma-Lorger, A. Mateus, and G. R. Mitchell, "Multiscale Structure Evolution in Electrically Conductive Nanocomposites Studied by SAXS," *Procedia Manuf.*, vol. 12, no. December 2016, pp. 79–88, 2017.
- [29] N. Gundlach and R. Hentschke, "Modelling filler dispersion in elastomers: Relating filler morphology to interface free energies via SAXS and TEM simulation studies," *Polymers (Basel)*, vol. 10, no. 4, 2018.
- [30] G. P. Baeza et al., "Studying twin samples provides evidence for a unique structure-determining parameter in simplified industrial nanocomposites," *ACS Macro Lett.*, vol. 3, no. 5, pp. 448–452, 2014.
- [31] S. Khalid and S.-Y. Park, "Preparation and Properties of Multiwalled Carbon Nanotube/Polycaprolactone Nanocomposites," *J. Appl. Polym. Sci.*, vol. 104, pp. 1957–1963, 2007.
- [32] Y. Jen-Taut, Y. Ming-Chien, W. Ching-Ju, and W. Chin-San, "Preparation and Characterization of Biodegradable Polycaprolactone/Multiwalled Carbon Nanotubes Nanocomposites," *J. Appl. Polym. Sci.*, vol. 112, pp. 660–668, 2009.
- [33] T. P. Gumede, A. S. Luyt, and A. J. Müller, "Review on PCL, PBS, AND PCL/PBS blends containing carbon nanotubes," *Express Polym. Lett.*, vol. 12, no. 6, pp. 505–529, 2018.
- [34] S. J. Chin et al., "Electrical conduction and rheological behaviour of composites of poly(ϵ -caprolactone) and MWCNTs," *Polymer (Guildf.)*, vol. 58, pp. 209–221, 2015.
- [35] N. Hu, Y. Karube, C. Yan, Z. Masuda, and H. Fukunaga, "Tunneling effect in a polymer/carbon nanotube nanocomposite strain sensor," *Acta Mater.*, vol. 56, no. 13, pp. 2929–2936, 2008.

- [36] L. Pan, X. Pei, R. He, Q. Wan, and J. Wang, "Multiwall carbon nanotubes/polycaprolactone composites for bone tissue engineering application," *Colloids Surfaces B Biointerfaces*, vol. 93, pp. 226–234, 2012.
- [37] T. Chatterjee and R. Krishnamoorti, "Rheology of polymer carbon nanotubes composites," *Soft Matter*, vol. 9, no. 40, pp. 9515–9529, 2013.
- [38] P. Pötschke, M. Abdel-Goad, I. Alig, S. Dudkin, and D. Lellinger, "Rheological and dielectrical characterization of melt mixed polycarbonate-multiwalled carbon nanotube composites," *Polymer (Guildf)*, vol. 45, no. 26, pp. 8863–8870, 2004.
- [39] T. P. Gumedde, A. S. Luyt, M. K. Hassan, R. A. Pérez-Camargo, A. Tercjak, and A. J. Müller, "Morphology, nucleation, and isothermal crystallization kinetics of poly(ϵ -caprolactone) mixed with a polycarbonate/MWCNTs masterbatch," *Polymers (Basel)*, vol. 9, no. 12, 2017.
- [40] B. Dimitrios, "Microstructure and Properties of Polypropylene/Carbon Nanotube Nanocomposites," *Materials (Basel)*, vol. 3, pp. 2884–2946, 2010.
- [41] K. T. Kashyap and R. G. Patil, "On Young's modulus of multi-walled carbon nanotubes," *Bull. Mater. Sci.*, vol. 31, no. 2, pp. 185–187, 2008.
- [42] C. Li and T. W. Chou, "Multiscale modeling of compressive behavior of carbon nanotube/polymer composites," *Compos. Sci. Technol.*, vol. 66, no. 14, pp. 2409–2414, 2006.
- [43] E. K. Sichel, *Carbon black-polymer composites: the physics of electrically conducting composites*. New York: M. Dekker, 1982.
- [44] B. P. Grady, "Effects of carbon nanotubes on polymer physics," *J. Polym. Sci. Part B Polym. Phys.*, vol. 50, no. 9, pp. 591–623, 2012.
- [45] G. Strobl, *The physics of polymers: Concepts for understanding their structures and behavior*. 2007.
- [46] T. Kamal, T. J. Shin, and S. Y. Park, "Uniaxial tensile deformation of poly(ϵ -caprolactone) studied with SAXS and WAXS techniques using synchrotron radiation," *Macromolecules*, vol. 45, no. 21, pp. 8752–8759, 2012.
- [47] R. J. Matyi, B. Crist, Jr., "Small-Angle X-Ray Scattering I by Nylon 6," *J. Polym. Sci. Polym. Phys. Ed.*, vol. 16, pp. 1329–1354, 1978.
- [48] N. S. Murthy and D. T. Grubb, "Tilted Lamellae in an Affinely Deformed 3D Macrolattice and Elliptical Features in Small-Angle Scattering," *J. Polym. Sci. Part B Polym. Physics*, vol. 44, pp. 1277–1286, 2006.
- [49] G. Elsner, M. H. J. Koch, J. Bordas, and H. G. Zachmann, "Time resolved small angle scattering during isothermal crystallization of unoriented poly(ethylene terephthalate) using synchrotron radiation," *Die Makromol. Chemie*, vol. 182, no. 4, pp. 1263–1269, 1981.
- [50] B. S. Hsiao, K. C. H. Gardner, D. Q. Wu, and B. Chu, "Time-resolved X-ray study of poly(aryl ether ether ketone) crystallization and melting behaviour: 1. Crystallization," *Polymer (Guildf)*, vol. 34, no. 19, pp. 3986–3995, 1993.
- [51] H. Hama and K. Tashiro, "Structural changes in non-isothermal crystallization process of melt-cooled polyoxymethylene[II] evolution of lamellar stacking structure derived from SAXS and WAXS data analysis," *Polymer (Guildf)*, vol. 44, no. 7, pp. 2159–2168, 2003.
- [52] C. Y. Li, L. Li, W. Cai, S. L. Kodjie, and K. K. Tenneti, "Nanohybrid shish-kebabs: Periodically functionalized carbon nanotubes," *Adv. Mater.*, vol. 17, no. 9, pp. 1198–1202, 2005.
- [53] M. M. L. Arras et al., "In Situ Formation of Nanohybrid Shish-Kebabs during Electrospinning for the Creation of Hierarchical Shish-Kebab Structures,"

- Macromolecules*, vol. 49, no. 9, pp. 3550–3558, 2016.
- [54] C. H. Seager and G. E. Pike, “Percolation and conductivity: A computer study. II,” *Phys. Rev. B*, vol. 10, no. 4, pp. 1435–1446, 1974.
 - [55] Y. Miao, Q. Yang, L. Chen, R. Sammynaiken, and W. J. Zhang, “Modelling of piezoresistive response of carbon nanotube network based films under in-plane straining by percolation theory,” *Appl. Phys. Lett.*, vol. 101, no. 6, 2012.
 - [56] W. Bauhofer and J. Z. Kovacs, “A review and analysis of electrical percolation in carbon nanotube polymer composites,” *Compos. Sci. Technol.*, vol. 69, no. 10, pp. 1486–1498, 2009.
 - [57] H. E. Stanley et al., “Scaling concepts and complex fluids: long-range power-law correlations in DNA,” *J. Phys. IV JP*, vol. 3, no. 1, pp. 15–25, 1993.
 - [58] C. Feng and L. Y. Jiang, “Investigation of uniaxial stretching effects on the electrical conductivity of CNT-polymer nanocomposites,” *J. Phys. D. Appl. Phys.*, vol. 47, no. 40, 2014.
 - [59] C. Feng, Y. Wang, S. Kitipornchai, and J. Yang, “Effects of reorientation of graphene platelets (GPLs) on young’s modulus of polymer nanocomposites under uni-axial stretching,” *Polymers (Basel)*, vol. 9, no. 10, 2017.
 - [60] D. Sánchez-Portal, E. Artacho, J. M. Soler, A. Rubio, and P. Ordejón, “Ab initio structural, elastic, and vibrational properties of carbon nanotubes,” *Phys. Rev. B - Condens. Matter Mater. Phys.*, vol. 59, no. 19, pp. 12678–12688, 1999.
 - [61] L. Lu et al., “Mechanical study of polycaprolactone-hydroxyapatite porous scaffolds created by porogen-based solid freeform fabrication method,” *J. Appl. Biomater. Funct. Mater.*, vol. 12, no. 3, pp. 145–154, 2014.
 - [62] W. Kuhn and F. Grün, “Beziehungen zwischen elastischen Konstanten und Dehnungsdoppelbrechung hochelastischer Stoffe,” *Kolloid-Zeitschrift*, vol. 101, no. 3, pp. 248–271, 1942.
 - [63] R. Prez, S. Banda, and Z. Ounaies, “Determination of the orientation distribution function in aligned single wall nanotube polymer nanocomposites by polarized Raman spectroscopy,” *J. Appl. Phys.*, vol. 103, no. 7, 2008.
 - [64] M. van Gurp, “The use of rotation matrices in the mathematical description of molecular orientations in polymers,” *Colloid Polym. Sci.*, vol. 273, no. 7, pp. 607–625, 1995.
 - [65] “Curve Fitting Toolbox - MATLAB.” [Online]. Available: <https://www.mathworks.com/products/curvefitting.html>. [Accessed: 04-Nov-2019].
 - [66] J. J. Mor and Sorensen D.C., “Computing a Trust Region Step,” *SIAM J. Sci. Stat. Comput.*, vol. 4, no. 3, pp. 553–572, 1983.

Chapter 5: Design and configuration of a 3D printer system for thermosetting polymer-based nanocomposites

5.1 INTRODUCTION

In order for 3D printing to be a more functional means of manufacturing, printers, as well as printable materials, need to move beyond the current focus of manufacturing. Nowadays, 3D objects are manufactured by additive manufacturing (AM) in a layer-by-layer fashion whether the material is plastic, metal or concrete. Due to the limited number of printable polymers, printing technology is not able to make adequate progress in terms of polymers or their composites. Significant printable polymers include polylactic acid, acrylonitrile-butadiene-styrene, polyamide, polyethylene terephthalate and few UV-curable thermoset resins. Therefore, a serious demand exists to extend the range of printable polymers or their composites. The literature suggests that most of the AM technology is focused on printing of thermoplastic polymers and relatively less attention was paid towards the printing of thermosets. Due to structural integrity, thermosets offer superior characteristics, mechanical, chemical and heat resistance, over thermoplastics. The significance of thermoset polymers evidenced from applications, where parts can bear high temperature contrary to parts printed using thermoplastic polymers that are not able to fulfil requirements due to melting. Thermosets is a class of plastics that are irreversibly cured or hardened by cross-linking of polymer chains. The main types of thermoset resins are epoxy resins, urea, melamine resins, unsaturated polyester resin, phenolic, and polyurethane resins [1]. The curing process changes the soft solid or viscous liquid prepolymer or resin into an insoluble polymer network [2]. Curing can be induced by heat, pressure or through a catalyst. It results in chemical reactions that create extensive cross-linking between polymer chains to create an infusible and insoluble polymer network. On contrary to the thermoplastic polymers which are widely used for the 3D printing, reheating thermosets for reshaping is not possible. This makes the print process challenging when dealing with thermoset polymers or it's composites. Also, many thermosets require long-term curing under harsh conditions, which is not compatible with rapid 3D printing processing. 3D printing of these thermosets remains

a challenge [3]. The control over the cure allows printing in such kind of polymers. Existing printing systems for thermosets have two key issues. First, the printing process involves complex optics and control system. Second, printing systems are expensive and limited to UV-curable thermosets. One example of such printing systems is a stereolithography system [4] [5]. Thermoplastic polymers require heat to soften pellets or filament to become fluid and therefore need cooling time to solidify. The thermoset advantage lies in the cross-linking of polymers between printed layers resulting in stronger, more thermo-tolerant products. Compared to thermoplastic polymers, thermoset materials significantly increase strength, decreasing thermal expansion and optimizing isotropic expansion [6]. Besides, one of the key issues in the broad implementation of additive manufacturing is the printing of components with enhanced features or components with some sort of functionality [7]. Therefore, carbon nanotubes are used as an electrically conductive nanostructures filler particles into the epoxy resin. Their distribution in the epoxy system is chaotic as the overall quality of dispersion of the conducting nanotubes within the polymer matrix is affected through different parameters including mixing conditions, sonication, polymer chemistry, composition and type [8]. The formation of conductive pathways in such a distribution provides a route for electronic conduction. Percolation theory is used to study conductivity in such kind of complex systems [9]. The literature suggests that these conductive paths could be due to the physical touch of nanotubes [10] or through a tunnelling distance [11].

With the consideration of the above-mentioned aspects, the design and configuration of an AM system and a material preparation methodology are disclosed in this chapter using thermoset polymer-based nanocomposites. Comprehensive and significant information is disclosed related to the configuration and design of the printing system. It includes overall design and structure of the printer system, configuration of axes, calibration of axes, extrusion principle, control parameters, deposition system, electronics and software systems. The configured printing system work on extrusion principle for the printing of a thermoset polymer-based composite material in an additive way. A methodology for material preparation is provided that includes a thermoset epoxy resin, a limited proportion of thermoplastic polymer and carbon nanotubes as nanostructure conductive particles. Thermoset epoxy resin is used as a thermoset polymer matrix while a thermoplastic polymer, polycaprolactone, and carbon nanotubes used in small proportion as an additive material restricting the

molecular mobility of epoxy resin [12] and hence prolong the hardening time. In this way, the presence of polycaprolactone and carbon nanotubes provide a working window for 3D printing of epoxy-based electrically conductive nanocomposite material. Thermal energy consumption in thermoplastic additive manufacturing is equivalent to injection moulding, whereas reactive additive manufacturing requires even less energy, as there is no heated chamber or heated bed in the current configuration. A brief methodology is described for the printing of thermoset polymer-based nanocomposites with key limitations and issues that were observed for the sake of thermoset printing. A thorough characterization is performed on printed samples using a variety of techniques characterising electrical, thermal and morphological response and results are presented in chapter 6.

5.2 OVERALL DESIGN AND STRUCTURE

The configured printing system for printing of thermoset resin-based nanocomposites is presented in Figure 5.1, which is based on the Cartesian gantry positioning system [13] driven by stepper motors. These stepper motors are connected with gears, which move the printing nozzle through aluminium guide over the desired position. The printer works on gel extrusion principle for deposition of material [14] during the print process. A syringe- plunger system is used to serve the purpose. A specially designed and 3D printed hardware assembly is attached with the printer for mounting of the material loaded syringe. A linear stepper motor (12 V) is used to control the plunger motion for deposition of material through the printing nozzle. The electronics of the system was provided for three-dimensional movement through single-phase induction stepper motors with 24 V operating voltage. Two limit switches per axis are used for positioning of the printing head and limiting the motion across two ends. The software and firmware can support up to six axes of control in their current version for the case when the system requires an update. Arduino Mega board is used as a microcontroller, which controls the positioning of the axes and it is in communications through a micro SD card. An LED display is used to set parameters of interest. Besides, the printer system lets the user connect via a USB port to a PC. Therefore, an application running on the PC displays the real-time status of the printer numerically and graphically. It allows the user to position the axes, and perform basic modifications to G-code data for the geometry of the desired part. The concept design has focused on ease of use, reliability and affordability compare to complex control

system and cost. The effort is based on a modest availability of technical tools and skills for nanocomposite printing. Basic assembly tools including screwdrivers, scissors, pliers, and soldering iron are used during development.

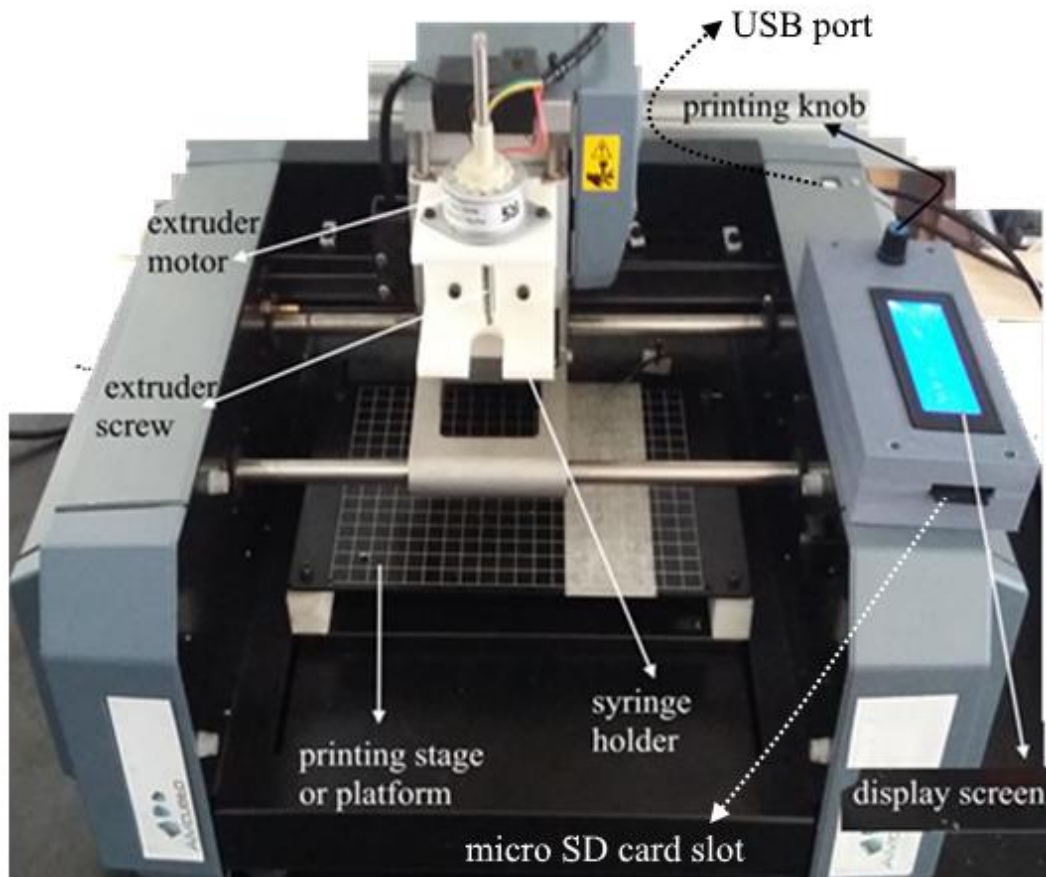


Figure 5.1 Presentation of the printer system.

The structure of the printing system consists of injection moulded plastic parts, 3D printed plastic parts and CNC designed aluminium and steel parts. The body parts are joined through nuts, screws threaded inserts and bolts for the positioning of the components for the overall body structure. Appropriate power rated cables are used to connect different components of the printer including microcontroller, the motors, and end switches. The overall body dimension of the printer constitutes a volume of 56 x 40 x 38 cm³.

5.3 CONFIGURATION OF AXES AND 3D MOTION

The linear motion of the printing nozzle is controlled through three stepper motors along X, Y and Z-axes as shown in Figure 5.2. The X- and Z - axes are in a gantry configuration with the deposition tool riding on the X-axis. The Y-axis moves

the build surface or platform independently from the X and Z. Single-phase induction motors are used for the X-, Y-, and Z-axes movement having the gear for movement of axes. In the case of the X and Z -axis, aluminium wire and pulleys are used to perform motion along respective axes. A linear guide bearing brass over an aluminium cylinder is used for a guide or stable movement. The fourth motor is used for plunger movement within the barrel facilitating syringe-plunger system for material deposition through the nozzle. The motion of the syringe holder was controlled through the two axes (X, and Z-axes). These axes can travel a maximum distance of 170 mm and 67 mm, respectively. The printer has a rectangular stage having dimensions 250 mm and 160 mm. The stage can move along the Y-axis covering a maximum distance 95 mm from home position. The home position is set at the extreme bottom left corner of the stage where $X = 0$, $Y = 0$, for a particular Z-position. Two end switches are used along each axis describing the region of interest for printing to avoid collision with the body of the printer.

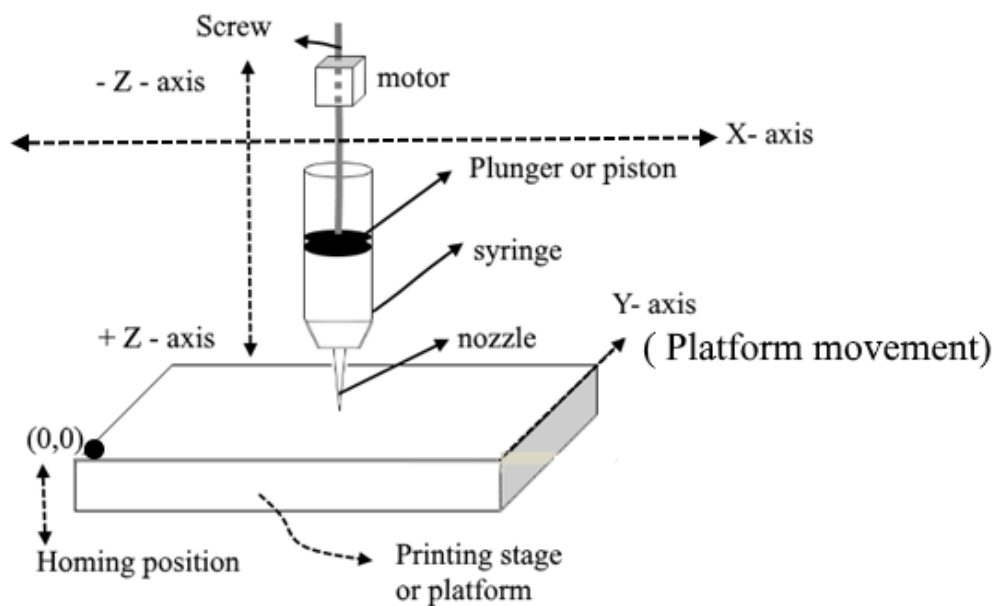


Figure 5.2 Presentation of the printer system

5.3.1 Calibration of axes

It is important to calibrate the printer to print parts with consistent accuracy. Such machines use stepper motors, which rotate by small steps to move axes. In other words, the calibration of a stepper motor involves determining the relationships between steps and linear distance along a particular axis. The four stepper motors (X, Y, Z and extruder) were calibrated based on physical move, measure and edit principle.

The print head moved an arbitrary distance through a command line or graphical user interface, keeping other axes constant. The travelled distance was measured and it was compared with the distance instructed to move the particular axis. In case, no difference found, the stepper motor was calibrated along that particular axis. If there exists some difference than need to modify the number of steps for the stepper motor through editing the header file using the Arduino interface. The process was repeated until distance travelled by the stepper motor for a particular axis becomes exactly equal to the instructed distance. The process was repeated for all the stepper motors including stepper motor controlling the material extrusion. The motion velocity is limited between 0.1 mm/s to 10 mm/s for all the motors used to control axis and the extruder. Finally, some random point was assigned to the extruder nozzle and it was measured (position) manually proving that the printer was in the right position. Besides, the platform or stage is levelled to ensure reasonable print quality. A Spirit Level tool is used to the level of the printing platform.

5.4 EXTRUSION PRINCIPLE

The principle of extrusion of material is based on a piston system in which a plunger movement is used to control material flow through the printing nozzle. The material flow is regulated by controlling the plunger movement through a 12-volt stepper motor. It starts (or stops) extrusion by generating (or releasing) force on the plunger. A direct current 12-volt motor is used to control plunger motion to push material for deposition or in the opposite direction. The fourth dimension was designated for the stepper motor used to control the piston (plunger) movement towards / away extrusion of material through the nozzle. The amount of material extruded through the syringe depends on piston movement or extrusion rate. Plunger-barrel extruder is a reported printing system for gel or a paste extrusion [15]. The appropriate extrusion rates depend on material composition and nozzle size. The printer allows to using syringes with different diameter if not appropriate for a particular composition. However, the length of the syringe between 10 – 16 mm is considered appropriate as longer syringes require relatively an increased force to push material for printing.

5.5 MATERIAL DEPOSITION ASSEMBLY

A syringe-plunger system is selected to include in the design of the printer system for carrying and deposition of the material. This is selected because of piston extrusion mechanism and being disposable in case material cure within the barrel, as thermosets cure through bonding or reacting chemically and removal of residue is a time-consuming and hard process. The syringe tool assembly is shown in Figure 5.3 (a). The plunger was designed according to barrel diameter and it was 3D printed using CAD design. A licensed version software package “SolidWorks” [16] is used to design CAD models for the desired plunger. Other parts including barrel, nozzle and seal are replaceable after processing 2-3 compositions.

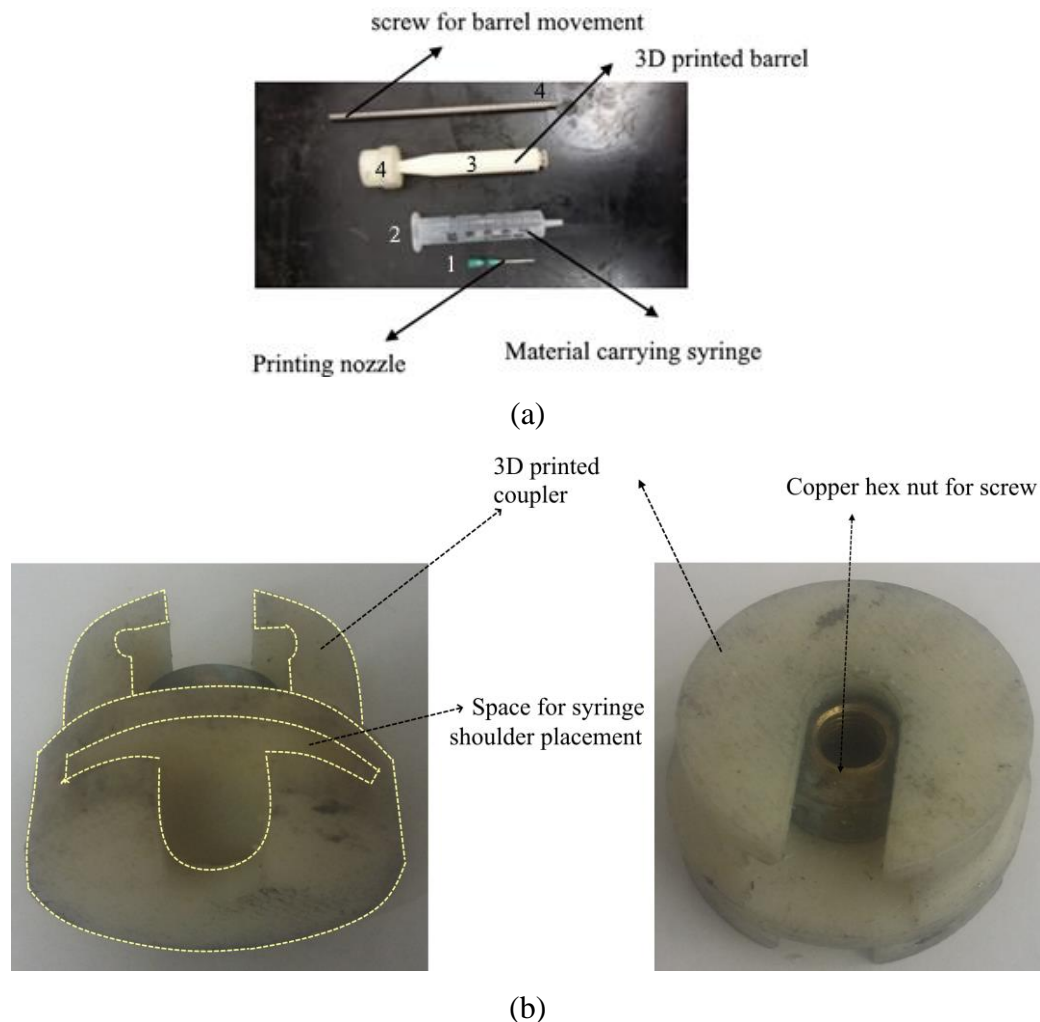


Figure 5.3 (a) The syringe-plunger system is shown for the printing system with its components that are used to carry material for the sake of dispensing material through the printing nozzle. (b) The 3D printed coupler with a copper hex is presented in this Figure. This was used for joining plunger and long screw for plunger movement for deposition of material through the printing nozzle.

A long screw is used to push plunger through a 12 V motor, which is not captive in the motor. One end of screw passes through the motor while its other end is captive in a cylindrical copper nut. The copper nut is housed in a 3D printed coupler as shown in Figure 5.3 (b). The current syringe system can carry a maximum material volume around $10 \pm 0.3 \text{ cm}^3$ and it was obtained from EFD, Inc., Portugal.

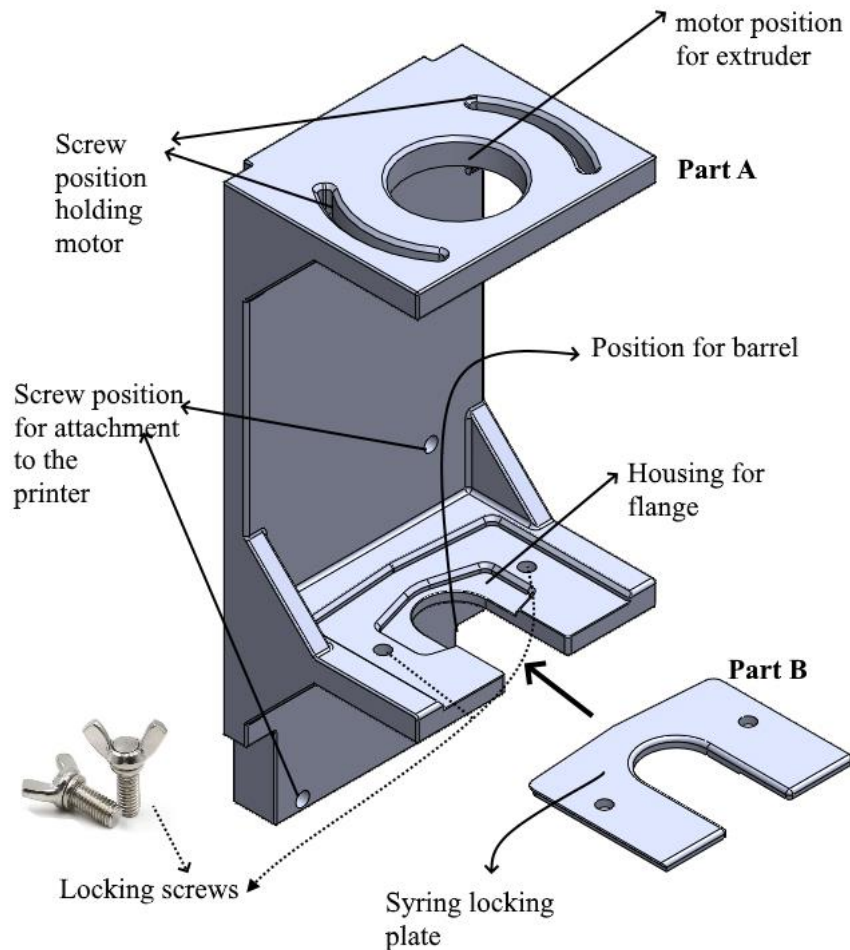


Figure 5.4 CAD model of the support holding the syringe plunger system during printing.

The dimension of the plunger was considered based on internal diameter and length of the barrel. It can easily snap in and out through the syringe and for the 3D printed plunger to be quickly attached and released from the motor screw for a change of material. The metal nut fits tightly inside the coupler, and one end of the motor screw has to be a thread to match the nut. When firmly threaded into the nut, the screw is prevented from rotating with the motor rotor, and hence the rotor motion is converted to linear motion. Manually unscrewing the screw from the nut allows change of material or nozzle. A linear stepper motor controls the position of the plunger that

moves within the barrel. A 12 V stepper motor with a rotor mounted lead nut is used for plunger movement.

The working of the syringe-plunger system depends on part holding syringe during material extrusion. A Computer-aided design (CAD) is generated for the part and it was 3D printed for holding syringe-plunger system without slipping, jerking or vibrating. The CAD designs were generated in SolidWorks [16]. During practical use, the design was optimized in light of emerging issues. It consists of two parts (Part A & Part B) as shown in Figure 5.4. These parts were 3D printed using the CAD design mentioned in Figure 5.4. Stratasys uPrint [17] professional desktop 3D Printer (was used to print parts using acrylonitrile butadiene styrene polymer. The syringe-plunger system with loaded material is connected through the coupling part such that the flange of barrel sits in the housing of part A. The part B will be used as an upper plate for locking the flange through two right and left screws. The syringe-carrying holder can move a maximum distance of 62.7 mm. This motion was controlled through a stepper motor along the z-axis keeping an appropriate distance between the platform and the printing nozzle. The printer assembly was contained following key components:

- Stepper motors for 3D control, extruder motor, extruder screw, switches or end stops, an Arduino Mega board(Figure 5.6)
- Printing stage, Syringe-barrel system, needles of different sizes,
- Syringe holder assembly (Figure 5.4)

5.6 COMMAND AND CONTROL SYSTEM

The printer has an LED display Figure 5.5(a) on its right side for the command and control of the printer. It has a Knob that can rotate clockwise or anti-clockwise to scroll parameter of interest and once the parameter of interest is found it is altered through pressing the knob downwards. The value can increase or decrease through rotating knob clockwise or anticlockwise. The system also allows connecting with a PC through a USB cable (type A-B). The application used to connect with the printer is known as “Printrun” [18]. The graphical user interface (GUI) of Prinrun is presented in Figure 5.5(b).

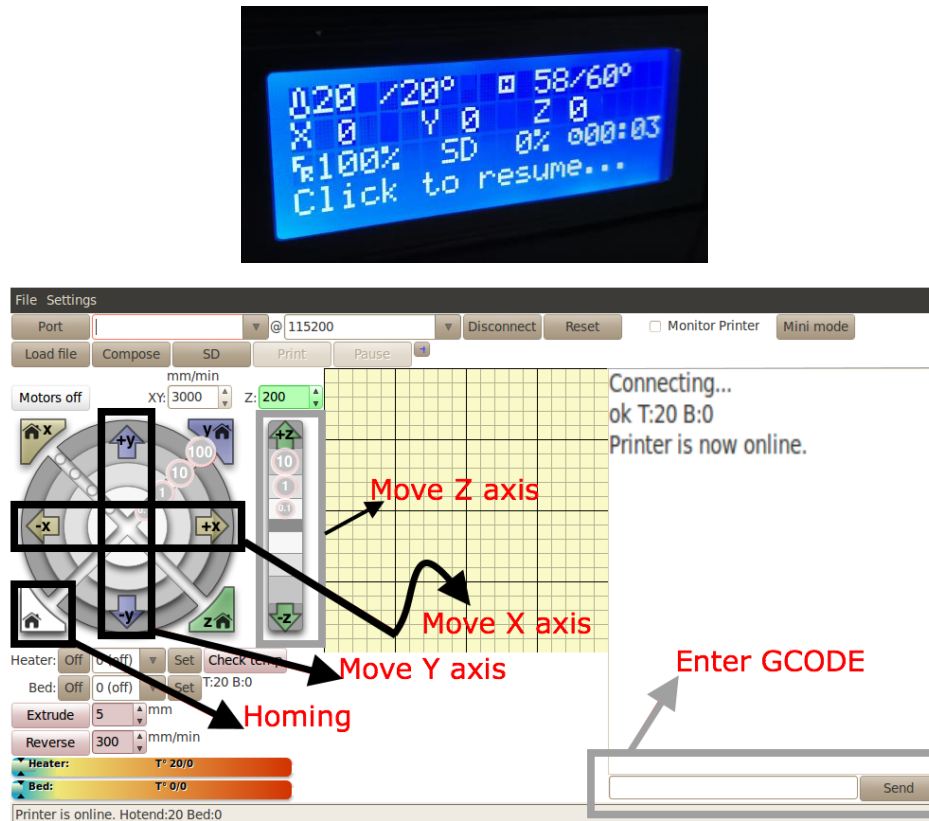


Figure 5.5 (a) LED display used to control printer system, (b) A graphical user interface “Printrun” is used to control and monitor online printing of part.

5.7 ELECTRONICS AND SOFTWARE

Arduino ATmega 2560 (Figure 5.6) is used as a microcontroller with an on-chip USB2.0 peripheral. A direct USB connection is preferred for the sake of connection between a PC and the printer system. The maximum length and width of the ATmega 2560 PCB are 4 and 2.1 inches respectively. Three screw holes allow the board to be attached to a surface or case. The Arduino Mega can be powered via the USB connection or with an external power supply. The microcontroller is a very high performance, 16 MHz, flash-memory microcontroller with a wealth of peripheral functions for future expansion including counter, timers, real-time clock etc. Besides, it has 512 KB of flash memory, and 40 kB of random access memory (RAM). The large program memory has enabled us to make a very easily understood and extensible packet data protocol for communication between the PC application and the firmware. With our current protocol, we can buffer roughly 670 six-dimensional path points (for up to six axes of control). The high computational performance of the device enables the system to handle receiving and buffering path points, sending real-time status and position data, and controlling step and direction outputs for six axes at 5 kHz.

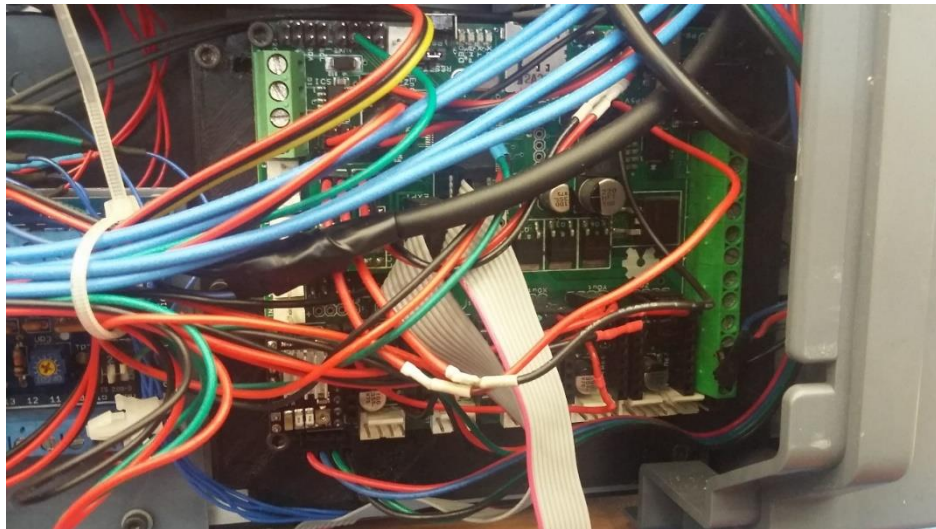


Figure 5.6 Arduino Mega board that was used to control stepper motors.

The Arduino Mega can be programmed with the Arduino software [18] using a simple hardware programming language called Processing, which is similar to the C language [19]. It can be programmed online and offline using the Arduino interactive development environment (IDE). The firmware performs the following main functions:

- receiving and parsing of packetized commands from the PC via the USB;
- buffering of motion path segments for fabrication paths;
- immediate execution of jog motion and emergency stop commands;
- configuration of limit switches (present/absent for each axis and direction);
- communicating axes positions, limit switch states, and another system status to the PC via the USB; and
- Controlling step and direction outputs for up to six axes at > 5 kHz step frequency.

The microcontroller has additional resources available for future expansion through modifying the firmware. The specs of the Arduino ATmega 2560 are presented in Table 5.1. Also, the application has been designed around the concept that with the possibility of updating the printer by the user including the hardware configuration, the types of materials, and parameters for depositing materials would be far simpler.

Table 5.1 The specs of Arduino Mega 2560 microcontroller used to control the designed printing system.

Microcontroller	ATmega2560
Operating Voltage	5V
Input Voltage (recommended)	7-12V
Input Voltage (limits)	6-20V
Digital I/O Pins	54 (of which 14 provide PWM output)
Analog Input Pins	16
DC Current per I/O Pin	40 mA
DC Current for 3.3V Pin	50 mA
Flash Memory	256 KB of which 8 KB used by bootloader
SRAM	8 KB
EEPROM	4 KB
Clock Speed	16 MHz

5.8 MODEL DEFINITION AND INPUT FOR PRINTING

The aforementioned 3D printer communicates via a language called G-code, primarily used for Computer Numerical Controlled (CNC) machines. This simple and versatile language provides a set of human-readable commands that a 3D printer performs for controlling of different actions. A list of G –codes with sufficient explanation can be found on the webpage [20]. The 3D models are translated into a series of G-code commands for producing a solid part. Amongst all G – codes, start and end G- codes are of special significance. These two highly customizable scripts are the key codes for acquiring a printed part. The purpose of the start G- code script is to prepare 3D printer for producing the desired object through moving some distance while end G- code stops the print after moving some distance in a 2D plane and these are defined as G1 and M84, respectively. It is important to mention that M84 code turns off all the stepper motors. At a minimum, the extruder and printing stage or platform needs to be homed. The home is a position where all axis (x, y and z) are defined as (0, 0, 0) and it is defined in G-codes as G28. Figure 5.7 shows the order of writing G - code file for the parts printed using the printer mentioned in Figure 5.1.

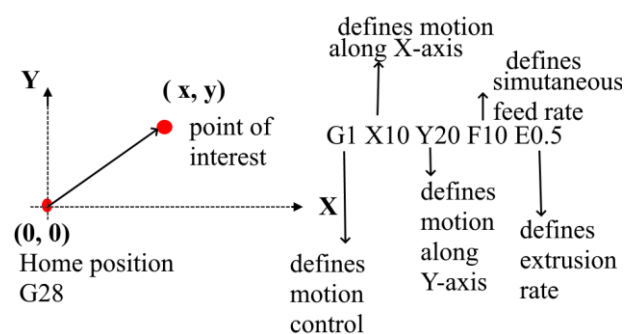


Figure 5.7 The structure adopted to write G-codes controlling the printer motion along two axes (x and y-axis) and extrusion of material with a defined feed rate.

FX– sets the federate for all subsequent moves. F stands for feed and X defines the particular rate used to define movements e.g. F100 defines feed rate 100. The units used in the current study are mm/min. EX – sets the extrusion rate for the printable material and E stands for extrusion while X defines the rate of extrusion.e.g. E0.5 defines an extrusion rate of 0.5 mm/min. The significant codes to create a G- code file for the printing of samples are as follows:

G0 – move without extrusion

G1 – Perform a synchronized movement

G28 – Home 3D printer or move the tool head to the origin

G90 – Set all future commands to use absolute coordinates (as opposed to a relative position from the last location)

G92 – Define the current physical position to user-specified values.

5.9 MEASUREMENT OF FLOW RATE

The flow rate is the volume flow rate (or mass flow rate) of a material, which passes per unit time through the nozzle and deposit on the platform or stage. The volume flow rate (Q) of the printable material is defined as

$$Q = (V/t) \quad (6.1)$$

Where Q, V and t represent a volume flow rate of the material, the volume of the extruded material and time during which volume V extruded through the nozzle. The mass flow rate can also be determined using volume flow rate (Eq. 6.1) and it is given as

$$(m/t) = \rho(V/t) \quad (6.2)$$

Here ρ is a density of the material. A volume of $(20 \times 20 \times 1) \text{ mm}^3$ were printed and print time recoded accordingly. An electronic balance was used to measure the mass of the printed object. The volume of the printed object is also determined through direct measurement of physical dimensions of the printed part. A slight increase in volume (2.5 -5.0 %) was found for the part when it was measured experimentally. The measured volume and mass are used to find the density of the material, which was $0.94 \pm 0.03 \text{ g/cm}^3$. The experimentally measured mass and recoded time for the printed part was used for the mass flow rate of the material. The mass flow rate was measured as $32.8 \pm 0.98 \text{ mg/min}$. The measurement was conducted from two different samples and the average results are provided here.

5.10 PROCESS PARAMETERS

Once the epoxy-based nanocomposite preparation process was established, the printing method was refined to obtain optimum printed structures by testing different printing conditions. Feed rate or print speed and extrusion rate are two significant parameters that have a direct influence on the printing of a part [21]. The feed rate is a speed with which the printer head moves from one position to another position and the extrusion rate defines the speed with which material is pushed towards nozzle for deposition on the printing stage. It is important to mention that the feed rate defines the same speed for X, Y, and Z- axes. Extrusion rate is defined separately to control material flow acquiring optimum print quality. A fast feed rate combined with a slow extrusion rate leads to a smaller filament diameter since the filament is stretched out of the nozzle during the printing. The magnitude of these two parameters affected through the viscosity of material and printing nozzle. The material deposition is affected by nozzle diameter. A higher nozzle size leads to bigger layer diameter, which affects infill properties for printable parts.

5.11 CASE STUDY

A description of materials is provided in Ch. 3 that is used to conduct a case study. These include thermoset epoxy resin, a hardener, PS, PCL and carbon nanotubes. Initially, attempts were taken to acquire 3D printing of pure epoxy (DGEBA/TETA) samples, which were not possible due to rapid reaction between DGEBA resin and TETA causing the material to harden within the mixing pot regardless of using different formulations. It becomes practically impossible to print desired parts using the pure epoxy system. It is reported in numerous other studies that a presence of filler particles increase the viscosity of the overall composition [22]. Besides this, the purpose of the study is to print epoxy-based electrically conductive nanocomposites. Therefore, compositions were prepared using DGEBA resin with a TETA as a crosslinker and MWCNTs as electrically conductive nanostructures. Different formulations and composition were tested employing different concentration of MWCNTs to prolonged cure rate and thereby to avoid nozzle clogging. It is found that compositions were not printable due to rapid crosslinking occur between DGEBA resin and TETA even in the presence of MWCNTs. It was observed that the compositions were cured within the barrel and motor was not able to push material down towards nozzle. This lead to a failure of the print process regardless of the

variation in compositions. All such efforts lead towards no extrusion at all or little extrusion due to rapid curing. The prominent issues were recorded include rapid curing or incomplete curing. Rapid curing was resulted due to relatively lower MWCNTs loading or in the absence of MWCNTs while incomplete curing caused by relatively higher MWCNTs. The problem was addressed using the same methodology that the presence of another phase restricts monomers mobility and reaction between them. The approach adopted to address these issues was the use of a thermoplastic polymer but relatively in a small proportion compared to epoxy resin. Based on the literature review, two polymers were selected for epoxy/ thermoplastic mixture for the sake of additive manufacturing, namely Polystyrene (PS) and Polycaprolactone (PCL). In the first instance, the problem was addressed through variation in the polystyrene (PS) loading in the DGEBA resin. Compositions were prepared for 3D printing but it gets phase-separated after the removal of organic solvent used to disperse MWCNTs. The phase separation is quite clear and issues of nozzle clogging become obvious. On the other hand, PCL mixture with epoxy resin proves to be useful and samples were printed with smooth material flow. PCL was used in the epoxy resin based on the literature [23]. The extrusion of the nanocomposite through the nozzle using PCL in the presence/absence of MWCNTs indicated that PCL is an appropriate entity to control the flow of material acquiring 3D printing. It was still difficult to print samples without MWCNTs, as material behaviour is nearly the same as without PCL and still curing occurred rapidly but without nozzle clogging. It was considered that motion of monomers was restricted under the combined effect of the inclusions of PCL and MWCNTs. In other words, together with PCL and MWCNTs offer optimum print quality required to print desired samples. The preparation scheme for an epoxy-based nanocomposite containing PCL and MWCNTs is provided in the proceeding section.

5.12 NANOCOMPOSITE PREPARATION (CONDUCTIVE INK)

Different formulation and compositions were prepared and tested for printing. In this section, a specific composition is disclosed that was used to print epoxy-based nanocomposites. Electrically conductive nanocomposites were prepared with the aid of MWCNTs dispersed in a DGEBA resin in the presence of Polycaprolactone (PCL). PCL was used to achieve optimum flow characteristics in the nanocomposites. First, MWCNTs were measured and mixed with Triton X - 100 in the presence of chloroform using a glass bottle (50 ml). An ultrasonic probe (Ch.3, section 3.11), with a pulse

mode, is used for 5.0 min to disperse MWCNTs in the chloroform and Triton X-100 solution. Triton X - 100 was used as 2.0 % w/w, in all compositions, concerning epoxy weight (DGEBA + TETA). The solution was left in the incubator (Ch.3, section 3.10) set at 100 rpm with 50 °C for 15 min after adding PCL. The solution was kept in the water bath for 1.0 min after taking it from the incubator, avoiding excessive evaporation of chloroform. The solution was mixed with DGEBA resin following the use of ultrasonication for 5.0 min in the pulse mode. Again, the solution was left in the incubator for 18 hrs using the conditions mentioned above. After 18 hours passed, a stable dispersion was visualised from the composition.

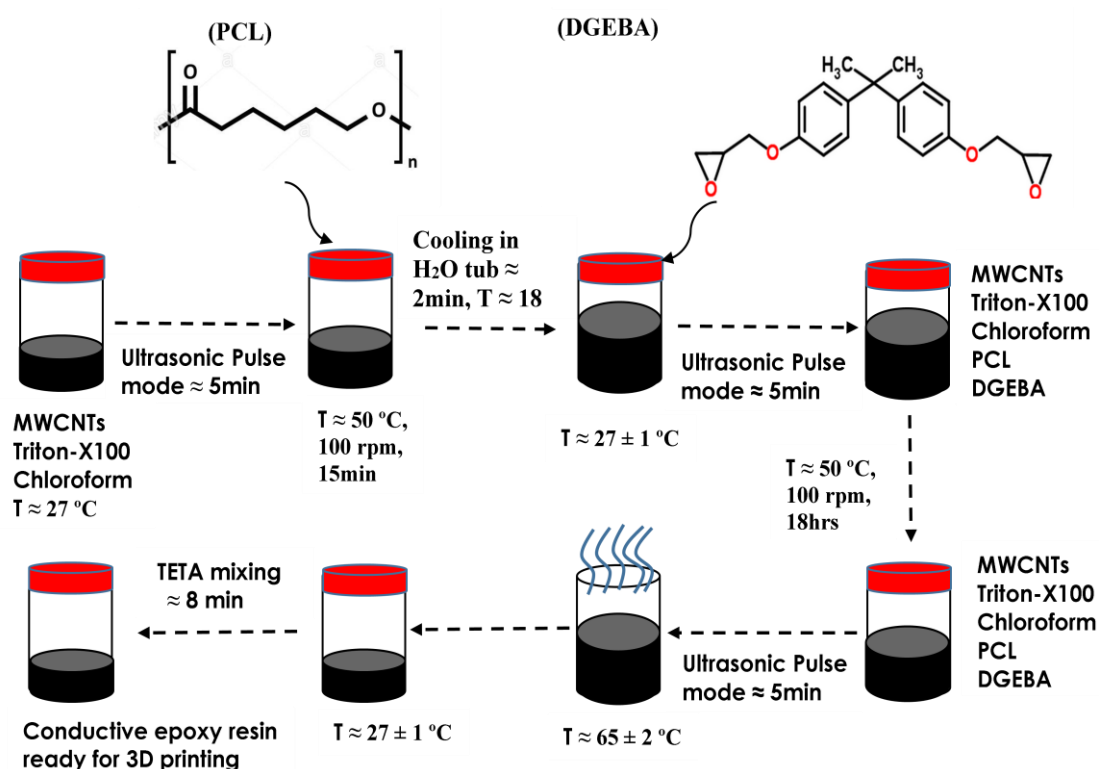


Figure 5.8 Scheme used to prepare the composition for the printing of epoxy-based electrically conductive nanocomposites.

The solution was poured into a ceramic pan and chloroform was allowed to evaporate under the effect of temperature using a heat-stage, mentioned in Ch.3, section 3.9, set at $65 \pm 2^\circ\text{C}$. The visual inspection of the bubble formation in the material is an indication of the presence of the chloroform in the material. It took approximately 8.0 min to evaporate the chloroform from the composition. It becomes a fluffy paste after chloroform evaporated from the material. The material was let to cool at room temperature ($27 - 28^\circ\text{C}$) for 5 min. TETA was mixed to the fluffy paste manually using a spatula. The paste was mixed with TETA manually for 8.0 ± 0.5 min

acquiring homogenous mixing. The syringe carrying material was filled with the help of a spoon and spatula, simultaneously. The scheme of nanocomposite preparation is shown in Figure 5.8. Table 5.2 briefly explains the order of composition used to print samples. Three different compositions were prepared studying effect of % (w/w) MWCNTs, % (w/w) PCL, and % (w/w) TETA. These compositions are prepared to study electrical conductivity variation in 3D printed samples. The results will be presented in a similar order in the results section.

Table 5.2 Description of compositions used to print samples studying electrical conductivity variation.

Formulation	MWCNTs % (w/w)	PCL % (w/w)	TETA %(w/w)
Formulation 1	V	X	X
Formulation 2	X	V	X
Formulation 3	X	X	V

V: Variable parameter, X: constant parameter

5.13 PRINTING OF SAMPLES

In this section, 3D printing of DGEBA resin-based nanocomposites is explained in detail using the nanocomposites preparation scheme mentioned in the preceding section. The samples were printed at room temperature and these were in the form of a viscous paste. The samples were printed at ambient temperature (27 ± 2 °C) and a post-curing was required for solidification. The printed samples were removed from the platform and cured at room temperature (27 ± 2 °C) by placing them on another platform. The samples solidly in 72 hours and these were separated from adhesive tape for further study, which will be discussed in detail in Ch. 6. The route to printing samples is indicated in Figure 5.9. The printing of samples suggested that compositions prepared using 10 % (w/w) PCL with 1.0 % (w/w) MWCNTs offer optimum print quality. Excess loading of either or both of them leads to the printing of samples having a rough texture. The printing itself becomes difficult due to nozzle clogging caused by viscosity rise and inhomogeneous mixing. On the other hand, lower loading of

MWCNTs or PCL also results in rapid curing and material starts to cure in the barrel and jam the nozzle.

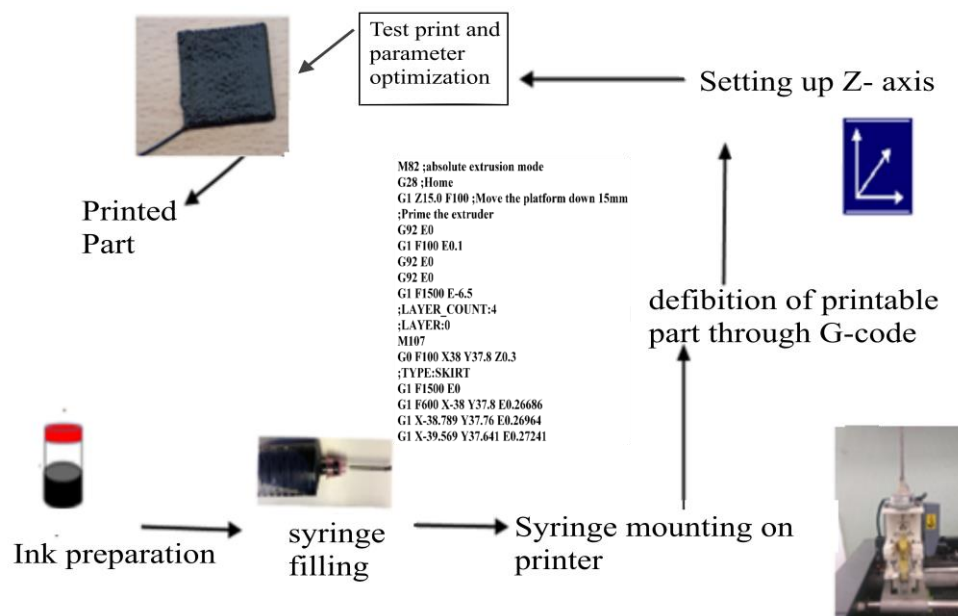


Figure 5.9 The print process flow scheme used to print epoxy-based electrically conductive nanocomposites.

Samples prepared with slightly lower TETA loading resulted in the collapse of material during printing on the platform, which is an indication that less number of reactive sites are available for crosslinking. Square and rectangular shape samples were printed using the nanocomposite ink containing DGEBA resin, PCL, MWCNTs, TETA and Triton X - 100 as a surfactant. The print process flow scheme is shown in Figure 5.10. Variety of compositions were prepared to achieve optimum printing. It is observed that PCL, TETA and MWCNTs when used 10 ± 3 % (w/w), 8 ± 2 % (w/w) and (0.5 - 2) % (w/w), respectively, smooth printing of samples is possible while samples are not printable beyond these limits. Few of the samples printed are shown in Figure 5.9. All samples are printed using a print speed (F) 100 mm/m and extrusion speed (E) 0.1 ± 0.03 mm/m. It is important to mention that the print speed parameter defines the movement of a nozzle that how fast or slow it moves during printing while extrusion parameter controls the flow of material. These numbers are revealed through the printing of a variety of samples. A print speed higher than 100 mm/m deposit less material on stage. This results thinning and dragging of filament on the stage. Because of these effects, filament adhesion to each other becomes an issue during smooth printing. Lower print speed and higher extrusion speed both have a similar effect. A higher amount of material results when the print is slower than (F) 100 mm/m or

extrusion speed increases than 0.1 mm/min . These samples were printed on the surface of an adhesive tape that was on the printing stage during part printing. It facilitates to remove samples from the printing stage after printing. Each sample was removed from the printing stage after passing at least 30 min .

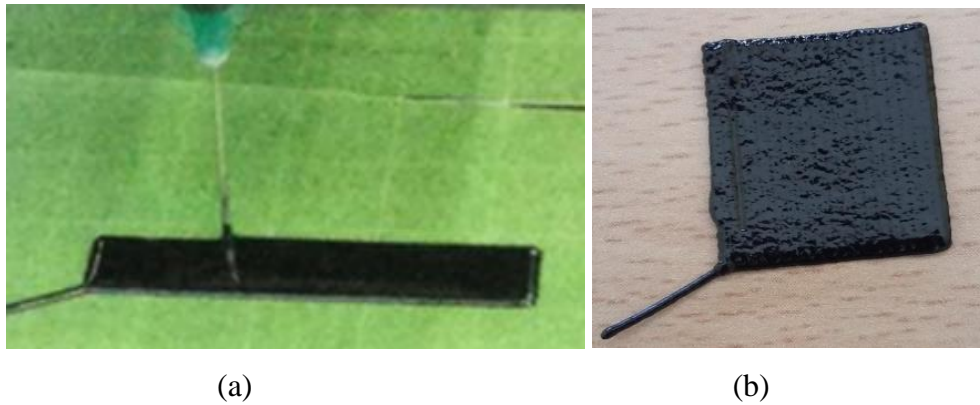


Figure 5.10 Images of 3D printed electrically conductive samples which are printed using the printer mentioned in Figure 5.1 and the material preparation methodology mentioned in Figure 5.8. The composition was based on a DGEBA resin, PCL and MWCNTs. (a) A rectangular sample during printing and (b) the printed and fully cured sample.

5.14 THE WORKFLOW SCHEME

As described above, the printing of epoxy-based nanocomposite predominantly composition dependent. Therefore, the printer system needs to keep in a standby position as prepared composition allow a specific working window (time) for the printing of nanocomposite. The printing process workflow is composed of the following:

- Connecting the PC to the printer via USB cable and plugging in the printer's power supply.
- Starting the Printron application;
- An adhesive tape is used on the platform to avoid material bonding with the platform.
- Loading the syringe with material, plunger, nozzle, and mounting it using the tool; threading the tool leadscrew into the piston nut.
- Defining the desired model through the G-code file using a micro SD card slot or through PC using Printron Package.
- Setting printing nozzle to the home position ($X=0$, $Y=0$)

- Setting offset for Z-axis for an appropriate distance between the printing nozzle and platform.
- Selecting the G-code file from micro SD card through knob and LED display.
- The knob with LED display can be used to increase/decrease the print speed
- In case there is an issue during printing, a pause option can be used from Knob on the printer or through the Printron.
- Once the desired part is printed, it is left for around 30 minutes on the platform for some level of curing. The part is taken off from the platform through removing the adhesive tape and placed on a smooth surface at ambient temperature (27 ± 2 °C).
- Removing syringe right after printing to avoid material sticking against the walls of the syringe and rest of assembly.

5.15 CONSTRAINTS AND LIMITATIONS

Amongst other limitations, the very first things are how big an object the printer can print considering the working window (optimum curing and viscosity) that allows printing parts without nozzle clogging and sticking in the barrel. Nanocomposites samples are printed with maximum dimensions leading to a volume $5 \times 5 \times 0.2 \text{ cm}^3$. Secondly, it is not possible to print objects with syringe gauges larger than G21 (internal diameter = 0.514 mm) due to nozzle clogging. Finally, relatively higher MWCNTs content (more than 2.0 % w/w) leads to imperfect print and nozzle blocking starts to occur which limits smooth printing. On a similar way, PCL loading higher than 10.0 % (w/w) and TETA loading higher than 10.0 % (w/w) becomes a source of nozzle clogging while lower loadings result to layer collapse during printing. This could be a tremendous rise in the viscosity of the material.

5.16 FUTURE UPDATE

Onspot heating the material using a direct laser or source of heat during the print process. It will shorten the long cure time for the solidification of the material. This kind of arrangement demands energy-efficient and regulating heat source. Few changes in assembly side are also desired to mount such a source object.

5.17 CONCLUSION

- A printer system is configured for the printing of epoxy-based composites.
- The study suggests that printing of pure epoxy is not possible, however, the addition of a thermoplastic polymer in a relatively small proportion can help to overcome rapid curing and provide a working window in which material is printable up to a certain extent in terms of printable volume.
- The addition of thermoplastic into thermoset is also critical as phase separation of polymers occur during the printing and limit print process.
- Epoxy-based compositions with the addition of polycaprolactone are printable while compositions contain polystyrene are not printable due to phase separation issue.
- The printer can print small scale volume around 10 cm³.

5.18 REFERENCES

- [1] H. Dodiuk and S. H. Goodman, Eds., *Handbook of Thermoplastics*, vol. 1. California: Elsevier Inc., 2014.
- [2] J. Gotro and R. Bruce Prime, "Thermosets," in *Encyclopedia of Polymer Science and Technology*, no. 2, John Wiley & Sons, Inc., 2017.
- [3] D. Lei et al., "A general strategy of 3D printing thermosets for diverse applications," *Mater. Horizons*, vol. 6, no. 2, pp. 394–404, 2019.
- [4] C. Schmidleithner and Deepak M. Kalaskar, "Stereolithography," in *3D Printing*, Dragan Cvetković, Ed. IntechOpen, 2016, pp. 3–22.
- [5] Paulo Jorge Bartolo, Ed., *Stereolithography Materials, Processes and Applications*. New York: Springer, 2011.
- [6] "RAM System Allows Large-Scale Thermoset 3D Printing - 3D Printing." [Online]. Available: <https://3dprinting.com/3dprinters/ram-system-allows-large-scale-thermoset-3d-printing/>. [Accessed: 04-Feb-2020].
- [7] Olga S. Ivanova, C. B. Williams, and T. A. Campbell, "Additive Manufacturing and Nanotechnology: Promises and challenges," *Rapid Prototyp. J.*, vol. 19, no. 5, pp. 353–364, 2013.
- [8] P. T. Lillehei, J. W. Kim, L. J. Gibbons, and C. Park, "A quantitative assessment of carbon nanotube dispersion in polymer matrices," *Nanotechnology*, vol. 20, no. 32, 2009.
- [9] N. A. Mohd Radzuan, A. B. Sulong, and J. Sahari, "A review of electrical conductivity models for conductive polymer composite," *Int. J. Hydrogen Energy*, vol. 42, no. 14, pp. 9262–9273, 2017.
- [10] C. Min, X. Shen, Z. Shi, L. Chen, and Z. Xu, "The electrical properties and conducting mechanisms of carbon nanotube/polymer nanocomposites: A review," *Polym. - Plast. Technol. Eng.*, vol. 49, no. 12, pp. 1172–1181, 2010.
- [11] L. Chang, K. Friedrich, L. Ye, and P. Toro, "Evaluation and visualization of the percolating networks in multi-wall carbon nanotube/epoxy composites," *J. Mater. Sci.*, vol. 44, no. 15, pp. 4003–4012, 2009.
- [12] S. G. Prolongo, M. R. Gude, and A. Ureña, "The curing process of

- epoxy/amino-functionalized MWCNTs: Calorimetry, molecular modelling, and electron microscopy,” *J. Nanotechnol.*, vol. 2010, 2010.
- [13] “Gantry Systems: Working Outside the Envelope - Macron Dynamics.” [Online]. Available: <https://www.macrondynamics.com/job-stories/gantry-systems-overview>. [Accessed: 04-Feb-2020].
- [14] A. Atala and J. J. Yoo, *Essentials of 3D Biofabrication and Translation*. Elsevier Inc., 2015.
- [15] K. Pusch, T. J. Hinton, and A. W. Feinberg, “Large volume syringe pump extruder for desktop 3D printers,” *HardwareX*, vol. 3, no. February, pp. 49–61, 2018.
- [16] “3D CAD Design Software | SOLIDWORKS.” [Online]. Available: <https://www.solidworks.com/>. [Accessed: 04-Feb-2020].
- [17] “uPrint SE Plus Desktop 3D Printer | Compact and Professional 3D Printer.” [Online]. Available: <https://proto3000.com/product/uprintse/>. [Accessed: 04-Feb-2020].
- [18] “Arduino - Software.” [Online]. Available: <https://www.arduino.cc/en/main/software>. [Accessed: 04-Feb-2020].
- [19] “Arduino programming for beginners.” [Online]. Available: <https://www.hackerearth.com/blog/developers/arduino-programming-for-beginners>. [Accessed: 04-Feb-2020].
- [20] “Most used 3D Printer G-Codes - Commands detailed.” [Online]. Available: <https://3dprinterchat.com/3d-printer-g-codes/>. [Accessed: 04-Feb-2020].
- [21] P. Geng et al., “Effects of extrusion speed and printing speed on the 3D printing stability of extruded PEEK filament,” *J. Manuf. Process.*, vol. 37, no. January, pp. 266–273, 2019.
- [22] K. Al-ahdal, N. Silikas, and D. C. Watts, “Rheological properties of resin composites according to variations in composition and temperature,” *Dent. Mater.*, vol. 30, no. 5, pp. 517–524, 2014.
- [23] X. Luo, R. Ou, D. E. Eberly, A. Singhal, W. Viratyaporn, and P. T. Mather, “A thermoplastic/thermoset blend exhibiting thermal mending and reversible adhesion,” *ACS Appl. Mater. Interfaces*, vol. 1, no. 3, pp. 612–620, 2009.

Chapter 6: Characterization of samples printed through newly designed printer system

6.1 INTRODUCTION

To introduce the designed printer (Ch. 5) as a valid printer system for epoxy-based materials, it is important to characterise printed parts in terms of structure, chemistry and functionality. For the sake of this, square and rectangular shape samples are printed using the printer and material system mentioned in Ch. 5. and Results are presented and discussed in the current chapter. Thermosets are plastics that are irreversibly cured or hardened by cross-linking of polymer chains. The curing process changes the resin into an insoluble polymer network. It is evidenced from preliminary sample printing in Ch. 5 that the inclusion of carbon nanotubes and polycaprolactone to the epoxy system provides a working window in which material is printable. As a consequence of this, samples were printed using compositions with different weight fractions to determine the limiting value of weight fractions in which material is printable without compromising on printing and property of interest (electrical conductivity). In this context, the electrical conductivity is of significance when it comes to an application. Hence, electrical conductivity is studied in printed parts with the variation of compositional entities including carbon nanotubes, polycaprolactone and triethylenetetramine.

The printed samples were characterised in terms of the level of crosslinking, direct current electrical conductivity, alternating current electrical conductivity, structural and morphological characterization, and thermal response of the printed samples. The printed samples were electrically conducting and these were subject to a variety of characterization techniques studying microstructure. In terms of understanding, the results are presented and discussed in an order in which the effect of the concentration of carbon nanotubes is presented in the early part of this chapter. In the second and third part, results are presented with the variation of polycaprolactone and triethylenetetramine, respectively. Discussion of the results, an analogous circuit model and important conclusions from the research will be addressed

in the last part of the article. In short, the chapter presents results obtained through a detailed characterization of the 3D printed sample using epoxy-based matrix material.

6.2 RESULTS AND DISCUSSION

6.2.1 3D printed epoxy-based nanocomposites under the effect of MWCNTs (% w/w) loading

Results are presented in this section for 3D printed DGEBA/PCL material and its nanocomposites containing MWCNTs using verities of techniques. Results are presented in this section and discussed characterising 3D printed samples under the effect of variation in MWCNTs (% w/w).

Chemical analysis of 3D printed samples

PCL is used in the epoxy/PCL/MWCNTs nanocomposites acquiring optimum print quality. It is considered important studying mid Fourier transform infrared spectrum (FTIR) of PCL before going towards a detailed analysis of the nanocomposites. This can help to locate significant functional groups present in the nanocomposites. The FTIR spectra of PCL is shown in Figure 6.1 with designated prominent absorption peaks. These peaks appear in the spectrum around 1200 cm^{-1} , 1300 cm^{-1} , 1800 cm^{-1} , and $(2850 - 2950)\text{ cm}^{-1}$ and these are related to C-O stretching vibration in gauche conformation, (C-O and C-C) stretching in the crystalline phase, C = O stretching of carbonyl belonging to an aliphatic ester and CH_2 symmetric and asymmetric stretching, respectively [1].

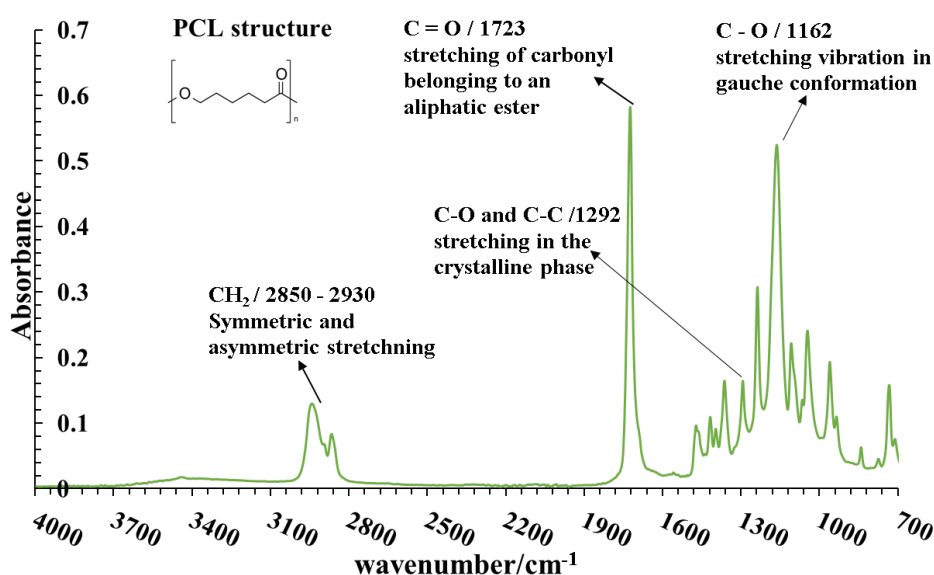
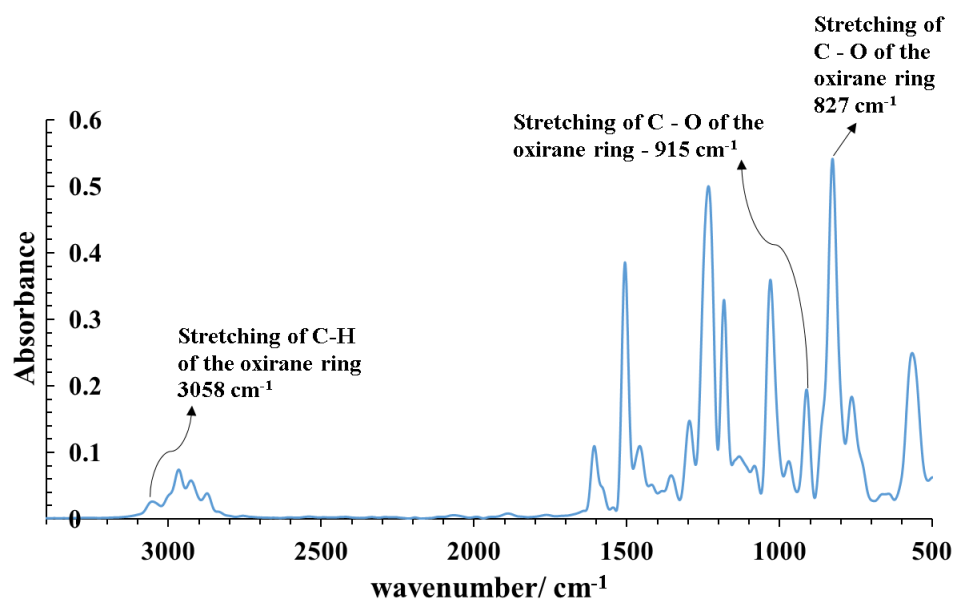
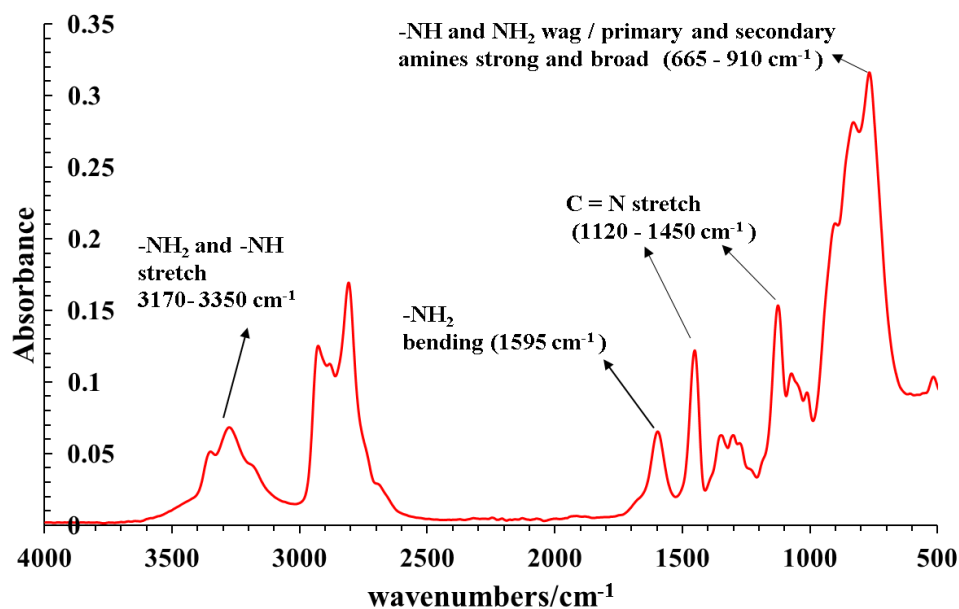


Figure 6.1 FTIR spectra of PCL that is used in the study with significant absorption peaks.

Characterization of DGEBA epoxy using FTIR spectrum involves the location of the oxirane ring bands. Table 6-1 shows the assignation of significant bands for the DGEBA resin in the mid-infrared range using the spectrum given in Figure 6.2(a). The C-O deformation band of oxirane group is centered at 915 cm^{-1} and 826 cm^{-1} while C-H stretching of terminal oxirane group is observed at 3050 cm^{-1} in DGEBA resin [2]. There is also a band corresponding to the ether linkage located at 1031 cm^{-1} .



(a)



(b)

Figure 6.2 FTIR spectra of (a) DGEBA resin and (b) TETA reagent or hardener used in the current study.

Figure 6.2 (b) shows FTIR spectra for TETA. TETA is used as a reagent or crosslinker for DGEBA epoxy resin. In the mid-FTIR range, the bands of significance are primary and secondary amines. There are differences between the absorptions of primary and secondary amines. The aliphatic primary amines (NH_2) stretch in the region $3400\text{--}3000\text{ cm}^{-1}$ [3]. These bands are weaker and sharper than those of the alcohol O–H stretches which appear in the same region [4]. Specifically, there are two bands in this region, the asymmetric and the symmetric NH_2 stretch. These overtones are located at 3350 cm^{-1} and 3280 cm^{-1} [5], respectively, being the symmetric more intense. Also, the emergence of a shoulder is evident around 3180 cm^{-1} towards a low-frequency side of the symmetric NH_2 stretch [5]. This shoulder is attributed to the first overtone of NH_2 scissoring enhanced by Fermi resonance interaction with the NH_2 symmetric stretching mode [6]. Secondary amines (NH) show only a single weak band in the $3300\text{--}3000\text{ cm}^{-1}$ region, as they have only one N–H bond. Tertiary amines (-N) do not show any band in this region since they do not have an N–H bond. The bending vibration of primary amines (NH_2) is observed in the region $1650\text{--}1580\text{ cm}^{-1}$ [4]. Specifically, the bending vibration of primary amines (NH_2) is observed at 1595 cm^{-1} . Usually, secondary and tertiary amines do not show a band in this region [4]. The C–N stretching vibration of aliphatic amine is observed as medium or weak bands at $1450\text{--}1120\text{ cm}^{-1}$ wavenumbers. Another band attributed to amines is observed in the region $910\text{--}665\text{ cm}^{-1}$. This strong, broadband is due to N–H wag and observed only for primary and secondary amines [4]. The results are summarised in Table 6-1. The stoichiometry information regarding the reactivity of the DGEBA-based epoxy resin with Triethylenetetramine indicates that it progresses by the reaction of its epoxide groups through blocking, coupling, branching, and crosslinking through bonding reactions with the amine groups [7]. Triethylenetetramine molecules react with the epoxide group via the transformation of the hydrogen atom of the amine functionality and this reaction proceed until all amines have reacted with the epoxide group. The curing behaviour of DGEBA epoxy resin with TETA is briefly described in Ch3. Section 3.3.2. The TETA molecule can link as many as six DGEBA molecules discussed by [7]. It was reported that at different resin/hardener ratios, the changes in the relative ion intensity of the ions were indicative of the unreacted and partially reacted hardener molecules, which were proportional to the hardener concentration [8]. The crosslinking reaction progresses through the initial steps of coupling and branching reactions. The final network structure and density depend greatly on the

conversion process of coupling and branching into crosslinking, which in turn depends on the overall curing reaction conditions [7]. The addition of monomers into a mixture leading to increases molecular weight and forming a molecule through the process of attachment on active ends of a chain.

Table 6-1 Significant vibrational frequencies observed in the DGEBA and TETA spectrum.

Material	Peak position/ cm ⁻¹	Assignment
DGEBA	3058	Stretching of C-H of the oxirane ring
	2968 - 2875	Stretching C-H of CH ₂ and CH aromatic and aliphatic
	1606	Stretching C = C of aromatic rings
	1507	Stretching C - C of aromatic rings
	1031	Stretching C-O-C of ethers
	914	Stretching of C-O of oxirane group
	827	Stretching of C-O of oxirane group
	766	Rocking CH ₂
T E T A	3380–3180	3350 -NH ₂ Asymmetric stretch (primary amine) 3280 -NH ₂ Symmetric stretch (primary amine) 3180 -NH stretch (secondary amine)
	1100 -1650	1595 -NH ₂ bending (primary amine)
		1120, 1450 C- N Stretch
	910-665	765 -NH and -NH ₂ wag

The overall kinetics of the reaction depends on the concentration of four species: Oxirane ring, primary, secondary, and tertiary amine [2]. Therefore, quantification of crosslinking can be done by observation of concentration of these four species using IR spectroscopy. The curing reaction between DGEBA resin and TETA hardener results in a decrease in the concentration of functional group associated with the monomer and the progress of the reaction can be determined by observing relative intensities of absorption peaks [9]. Figure 6.3 shows FTIR spectra of DGEBA resin with and without curing with TETA and the epoxy/PCL/MWCNTs nanocomposites.

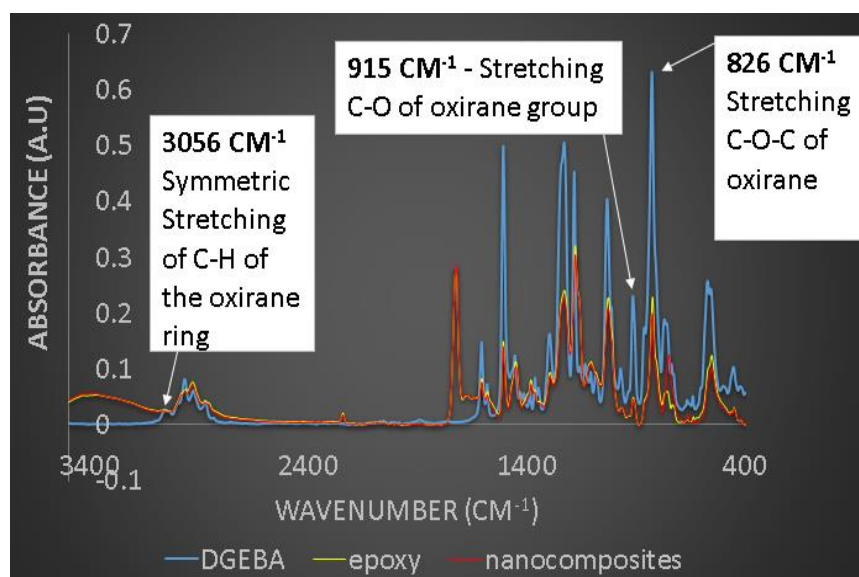


Figure 6.3 FTIR spectra of DGEBA resin and DGEBA resin after reaction with TETA in the absence (epoxy) and presence of MWCTs (nanocomposite). The arrows indicate significant relevant vibrational modes in the oxirane group with peak positions.

Prominent peaks are highlighted in these spectra. A clear decrease in the epoxy peak, at 915 cm^{-1} , confirms the polymerization of DGEBA resin caused by TETA monomer in the presence of PCL and MWCNTs. In literature, different researchers use different epoxy peaks for the sake of this calculation. The reference peaks reported in the literature for the quantitative analysis of the oxirane ring include 830 cm^{-1} [10], 1183 cm^{-1} [11]–[13], and 1509 cm^{-1} [10], [14]. All these peaks are a stable aromatic ring. In the mid-IR region, 915 cm^{-1} is the most commonly used peak which is assigned to C – O stretching vibration in the oxirane ring [10], [15]. Peak 915 cm^{-1} is a sharp, well separated and clear from rest of the peaks in the fingerprint region. Therefore, it is preferably used in comparison to the aforementioned reference peaks. In the current work, 915 cm^{-1} is considered as an epoxy peak with 1183 cm^{-1} as a reference peak for the quantification of crosslinking of DGEBA resin and TETA hardener in the presence of MWCNTs and PCL. In general, vibrational bands are shifted by an H-bond toward a lower frequency when the sample state changes from a dilute solution to pure condensed phase [5].

A quantitative analysis is performed on these peaks and results are presented in Figure 6.4 under the effect of MWCNTs % (w/w) for 3D printed nanocomposite using additive manufacturing. Results indicate that the amount of epoxy conversion reduces as the carbon nanotubes increased in the composition.

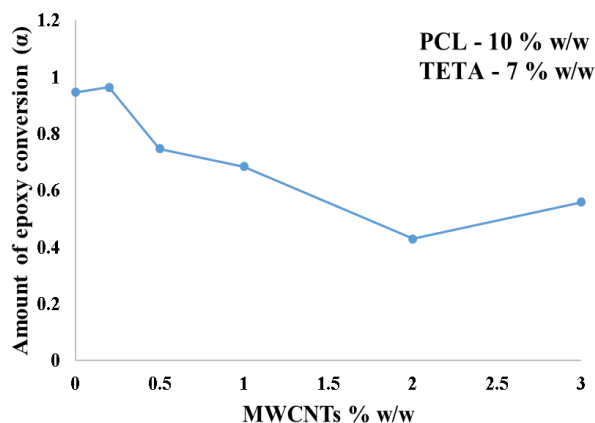


Figure 6.4 The parameter α (amount of epoxy conversion) is calculated using the FTIR spectrum from 3D printed samples and it is plotted against variation in MWCNTs (% w/w).

This indicates that a relatively higher amount of carbon nanotubes hinder or restrict the mobility of monomers due to which it will take a longer time to cure the epoxy resin [16]. The literature suggests that the degree of carbon nanotubes dispersion and viscosity are primarily responsible for the cure kinetics of epoxy-based nanocomposite. Also, heterogeneous composites and high viscosity have a greater effect on slowing the cure of the epoxy resin and reduce the curing heat of the reaction [17]. The final cure characteristics of epoxy nanocomposites are controlled by the competition of the viscosity-increasing effect and the heat-sink effect of carbon nanotubes. The accelerating or decelerating effect of carbon nanotubes on the curing process depends on carbon nanotubes content, its aspect ratio and temperature of isothermal cure [16].

Electrical characterization

DC electrical conductivity

The DC electrical conductivity is calculated in 3D printed nanocomposite (epoxy/PCL/MWCNTs) samples and the results are shown in Figure 6.5. A rise in the DC electrical conductivity is for 3D printed samples in the DGEBA based epoxy resin containing different loadings of carbon nanotubes. A five-order increase in electrical conductivity is obvious with 0.5 % (w/w) MWCNTs loading. As there is no appreciable, electronic current measured for compositions below 0.5 % (w/w) MWCNTs, therefore, 0.5 % (w/w) MWCNTs is considered as percolation threshold. The critical content of MWCNTs, at which a transition occurred from an insulator to a conductor, is commonly termed as the electrical percolation threshold [18].

Percolation threshold was measured through extrapolating line of best fit towards the horizontal axis (Figure 6.5(a)). The intercept on the horizontal axis is considered as percolation point or threshold value for percolation of MWCNTs into the epoxy/PCL matrix. A percolation threshold of 0.21 was measured from the analysis. The critical values of dimensionality (t) is calculated as 2.7 considering a percolation threshold 0.21. Literature suggests 3D percolating networks typically correspond to the empirical critical exponent of dimensionality values ranging between $1.5 \leq t \leq 11$ [19] for random distribution of nanotubes into polymer-based nanocomposite.

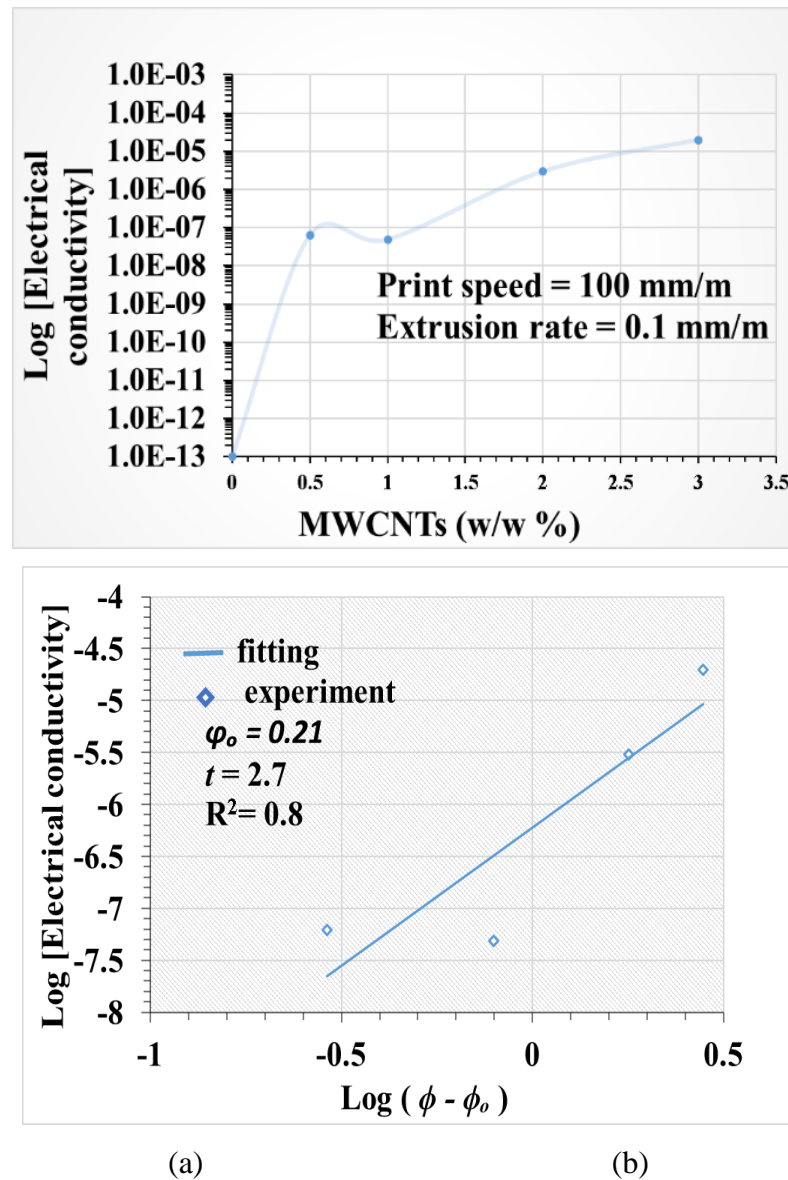


Figure 6.5 (a) A semi-log plot of a DC electrical conductivity is presented for 3D printed samples prepared using nanocomposites (DGEBA/PCL/MWCNTs) with the variation in MWCNTs (% w/w), (b) corresponding log-log plots of the DC electrical conductivity.

The deviation of the critical exponent can be attributed to some parameters e.g. the composition of the composite system, the type of the conduction mechanism, the difference between a perfect lattice of inclusions and a real polymer–particles system (orientation, aspect ratio), the degree of dispersion of the filler, the method of fabrication etc. Polymer matrix kinetics and interactions between phases as well as between conductive particles are some of the reasons that constitute this discrepancy in the critical exponent [20]. The value of critical exponent determined using plot in Figure 6.5(b) strongly supporting the existence of three-dimensional (3D) percolating conductive networks of MWCNTs permeating in the host matrix [21], [22]. Two possibilities exist for compositions (0.2 % w/w and 0.3 % w/w) below 0.5 % (w/w) MWCNTs for not having measurable electronic current; (1) there is a percolation of MWCNTs but the magnitude of electric current is below the detection limit of the measuring unit, (2) MWCNTs are not able to form percolative pathways leading to non-conductive pathways. Percolation pathway can be considered as an electrically conductive channel in which charges transport from once MWCNT to another nearby MWCNT through tunnelling phenomenon [22], [21] under a suitable external bias. The classical percolation theories have been proposed in different studies, which essentially examine the formation of conductive pathways inside the polymer matrix in the form of uninterrupted clusters of connected carbon nanotubes [23]. Above the percolation threshold, a higher amount of current, at relatively low voltage, suggests an Ohmic-type behaviour for samples printed at room temperature. The composition prepared with 2.0 % (w/w) MWCNTs is considered an upper limit to achieve optimum print quality accompanied by an eight-order increase in electrical conductivity. Both, preparation of compositions and printing of samples, are quite challenging when MWCNTs are used higher than 2.0 % (w/w). This happens due to a tremendous rise in viscosity. These samples take a relatively long time to cure. Optimum print quality is achieved for samples with MWCNTs concentration of 1.0 % (w/w).

Effect of print direction on DC electrical conductivity

In some of the cured sample, electrical conductivity is calculated along and normal to the print direction. This can help to understand whether or not the extrusion process itself can affect the electrical conductivity. Figure 6.6 is used to show the results of the samples. Electrical conductivity is relatively higher along the print direct

when calculated against the print direction. This indicates that the flow direction of the material has an effect on the network of MWCNTs along and normal to print direction.

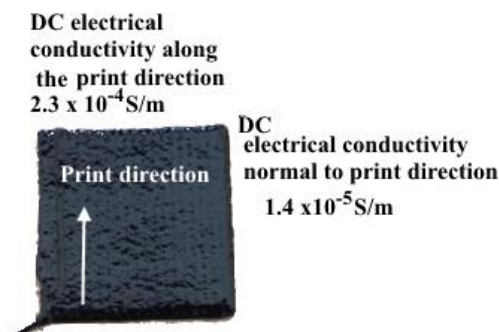


Figure 6.6 Electrical conductivity behaviour in 3D printed nanocomposite sample containing 1.0 % (w/w) MWCNTs along and normal to print direction. The samples are printed using the following print conditions $F = 100$ mm/m and $E = 0.1$ mm/m.

The print process can facilitate to align MWCNTs up to a certain extent due to which the electrical conductivity increases in the nanocomposites. Since epoxy is an amorphous material, the other possibility is the PCL lamellar organization which affect the overall networks of MWCNTs in the printed samples.

Broadband dielectric spectroscopy analysis

The frequency response of 3D printed nanocomposite material is studied using broadband dielectric spectroscopy. For these experiments, samples are selected based on smooth surface acquiring reasonable contact with the electrodes. The outcome of the experiments reveals information about the complex AC electrical conductivity, complex impedance, complex dielectric constant of the material under the effect of frequency and alternating voltage. These are discussed thoroughly in the following subsections.

AC electrical conductivity measurement

The real component of complex AC electrical conductivity is measured as a function of frequency for different loading of MWCNTs and the results are shown in Figure 6.7. It increases with MWCNTs (% w/w) loading. A five - order increase in AC electrical conductivity is measured in 3D printed nanocomposite samples using 2.0% (w/w) MWCNTs compare to epoxy/PCL samples. It is evident from the plot that AC electrical conductivity increases with frequency and it converges at relatively high frequency (1×10^6 Hz) for 3D printed nanocomposite samples.

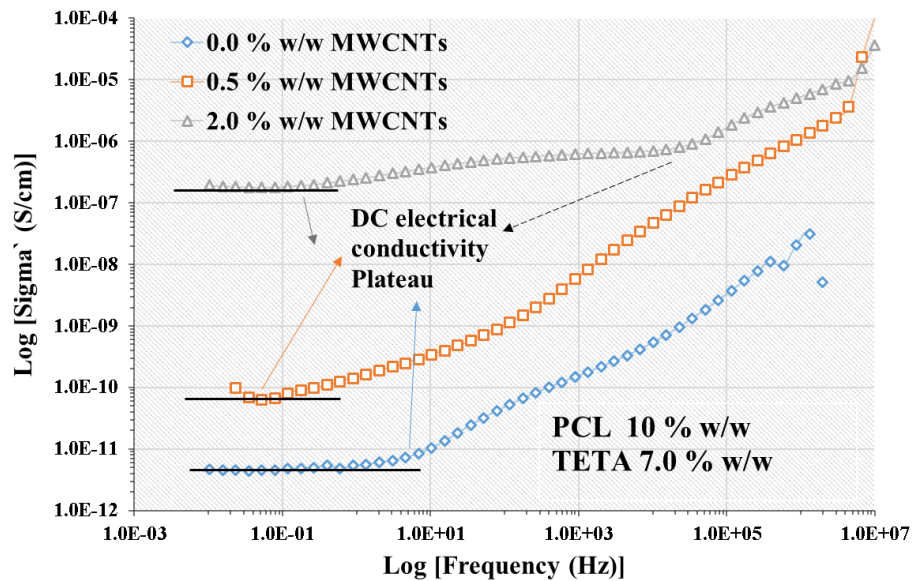


Figure 6.7 Plot indicating frequency response of AC conductivity in 3D printed samples with an increase in MWCNTs (% w/w) loading. These samples are printed using $F=100$ mm/m and $E=0.1$ mm/m.

The analysis of plots in Figure 6.7 suggests that the real part of the complex AC electrical conductivity becomes frequency independent in the low-frequency region ($<10^4$ Hz) and it is identified as the DC conductivity of the sample under test. This is particularly the case for samples printed using 2.0 % w/w MWCNTs. Solid lines are drawn on AC electrical conductivity plots disclosing the DC electrical conductivity plateau. The DC electrical conductivity plateau becomes prominent in the samples printed using 2.0 % (w/w) MWCNTs as compare to samples using 0.5 % (w/w) MWCNTs. This indicates that the frequency region of constant conductivity extends to higher frequencies with increasing weight fraction of MWCNTs. Not much literature is available studying nanocomposites (epoxy/PCL/MWCNTs) for the sake of comparative study. The levelling of the conductivity (plateau formation) is representative of the DC conduction due to a gradually forming network of nanotubes embedded within the matrix. However, for low filler fraction, many isolated nanotubes are still acting as nano capacitors, thus for a certain frequency f_0 , the capacitive behaviour (frequency-dependent) becomes more important than the DC transport [24]. Hence, results are compared from the nanocomposites prepared using carbon nanotubes into either PCL or epoxy polymer. Similar kind of AC electrical conductivity is reported in the literature for the preparation of nanocomposites using carbon nanotubes as electrically conductive nanostructures [25]. The frequency dependence of the alternative current electrical conductivity follows a power-law

behaviour. The *AC* electrical conductivity (real part) is related to *DC* electrical conductivity through Eq. (6.3) [26], in a material as a contribution from both of them.

$$\sigma'(f) = \sigma_{DC} + A.(f)^s \quad (6.3)$$

Where $\sigma'(f)$ is the angular frequency, σ_{DC} is the frequency-independent part of conductivity or *DC* conductivity ($f \rightarrow 0$), A is the constant dependent on temperature T , and s is an exponent dependent on both frequency and temperature with values in the range 0 - 1. This type of behaviour is referred to as a universal dynamic response [27] because of a wide variety of materials that displayed such behaviour. The value of σ_{DC} can be estimated from the plateau values in the plot of *AC* conductivity. A power law can be observed in the *AC* electrical conductivity plot beyond the critical frequency for a 3D printed sample prepared using 2.0 % w/w weight fraction of MWCNTs. The definition of the critical frequency proposed by [28] and it can be determined such that $\sigma_{AC}(\omega) = 1.1\sigma_{DC}$. It is applied to the frequency-dependent conductivity curves reported in Figure 6.7 and the extracted parameters are tabulated in Table 6-2. The value of s is in the range what was reported from other studies [24], [28], [29].

Table 6-2 Parameters describing charge transport in 3D printed epoxy-based nanocomposites.

MWCNT Loading (%w/w)	σ_{DC}	F_c	s	A
0	6.6E-12	3.05	0.61	3.34288E-13
0.5	6.8E-11	7.94E-02	1	8.56423E-11
2	0.0000002	2.68E-01	0.71	5.09395E-08

It has been shown that a power-law behaviour with $0.7 < s < 1.0$ is a characteristic of the hopping phenomenon in a disordered material where hopping charge carriers are subject to spatially random and varying energy barriers [29]. This agrees well with the fluctuation induced tunnelling model where the nanotube – nanotube barriers vary due to local random temperature fluctuations [28]. The results from this analysis indicate that σ_{DC} and F_c increase with weight fraction of MWCNTs at room temperature. These observations are in agreement with the experimental results reported in other studies using carbon nanotubes for the preparation of nanocomposites, suggesting that the nature of the polymer matrix is not essential in the transport properties.

Effect of delay time between successive sample printings on the AC electrical conductivity

Figure 6.8 shows the frequency response of AC electrical conductivity in the nanocomposite samples printed one after other containing 0.5% MWCNTs. An order decrease in the AC electrical conductivity is measured in the sample printed after the first sample for the same composition and print conditions in the whole frequency range. Even though, the electrical conductivity increases linearly with frequency but it is segmented into two gradients. This is possibly caused by the relaxation of material. The feed rate and extrusion rate were used as 100 mm/m and 0.1 mm/m, respectively. The conductivity

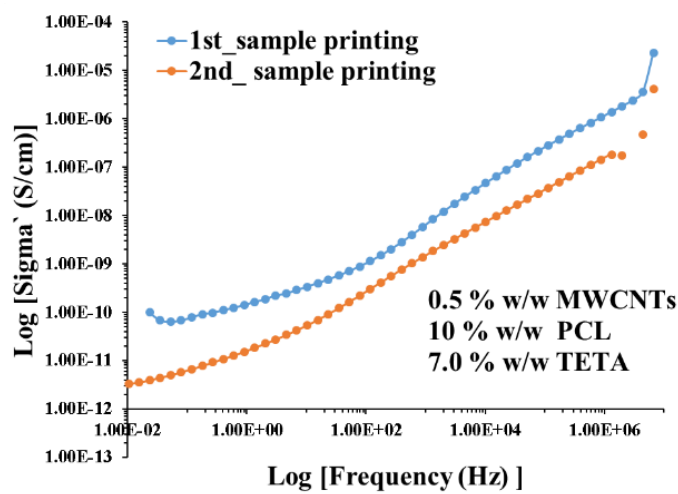


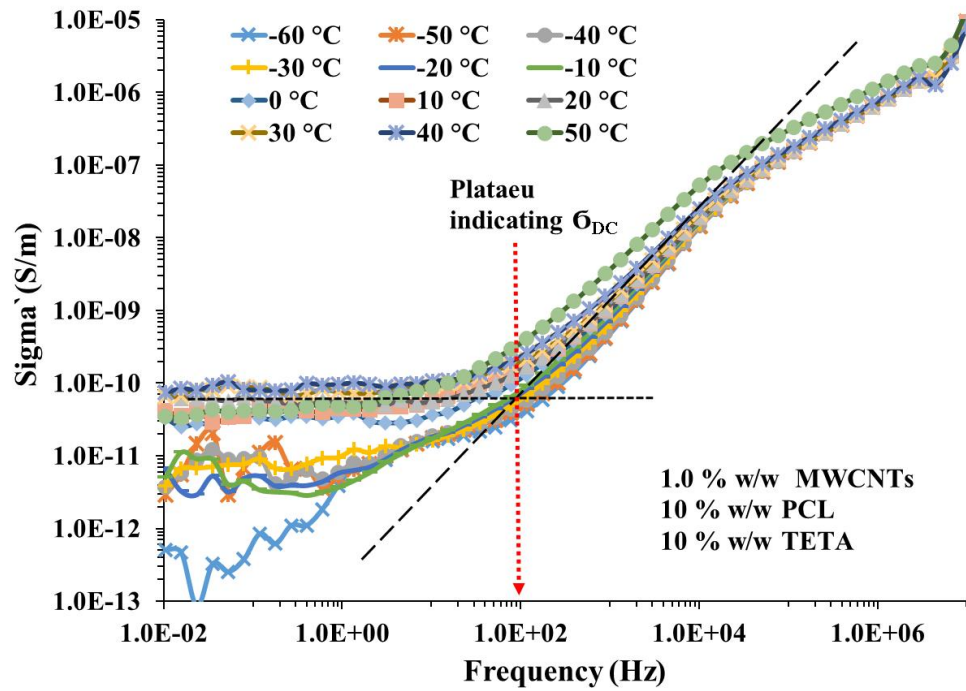
Figure 6.8 Plot indicating frequency response of AC conductivity in 3D printed samples with an increase in MWCNTs (% w/w) loading. These samples are printed using $F = 100 \text{ mm/m}$ and $E = 0.1 \text{ mm/m}$.

Effect of temperature on the AC electrical conductivity

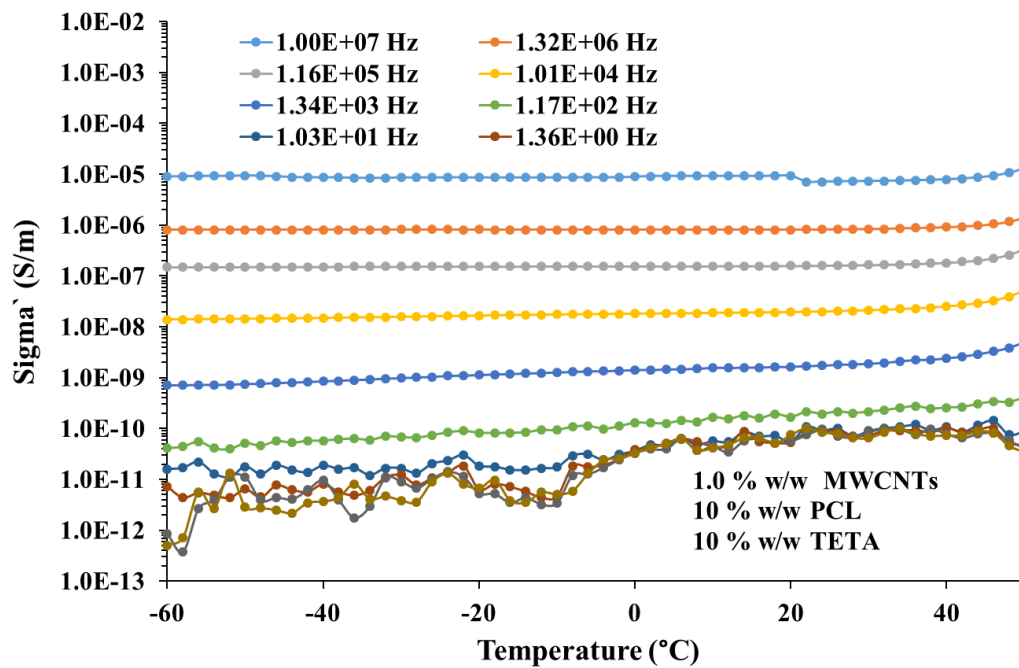
The frequency response of the AC electrical conductivity is measured under the effect of temperature and results are highlighted in Figure 6.9. It is obvious from the plots that the dependence of the electrical conductivity with frequency exhibits three distinct regions, associated with different dissipating effects [30]. An increase of AC electrical conductivity σ' (real part) is observed with the temperature at low frequencies, which can be regarded as low frequency- region. The range of low-frequency region can be assigned as $10^{-2} - 10^2 \text{ Hz}$ taking into consideration the levelling off conductivity. The AC electrical conductivity exhibits a levelling off or a plateau in this frequency region. The plateau is a representative of the direct electronic current conduction due to the formed network of nanotubes dispersed within the epoxy/PCL matrix [31]. The solid black lines are used to show DC electrical

conductivity plateau separating frequency-dependent and frequency independent response in 3D printed samples. Therefore, the conductivity can be considered as the *DC* electrical conductivity in the low-frequency region as it is frequency independent in this region. The dotted lines are used to show *DC* electrical conductivity plateau separating frequency-dependent and frequency independent response in 3D printed samples. It is important to emphasize that the low-frequency region starts appearing in a relatively high-temperature region, specifically above 0 °C. The *DC* electrical conductivity increases significantly with increasing temperature. The intermediate region can be considered between the boundaries of low frequency region and high frequency region. The range of this region is considered as $10^2 - 10^5$ Hz. The conductivity starts to evolve with temperature towards relatively high frequencies. The third region is beyond intermediate frequency region towards following high frequency region and this is considered as high frequency region. In high frequency region, the conductivity obeys the universal dielectric response law, which is a characteristic of a capacitive behaviour [31]. Figure 6.9 indicates that frequency has a significant effect on AC electrical conductivity compared to temperature [26] and the temperature effect is relative to less significance at frequencies higher than 10 M Hz. There is a clear rise in the *DC* and the AC electrical conductivity in the low-frequency region (< 100 Hz) and high-frequency region, respectively, under the effect of temperature. However, the order of increment in the *DC* electrical conductivity is relatively higher than AC electrical conductivity under the effect of a rise in temperature. The interpretation of this increase in the electrical conductivity could be the rearrangement of MWCNTs and charge carriers present in the PCL matrix. Carbon nanotubes are present in the PCL as well as epoxy matrix considering a mixture of epoxy/PCL for the preparation of nanocomposite. The application of temperature oppositely affects the epoxy and PCL. The increase in temperature results in the curing (solidify) of epoxy if there exists unreacted Triethylenetetramine while PCL melts in the nanocomposite. The melting of PCL allows the trapped MWCNTs to rearrange themselves under the effect of temperature rise. The MWCNTs in a PCL matrix can now interact with nanotubes in their neighbourhood and form new networks. These networks are relatively stable which can be observed in the low-frequency region under the effect of increased temperature. Segments of the PCL chains started to move under the effect of an increased temperature thereby releasing the trapped charges. The release of trapped charges is intimately associated with molecular motions. The

increase in the electric current with temperature is attributed to two main parameters, charge carriers and mobility of these charges [32].



(a)



(b)

Figure 6.9 (a) Plot indicating frequency response of AC conductivity in 3D printed samples with the rise in temperature and (b) Plot indicating temperature response of AC conductivity in 3D printed samples with frequency. These samples are printed using $F = 100$ mm/m.

Dielectric constant measurement

The dielectric constant represents the polarization response of a material to an electric field [33] and it is studied in 3D printed nanocomposites (epoxy/PCL/MWCNTs) containing MWCNTs. The real and imaginary parts of the dielectric constant of 3D printed samples with and without MWCNTs are shown in Figure 6.10(a, b). The real and imaginary parts of the dielectric constant increase with MWCNTs loading. Moreover, the real part of dielectric constant increases one order of magnitude for an addition of 0.5 % (w/w) MWCNTs and four orders of magnitude for 2.0 % (w/w) MWCNTs compare to epoxy/PCL samples. The effects of the nanotubes on the dielectric constant of the nanocomposite are based on their effect on the polarization process. These results indicate that the polarization of the inner electric dipole in dielectrics was unable to keep pace with the change at high frequency [34].

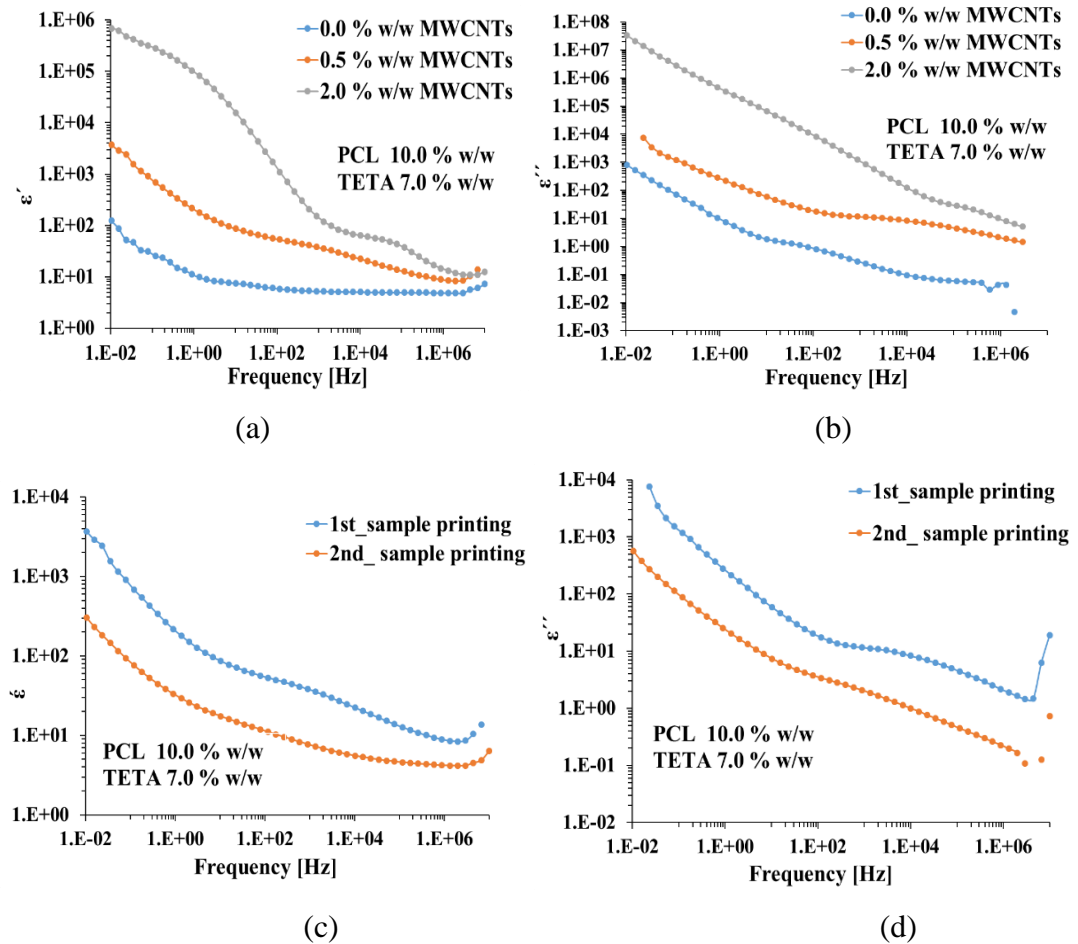


Figure 6.10 Dielectric response of 3D printed samples; (a, c) Real part of dielectric constant, (b,d) imaginary part of dielectric constant in 3D printed samples with different loading of MWCNTs (% w/w) and for two samples printed one after the other using same composition, respectively. These samples are printed using $F = 100 \text{ mm/m}$ and $E = 0.1 \text{ mm/m}$.

Therefore, the polarization gets weaker due to which the dielectric constant rapidly decreases in the high-frequency region. For heterogeneous polymers, there are electronic, atomic, orientation and interfacial polarization. Both the conductivity of the tubes and the interface adhesion between the tubes and epoxy determined the electric response of the composites [33]. On the other hand, real and imaginary parts of dielectric constant decrease at relatively higher frequencies following the regular rules of polarization relaxation [35].

Similar results are obtained for samples printed one after the other using the same composition. The real and imaginary part of the dielectric constant for these samples are shown in Figure 6.10(c, d). The literature suggests that carbon nanotubes based nanocomposites show high-frequency dependence [33]. It is considered that the frequency dependence of the dielectric constant of the MWCNTs composites comes from three effects, i.e. the dispersion of MWCNTs in a polymer matrix, the polarizability between isolated various MWCNTs aggregates, and the anomalous diffusion within aggregates [36].

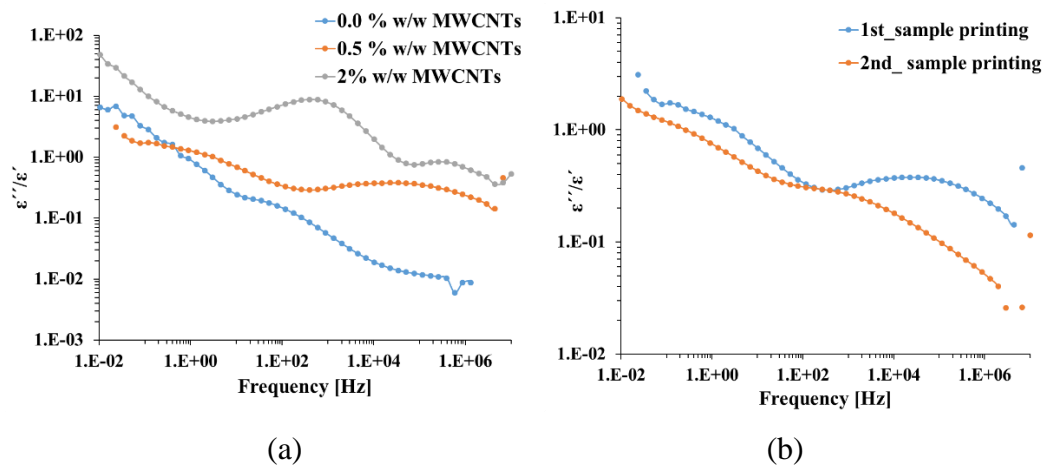


Figure 6.11 Dielectric response of 3D printed samples; the ratio of imaginary to the real part of dielectric constant in 3D printed samples with (a) different loadings of MWCNTs (% w/w), (b) repetition of printing using the same composition for two samples. These samples are printed using $F = 100$ mm/m and $E = 0.1$ mm/m.

Under the effect of an electrical field, the charges move inside the MWCNTs aggregates according to the direction of the electrical field in each half-cycle. Charges accumulate in the interfacial boundaries between MWCNTs aggregates and epoxy, and a dipole moment is imparted to a whole cluster for an isolated aggregate [33]. There are some relaxation modes evident in the real and imaginary part of dielectric constants. The ratio between the real and imaginary parts is calculated and it is plotted

against the frequency to visualise the relaxation modes clearly in the printed samples. Figure 6.11(a, b) shows plots of the ratio between the real and imaginary parts under the effect of MWCNTs loadings and for samples printed one after the other using the same compositions and print conditions. The broad peaks in Figure 6.11(a, b) shows relaxation modes due to dipoles. Two dielectric relaxation modes are revealed in the ratio plots for nanocomposites compare to epoxy/PCL sample. These relaxation modes are related to the presence of dipoles in the nanocomposites. It will be a lot easier for a dipole to follow an oscillating electric field compared to a crystal [37]. This indicates that the presence of relaxation modes in the nanocomposites (epoxy/PCL/MWCNTs) belong to epoxy monomers without a significant contribution from PCL, being semicrystalline.

Impedance measurement

The impedance of 3D printed samples is measured and the data is plotted in the form of Nyquist plot. Figure 6.12 shows Nyquist plots obtained for epoxy/PCL and its nanocomposites containing 0.5 % w/w and 2.0 % w/w MWCNTs. A semicircle is obtained for epoxy/PCL sample which changes to a linear for lower loading of MWCNTs (0.5 % w/w) and it splits into two semicircles for relatively higher loading of MWCNTs (2.0% w/w). The semicircle is a characteristic of a material having a single time constant (τ). The time constant is a measure of the delay in an electrical circuit resulting from either an inductor and resistor or capacitor and resistor [38] and it is given in Eq. (6.4)

$$\tau = RC = L/R \quad (6.4)$$

The single-time constant is a time for the voltage to decay to $1/2.72$. From this analysis, it is obvious that there is one time constant for epoxy/PCL sample while two-time constants exist for nanocomposites printed with 2.0 % w/w MWCNTs. Besides, the diameter of the semicircle represents the overall resistance of the material [39] which is the case for the sample printed using epoxy/PCL material. In the nanocomposites containing 2.0% w/w MWCNTs, the first semicircle at a lower frequency can be assigned to the bulk resistance of the nanocomposite material while the second semicircle at a higher frequency can be assigned to the interface resistance [39]. Another important result from these plots is the value of impedance in the lower frequency region. The impedance of the nanocomposite decrease one order with 0.5 % (w/w) loading of MWCNTs and it decreases to nearly four orders of magnitude for

2.0% (w/w) MWCNTs. These results indicate that the impedance of the nanocomposites decreases with the increase in MWCNTs loading. Such kind of behaviour is also reported in other studies [40]. A difference in the impedance is also observed in the low-frequency region for 3D printed samples printed one after the other using the same composition and print conditions.

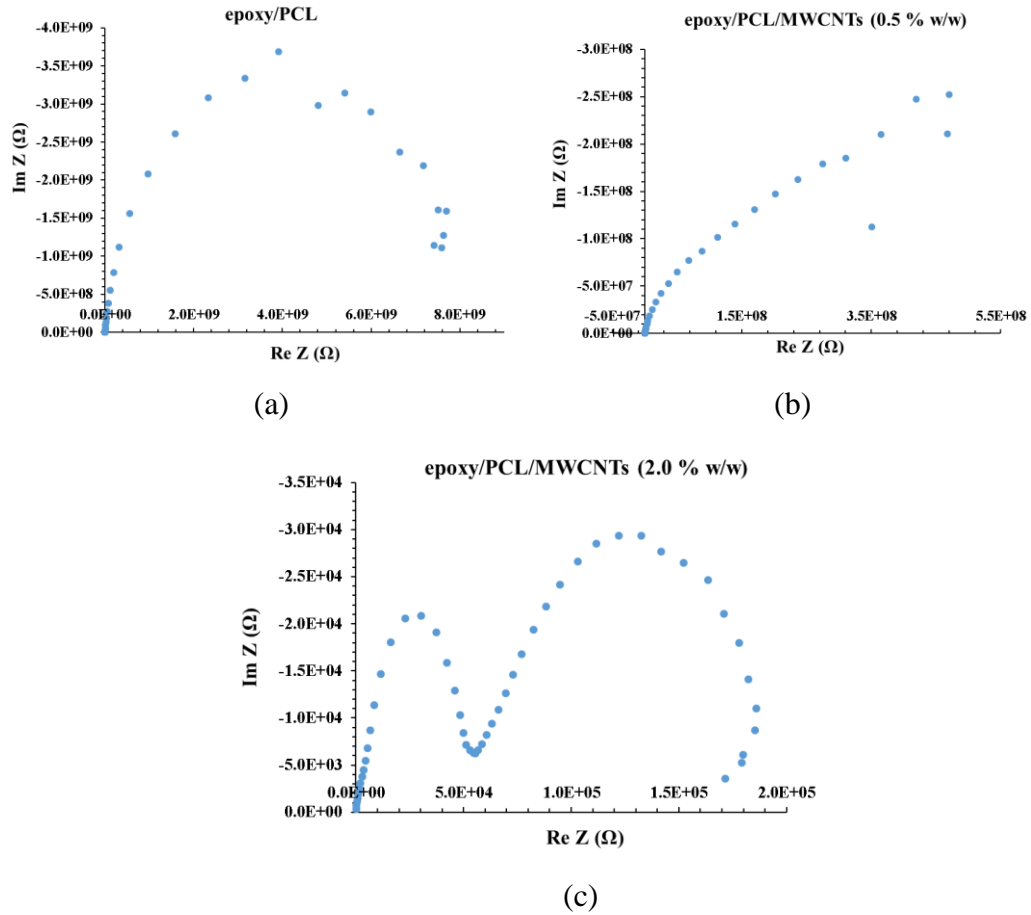


Figure 6.12 Real, imaginary and ratio of imaginary to the real part of dielectric constant, respectively, in 3D, printed samples (a) with the loading of MWCNTs and (b) with repetition of printing. These samples are printed using $F = 100 \text{ mm/m}$ and $E = 0.1 \text{ mm/m}$.

Figure 6.13 shows the Nyquist plots obtained from the impedance data for these samples. The magnitude of the impedance is nearly a straight line. However, an order of increase is observed in impedance for the sample printed after a period using the same composition and print conditions. This can be happened either due to curing or inhomogeneous distribution of MWCNTs. These plots indicate a typical capacitive response of the material with 0.5 % w/w loading of MWCNTs and it is indicating that the dielectric properties of the polymer dominate the conduction characteristics of the composite [41].

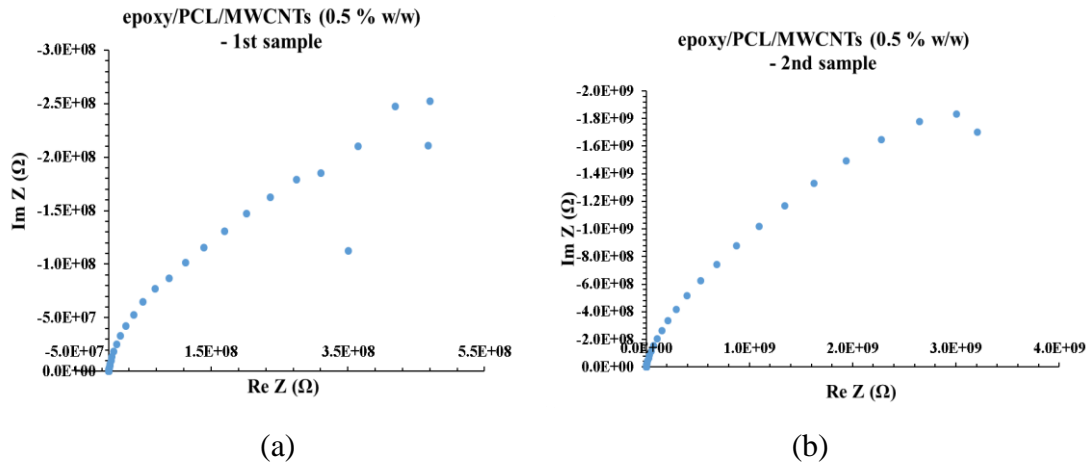


Figure 6.13 Real, imaginary and ratio of imaginary to the real part of dielectric constant, respectively, in 3D, printed samples (a) with the loading of MWCNTs and (b) with repetition of printing. These samples are printed using $F = 100 \text{ mm/m}$ and $E = 0.1 \text{ mm/m}$.

The impedance response of 3D printed samples under the effect of frequency at different temperatures is shown in Figure 6.14. The behaviour changes from linear to a typical semi-circular arc in the temperature range of $0 - 50^\circ\text{C}$. In general, whether a full, partial or no semicircle arc is obtained depending on the strength of relaxation and experimentally available frequency range.

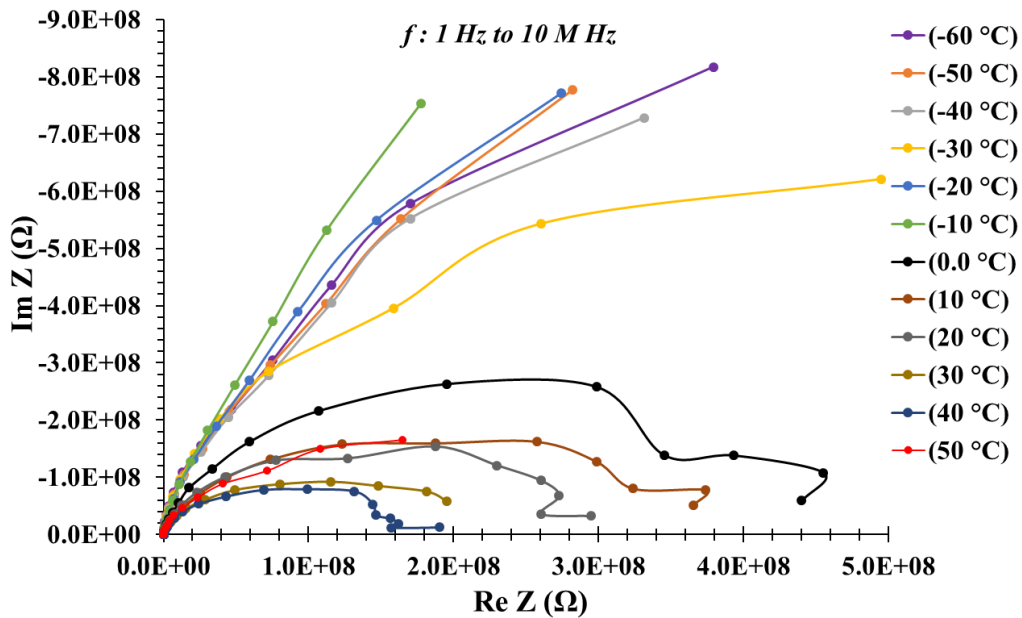


Figure 6.14 The plot is indicating variation in the Nyquist plot under the effect of temperature increase in 3D printed nanocomposite containing 1.0 % w/w MWCNTs using the print conditions $F = 100 \text{ mm/m}$ and $E = 0.1 \text{ mm/m}$.

With an increase in temperature the diameter of the semicircle decreases, which signify the increase in conductivity. In other words, a capacitive impedance of the material starts to behave as a combination of resistive and capacitive elements when the material is subject to a relatively higher temperature. The overall impedance decreases with increase in frequency as well as temperature. However, the high-frequency impedance is temperature independent.

Structure and morphological analysis

The morphology and structure of 3D printed samples are studied using small angle x-ray scattering (SAXS) and wide angle x-ray scattering (WAXS). The data is obtained in the form of 2D images, which are integrated acquiring 1D profile of scattering intensity (I) against scattering vector (q) considering a q -range $0.003 - 0.11 \text{ \AA}^{-1}$. SAXS 1D profiles are shown in the form of log-log plot, Figure 6.15, for different loading (% w/w) of MWCNTs. Gradients are measured from these plots and these are indicative of fractal morphology. A gradient between $-4 \leq \text{Gradient} \leq -3$ is calculated in 3D printed epoxy/PCL sample which is indicative of surface fractal morphology in the epoxy/PCL samples [42]. In contrary to this, gradients between -2 and -3 are calculated for samples containing different 0.5 % (w/w) and 1.0 % (w/w) MWCNTs which are indicative of mass fractal morphology [42]. The plots are nearly linear for relatively lower loadings of MWCNTs (0.5 % w/w and 1.0 % w/w) but a well broad hump can be observed for higher loadings (2.0 % w/w and 3.0 % w/w) of MWCNTs.

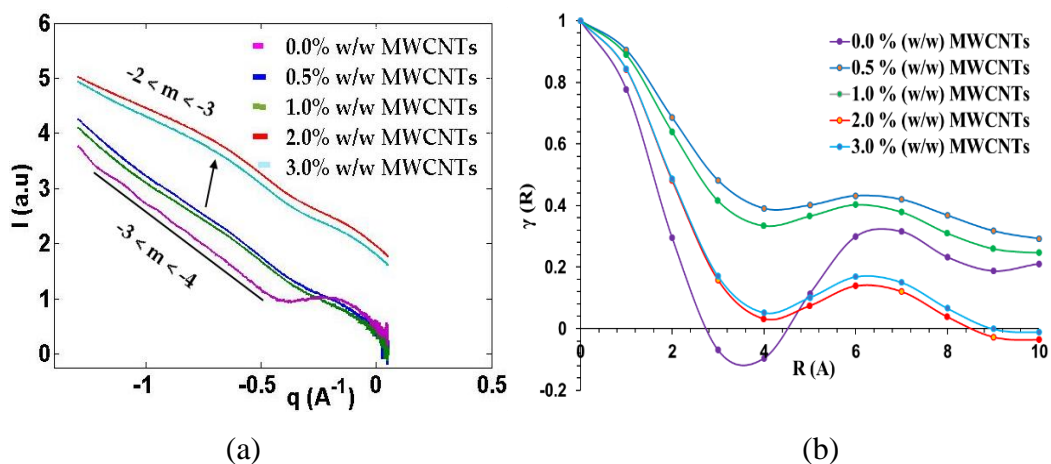


Figure 6.15 1D SAXS plot of scattering intensity (I) against scattering vector (q) obtained after integration and averaging 2 D patterns of epoxy/PCL and its nanocomposites under the effect of MWCNTs loading (% w/w) and (b) 1D correlation plots obtained using data in (a) to find out microstructure parameters. These samples are printed using $F = 100 \text{ mm/m}$ and $E = 0.1 \text{ mm/m}$.

The dissection of gradient into different parts unfolds information about mass fractals and surface fractals into nanocomposites. The gradients are calculated as -2 and -2.5 in lower and intermediate q -regions of the double logarithmic plot, respectively, for nanocomposites containing more than 1.0 % (w/w) MWCNTs. These kind of gradients are suggestive of mass fractal dimension [43] while gradient at high q -region, -3 , is indicative of a surface fractal morphology [42]. Numerous other studies reported similar kind of results using carbon nanotubes as conductive nanostructures for the preparation of electrically conductive nanocomposites. This indicates that fractal morphology evolves from surface fractal to mass fractal with the insertion of MWCNTs. Mass fractal scaling can be associated with the packing efficiency and type of an aggregate of MWCNTs [44], [45]. While, surface fractal scaling only relates to the perimeter of an MWCNT or aggregate of MWCNTs that could be correlated with its specific surface area [45], [46]. There is no change in mass fractal morphology with the increment in PCL or TETA into nanocomposites and shape of plots remain same regardless of these species in the nanocomposite. This is further discussed in the coming sections of this chapter. However, MWCNTs loading has an impact on the gradients and shape of the plot. The ID -correlation plots are used to find microstructure parameters, namely long period (L_p), crystalline lamellar thickness (L_c) and amorphous lamellar thickness (L_a). Figure 6.15(b) shows the ID -correlation plots under the effect of MWCNTs (% w/w). Table 6-3 is given below highlighting significant parameters extracted from the data analysis using ID correlation plots. The L_p is decreased slightly while L_c is increased with the insertion of MWCNTs. These characteristics are typical of a semicrystalline polymer and belong to PCL.

Table 6-3 Data is extracted from the ID -correlation plots for 3D printed samples containing different loadings of MWCNTs. These samples are printed using $F = 100$ mm/m and $E = 0.1$ mm/m.

MWCNTs (% w/w)	L_c (Å)	L_p (Å)	L_a (Å)	Crystallinity (%)
0.0	2.8	7	4.2	40.0
0.5	3.4	6	2.6	56.7
1.0	3.3	6	2.7	55.0
2.0	3.25	6	2.75	54.2
3.0	3.3	6	2.7	55.0

Figure 6.16(top) show 2 D SAXS patterns of epoxy/PCL and its nanocomposites containing MWCNTs. Isotropic scattering is revealed from these patterns except for nanocomposites containing 0.5 % (w/w) and 1.0 % (w/w) MWCNTs. The little anisotropy could be caused by the alignment of either MWCNTs or crystalline lamellae of PCL in the nanocomposites. The scattering was measured in the 2D SAXS patterns along the meridian and equatorial direction in the first three patterns (0, 0.5% and 1.0% w/w) mentioned in Figure 6.16. The ratio between two is used to describe the level of anisotropy caused by the alignment of MWCNTs in the epoxy/PCL mixture. The measurement showed that the patterns without MWCNTs are isotropic as evidenced by the ratio (= 1) of equatorial to meridian scattering. This indicates that MWCNTs are randomly distributed in the epoxy/PCL mixture. The other two patterns yield a ratio as 1.17 and 1.066, which corresponds to 17 % and 6.6 % alignment of MWCNTs along the meridian and thereby causing scattering along the equatorial direction.

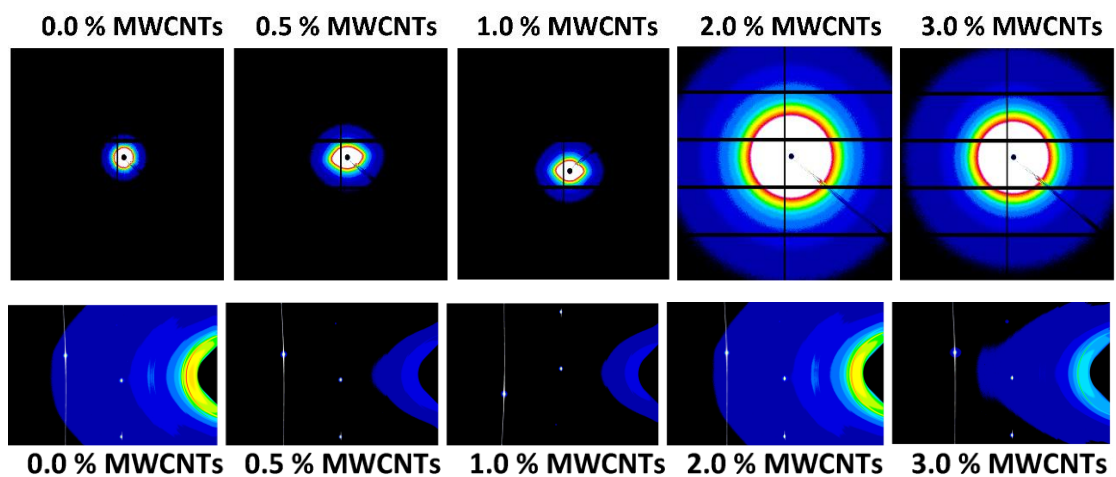


Figure 6.16 2 D SAXS patterns and (bottom) 2DWAXS patterns of 3D printed epoxy/PCL material and its nanocomposites containing MWCNTs. These samples are printed using $F = 100 \text{ mm/m}$ and $E = 0.1 \text{ mm/m}$.

One reason for such anisotropic patterns for relatively lower concentration can be a relatively higher nanotube – nanotube distance and lower viscosity. Under the effect of these two conditions, nanotubes can align along the flow direction during the print process, as the material is not cured up to the extent that it transforms into a solid-state. It is obvious from the patterns for 2.0 % and 3.0 % (w/w) MWCNTs that nanotubes are randomly dispersed in the epoxy/PCL mixture leading to isotropic scattering patterns. For relatively higher concentrations (2.0 % w/w and 3.0 %), interparticle distance increases besides sharp increase in viscosity which leads to aggregation of nanotubes and they have less space available to align during the print process.

2D WAXS patterns are also shown in Figure 6.16(bottom) for epoxy/PCL mixture and its nanocomposites containing MWCNTs. A broad scattering is evident for epoxy/PCL and its nanocomposite with relatively higher MWCNTs loading (2.0 % and 3.0 % w/w). A narrower scattering is revealed for nanocomposite containing 0.5 and 1.0 % (w/w) MWCNTs. This shows that there is some kind of alignment of either MWCNTs or crystalline lamellae of PCL for relatively lower loading of MWCNTs in the nanocomposite. The results are shown in Figure 6.17 after integrating 2D WAXS patterns.

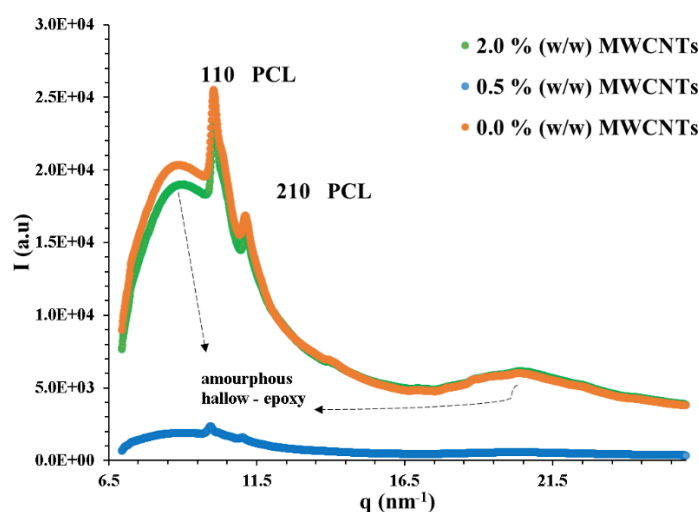


Figure 6.17 The 1DWAXS profiles are obtained from 3D printed epoxy/PCL and its nanocomposites containing 0.5 % (w/w) and 2.0 % (w/w) MWCNTs. The print conditions used are $F = 100 \text{ mm/m}$ and $E = 0.1 \text{ mm/m}$.

Two peaks are visible around $2\theta = 10^\circ$ and $2\theta = 11^\circ$ while two broad hollows appear at $2\theta = 8.9^\circ$ and $2\theta = 20.5^\circ$. The two peaks appear at 10° and 11° belong to crystalline lamellae of PCL while the two broad hollows belong to epoxy [14]. The presence of MWCNTs shifts PCL peaks and broad hallow towards high q region (or high 2θ angle). The shifting of peaks towards relatively high- q region is an indication that the thickness of crystalline lamellae reduces with MWCNTs loading. It is considered that the broad hallow appears at relatively high- q belongs to scattering from the epoxy phase. The position of this hallow does not change significantly with the loading of MWCNTs.

Bright field scanning electron microscopy is used for the visual inspection and the measurement of dimensions of MWCNTs. Figure 6.18(a - b) shows scanning electron microscopy images for MWCNTs. It is not possible to measure the length of nanotubes due to entanglement and difficulty in finding exact ends. The images

indicate that MWCNTs have a variable diameter ranging between 3 – 15 nm. The diameter of MWCNTs provided by the supplier is 6-9 nm. The measurement of diameter indicates that nanotubes have large diameter compare to the one, which was provided by the supplier. In terms of structure, MWCNTs appeared as a mixture of straight, curly and spring-like structures. The morphology of the epoxy/Polycaprolactone mixtures is strongly dependent on composition and there exists sufficient interfacial adhesion between the two phases [47]. The examination of scanning electron microscopy images indicates a strong adhesion between the epoxy - rich and Polycaprolactone - rich phases as revealed from Figure 6.18(c).

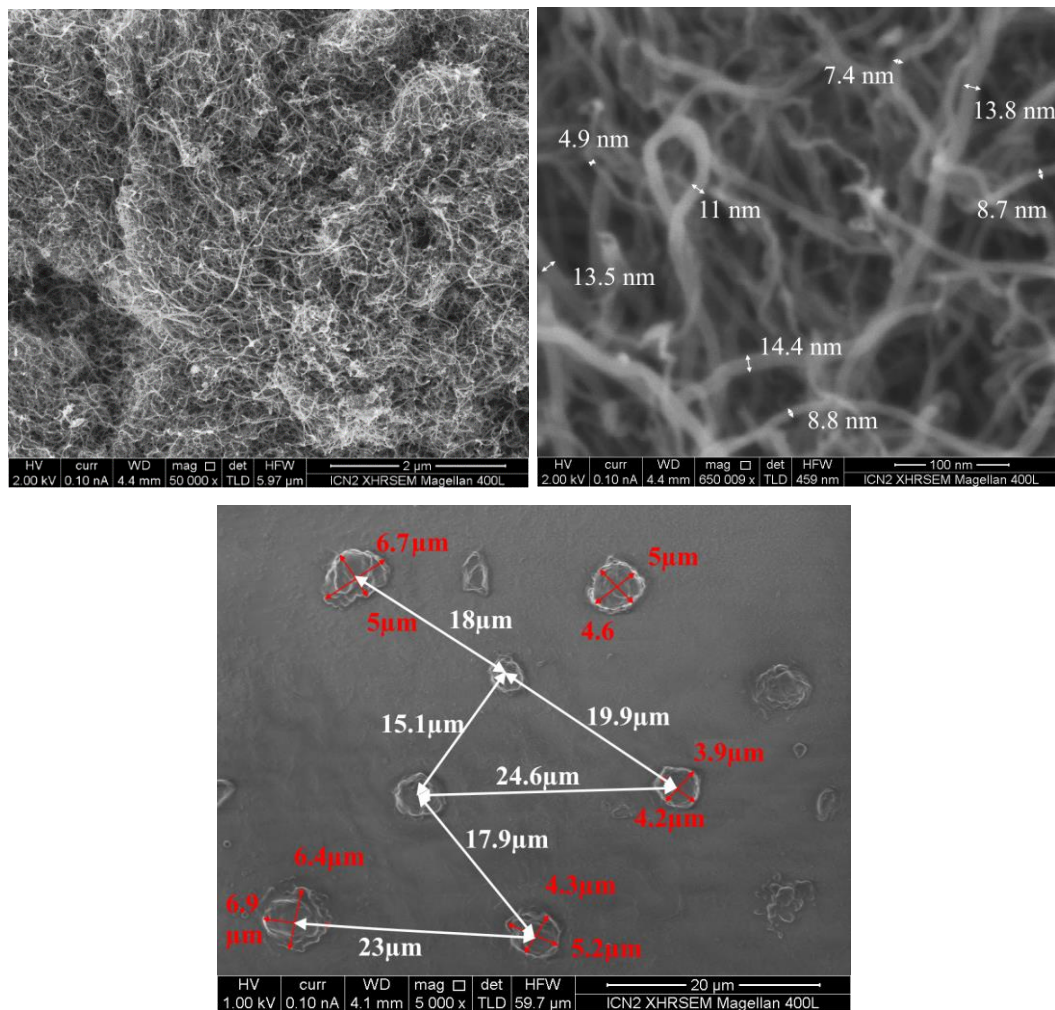


Figure 6.18 SEM images of (a-b) pristine MWCNTs at micrometre to nm scale, respectively, (c) morphology of 3D printed sample (epoxy/PCL).

It is concluded from the SEM image that PCL and epoxy initially form a miscible mixture which undergoes a - induced phase separation during crosslinking of the epoxy [48]. Such a morphological development can be regarded as

matrix/droplet morphology in which PCL droplets are dispersed in an epoxy matrix. The matrix/droplet morphology was also reported in other studies [49]. It is clear from scanning electron microscopy image that PCL droplets are having a nearly spherical shape with the size around $400 - 700 \text{ nm}$. An approximate distance between the PCL distributions is around $20 \pm 5 \mu\text{m}$. The surface of the PCL particulates appears as a rough surface as shown in Figure 6.18(c). It is worth emphasizing that the epoxy/PCL/MWCNTs nanocomposite exhibit entirely different phase morphology as compare to epoxy/PCL mixture as evidenced from Figure 6.19(a-c). MWCNTs are well dispersed in the epoxy/PCL mixture for all % w/w loading except 3.0 % (w/w).

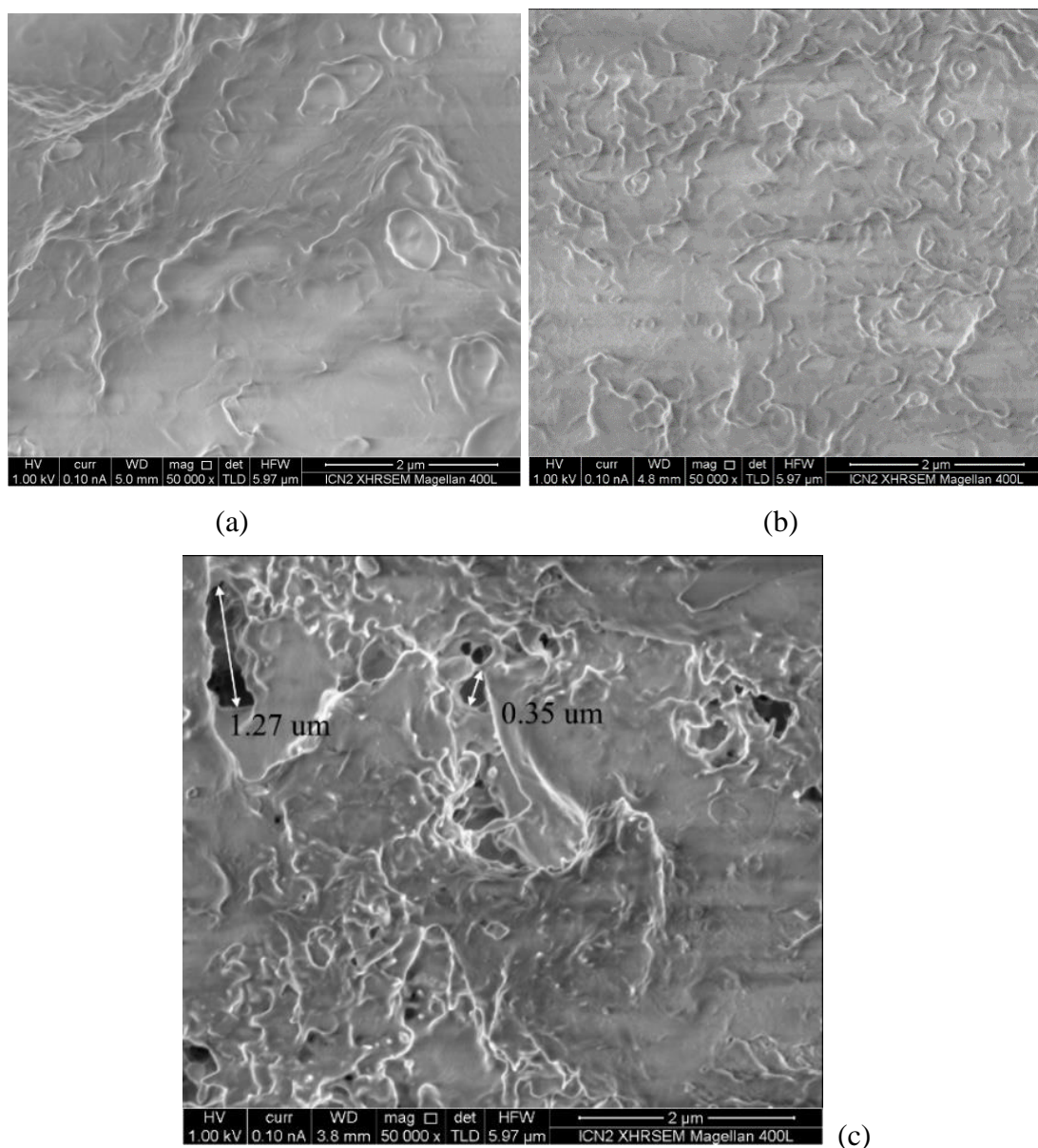
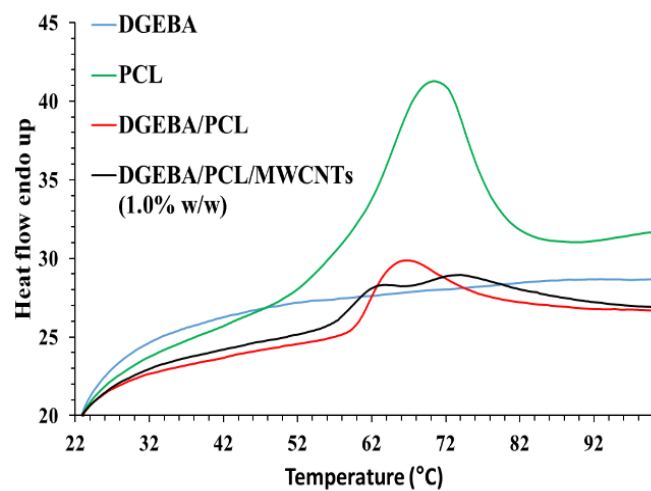


Figure 6.19 SEM images of (a-b) pristine MWCNTs at micrometre to nm scale, respectively, (c-d) epoxy/PCL mixture and (e-g) its nanocomposite containing 0.5 % w/w, 1.0 % w/w and 3.0% w/w MWCNTs, respectively.

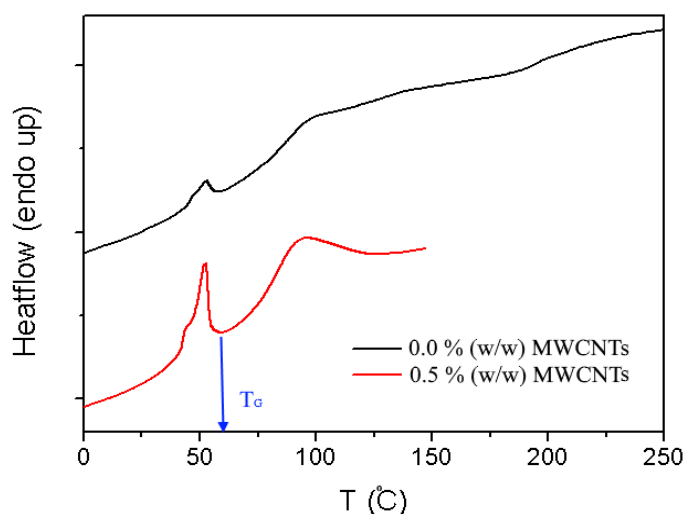
For a relatively lower concentration of MWCNTs, nanotubes look elongated while they are starting to curl for relatively increased loading of MWCNTs in the epoxy/PCL mixture. Besides, PCL droplets morphology disappear due to the presence of MWCNTs as no sign of PCL droplets are visible in the scanning electron microscopy micrographs (Figure 6.19 (a-c)). Homogenization and mixing become challenging at 3.0 % (w/w) loading of MWCNTs. This lead to imperfect printing in the form of defects (cracks) and these are of variable sizes as shown in Figure 6.19(c).

Thermal analysis

The DSC plots of 3D printed epoxy/PCL and its nanocomposite containing MWCNTs DGEBA resin, TETA and PCL are shown in Figure 6.20(a). A clear peak is visible for PCL when it is heated from 22 °C to 100 °C contrary to DGEBA resin, which did not show any peak in the mentioned temperature range. The temperature corresponds to such a peak is regarded as the melting temperature of the material under test [50]. The plots corresponding to the epoxy/PCL mixture not only moves towards lower temperature side but also lowered the peak height. Further, the presence of MWCNTs starts to split this peak resulting to emerge two peaks one slightly before and other slightly after PCL peak. The significant parameters extracted from these plots are mentioned in Table 6-4. The results indicate that PCL crystallinity decrease when mixing with DGEBA resin and MWCNTs. The average (%) crystallinity measured per three samples ≈ 33.4 %, which was reduced to 25.4 % and 23.7 % when mixing with epoxy and epoxy/MWCNTs, respectively. This is an indication that both DGEBA resin and MWCNTs hinder lamellar motion. During DGEBA resin curing, the crystallization of PCL becomes complex. In general, curing results in an increase in the overall crystallization rate in the mixtures and a more profound depression of equilibrium melting point. Also, curing can change the nucleation mechanism of PCL and enhance the nucleation rate [51]. The presence of MWCNTs, the addition of MWNTs to PCL induces heterogeneous nucleation at lower loading and reduces the transportation ability of polymer chains during crystallization processes at relatively higher loading [52].



(a)



(b)

Figure 6.20 Thermal response plots are presented from (a) 3D printed epoxy/PCL material, its nanocomposite containing MWCNTs (1.0 % w/w) and its constituents using a DSC. (b) Thermal response plots are presented from 3D printed samples of epoxy/PCL and its nanocomposite containing 0.5 % (w/w) MWCNTs.

This is probably the reason that the introduction of MWNTs to PCL causes a decrease in the free volume for the molecular chain mobility. The restricted molecular chain mobility accompanied by reduced transportation ability of molecular chains during DGEBA resin curing results in the reduction of % crystallinity. A confined motion of lamellae is resulting in disordered arrangement due to which crystallinity of the epoxy/PCL mixture and its nanocomposite decrease. The glass transition temperature (T_g) is detected around 60 °C for samples epoxy/PCL and epoxy/PCL/MWCNTs (0.5% w/w) as shown in Figure 6.20(b). This indicates that 3D printed samples are in their glassy state when cured at ambient temperature.

Table 6-4 Parameters of interest extracted from the plots mentioned in Figure 6.26. The onset of melting temperature and melting peak is represented as T_o and T_m in the table, respectively. MWCNTs are 1.0 % (w/w), wherever mentioned in the table. The values in the bracket indicate the 2nd split peak due to MWCNTs into epoxy/PCL mixture, where X_{nity} indicates crystallinity.

Samples	T_o (°C)	T_m (°C)	ΔH_m (J/gm)	X_{nity} (%)	X_{nity} (%)
DGEBA-1	-	-	-	-	-
DGEBA-2	-	-	-	-	-
PCL-1	60.7	67.75	46	32.9	33.4
PCL-2	61	68.3	42.6	30.5	
PCL-3	60.9	69.5	51.3	36.7	
DGEBA/PCL -1	59.8	65.8	33.8	24.2	25.4
DGEBA/PCL -2	59.4	65.5	37.4	26.8	
DGEBA/PCL -3	59.8	65.8	35.2	25.2	
DGEBA/PCL/MWCNTs (1)	57.1	72.9 (63.5)	33.1	23.7	23.7
DGEBA/PCL/MWCNTs (2)	56.8	72.3 (61.7)	30.4	21.8	
DGEBA/PCL/MWCNTs (3)	57.8	72.6 (63.9)	35.8	25.7	

The DSC thermograms of epoxy/PCL and its nanocomposites under the effect of MWCNTs loading are shown in Figure 6.21. The endothermic peaks, mentioned in earlier plots, are evidenced by these thermograms. MWCNTs split the endothermic peak of PCL into two sharing a common shoulder.

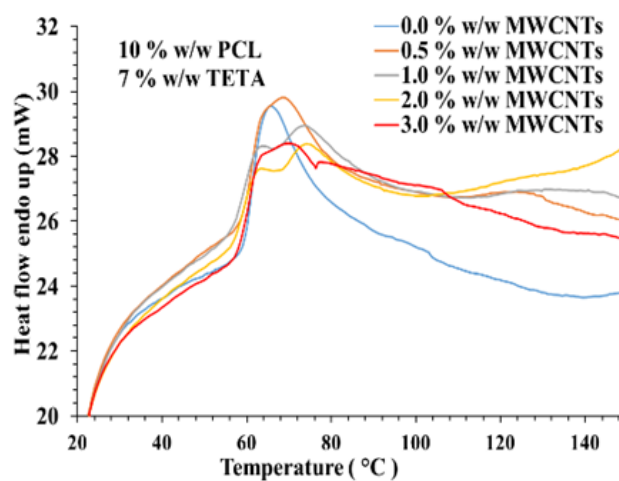


Figure 6.21 Thermal response plots of 3D printed nanocomposite (DGEBA/PCL/MWCNTs) under the effect of carbon nanotubes loading. These samples are printed using $F = 100$ mm/m and $E = 0.1$ mm/m.

One of the possible explanation for the splitting of endothermic peak and lower % crystallinity of the nanocomposite could be an adverse effect of MWCNTs on the nucleation of the crystalline lamellae. It is also possible that heat supplied to material partially consumed to melt crystalline lamellae while a portion of heat is absorbed by MWCNTs. The literature suggests that the presence of such a shoulder is due to the phase separation of PCL from the crosslinked epoxy matrix [53]. The results are obtained from DSC Plots and these are tabulated in Table 6-5.

Table 6-5 Parameters of interest extracted from the plots mentioned in Figure 6.27.

MWCNTs % w/w	T _o (°C)	T _m (°C)	ΔH _m (J/gm)	Crystallinity (%)	Ave. Crystallinity (%)
0	59.8	65.8	33.8	24.2	25.4
0	59.4	65.5	37.4	26.8	
0	59.8	65.8	35.2	25.2	
0.5	59.3	68	30.8	22.1	22.0
0.5	59.3	68	30.8	22.1	
0.5	59.1	67.3	30.5	21.9	
1	57.1	72.9 (63.5)	33.1	23.8	23.8
1	56.8	72.3 (61.7)	30.4	21.8	
1	57.8	72.6 (63.9)	35.8	25.7	
2	57.8	73.9 (63.9)	35.1	25.2	26.7
2	57.1	73.5 (63.3)	35.7	25.6	
2	57.8	72.9 (63.7)	40.8	29.2	
3	58.5	68.8	39.1	28.0	27.1
3	58.1	69.8	41.5	29.7	
3	58.3	63.5	33	23.7	

The results are interesting in the sense that relatively lower loading of MWCNTs (0.5 % w/w and 1.0 % w/w) results in the reduction of % crystallinity while % crystallinity increased for relatively higher (2.0 % w/w and 3.0 % w/w) MWCNTs loading. This effect is understandable as the viscosity of the epoxy/PCL mixture increases with the loading of MWCNTs [54]. The viscosity rise hinders the dispersion of MWCNTs and leads to aggregation. Well dispersed MWCNTs spread throughout within the polymer matrix and possibly, hinders lamellar motion due to which % crystallinity reduces. Accumulation of MWCNTs occurs when nanotubes are not well

dispersed throughout the polymer matrix. This results in a non-uniform distribution of MWCNTs within the polymer matrix. Hence, some regions have relatively higher % crystallinity than in the neighbours. In short, lower nanotubes loading results in the uniform distribution which causes to decrease % crystallinity of the nanocomposite.

Thermogravimetry data is obtained for 3D printed nanocomposites and its constituents in the form of % weight loss curves characterising their thermal stability. The gradients are measured from the % weight loss curve, which denotes the temperature at which the weight loss begins in the material. This is represented in Figure 6.22(a) for DGEBA, PCL, epoxy/PCL and its nanocomposites (epoxy/PCL/MWCNTs) containing MWCNTs. The thermogravimetry plots for 3D printed epoxy/PCL and its nanocomposites follow a single step degradation and are stable up to 350 °C, irrespective of the curing agent and curing condition.

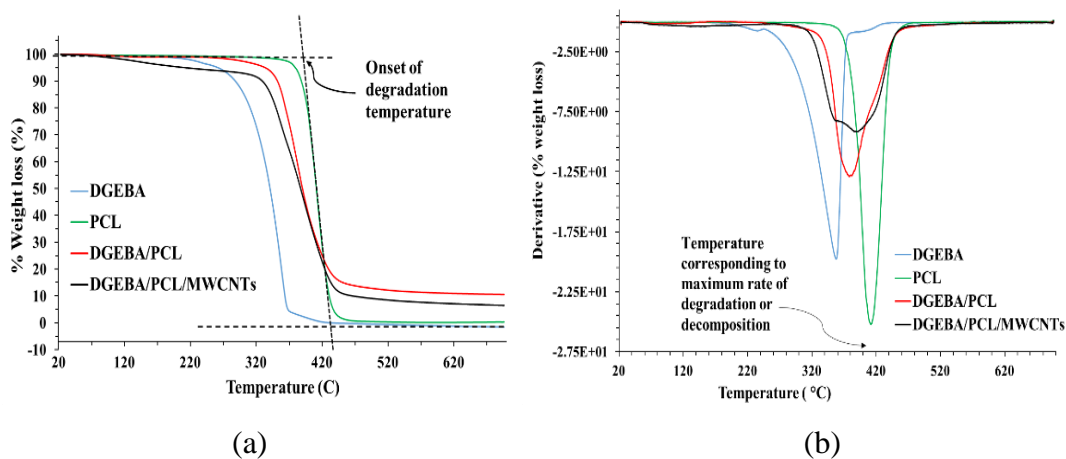


Figure 6.22 (a) Thermogravimetry plots are used to show weight loss and the onset of degradation temperature in pure DGEBA, pure PCL, and 3D printed samples of epoxy/PCL and its nanocomposites containing 0.5 % (w/w) MWCNTs. (b) The derivative of thermogravimetry plots is used to locate the inflexion point corresponding to samples mentioned in (a). These samples were printed using $F = 100$ mm/m and $E = 0.1$ mm/m.

Similar kind of behaviour is reported in other studies [49]. It is clear from the thermograms that onset of degradation temperature is different for DGEBA resin, PCL and 3D printed epoxy/PCL mixture and its nanocomposites containing MWCNTs. The onset of degradation temperature is lower for DGEBA resin compares to PCL. The onset of degradation temperature delays (shifts towards higher temperature) with the inclusion of PCL into DGEBA resin as shown in Figure 6.22(a). On the other hand, the inclusion of MWCNTs shifts onset of degradation temperature towards low temperature suggesting thereby the degradation initiates relatively earlier than

epoxy/PCL mixture [49]. It is worth noticing that the residual weight fraction for the epoxy/PCL mixture is higher than that of DGEBA resin, PCL and nanocomposites (epoxy/PCL/MWCNTs). This is contrary to a study reported in [49].

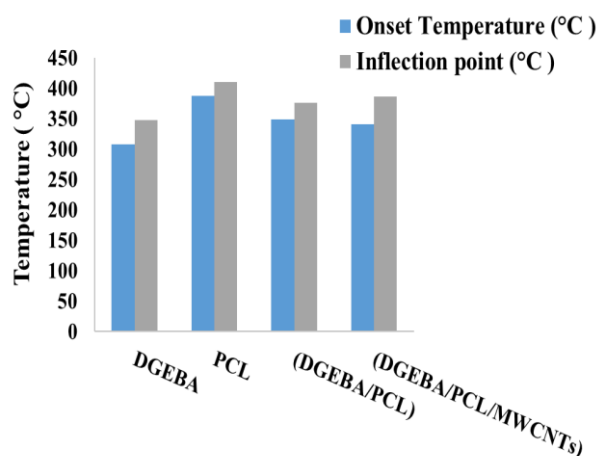


Figure 6.23 Results are plotted from TGA plots mentioned in Figure 6.16 (a-b). MWCNTs are used as 0.5 % (w/w). These samples are printed using $F = 100 \text{ mm/m}$ and $E = 0.1 \text{ mm/m}$.

The next calculation that is useful for the characterization of 3D printed epoxy/PCL and its nanocomposites is the peak calculation of the first derivative of the weight loss curve as shown in Figure 6.22(b). The peak of the first derivative indicates the temperature of the greatest rate of change in weight loss. This is also known as the inflexion point. Clear peaks are observables in Figure 6.22(b) except for nanocomposite containing MWCNTs. The presence of MWCNTs has broadened the peak region indicating thereby that portion of heat was absorbed by the MWCNTs. This results in the appearance of a shoulder rather than a distinct peak. The results are presented from the analysis of TGA plots in Figure 6.23. The change in weight (%) begins at 57°C for 3D printed epoxy/PCL sample and at 59°C for the epoxy/PCL/MWCNTs sample containing 0.5 % (w/w) MWCNTs as indicated in the blue circle in Figure 6.24(a). The slope changes at around 126°C and again at 253°C for the epoxy/PCL sample. For the epoxy/PCL/MWCNTs sample, the slope changes at 180°C and again at 275°C . At 300°C , the weight has changed by 3 % for both samples. Besides, results are presented in Figure 6.24(b) studying the effect of MWCNTs loadings (% w/w) on the onset of degradation temperature and inflexion point.

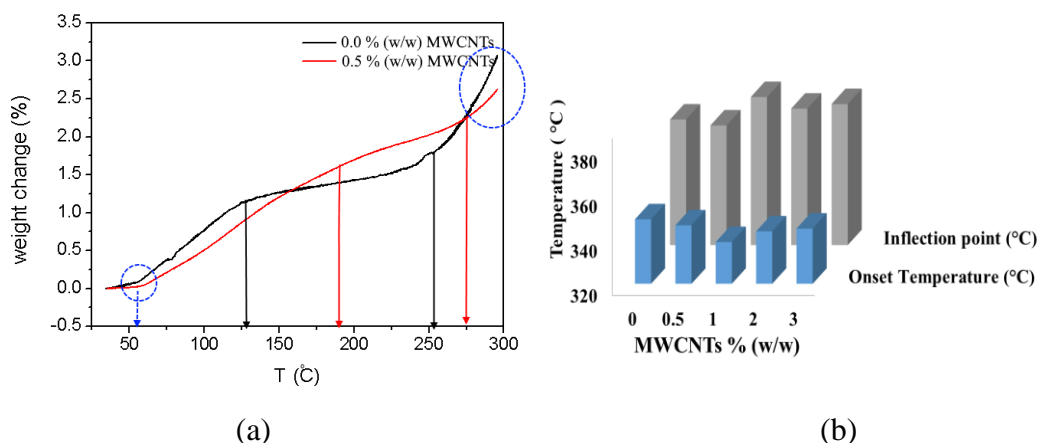


Figure 6.24 Thermogravimetry plots are used to show (a) weight loss in 3D printed samples with and without MWCNTs. (b) the onset of degradation temperature and the inflexion point obtained from data analysis using the TGA plots under the effect of MWCNTs loadings (% w/w). These samples are printed using $F = 100$ mm/m and $E = 0.1$ mm/m.

It is obvious from these plots that onset of degradation temperature decreases while inflexion point increases for relatively lower loading of MWCNTs (0.5 % w/w and 1.0 % w/w) and the behaviour is reverse for relatively higher MWCNTs loading (2 % w/w and 3 % w/w).

6.2.1.1 3D printed epoxy-based nanocomposites under the effect of Polycaprolactone loading

Chemical analysis

PCL is used in the composition to delay crosslinking that further facilitate to print composition. Different compositions were prepared using different % (w/w) PCL for the purpose to identify PCL concentration, which results in optimize print quality. Figure 6.25(a) shows FTIR spectra and Figure 6.25(b) reveals results from the spectra for different loading of PCL (% w/w). It is obvious from the bar plots that amount of epoxy conversion (α) is relatively higher for lower loading of PCL in the nanocomposite. The epoxy conversion parameter is explained in detail earlier in section 6.4.1.1. However, it is not possible to print a part with 15 % (w/w) PCL even for lower loading of MWCNTs. This suggests that PCL is not only facilitating rheology of nanocomposites but it provides a working window in which nanocomposite can be used as a printable material. The main drawback of epoxy thermosets is its brittleness and the possible rout to tackle this issue is the mixing of a thermoplastic polymer in it. PCL is partially miscible with three aromatic-amine-cured

epoxy resins [55]. On similar grounds, epoxy conversion reduced as PCL is increased in the composition. IR spectroscopy is particularly useful in describing miscibility because changes in the molecular environment of the polymer will generally result in perturbations in the IR spectra.

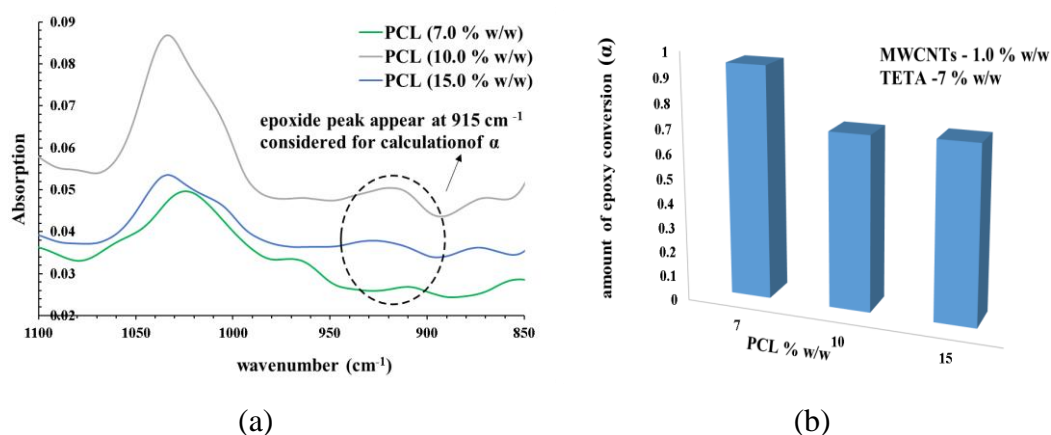


Figure 6.25 (a) A comparative FTIR spectrum of 3D printed electrically conductive samples printed with the variation of PCL content into nanocomposite. (b) Quantitative results of the data obtained through the measuring of epoxide peak appearing at 915 cm^{-1} relative to reference peak appearing at 1182 cm^{-1} with the variation in PCL (% w/w).

The proportion of PCL ester groups which are hydrogen-bonded to the epoxy resin (PCL does not appreciably hydrogen bond to itself) is, therefore, a direct measure of how well the polymers are mixed on a molecular level [55]. It has been demonstrated that an epoxy/PCL mixture features unique differential expansive “bleeding” that enables excellent thermal-mending performance and applicability as a rigid and reversible adhesive brick and mortar [48].

Electrical characterization

PCL play a central role in the print process of epoxy-based additive manufacturing. Compositions are prepared using different PCL loading to find the one that not only delays the robust crosslinking between TETA and DGEBA but also facilitates smooth printing. Figure 6.26 shows that relatively higher (one order) electrical conductivity is observed in 3D printed samples containing 10 % (w/w) PCL compare to samples with 7 % (w/w) and 15 % (w/w) PCL. Phase separation becomes prominent when PCL is used higher than 10 % (w/w) which blocks the printing nozzle. Similarly, relatively, a decrease in electrical is observed in samples printed with higher % (w/w) TETA. This indicates that a low level of crosslinking is favourable for carbon nanotubes network formation, which facilitates charge transport for electronic

conduction. In other words, the formation of a tightly cross-linked network hinders the transport of charge carriers in nanocomposites, resulting in a significant decrease in the electric conductivity [56].

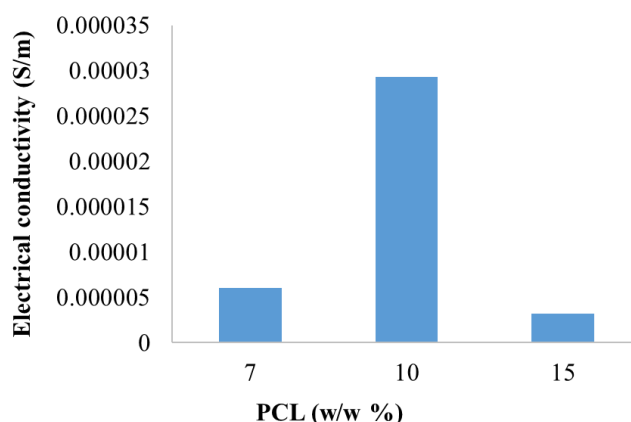


Figure 6.26 Plot is shown indicating an electrical conductivity behaviour in 3D printed samples containing MWCNTs into epoxy/PCL/DGEBA matrix material with the variation in PCL % (w/w).

Structure and morphological analysis

Small and wide-angle x-ray scattering 2D patterns are shown in Figure 6.27(bottom) for 3D printed epoxy/PCL/MWCNTs nanocomposites with different loadings of PCL. Small angle x-ray scattering patterns are symmetrically indicating a random distribution of MWCNTs and PCL phase into epoxy resin. The scattering intensity is integrated radially in these patterns and the average 1D result is plotted as a double logarithm of scattering intensity against scattering vector (q) as shown in Figure 6.28(a). These 1D plots appear the same in term of the shape of the plot and gradients measured under the effect of PCL loading.

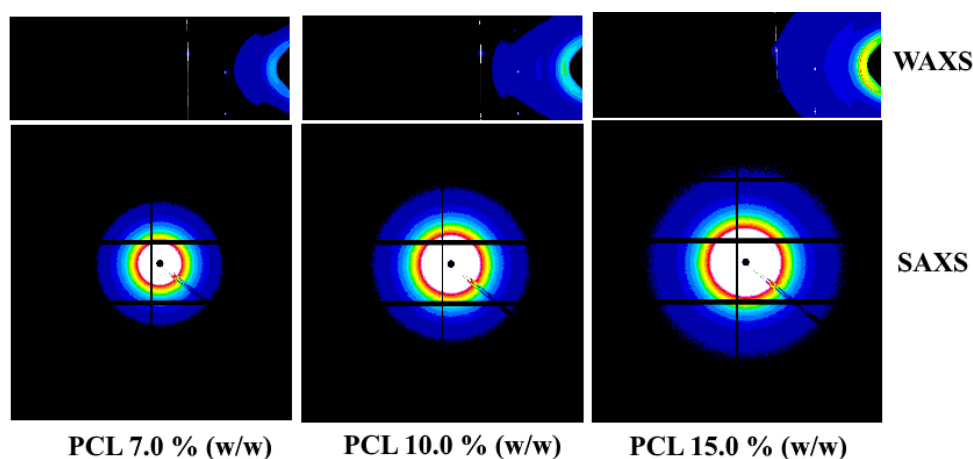


Figure 6.27 2D patterns (bottom) SAXS and (top) WAXS patterns obtained from 3D printed samples with the variation in PCL loading.

The gradients are measured in these plots as - 2, - 2.5 and - 3.0 within the q -range $0.03 - 1.1 \text{ nm}^{-1}$. The gradients in the low and middle q -ranges indicate a fractal morphology in the nanocomposites. The gradients measured in the low - q range indicate a disk-like morphology while a gradient in the middle q - range indicates a branched or network morphology in the nanocomposites for all PCL loadings. The gradient in the relatively high q - range indicates a surface fractal morphology for all PCL loadings without any noticeable difference.

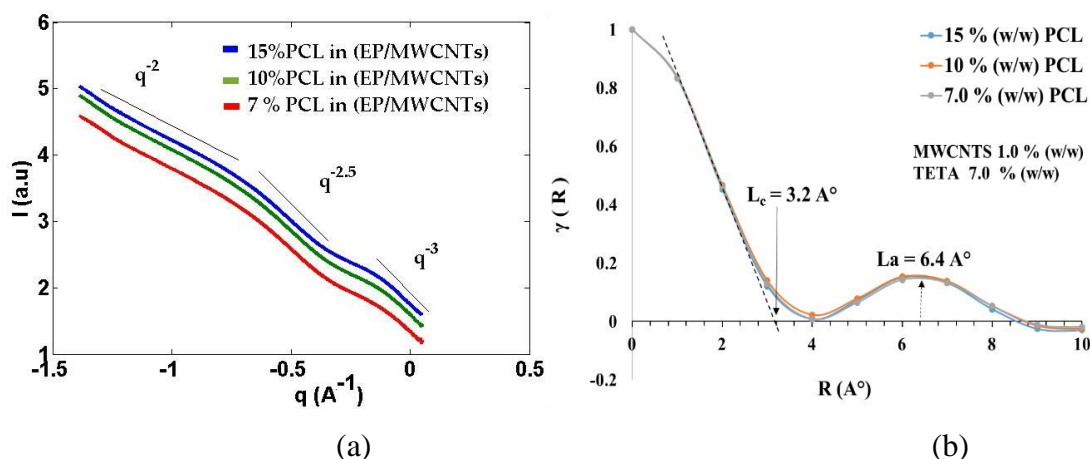


Figure 6.28 1D plot of scattering intensity (I) against scattering vector (q) obtained after integration and averaging 2 D patterns of epoxy/PCL and its nanocomposites under the effect of MWCNTs loading (% w/w) and (b) 1D correlation plot obtained using data in (a) to find out microstructure parameters.

The 1D-correlation plots are used (Figure 6.28(b)) to find structural parameters including the long period and crystalline phase. It is evidenced from the 1D correlation plots that there is no significant difference with the variation in PCL loading in the nanocomposites. The long period and crystalline lamellar thickness measured from the 1D correlation plots are 6.4 \AA and 3.2 \AA , respectively. This suggests that the % crystallinity of 3D printed nanocomposite samples did not change through PCL loading and print process. 2D WAXS patterns are also shown in Figure 6.27(top) for nanocomposite containing MWCNTs with different loading of PCL (% w/w). Relatively higher scattering is evident for nanocomposite with relatively higher PCL loading. Figure 6.29 shows 1D WAXS plots under the effect of PCL loading. Two results are obvious from these plots. First, a higher PCL loading causes to scatter more relative to lower PCL loadings. Secondly, the peak positions correspond to PCL shift towards higher 2θ with PCL loading in nanocomposite (epoxy/PCL/MWCNTs). The shifting of PCL peaks is due to a change in the structure of nanocomposite. It seems

that the PCL lamellae are confined in a relatively narrow space due to which the structure decreases in the nanocomposite which appears in the form of peak shifting towards higher 2θ or q vector. This suggests that relatively higher loading of PCL results in the smaller crystalline lamellae.

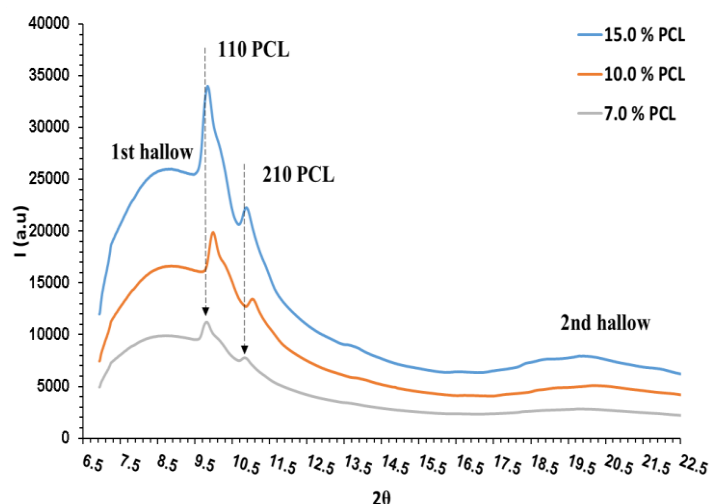


Figure 6.29 The 1D scattering profile of nanocomposite (I) under the effect of PCL loading.

These peaks are visible at $2\theta\ 9.9 \pm 0.1^\circ$ and $2\theta = 10.95 \pm 0.1^\circ$ while two broad hollows appear at 8.8° and 20.5° positions in the plot of Figure 6.29. The two peaks appear at 9.9° and 10.95° belong to crystalline lamellae of PCL [14]. It is considered that the broad hollow appears at relatively low and high- q belongs to scattering from the epoxy phase [14]. The position of this hollow does not change significantly with the loading of PCL.

Thermal analysis

DSC thermograms are given in Figure 6.30 studying the effect of PCL loading on the % crystallinity of 3D printed samples. These results are obtained keeping same loading of TETA (% w/w) and MWCNTs (% w/w). These plots show that endothermic peak slightly gets narrower for 15 % (w/w) compare to 7.0 % (w/w) of PCL. Further, peak broadening is evident for 10.0 % (w/w) compare to 7.0 % (w/w) of PCL. It is considered that MWCNTs are well dispersed in the epoxy/PCL mixture with 10.0 % (w/w) compare to 7.0 % (w/w) and 15 % (w/w) of PCL.

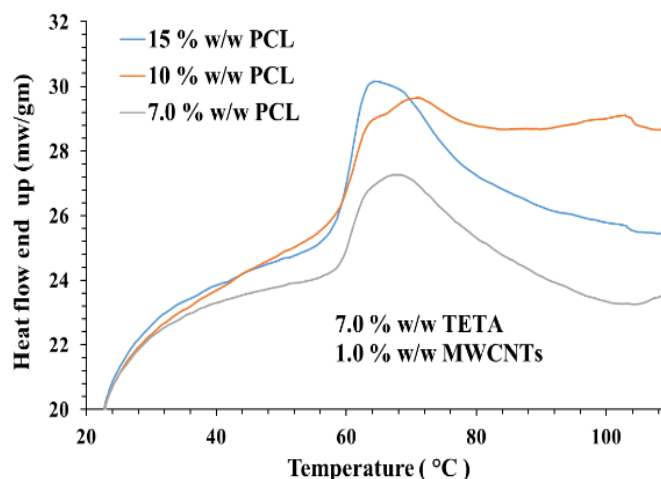


Figure 6.30 Thermal response plots of 3D printed nanocomposite (DGEBA/PCL/MWCNTs) under the effect of PCL loading.

The results are shown in Table 6-6. The significant parameter amongst these is the average crystallinity. The average crystallinity increases in the nanocomposite with PCL loading. The onset of melt temperature (average per three samples) slightly decrease from 59.8 °C to 58.8 °C with PCL loading from 7.0 % (w/w) to 15 % (w/w). Similarly, the melt peak temperature (average per three samples) reduces from 66.8 °C to 64.7 °C.

Table 6-6 Parameters of interest extracted from the plots mentioned in Figure 6.36.

% PCL	T _o (C)	T _m (C)	ΔH (J/gm)	Crystallinity (%)	Avg. Crystallinity (%)
7	60	67.5	16.2	12.1	12.5
7	59.7	66.5	17.5	12.5	
7	59.6	66.4	17.9	12.8	
10	59	69.2	37.3	26.7	27.8
10	59	69	41	29.4	
10	59.2	70.1	38.1	27.3	
15	58.8	64.7	42.4	30.4	31.3
15	58.9	65.1	45.1	32.3	
15	58.7	64.3	43.4	31.1	

Thermogravimetry experiments were conducted to study weight loss in 3D printed samples containing different loadings of PCL (7.0, 10, 15 % w/w). TGA plots are analysed to find the onset of degradation temperature and inflexion point. The onset

temperature indicates initial decomposition temperature where the material starts to disintegrate and it is the measure of thermal stability of the material. The extrapolated gradients are used from the % weight loss curves that denote the temperature at which the maximum weight loss occurs in a particular sample. The extracted parameters are represented in Figure 6.31 for epoxy/PCL/MWCNTs nanocomposites under the effect of PCL loading. It is obvious from these plots that onset of degradation temperature and inflexion point decreases with PCL loading. The presence of PCL makes the epoxy composite thermally less stable compare to pure epoxy material. The onset of degradation temperature and inflexion point decrease (shifts towards lower temperature) at relatively higher loadings of PCL into DGEBA resin.

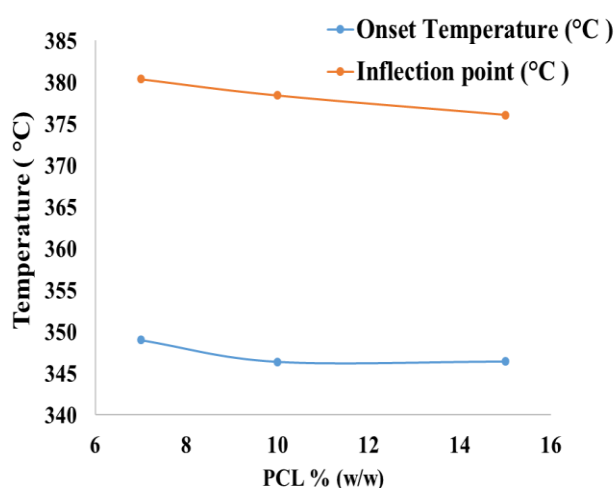


Figure 6.31 Results are obtained from TGA plots showing (a) onset of degradation temperature and (b) the inflexion point (the temperature at which maximum rate of decomposition occur) for 3D nanocomposites with PCL loading. [Composition, and print conditions]

6.2.1.2 3D printed epoxy-based nanocomposites under the effect of Triethylenetetramine loading

Chemical analysis

Different compositions were prepared using different loading (2.0 %, 7.0 %, 10.0 % and 15.0 % w/w) of TETA for the purpose to identify TETA concentration, which results to optimize print quality. Concentration below 7.0 % (w/w) is leading to collapse at the time of printing while concentration above 10.0 % (w/w) lead to fast curing which becomes the source of nozzle clogging. A relatively higher amount of TETA in the system is leading to reduce the time for epoxy conversion as the material start curing within the syringe. This leads to clogging nozzle, which limits the print

process. Samples are printed using only 7.0 % (w/w) or 10.0 % (w/w) TETA. Figure 6.32 shows results from FTIR spectrum for 7.0 % and 10.0 % w/w loading of TETA. It is obvious from the bar plots that amount of epoxy conversion (α) increases with TETA loading in the nanocomposite.

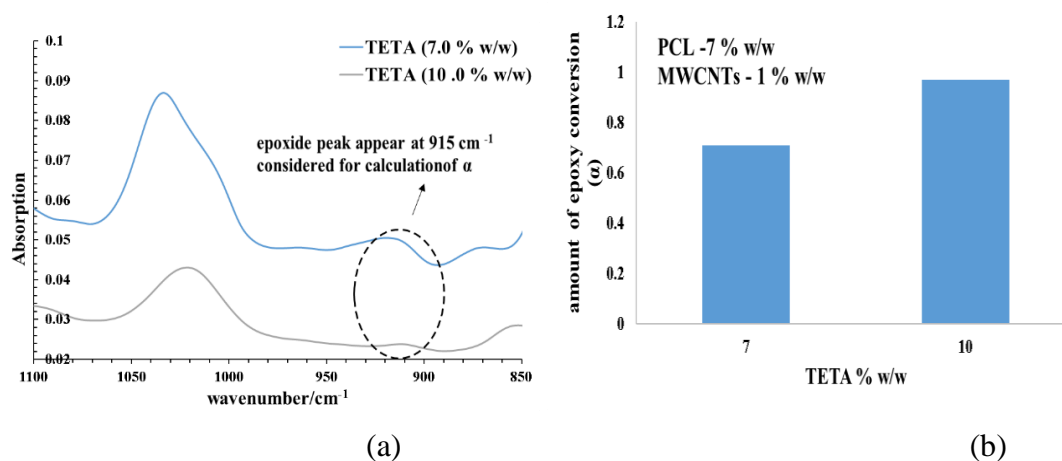


Figure 6.32 (a) The FTIR spectra of 3D printed nanocomposite with the variation in TETA (b) Bar plot is indicating that relatively higher amount of TETA reacts with more epoxide and hence epoxy conversion increased in the nanocomposite.

Electrical characterization

TETA is a crosslinker and plays a central role in the printing of epoxy-based nanocomposites. Different compositions are prepared using TETA to find the one that not only delays the robust crosslinking between TETA and DGEBA resin but also facilitates smooth printing.

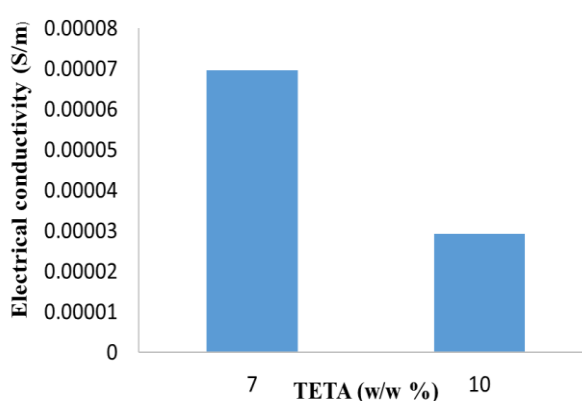


Figure 6.33 Plot is shown indicating an electrical conductivity variation in 3D printed samples containing MWCNTs in the epoxy/PCL matrix with the variation in TETA % (w/w).

This indicates that a low level of crosslinking is favourable for carbon nanotubes network formation, which facilitates charge transport for electronic conduction. In other words, the formation of a tightly cross-linked network hinders the transport of charge carriers in nanocomposites, resulting in a significant decrease in the electric conductivity [56]. Figure 6.33 shows that relatively higher (2 times) electrical conductivity is observed in 3D printed samples containing 7.0 % (w/w) TETA compare to samples with 10.0 % (w/w) TETA. Phase separation becomes prominent for concentrations lower than 7.0 % w/w TETA while higher loadings 15.0 % (w/w) causing too rapid curing which blocks printing nozzle.

The real part of AC electrical conductivity against frequency is shown in Figure 6.34 for 3D printed nanocomposites using 7.0 % w/w and 10.0 % w/w. It is obvious from a plot that the real part of AC electrical conductivity increases with the concentration of TETA. Literature suggests that the hardener used to cure an epoxy resin also has a definite effect on the electrical properties of the resin system in the composition [57].

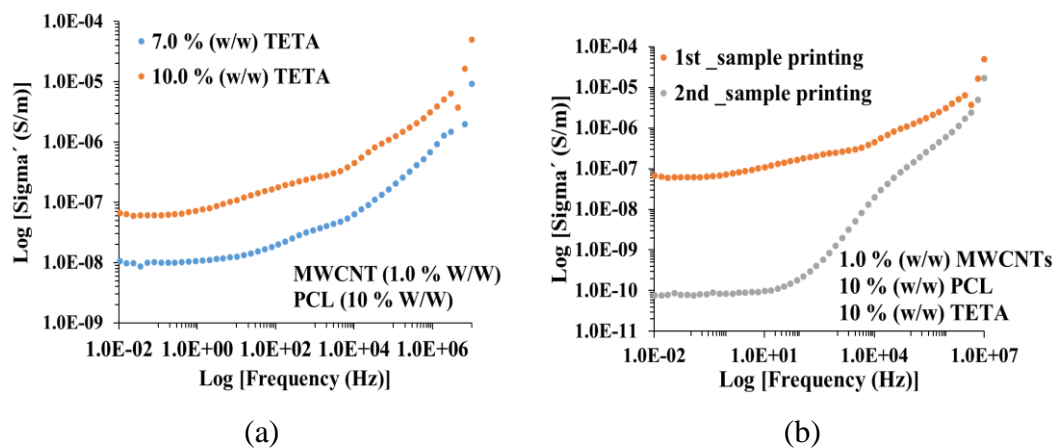


Figure 6.34 Variation in AC electrical conductivity (real part) in 3D printed samples with variation in (a) TETA (% w/w) and (b) for two different samples printed one after other using the same composition.

A relatively higher concentration of the amine results in the shorter pot life. It can be deduced that a relatively higher amount of TETA freezes the structure through fast curing and prevents material from relaxing which causes to disrupt and breaks networks of MWCNTs. The AC electrical conductivity was measured in two different samples prepared using the same composition. The results are shown in Figure 6.40b. It is evident from the plots in Figure 6.40b that the AC electrical conductivity is three order higher in the sample printed earlier than later. The decrease in AC electrical

conductivity is attributed to the relaxation of materials and print process. The print process affects the networks of MWCNTs significantly as the material is semi-cured. This could be caused by improper mixing of hardener and epoxy resin and/or improper ratio of hardener to the epoxy that degraded the electrical properties of an epoxy-hardener system [57].

Figure 6.35 (a, b) shows dielectric constant (real and imaginary components) measured in 3D printed samples when prepared using a different amount of TETA. The dielectric constant increase in the nanocomposite as the amount of TETA increase in the composition.

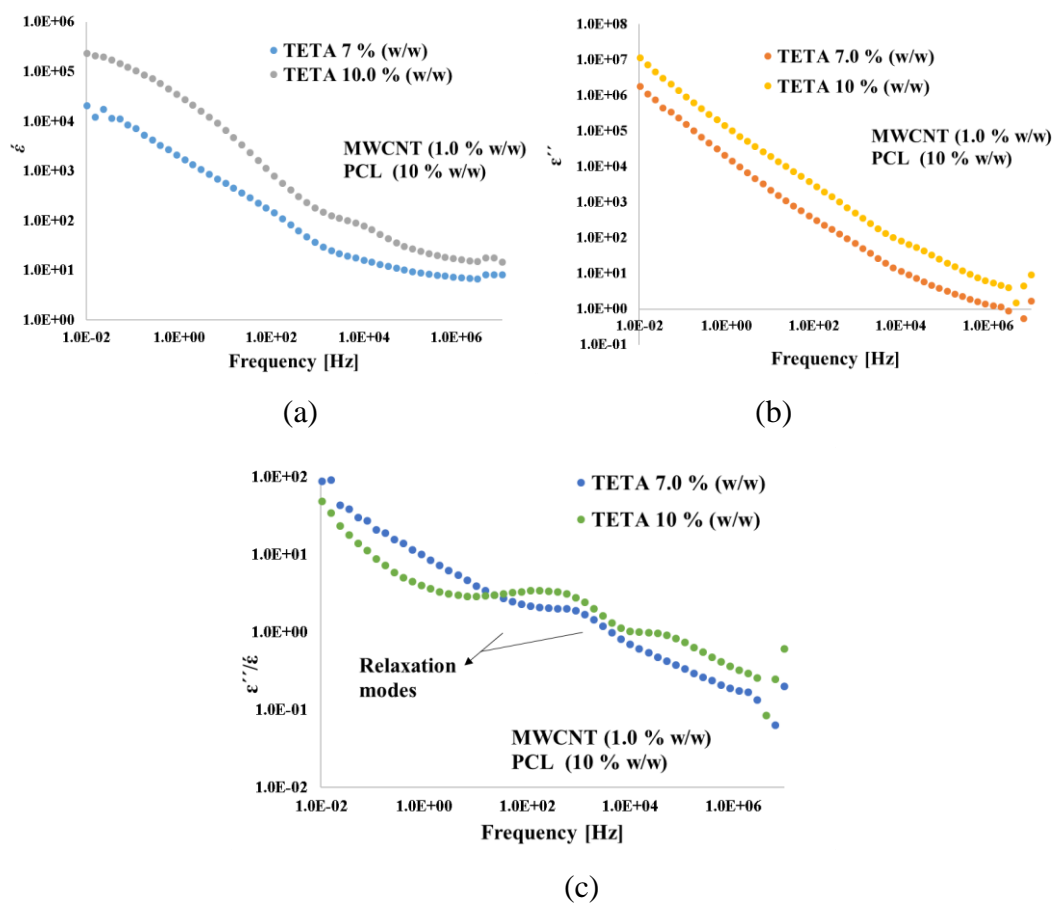


Figure 6.35 (a-c) Real, imaginary and the ratio of imaginary to the real part of dielectric constant, respectively, in 3D, printed samples with the loading of TETA.

The dielectric constant of the material denotes the ability of a material to store charges. Further, the ratio imaginary to real component of the dielectric constant (Figure 6.35(c)) is used to explore relaxation modes, if exists, in the nanocomposites. The arrows are shown in Figure 6.35(c) highlighting relaxation modes exist in the nanocomposites. These relaxation modes are related to molecular fluctuations of

dipoles due to the movements of molecules or parts of them in a potential landscape. Other contributions can be caused by the motion of mobile charge carriers (electrons, ions, or charged defects) causes conductive contributions to the dielectric response [58].

The impedance response of the material is also measured in 3D printed samples under the effect of TETA loading and the data is plotted in the form of the Nyquist plot. The Nyquist plot is obtained through the plotting of real and imaginary components of the complex impedance of 3D printed samples and is shown in Figure 6.36. Two features are evident in the Nyquist plots. First, a semicircle is observed with a shoulder appear towards the high-frequency region. Secondly, the impedance in 3D printed samples decreases with the increase of TETA in the composition. These results show that the impedance of the material decreases three times in 3D printed sample when the TETA is increased three times in the composition.

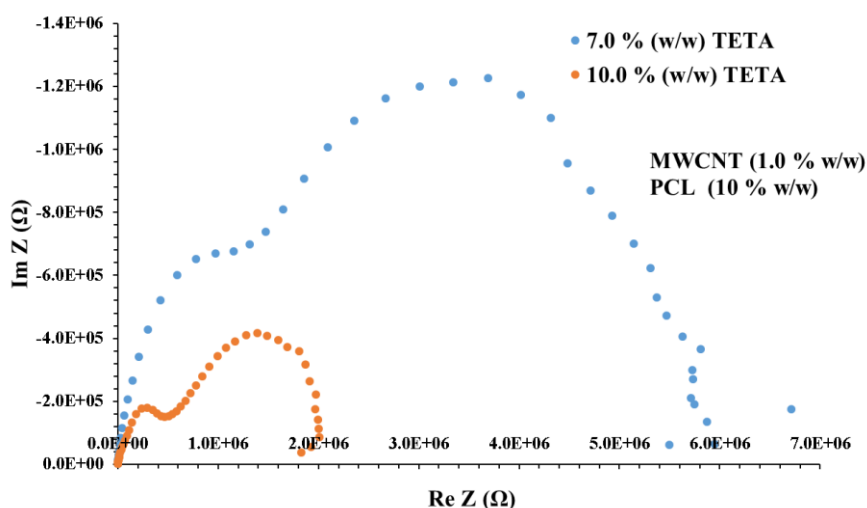


Figure 6.36 Nyquist plot obtained using complex impedance data from 3D printed nanocomposites under the effect of TETA loading.

Structure and morphological analysis

Simultaneous small-angle and wide-angle data are collected for 3D printed epoxy/PCL/MWCNTs nanocomposites under the effect of TETA loading and the 2D patterns are shown in Figure 6.37. Symmetrical 2 D SAXS patterns comes from scattering experiments and this indicates MWCNTs are randomly distributed in the epoxy/PCL/MWCNTs mixture. The extrusion process does not affect MWCNTs distribution. Figure 6.38(a) shows the SAXS scattered intensity as a function of the scattering vector q in the form of a double logarithmic plot for 3D printed

epoxy/PCL/MWCNTs nanocomposites under the effect of TETA loading. The results are plotted in a double logarithmic scale to find the power-law relationship.

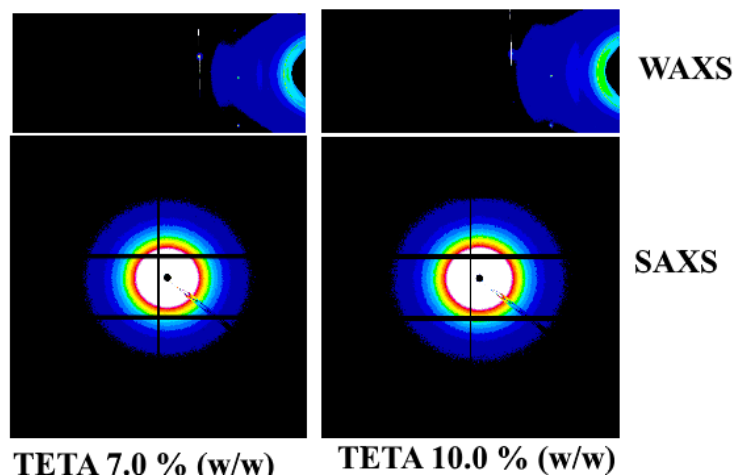


Figure 6.37 The 2 D patterns (bottom) SAXS and (top) WAXS obtained from 3D printed samples under the effect of TETA loading.

There is no significant difference observed in the 1D plots under the effect of TETA loading which indicates that variation of TETA does not affect the morphology of the nanocomposites. The gradients are measured as -2.0 ± 0.1 , -2.5 ± 0.1 and 3.0 ± 0.2 in the log-log plot for both compositions which indicates mass and surface fractal morphologies in the nanocomposites in the q -range $0.03 - 1.1 \text{ nm}^{-1}$. A mass fractal morphology represents an aggregate structure [59]. This is observed in the low $-q$ and middle q - regions with values -2.0 and -2.5 respectively. The scattering entities (MWCNTs) behaviour is like discs with gradient -2.0 and decreases likely something between spheres and discs for a gradient -2.5 . The power law scattering in the region $0.07 < q < 1 \text{ nm}^{-1}$ with a gradient in the range between -2 and -3 , is a characteristic of branched or disordered structures consisting of thin bundles inside the nanoropes [60]. The slope or gradient values of -3.0 are indicating that MWCNT aggregates form fractal structures, i.e. the entity that causes the scattering comes from clusters of entangled nanotubes, as observed by other authors [61], [62]. Morphologically, a lower gradient corresponds to the lower branch structure [63]. These slope values point out the absence of only individual rod-like scatters which would produce a gradient $= 1$ [61].

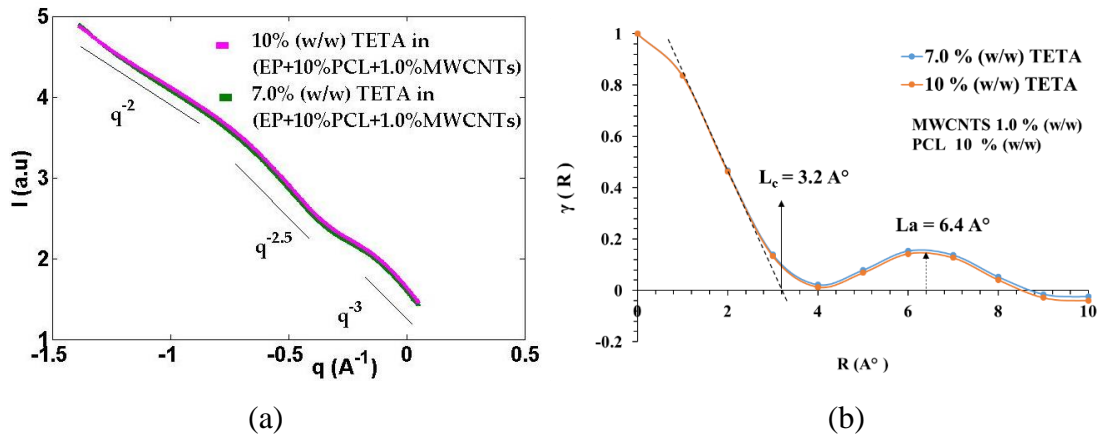


Figure 6.38 (a) 1D plot of scattering intensity (I) against scattering vector (q) obtained from 2 D patterns of epoxy/PCL/MWCNTs nanocomposites under the effect of TETA loading (% w/w), (b) 1D correlation plot is obtained using data in (a) to find out microstructure parameters.

For MWCNTs, the material corresponds to a surface fractal when $-4 < \text{slope} < -3$, instead of a mass fractal for which gradient is < -2 or -2.5 . For a surface fractal, [64]

$$I(q) \propto q^{-(6-D_s)} \quad (6.5)$$

Thus, the surface fractal dimension, D_s , of the nanocomposite is -2.9 (Eq. 6.5). The value of surface fractals (-2.9) obtained are comparable to those reported in the work [45], [65]. The gradient in the range between $-4 \leq \text{gradient} \leq -3$ is due to the presence of fractal surface [42]. Figure 6.38(b) shows the 1D correlation plot obtained with the help of Fourier transform using 1D scattering data. This is used to extract microstructure parameters namely long period, crystalline lamellar thickness and amorphous phase thickness. The measured values are 3.2 \AA° and 6.4 \AA° for lamellar thickness and long period respectively. Both kinds of samples reveal similar results without any significant difference. Figure 6.39 shows 1D wide-angle x-ray scattering profiles for the above-mentioned compositions. A prominent peak with a shoulder peak and a broad hallow are observed in these patterns. No significant change is observed either in peak shifting or in peak broadening. These peaks belong to the crystalline lamellae of PCL [14]. These results are similar as discussed in section 6.4.1.5., without any noticeable differences.

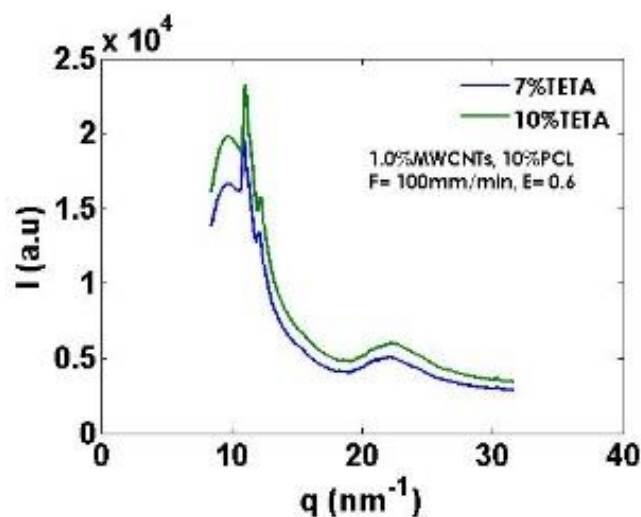


Figure 6.39 WAXS 1D plot of scattering intensity (I) against scattering vector (q) obtained from 2 D patterns of epoxy/PCL/MWCNTs nanocomposites under the effect of TETA loading (% w/w).

Thermal analysis

Figure 6.40 shows differential scanning calorimetry thermograms studying TETA effect on the endothermic peak. A relatively higher amount of TETA (10.0 % w/w), compare to 7.0 % w/w, results in the reduction of average crystallinity in the nanocomposites.

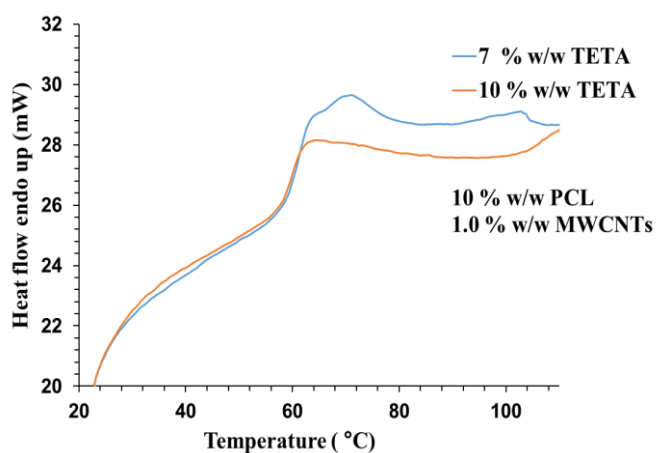


Figure 6.40 Thermal response plots of 3D printed nanocomposite (DGEBA/PCL/MWCNTs) under the effect of TETA loading.

Both, the onset of melt temperature and peak temperature decreases with TETA loading. It can be concluded that a relatively higher amount of TETA crosslink with epoxy resin efficiently and resulting to freeze structure. In this, PCL is not able to organise from it is nearly solution state to solid state which results in the reduction of crystallinity. The results from thermograms are given in Table 6-7.

Table 6-7 Parameters of interest extracted from the plots mentioned in Figure 6.41.

TETA %	Melt onset Temperature (C)	Melt peak Temperature (C)	Enthalpy of fusion (J/gm)	Crystallinity (%)	Avg. % Crystallinity
7	59.2	69.3	34.4	24.65949821	20.9
7	59.1	64.4	27.2	19.49820789	
7	59.2	68.6	26	18.63799283	
10	57.9	62.7	14.7	10.53763441	9.3
10	58.5	63.1	13.5	9.677419355	
10	57.4	62.9	10.8	7.741935484	

The extrapolated gradient are used from the % weight loss curves that denote the temperature at which the weight loss begins. The degradation temperature and inflexion point both decrease for epoxy/PCL/MWCNTs nanocomposites under the effect of TETA loading, as shown in Figure 6.41. It is clear from these thermograms that onset of degradation temperature is different for the nanocomposites containing different loadings of TETA. The onset of degradation temperature and inflexion point decrease (shifts towards lower temperature) at relatively higher loadings of TETA.

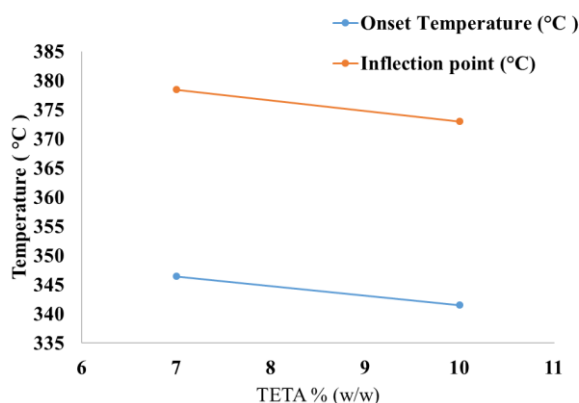


Figure 6.41 Thermogravimetry plots are used to show the onset of degradation temperature and the inflexion point (the temperature at which the maximum rate of decomposition occur) of 3D printed nanocomposite with TETA loading.

6.3 DISCUSSION

An AM system is developed and implemented for the printing of epoxy-based nanocomposites. A mass flow rate is measured from the printer as 32.8 ± 0.90 mg/min. Control over the cure is considered significant for the printing of epoxy resin, which was explored through testing different compositions. This is achieved through the inclusion of a thermoplastic polymer into epoxy resin. The selection of the

thermoplastic polymer is considered mandatory for the printing of epoxy resin as it prolongs curing to such an extent that part can be printed without nozzle clogging. Initially, PS is considered as an appropriate additive thermoplastic polymer, which was phase-separated during printing and blocked printing nozzle. However, PCL proves to be the right choice for this work as it was not phase separated during printing. PS has a relatively higher molecular weight compared to PCL that could be one of the reasons for phase separation in the case of PS [66]. Samples were printed using DGEBA epoxy resin containing a thermoplastic polymer (Polycaprolactone) and MWCNTs. Compositions were prepared with variation in loadings (% w/w) of MWCNTs, PCL, and TETA and these were used to print samples using the developed printer. Square and rectangular shape samples were printed using the printer. A sample volume $5 \times 5 \times 0.2 \text{ cm}^3$ was printed using the developed printer. The development and implementation of the printing for the printing of epoxy-based composites was the primary objective of the study. The samples were printed at room temperature.

The secondary concern of the study is the printing of parts, which are electrically conductive using the developed printer. In this way, the printed parts can be used efficiently for an example, as electrodes in energy storage applications including supercapacitors and batteries. Therefore, it is appropriate to characterise these samples in terms of epoxy conversion, electrical and thermal behaviour, structural and morphological developments. FTIR results indicate that epoxide conversion is affected through variation in loadings of MWCNTs or PCL or TETA when mixed with epoxy resin. The conversion parameter (α) decreases with loadings of MWCNTs and PCL while it increases with loadings of TETA. This is because MWCNTs and PCL act as barriers between resin molecules and TETA molecules and restrict their mobility leading to lower epoxide conversion. In other words, additives had an inhibiting effect on the curing of epoxy resin [67]. The epoxide conversion increases when there is a higher number of TETA molecules present in the neighbouring environment. The results show that epoxy conversion begins to decrease significantly at 3.0 % (w / w) MWCNTs which consequences to nozzle clogging. The clogging of material is evidenced during printing. This is because of a tremendous rise in the viscosity of the material. The experimental work suggested that compositions containing more than 3.0 % (w/w) MWCNTs are not printable. A higher loading and dispersion of MWCNTs becomes a source of viscosity rise in the polymer matrices [68]. Similarly, compositions were printable with addition of 7.0 % (w/w) to 10.0 % (w/w) PCL.

However, nozzle clogging had occurred when PCL was used 15 % (w/w). In terms of achieving reasonable printing of epoxy-based nanocomposites, compositions that contain 0.5- 2.0 % (w/w) MWCNTs, 7-10 % (w/w) PCL and 7-10 % (w/w) are considered appropriate. Results indicate that printed samples were electrically conducting and electrical conductivity had increased six orders of magnitude with loadings of 0.5 % (w/w) MWCNTs when tested for electrical characterization. A maximum electrical conductivity, eight orders of magnitude, was calculated for samples with 3.0 % (w/w) MWCNTs. These samples had a rough surface with micron-scale pore indicating poor print quality. The pores can be visualised in SEM image. Besides, electrical conductivity calculated along the print direction is higher than normal to print direction and thereby proves that printing has an effect on the organization of MWCNTs within the epoxy/PCL matrix. Extrusion process does affect MWCNTs organization during the layering process. No significant trend is observed in *DC* electrical conductivity with the variation in PCL and TETA loadings. This is attributed to inhomogeneous structure development due to MWCNTs and PCL inclusion into epoxy resin. The broadband dielectric spectroscopy data indicate that AC conductivity increases with higher loadings of MWCNTs. The AC electrical conductivity increases at higher frequencies. A plateau is observed in AC conductivity plots indicating a crossover point between AC and *DC* conductivity. The equation used to fit data suggests a hopping or tunnelling of electrons for electronic conduction [26] [29]. It is important to mention that a difference in conductivity is calculated for two samples printed from the same composition one after other. A higher conductivity is calculated for the sample printed earlier than later. This is attributed to the disruption of the MWCNTs network during printing for the samples printed later. The AC conductivity rises under the effect of a rise in temperature. The gradients are measured from double logarithmic plots of SAXS data suggest a mass fractal morphology in 3D printed samples. The mass fractal dimensions lie in $-3 < \text{mass fractal dimension} < -2$ for all compositions except for epoxy/PCL sample where the measured gradient suggests a surface fractal morphology [42]. The mass fractal dimension indicates an aggregate of MWCNTs [43]. This shows that MWCNTs aggregate in the epoxy/PCL matrix. The anisotropic SAXS patterns are revealed for a lower concentration of MWCNTs while isotropic patterns are obtained from samples containing a relatively higher amount of MWCNTs. The anisotropy is attributed to some level of orientation of MWCNTs along print direction. Such kind of orientation is not possible for higher loadings of

MWCNTs due to aggregation of nanotubes and comparatively less available free volume for movement and reorganization of MWCNTs into PCL matrix. This is also evidenced from viscosity rise behaviour at relatively higher loadings of MWCNTs. No significant peak shift is observed in WAXS 1D plots for all compositions. The peaks belongs to PCL crystalline lamellae having orthorhombic unit cell [69]. Networks of MWCNTs are obvious from SEM images and porosity is very much clear in the case of samples printed with 3.0 % MWCNTs. DSC data suggests that crystallinity in PCL decrease in 3D printed samples containing epoxy/PCL/MWCNTs. It is obvious from the results that crystallinity decreases for lower loadings (0.5 % w/w and 1.0 % w/w) of MWCNTs while it increases for relatively higher loadings (2 % w/w and 3 % w/w) of MWCNTs. The crystallinity in 3D printed samples (epoxy/PCL/MWCNTs) increases with a rise in loadings of PCL while it decreases with the rise in loadings of TETA. The decrease in crystallinity is caused by several factors including restricted lamellar motion because of MWCNTs and/or trapping of lamellae between crosslinked regions offering limited space for organization epoxy while an increase in crystallinity is attributed to heterogeneous [xxx] or inappropriate mixing of PCL and epoxy leading to PCL rich areas and epoxy rich areas. The literature suggests that the addition of MWNTs to PCL is induced heterogeneous nucleation at relatively lower loading while the transportation ability of polymer chains is reduced during crystallization processes at a higher MWNT loading [52]. The onset of degradation temperature decreases in 3D printed samples containing epoxy/PCL and epoxy/PCL/MWCNTs compare to PCL while it increases compare to DGEBA resin. This indicates a combined effect from both polymers. Similar kind of results is obtained for an inflexion point. However, the onset of degradation temperature first decreases and then increases with the increase in the loading of MWCNTs. On the contrary, an increasing trend is observed for inflexion point with an increase in loading of MWCNTs. However, the onset of degradation temperature and inflexion point decrease with rising in loadings of PCL and TETA. The electrical conductivity in 3D printed nanocomposite is attributed to networks of MWCNTs in the form of aggregates. For the sake of understanding, the system can be considered as a two-phase system; an insulator phase and a conductor phase. This analogy helps to predict conducting behaviour in 3D samples. A model is discussed and it is presented in the next section.

6.3.1 Model

In this section, the behaviour of the material in terms of equivalent circuit is modelled using impedance data which is a tertiary concern of the study. This is achieved with the consideration of appropriate circuit elements capable to depict the behaviour of relevant phases in the nanocomposites. Such kind of models was reported in the literature to deduce appropriate equivalent circuit model [40], [70], [71] to understand spatial arrangements of MWCNTs and polymer contributing to bulk electrical conductivity. Carbon nanotubes form a complex network in nanocomposites as a carbon nanotube curl, straighten and it can organize parallel or crossed to each other, as evidenced from SEM images. Such a configuration lead to exhibit integrated characteristics of a resistor and a capacitor in 3D printed nanocomposite samples. Besides, a fractal morphology is evidenced from SAXS study indicating a complex structure in nanocomposite due to presence of MWCNTs. In conjunction with this, integrated characteristics of MWCNTs as a resistor and/or a capacitor are non-ideal and complex into 3D printed electrically conductive nanocomposites.

Impedance plots in Figure 6.12 and Figure 6.36 illustrate a complex impedance plane in a plot obtained from 3D printed nanocomposite samples containing MWCNTs. Two semicircles are obvious from these plots which are decentralised and slightly depressed towards the horizontal axis. The literature suggests that two semicircles, without depression, in the experimental data indicate the presence of the two mechanisms that are representing a series combination of two parallel RC circuits in a model [72], [73]. As the two semicircles in the experimental data are depressed, the behaviour becomes complex revealing a fractal nature of circuit components [74]. It becomes obvious from preliminary data fitting that simple parallel RC circuits [72], [73] do not fit to the experimental data. Preliminary data fitting indicates that such complexity is caused by the capacitor elements in the sub-circuits. The complexity may originate from a non-Debye type behaviour in the nanocomposite material with distributed relaxation times which occur to disordered materials and it is modelled using an equivalent circuit incorporating constant phase element [75]. The Constant Phase Element (CPE) is a non-intuitive circuit element that is used commonly in the literature explaining depression in semicircles for the response of real-world systems [76]. A CPE is a mathematical realization of a system in which the phase angle between applied AC voltage and resulting current remains independent of the frequency [77]. The depressions are associated with some property of the system,

which is not homogeneous, or there is a distribution of the value of some physical property of the system [76]. The CPE is defined as [78].

$$Z^* = \frac{1}{Q(i2\pi f)^\alpha} \quad (6.6)$$

$$Re Z = \frac{C_\alpha}{Q(2\pi f)^\alpha} \quad Im Z = -\frac{S_\alpha}{Q(2\pi f)^\alpha} \quad (6.7)$$

$$C_\alpha = \cos\left(\frac{\pi\alpha}{2}\right) \quad S_\alpha = \sin\left(\frac{\pi\alpha}{2}\right) \quad (6.8)$$

Here f is the frequency while α and Q are CPE parameters. The value of α is distributed between 0 and 1. A value of $\alpha = 0$ leads to pure resistor while a value of $\alpha = 1$ leads to a pure capacitor. A value $0 < \alpha < 1$ leads to fractal behaviour which make the system complex [74]. In this context, CPE can be regarded as a fractal capacitor [41]. Therefore, two pure capacitor elements are replaced with two constant phase elements (Q_a , Q_I) in the series combination of two parallel RC circuits and these are provided in Figure 6.42(c, d).

The two mechanisms in the impedance spectra of 3D printed nanocomposite samples [79] are attributed to conductive aggregates of MWCNTs and areas acting as an interface among them in the impedance response plot of the nanocomposite.

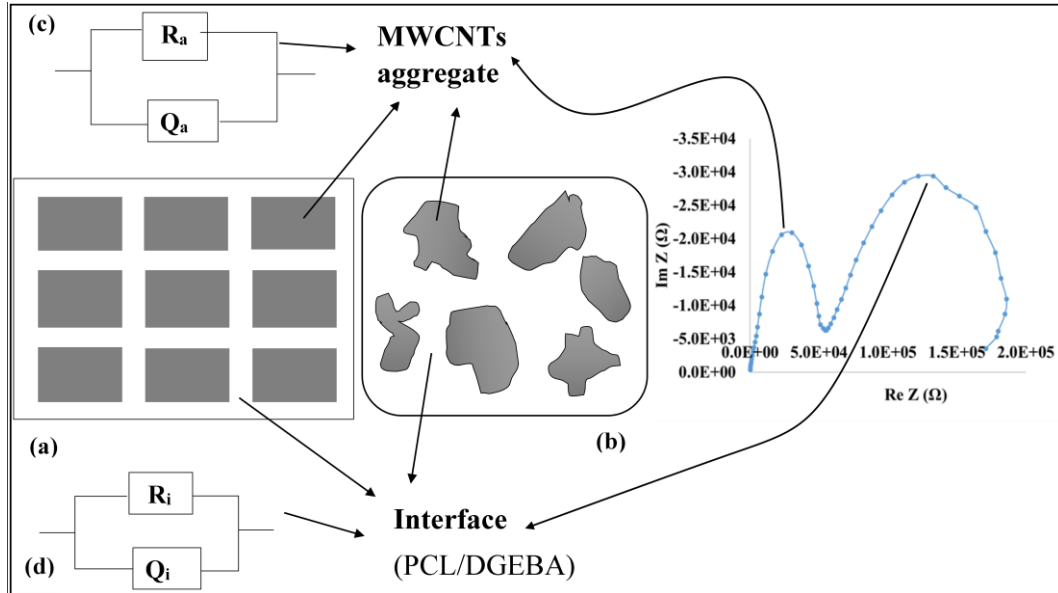


Figure 6.42 (a) Cartoon of bricklayer mode, (b) fractal aggregates of MWCNTs into epoxy/PCL matrix and corresponding equivalent circuit (c) for aggregates of MWCNTs and (d) and interface between aggregates composed of epoxy and PCL mixture. The R_a , R_i represents the resistance of MWCNTs and interface composed of PCL and epoxy resin, respectively. The Q_a and Q_i represent constant phase element for aggregates of MWCNTs and interfaces composed of PCL and epoxy resin, respectively.

A simple ‘bricklayer model’ is considered appropriate in conjunction with the equivalent circuit model [75], [80] studying collective behaviour (conductor-insulator) in the nanocomposite. The bricklayer model with equivalent circuit model comprises two parallel R//Q sub-circuits connected in series are illustrated in Figure 6.42. The circuit simulation is presented in Figure 6.42(c, d). In the context of the bricklayer model, these are assumed to represent the pure resistance and complex capacitance of (a) aggregates of MWCNTs (b) and the interfaces composed of epoxy and PCL. The impedance of the equivalent circuit is given as

$$Z^* = Z' + iZ'' \quad (6.9)$$

$$Z^* = \frac{R_a}{1 + (i2\pi f)^{\alpha_a} R_a Q_a} + \frac{R_I}{1 + (i2\pi f)^{\alpha_I} R_I Q_I} \quad (6.10)$$

$$Z' = \frac{R_a (1 + (2\pi f)^{\alpha_a} R_a Q_a c_{aa})}{1 + (2\pi f)^{\alpha_a} Q_a R_a (2c_{aa} + (2\pi f)^{\alpha_a} Q_a R_a)} + \frac{R_I (1 + (2\pi f)^{\alpha_I} R_I Q_I c_{aI})}{1 + (2\pi f)^{\alpha_I} Q_I R_I (2c_{aI} + (2\pi f)^{\alpha_I} Q_I R_I)} \quad (6.11)$$

$$Z'' = \frac{(2\pi f)^{\alpha_a} R_a^2 s_{aa} Q_a}{1 + (2\pi f)^{\alpha_a} Q_a R_a (2c_{aa} + (2\pi f)^{\alpha_a} Q_a R_a)} - \frac{(2\pi f)^{\alpha_I} R_I^2 s_{aI} Q_I}{1 + (2\pi f)^{\alpha_I} Q_I R_I (2c_{aI} + (2\pi f)^{\alpha_I} Q_I R_I)} \quad (6.12)$$

Here Z^* and f denote the complex impedance of the circuit and the frequency while Z' and Z'' are the real and imaginary part of complex impedance respectively. The parameters R_a and R_I indicate the resistance of aggregates of MWCNTs and interface composed of epoxy and PCL polymers, respectively. The parameters Q_a and Q_I represent constant phase element for aggregates of MWCNTs and interface composed of epoxy and PCL polymers, respectively. The fractal behaviour is explained from values of α_a and α_I which lie between 0 and 1. The case of $\alpha = 1$, describes an ideal capacitor while the case $\alpha = 0$ describes a pure resistor. A value in between 0 and 1 indicates a non-ideal behaviour of a capacitor or a resistor. There are various reasons for a non-ideal behaviour in 3D printed samples containing MWCNTs into the epoxy/PCL matrix. This includes an inhomogeneous distribution of MWCNTs, the surface roughness of samples, porosity in structure, and variable thickness of the sample. The two semicircles represent two components in 3D printed nanocomposite electrode where the first semicircle represents conducting networks (aggregates) of MWCNTs, the second semicircle represent the dielectric response of interface composed of PCL and DGEBA epoxy.

The evolution of the conductive network in 3D printed samples is modelled and studied with variation in MWCNTs in 3D printed samples. The results of parameter estimation are provided in Table 6-8 for 3D printed nanocomposite samples containing MWCNTs with 0.5 % (w/w) and 2.0 % (w/w) loadings.

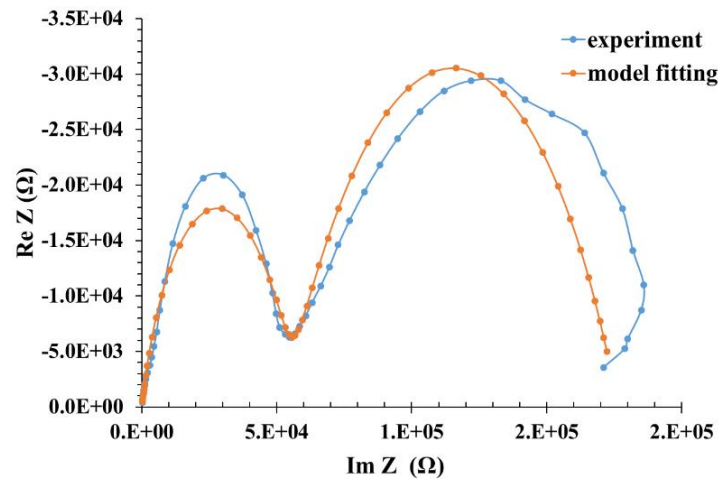


Figure 6.43 Experimental and model fitting impedance data in the form of Nyquist plots are presented from 3D printed samples with MWCNTs (2.0 % w/w).

From Table 6-8, it is obvious that the interphase shows an increase in constant phase element (Q_I) and a drop of resistance (R_I) for 3D printed samples with an increase in MWCNTs loading. A similar trend was observed for aggregates of MWCNTs for constant phase element of the aggregate (Q_a) and the corresponding resistance (R_a). For the sample without MWCNTs, constant phase parameters (α_I , α_a) for interphase and aggregate are similar and equal to one.

Table 6-8 Significant parameters extracted from data fitting using the equivalent circuit model using different loadings of MWCNTs.

	aggregates			interface			
%MWCNTs	R_a (Ω)	Q_a (S)	α_a	R_I (Ω)	Q_I (S)	α_I	$Khi2/N$
0	1.91E+09	6.06E-11	0.999	5.06E+09	2.15E-11	0.998	7.98E-02
0.5	1.12E+08	4.80E-10	0.873	7.31E+08	2.42E-09	0.714	7.51E-03
2	5.45E+04	3.88E-09	0.728	1.22E+05	2.25E-06	0.591	2.76E-02

The values are reasonable to consider as the sample is free from MWCNTs. For the sample containing MWCNTs, constant phase parameters (α_I , α_a) for interphase and aggregate are near to one. Such behaviour is indicative of the fractal nature of a capacitor instead of pure capacitor behaviour. The estimation is performed using a Matlab based programme [81], which minimises the following objective for each frequency sweep:

$$Khi^2 = \sum [\text{weightmatrix} * (\text{model} - \text{experiment})^2] \quad (6.13)$$

Where $\text{model} = [\text{Real}(Z_{\text{mod}}), \text{Imag}(Z_{\text{mod}})]$

$$\begin{aligned}
 Experiment &= [Real(Z_{exp}), Imag(Z_{exp})] \\
 weightmatrix &= [\frac{1}{Real(Z_{exp})}, \frac{1}{Imag(Z_{exp})}]
 \end{aligned}
 \tag{6.14}$$

While Z_{exp} and Z_{mod} are the experimental data that have to be fitted and the values returned by the modelling equivalent circuit. The weight matrix is the 2-columns matrix of the weight coefficients associated with each point. The weight coefficients are equalized through $1/Z_{exp}$ so that the high-valued points have the same weight than the low-valued points. This is commonly referred to as proportional weighting. The estimation is based on χ^2/N and visual quality of fitting to experimental data. The values of the parameters obtained in the previous sweep are used as a priori estimate for the desired solution. The data fitting in low frequencies region poorly fits the data compare to the high-frequency region. The sub-circuit belongs to aggregates of MWCNTs is fitting to relatively higher characteristic frequency region, with interfaces occupying the low-frequency part of the spectrum.

6.4 CONCLUSION

One of the key objectives of the study is the development and implementation of a 3D printer for printing of thermoset polymer-based nanocomposites. For the sake of this, a printing system is configured fulfilling basic requirements as an AM system. The system works on extrusion principle, using a syringe-plunger system. However, in terms of three-dimensional control, it is similar to a common 3D printer. The system was calibrated and a mass flow rate 33mg is measured using test samples. An epoxy resin, diglycidyl bisphenol –A, is considered appropriate for printing, being as a thermoset polymer when reacting with TETA. Compositions were prepared for the printing of electrically conductive samples containing multiwall carbon nanotubes as nanostructures. The preliminary work suggests that the addition of a thermoplastic facilitate the print process when used in relatively small proportion. With this consideration, PCL is considered appropriate when used around 10 % (w/w) into the DGEBA resin. Besides, MWCNTs were introduced into the DGEBA/PCL mixture acquiring 3D printed an electrically conducting samples. The printed samples were subject to a variety of characterization techniques to understand the structure-property relationship. The key objectives of the study are addressed in the form of the following conclusions:

- Design, development, calibration and implementation of an additive manufacturing system fulfilling the requirements for recognition as an additive manufacturing system that can print an epoxy-based composite material. This includes the material selection, preparation and implementation of a clear printing strategy capable of dispensing and processing the materials according to additive manufacturing norms.
- The introduction of thermoplastic material into a thermoset resin is considered necessary for the sake of acquiring an appropriate printing. In this context, polycaprolactone is considered appropriate in comparison to polystyrene. Polystyrene is phase-separated during printing and it blocks printing nozzles. Polycaprolactone has excellent miscibility with epoxy resin and it facilitates printing of epoxy resin when used in appropriate proportion.
- The print speed of the additive manufacturing system is limited to 100-150 *mm/min* with an extrusion rate of 0.1 ± 0.02 for the printing of epoxy-based nanocomposites samples. A relatively higher print speed leads insufficient layer adhesion while a lower speed allows the material to clog in the printing nozzle. Likewise, a higher extrusion rate results in excessive material flow through the printing nozzle causing the layer to collapse during printing while a lower extrusion rate leads to inappropriate layer and nozzle clogging.
- The additive manufacturing system disclosed in this study will extend the range of printable materials in context to thermoset printing. In additive manufacturing, printable materials are limited and the majority of polymers are based on melt extrusion of thermoplastic polymers e.g. Acrylonitrile butadiene styrene, Polylactic acid, and UV- curable resins. Thermoset polymers are a class of polymers and epoxy-based printing will open a window to print a variety of other thermosets e.g. polyurethanes and siloxanes.
- The epoxy-based composite printing is strongly dependent on the composition or the % loading of constituent entities. For example, an increase in loading of MWCNTs demands a decrease in PCL loading. This indicates there is an upper limit of constituents that can be used to print epoxy-based nanocomposite. On similar grounds, there is a lower limit for

constituents that can be used to prepare the composition. The use of constituents near a lower limit compromise not only on print quality rather it affects the functionality of interest.

- Functional materials are generally characterised as materials that possess particular native properties and functions of their own. Additive manufacturing is limited in terms of printing parts that have some functionality. Such functionality may include 3D printed parts with electrical conductivity, thermal conductivity, magnetic features or parts that have potential application areas such as solar cells, batteries or capacitors. One of the key objective addressed in this study is additive manufacturing of electrically conductive samples. Electrically conductive samples are printed and in particular, these are characterised in context to *AC* and *DC* electrical conductivity. The measured conductivity is considered appropriate for a variety of applications.
- The success of printing of epoxy-based nanocomposite material depends on the epoxy resin curing. The presence of intruder phases, MWCNTs and Polycaprolactone, affects kinetics and mobility of monomers and thereby limit epoxide conversion. FTIR spectra are used to confirm epoxide conversion concerning MWCNTs and PCL loadings. It is found that the amount of epoxide conversion reduces with the loading of MWCNTs and PCL.
- The % crystallinity is increased in the nanocomposites as evidenced by DSC and SAXS data. This is an indication that MWCNTs act as nucleating agent and promote the lamellar organisation in the nanocomposite.
- The microstructure of 3D printed samples is characterised using SAXS and WAXS. The data suggest that appropriate compositions are prepared for the printing of epoxy-based nanocomposites in which epoxy resin is crosslinked with TETA in the presence of MWCNTs and Polycaprolactone without undesired phase developments.
- An extrusion process based digital system is considered appropriate for filament printing. Such a system function under similar to the filament-on-demand approach with the desired resolution to harness the potential of additive manufacturing.

- The capability of using different types of printing nozzles and material carrying reservoir (syringe) to allow for a wider range of application-oriented thermoset polymer-based composites.
- Clamping system to hold the syringe carrying material that avoids nozzle vibration during printing. The Clamp is modifiable considering the design of the printer.
- Printing of electrically conductive samples with square and rectangular shapes. The system allows printing a single filament.
- Structural characterisation leading to confirm crosslinking in context to carbon nanotubes, TETA, and PCL loading. Compositional and dimensional constraints enhancing/ limiting the print quality of the printer.
- An equivalent circuit model is used to fit impedance data indicating complex behaviour of insulator phase in the printed samples. Such complexity is attributed to the presence of polycaprolactone with epoxy resin causing an inhomogeneous or heterogeneous structure. The resistance in 3D printed samples decreases with higher loadings of MWCNTs. The print process affected curing due to which electrical conductivity decreases with time. Relatively, higher electrical conductivity is calculated from samples printed using a higher amount of TETA.

6.5 REFERENCES

- [1] J. E. Oliveira, L. H. C. Mattoso, W. J. Orts, and E. S. Medeiros, "Structural and Morphological Characterization of Micro and Nanofibers Produced by Electrospinning and Solution Blow Spinning: A Comparative Study," vol. 2013, 2013.
- [2] T. Theophanides, *Infrared Spectroscopy – Materials Science, Engineering and Technology*, 1st editio. Croatia, 2012.
- [3] Sigma-Aldrich, "IR Spectrum Table & Chart," 2019. [Online]. Available: <https://www.sigmaaldrich.com/technical-documents/articles/biology/ir-spectrum-table.html>. [Accessed: 25-Aug-2019].
- [4] J. Coates, "Encyclopedia of Analytical Chemistry -Interpretation of Infrared Spectra, A Practical Approach," *Encyclopedia of Analytical Chemistry*. John Wiley & Sons Ltd, pp. 1–23, 2004.
- [5] J. G. G. Daimay Lin-Vien, Norman B. Colthup, William G. Fateley, *The Handbook of Infrared and Raman Characteristic Frequencies of Organic*. London: Academic Press, 191AD.
- [6] Barbara H. Stuart, *Infrared Spectroscopy: Fundamentals and applications*. Sussex: John Wiley & Sons, Ltd., 2004.
- [7] F. Awaja, M. Gilbert, B. Fox, G. Kelly, and P. J. Pigram, "Investigation of the postcure reaction and surface energy of epoxy resins using time-of-flight

- secondary ion mass spectrometry and contact-angle measurements," *J. Appl. Polym. Sci.*, vol. 113, no. 5, pp. 2755–2764, Sep. 2009.
- [8] F. Awaja, G. Van Riessen, G. Kelly, B. Fox, and P. J. Pigram, "Tof-sims Investigation of Epoxy Resin Curing Reaction at Different Resin to Hardener Ratios," *J. Appl. Polym. Science*, vol. 110, pp. 2711–2717, 2008.
- [9] S. B. Sagar T. Cholake, Mykanth R. Mada, R.K. Singh Raman, Yu Bai, XL Zhao, Sami Rizkalla!, "Quantitative Analysis of Curing Mechanisms of Epoxy Resin by Mid- and Near- Fourier Transform Infra Red Spectroscopy," *Def. Sci. J.*, vol. 64, no. 3, pp. 341–321, 2014.
- [10] R. E. Smith, F. N. Larsen, and C. L. Long, "Epoxy resin cure. II. FTIR analysis," *J. Appl. Polym. Sci.*, vol. 29, no. 12, pp. 3713–3726, 1984.
- [11] N. Poisson, G. Lachenal, and H. Sautereau, "Near- and mid-infrared spectroscopy studies of an epoxy reactive system," *Vib. Spectrosc.*, vol. 12, no. 2, pp. 237–247, 1996.
- [12] V. Strehmel and T. Scherzer, "Structural investigation of epoxy amine networks by mid- and near-infrared spectroscopy," *Eur. Polym. J.*, vol. 30, no. 3, pp. 361–368, 1994.
- [13] G. Nikolic, S. Zlatkovic, M. Cakic, S. Cakic, C. Lacnjevac, and Z. Rajic, "Fast fourier transform IR characterization of epoxy GY systems crosslinked with aliphatic and cycloaliphatic EH polyamine adducts," *Sensors*, vol. 10, no. 1, pp. 684–696, 2010.
- [14] F. Piscitelli et al., "Peculiarities in the structure - Properties relationship of epoxy-silica hybrids with highly organic siloxane domains," *Polymer (Guildf.)*, vol. 63, pp. 222–229, 2015.
- [15] M. C. Finzel, J. Delong, and M. C. Hawley, "Effect of stoichiometry and diffusion on an epoxy/amine reaction mechanism," *J. Polym. Sci. Part A Polym. Chem.*, vol. 33, no. 4, pp. 673–689, 1995.
- [16] E. Esmizadeh, A. A. Yousefi, and G. Naderi, "Effect of type and aspect ratio of different carbon nanotubes on cure behavior of epoxy-based nanocomposites," *Iran. Polym. J. (English Ed.)*, vol. 24, no. 1, 2014.
- [17] L. S. Cividanes, E. A. N. Simonetti, M. B. Moraes, F. W. Fernandes, and G. P. Thim, "Influence of carbon nanotubes on epoxy resin cure reaction using different techniques: A comprehensive review," *Polym. Eng. Sci.*, vol. 54, no. 11, pp. 2461–2469, 2014.
- [18] X. Zeng et al., "Characteristics of the electrical percolation in carbon nanotubes/polymer nanocomposites," *J. Phys. Chem. C*, vol. 115, no. 44, pp. 21685–21690, 2011.
- [19] M. Cattani, M. C. Salvadori, and M. Cattani, "Insulator-Conductor Transition: A Brief Theoretical Review." *University of São Paulo, Brazil.*, pp. 1–11, 2009.
- [20] I. Balberg, "A comprehensive picture of the electrical phenomena in carbon black-polymer composites," *Carbon N. Y.*, vol. 40, no. 2, pp. 139–143, 2002.
- [21] C. Gau, C. Y. Kuo, and H. S. Ko, "Electron tunneling in carbon nanotube composites," *Nanotechnology*, vol. 20, no. 39, 2009.
- [22] A. J. Wang et al., "Percolating conductive networks in multiwall carbon nanotube-filled polymeric nanocomposites: Towards scalable high-conductivity applications of disordered systems," *Nanoscale*, vol. 11, no. 17, pp. 8565–8578, 2019.
- [23] B. Vigolo, C. Coulon, M. Maugey, C. Zakri, and P. Poulin, "Fluid dynamics: An experimental approach to the percolation of sticky nanotubes," *Science (80-.)*, vol. 309, no. 5736, pp. 920–923, 2005.

- [24] Z. Špitalský, C. A. Krontiras, S. N. Georga, and C. Galiotis, "Effect of oxidation treatment of multiwalled carbon nanotubes on the mechanical and electrical properties of their epoxy composites," *Compos. Part A Appl. Sci. Manuf.*, vol. 40, no. 6–7, pp. 778–783, 2009.
- [25] and A. J. M. Thandi P Gumede, Adriaan S. Luyt, Mohammad K. Hassan, Ricardo A. Pérez-Camargo, Agnieszka Tercjak, "Morphology, Nucleation, and Isothermal Crystallization Kinetics of Poly(ϵ -caprolactone) Mixed with a Polycarbonate/MWCNTs Masterbatch," *Polymers (Basel)*, vol. 9, no. 12, p. 709, 2017.
- [26] S. Barrau, P. Demont, A. Peigney, C. Laurent, and C. Lacabanne, "DC and AC Conductivity of Carbon Nanotubes - Polyepoxy Composites," *Macromolecules*, vol. 36, pp. 5187–5194, 2003.
- [27] A. K. Jonscher, "The 'universal' dielectric response.," *Nature*, vol. 267, pp. 673–679, 1977.
- [28] B. E. Kilbride et al., "Experimental observation of scaling laws for alternating current and direct current conductivity in polymer-carbon nanotube composite thin films," *J. Appl. Phys.*, vol. 92, no. 7, pp. 4024–4030, 2002.
- [29] J. C. Dyre, "The random free-energy barrier model for ac conduction in disordered solids," *J. Appl. Phys.*, vol. 64, no. 5, pp. 2456–2468, 1988.
- [30] G. A. Kontos et al., "Electrical relaxation dynamics in TiO₂ - polymer matrix composites," *Express Polym. Lett.*, vol. 1, no. 12, pp. 781–789, 2007.
- [31] Z. Špitalský, S. N. Georga, C. A. Krontiras, and C. Galiotis, "Dielectric spectroscopy and tunability of multi-walled carbon nanotube / epoxy resin composites," *Adv. Compos. Lett.*, vol. 19, no. 6, pp. 179–189, 2010.
- [32] B. Hussien, "The D.C and A.C Electrical Properties of (PMMA -Al₂O₃) Composites," *Eur. J. Sci. Res.*, vol. 52, no. 2, pp. 236–242, 2011.
- [33] Z. G. Xiusheng Guo, Demei Yu, Yan Gao, Qin Li, Weitao Wan, "Dielectric properties of filled carbon nanotubes/epoxy composites with high dielectric constant," in *2006 1st IEEE International Conference on Nano/Micro Engineered and Molecular Systems*, 2006, pp. 295–298.
- [34] J. P. Peng, H. Zhang, L. C. Tang, Y. Jia, and Z. Zhang, "Dielectric properties of carbon nanotubes/epoxy composites," *J. Nanosci. Nanotechnol.*, vol. 13, no. 2, pp. 964–969, 2013.
- [35] K. J. Andrew, "Dielectric relaxation in solids," *J. Phys. D. Appl. Phys.*, vol. 32, no. 14, p. R57, 1999.
- [36] Y. Song, T. W. Noh, S. I. Lee, and J. R. Gaines, "Experimental study of the three-dimensional ac conductivity and dielectric constant of a conductor-insulator composite near the percolation threshold," *Phys. Rev. B*, vol. 33, no. 2, pp. 904–908, 1986.
- [37] "Dielectric spectroscopy – Laboratory for Soft Matter and Biophysics." [Online]. Available: https://fys.kuleuven.be/zmb/Research_themes/rt_dielectric/rt_dielectric. [Accessed: 22-Aug-2019].
- [38] BRYAN D. HIRSCHORN, "Distributed time-constant impedance responses interpreted in terms of physically meaningful properties," UNIVERSITY OF FLORIDA, 2010.
- [39] V. Kumar, S. Das, and T. Yokozeki, "Frequency independent AC electrical conductivity and dielectric properties of polyaniline-based conductive thermosetting composite," *J. Polym. Eng.*, vol. 38, no. 10, pp. 955–961, 2018.
- [40] J. Chang, G. Liang, A. Gu, S. Cai, and L. Yuan, "The production of carbon

- nanotube/epoxy composites with a very high dielectric constant and low dielectric loss by microwave curing,” *Carbon N. Y.*, vol. 50, no. 2, pp. 689–698, 2012.
- [41] R. Belhimria et al., “Fractal Approach to Alternating Current Impedance Spectroscopy Studies of Carbon Nanotubes/Epoxy Polymer Composites,” *Appl. Microsc.*, vol. 47, no. 3, pp. 126–130, 2017.
- [42] E. M. Anitas, “Complexity in Biological and Physical Systems: Bifurcations, Solitons and Fractals,” in *Complexity in Biological and Physical Systems: Bifurcations, Solitons and Fractals*, vol. i, R. Lopez-Ruiz, Ed. IntechOpen, 2018, p. 13.
- [43] E. M. Anitas, “Small-angle scattering from weakly correlated nanoscale mass fractal aggregates,” *Nanomaterials*, vol. 9, no. 4, pp. 1–10, 2019.
- [44] M. Klüppel, “The Role of Disorder in Filler Reinforcement of Elastomers on Various Length Scales,” *Adv. Polym. Sci.*, vol. 164, pp. 1–86, 2003.
- [45] R. Besselink, T. M. Stawski, A. E. S. Van Driessche, and L. G. Benning, “Not just fractal surfaces, but surface fractal aggregates: Derivation of the expression for the structure factor and its applications,” *J. Chem. Phys.*, vol. 145, no. 21, 2016.
- [46] Po - zen Wong and Alan J. Bray, “Porod Scattering from Fractal Surfaces,” *Phys. Rev. Lett.*, vol. 60, no. 13, p. 1344, 1988.
- [47] S. K. Siddhamalli, “Toughening of epoxy/polycaprolactone composites via reaction induced phase separation,” *Polym. Compos.*, vol. 21, no. 5, pp. 846–855, 2000.
- [48] X. Luo, R. Ou, D. E. Eberly, A. Singhal, W. Viratyaporn, and P. T. Mather, “A thermoplastic/thermoset blend exhibiting thermal mending and reversible adhesion,” *ACS Appl. Mater. Interfaces*, vol. 1, no. 3, pp. 612–620, 2009.
- [49] J. Parameswaranpillai et al., “Miscibility, Phase Morphology, Thermomechanical, Viscoelastic and Surface Properties of Poly(ϵ -caprolactone) Modified Epoxy Systems: Effect of Curing Agents,” *Ind. Eng. Chem. Res.*, vol. 55, no. 38, pp. 10055–10064, 2016.
- [50] M. R. Kessler, *Advanced topics in characterization of composites*. Trafford, 2004.
- [51] Q. Guo and G. Groeninckx, “Crystallization kinetics of poly (1 -caprolactone) in miscible thermosetting polymer blends of epoxy resin and poly (ϵ -caprolactone),” *Polymer (Guildf.)*, vol. 42, pp. 8647–8655, 2001.
- [52] T. M. Wu and E. C. Chen, “Crystallization behavior of poly(ϵ -caprolactone)/multiwalled carbon nanotube composites,” *J. Polym. Sci. Part B Polym. Phys.*, vol. 44, no. 3, pp. 598–606, 2006.
- [53] M. Larranaga et al., “Cure kinetics of epoxy systems modified with block copolymers,” *Polym. Int.*, vol. 53, no. 10, pp. 1495–1502, 2004.
- [54] J. Parameswaranpillai, N. Hameed, J. Pionteck, and E. M. Woo, *Handbook of epoxy blends*. 2017.
- [55] J. N. Clark, J. H. Daly, and A. Garton, “Hydrogen bonding in epoxy resin/poly(?????caprolactone) blends,” *J. Appl. Polym. Sci.*, vol. 29, no. 11, pp. 3381–3390, 1984.
- [56] T. Liu, A. Shinohara, G. Tan, C. Pan, and L. Wang, “The Cross-Linking Effect on the Thermoelectric Properties of Conjugated Polymer/Carbon Nanotube Composite Films,” *Macromol. Mater. Eng.*, vol. 304, no. 5, pp. 1–8, 2019.
- [57] C. F. Pitt, B. P. Barth, and B. E. Godard, “Electrical Properties of Epoxy Resins,” *IRE Trans. Compon. Parts*, vol. 4, no. 4, pp. 110–113, 1957.

- [58] C. A. W. Leszek A. Utracki, *Polymer Blends Handbook*. 2014.
- [59] A. Y. Cherny, E. M. Anitas, V. A. Osipov, and A. I. Kuklin, "The structure of deterministic mass and surface fractals: Theory and methods of analyzing small-angle scattering data," *Phys. Chem. Chem. Phys.*, vol. 21, no. 24, pp. 12748–12762, 2019.
- [60] D. W. Schaefer, J. Zhao, J. M. Brown, D. P. Anderson, and D. W. Tomlin, "Morphology of dispersed carbon single-walled nanotubes," *Chem. Phys. Lett.*, vol. 375, no. 3–4, pp. 369–375, 2003.
- [61] J. J. Hernández, M. C. García-Gutiérrez, A. Nogales, D. R. Rueda, and T. A. Ezquerro, "Small-angle X-ray scattering of single-wall carbon nanotubes dispersed in molten poly(ethylene terephthalate)," *Compos. Sci. Technol.*, vol. 66, no. 15, pp. 2629–2632, 2006.
- [62] B. J. Bauer, E. K. Hobbie, and M. L. Becker, "Small-angle neutron scattering from labeled single-wall carbon nanotubes," *Macromolecules*, vol. 39, no. 7, pp. 2637–2642, 2006.
- [63] R. Bourrat, X. Oberlin, A. Van Damme, H. Gateau, C., & Bachelar, "Mass fractal analysis of conducting carbon black morphology," *Carbon N. Y.*, vol. 26, no. 1, pp. 100–103, 1987.
- [64] R. J. Roe, *Methods of X-ray and neutron scattering in polymer science*. Oxford: Oxford University Press, 2000.
- [65] G. Faiella, F. Piscitelli, M. Lavorgna, V. Antonucci, and M. Giordano, "Effect of fabrication process on the electrical and morphological properties of MWNT-epoxy composites," in *ICCM International Conferences on Composite Materials*, 2009.
- [66] "Polymer Properties Database." [Online]. Available: https://polymerdatabase.com/polymer_physics/Phase_Equilibria3.html. [Accessed: 27-Oct-2019].
- [67] M. Harsch, J. Karger-Kocsis, and M. Holst, "Influence of fillers and additives on the cure kinetics of an epoxy/anhydride resin," *Eur. Polym. J.*, vol. 43, no. 4, pp. 1168–1178, 2007.
- [68] K. Al-ahdal, N. Silikas, and D. C. Watts, "Rheological properties of resin composites according to variations in composition and temperature," *Dent. Mater.*, vol. 30, no. 5, pp. 517–524, 2014.
- [69] W. Hoogsteen, A. R. Postema, A. J. Pennings, G. Ten Brinke, and P. Zugenmaier, "Crystal Structure, Conformation, and Morphology of Solution-Spun Poly(L-Lactide) Fibers," *Macromolecules*, vol. 23, no. 2, pp. 634–642, 1990.
- [70] A. Nikfarjam, R. Rafiee, and M. Taheri, "Electrical and Electromagnetic Properties of Isolated Carbon Nanotubes and Carbon Nanotube-Based Composites Electrical conductivity," *Polyolefins*, vol. 4, no. 1, pp. 43–68, 2017.
- [71] A. Bharati, M. Wübbenhorst, P. Moldenaers, and R. Cardinaels, "Dielectric Properties of Phase-Separated Blends Containing a Microcapacitor Network of Carbon Nanotubes: Compatibilization by a Random or Block Copolymer," *Macromolecules*, vol. 50, no. 10, pp. 3855–3867, 2017.
- [72] A. Battisti, A. A. Skordos, and I. K. Partridge, "Dielectric monitoring of carbon nanotube network formation in curing thermosetting nanocomposites," *J. Phys. D. Appl. Phys.*, vol. 42, no. 15, p. 19, 2009.
- [73] R. N. Othman and A. N. Wilkinson, "The impedance characterization of hybrid CNT-silica epoxy nanocomposites," *Int. J. Automot. Mech. Eng.*, vol. 10, no. 1,

- pp. 1832–1840, 2014.
- [74] J. Valsa, P. Dvořák, and M. Friedl, “Network model of the CPE,” *Radioengineering*, vol. 20, no. 3, pp. 619–626, 2011.
 - [75] J. R. (James R. Macdonald, *Impedance spectroscopy: emphasizing solid materials and systems*. Wiley, 1987.
 - [76] Dr. Bob’s Buzz, “The Constant Phase Element - CPE,” 2014. [Online]. Available: <https://electrochemistryresources.com/the-constant-phase-element-cpe/>. [Accessed: 01-Oct-2019].
 - [77] E. Barsoukov and J. R. Macdonald, *Impedance Spectroscopy Theory, Experiment, and Applications*, 2nd ed. New Jersey: John Wiley & Sons, Inc., 2005.
 - [78] J.-P. Diard, B. Le Gorrec, and C. Montella, *Handbook of Electrochemical Impedance Spectroscopy*. 2013.
 - [79] S. Pandey, D. Kumar, O. Parkash, and L. Pandey, “Equivalent circuit models using CPE for impedance spectroscopy of electronic ceramics,” *Integr. Ferroelectr.*, vol. 183, no. 1, pp. 141–162, 2017.
 - [80] N. J. Kidner, Z. J. Homrighaus, B. J. Ingram, T. O. Mason, and E. J. Garboczi, “Impedance/dielectric spectroscopy of electroceramics-part 1: Evaluation of composite models for polycrystalline ceramics,” *J. Electroceramics*, vol. 14, no. 3, pp. 283–291, 2005.
 - [81] D. Jean-Luc, “ZfitGUI - File Exchange - MATLAB Central.” Jean-Luc Dellis, Laboratoire de la Physique de la Matière Condensée, UFR des Sciences, Amiens, France.

Chapter 7: Conclusion and Future work

7.1 INTRODUCTION

Additive manufacturing (AM) is an additive process-based technology being the closest to the ‘bottom-up’ manufacturing where a structure is built into its designed shape using a ‘layer-by-layer’ approach. It is contrary to casting or forming technologies such as forging or machining. The technology has gained significant worldwide attention over the last decade. However, the widespread of additive manufacturing is limited as the process caters only limited materials [1]. Moreover, a need for a simple, low cost and easy to use additive manufacturing system exists to expand the printable functional materials e.g. electrically conductive nanocomposites. In this thesis, these issues are addressed primarily. For the sake of this, additive manufacturing systems are used to print thermoplastic and thermoset polymer-based nanocomposites which are electrically conductive under a suitable bias. Thermoplastic polymer-based nanocomposites are printed using an existing additive manufacturing system while a new printer system is developed for thermoset polymer-based nanocomposites. Compositions were prepared using polycaprolactone, a thermoplastic polymer, containing multiwall carbon nanotubes and the strands were printed using the bio-extruder as an additive manufacturing system. The prepared strands were studied under the effect of uniaxial deformation besides measuring electrical conductivity. In this regard, the key problem discussed in the presence of anisotropy in the microstructure of printed samples due to either carbon nanotubes or crystalline lamellae, which influence electrical conductivity. The knowledge will help to develop stretchable electrodes which result in the rapid advancement of high-performance stretchable system components such as stretchable sensors and actuators [2-3]. A printer is designed and configured for the printing of nanocomposite based on thermoset resin that contains multiwall carbon nanotubes. This is desired due to unique coalescence of properties in thermoset polymers including thermal stability [4-5], structural integrity [6], resistance to heat and chemicals [7] which direct their candidacy towards a wide range of applications. However, the printing of thermoset resin-based nanocomposites poses some challenges because of the dynamic increase in viscosity [8]. The variation of the system viscosity during thermosetting cure takes

place as a result of the physical and chemical phenomena that occur during the polymerisation reaction. In the case of an isothermal cure, the molecular structure changes caused by crosslinking lead to steadily increasing in viscosity until the crosslinking polymer molecules form an infinite network and cure (before gelation) takes place [9]. The control over the cure provides a route to use the material for printing purpose. For the sake of this purpose, a methodology is presented for the preparation of thermoset resin-based nanocomposites for additive manufacturing. Compositions were prepared using diglycidyl ether of bisphenol-A epoxy resin and carbon nanotubes and subject to printing acquiring samples that can pass an electronic current when a suitable bias is applied across the sample. The samples are characterised to deduce structural, morphological and electrical conclusions. Models are presented in respective studies wherever it is considered necessary for the sake of discussion of results extracted from experimental data. A summary of key findings is provided here in the final chapter, based on the research work presented in this thesis.

7.2 Overall conclusions

- Nanocomposites are prepared using polymer matrices (polycaprolactone, diglycidyl ether of bisphenol-A resin) containing carbon nanotubes. To do this, nanocomposites are prepared using extrusion-based additive manufacturing techniques. Electric resistance is calculated in the printed samples by measuring the electric current and the corresponding voltage drop upon application of a suitable bias. Further, electrical conductivity is calculated using samples dimensions and resistance calculations under the effect of an external bias. Printing of electrically conductive samples using additive manufacturing is suggestive of printing of functional devices, e.g. electrodes, capacitors and batteries.
- With the inclusion of MWCNTs in PCL, DC electrical conductivity in 3D printed strands and bulk films are significantly increased compared to pure PCL. An increase in electrical conductivity is attributed to the formation of conductive pathways due to the percolation of carbon nanotubes.
- The electrical conductivity is decreased after deformation in both samples i.e. a bulk films and 3D printed strands. There is a measurable electric current and voltage drop in the bulk films while no electric current and voltage drop is

detected in 3D printed strands after deformation. This is attributed to either network breaking or enhancement in tunnelling resistance caused by the straining of the sample. The 3D printed Strands, containing 1.0 % (w/w) MWCNTs, are strained nearly 200 % under the effect of uniaxial stress without breaking.

- It is revealed that electrical conductivity increases under the effect of low uniaxial deformation (< 200 %) while it decreases when samples are strained relatively higher than 200 %. This suggests that a low level of strain or deformation causes to reorient carbon nanotubes to a certain extent. Such an orientation increases the probability of conductive pathways due to which conductivity increase in the sample. At strain higher than 200 %, nanotubes reorient to such an extent that conductive pathways breaking is relatively higher than formation. This leads to a decrease in electrical conductivity in the sample.
- The study suggests that Young's modulus, yield strength, and fracture modes are slightly higher in bulk film relative to 3D printed strands. The yield strength and fracture modes are measured 12.7 N/mm² and 16 N/mm², respectively, in case of a bulk film, which decreases to 10 N/mm² and 12 N/mm² for 3D printed conductive strands. The elastic region, yield point and fracture point are decreased at a relatively high strain rate. Also, the plastic deformation region is prolonged at a relatively high strain rate.
- SAXS data analysis reveals a mass fractal morphology in 3D printed strands and bulk film, prepared using nanocomposite containing MWCNTs, comparing to pure PCL. The mass fractal dimension between -3 and -2 are measured from SAXS data while surface fractal dimension -3 is measured in case of pure PCL. The absence of morphology corresponding to -1 is an indication that MWCNTs form aggregates structure. Besides, 1D – correlation plots suggest that a long period decreases significantly under the effect of uniaxial strain for bulk film and 3D printed strands of pure PCL and nanocomposite strands (0.5 % w/w). In the case of strands printed with 1.0 % (w/w), the long period did not alter significantly. However, there is a difference in 1D – correlation plots along the meridian and equatorial direction that suggests relatively higher (12.0 %) long period along equatorial direction compare to the meridian in 3D printed strands with 1.0 % (w/w) MWCNTs.

However, a long period did not alter under the effect of uniaxial strain. The Kratky analysis indicates that the aggregate size of MWCNTs decreases under the effect of uniaxial strain in 3D printed strands.

- It can be concluded from the spherical harmonic analysis that nanotubes network failure or formation significantly affected in the elastic region while less number of tubes are affected in the plastic deformation region. This indicates that a significant portion of nanotubes is not in-network at relatively higher strain due to which electrical conductivity decreases appreciably.
- A new printer is designed for the printing of epoxy-based composites. It is based on an extrusion process and offering a simple control system to print thermoset resin-based composite material. A thermoplastic need to add, relatively small in proportion, providing an optimum flow during printing.
- The printing of epoxy-based composites material will provide another option for the manufacturing community. Therefore, the work extends the range of materials employed in additive manufacturing.
- The study suggests that the Triton X-100 is a suitable surfactant, to acquire dispersion of carbon nanotubes into a polymer matrix, accompany with ultrasonication.
- Organic solvents like Dimethylformamide and chloroform are considered appropriate for the dispersion of carbon nanotubes while acetone and hexane do not facilitate in the dispersion of carbon nanotubes.
- The blending of a thermoplastic polymer facilitates the printing of epoxy-based composites. Among thermoplastic polymer, polycaprolactone was proved useful contrary to polystyrene which phase separates during the print process and becomes the source of nozzle clogging.
- The concentration of polycaprolactone into nanocomposites (diglycidyl ether bisphenol-A epoxy resin /carbon nanotubes) is critical to acquire reasonable print quality. An optimum concentration range (7-10) % w/w is considered appropriate for reasonable print quality. A collapse of filament will result when the concentration of polycaprolactone is less than 7%w/w while nozzle-clogging result if the concentration is used more than 10% w/w.
- The study suggests that the upper limit for the concentration of carbon nanotubes into nanocomposites (diglycidyl ether bisphenol-A epoxy resin

/carbon nanotubes) is 2.0 % w/w to acquire reasonable print quality. Compositions with a higher concentration of carbon nanotubes lead to nozzle clogging.

- Additive manufacturing offers an enhanced control on the processing conditions as evidenced from morphological analysis of the printed samples.
- Morphological analysis of samples prepared using additive manufacturing is suggestive of mass fractal morphology.
- Anisotropy is observed in printed samples for concentrations at or slightly above the percolation threshold.
- The secondary objective of this research work is the modelling of the electrical conductivity in the polymer-based nanocomposites. There are numbers of factors, which can influence electrical conductivity in the nanocomposites amongst which polymer filler wettability, filler aspect ratio and filler electrical conductivity are the prominent factors. Therefore, based on experimental work and literature survey, a semi-empirical model is presented and data is fitted to the model. Electrical conductivity is also studied under the effect of uniaxial deformation as composite's properties are affected involving external effects. Another model is presented to describe the deformation effects on carbon nanotubes. It is possible to predict critical exponent and orientation of carbon nanotubes under the effect of uniaxial deformation through fitting the experimental data.
- The general properties of the one-dimensional electron density correlation function $\gamma(R)$, for a crystalline polymer with lamellar structure, can be used to find microstructure features including the crystallinity, the specific inner surface, and the electron density difference between amorphous and crystalline lamellae. Further, the electron density difference is exploited to find a favourable phase for carbon nanotubes settlement. The analysis suggests that carbon nanotubes settle into an amorphous phase of polycaprolactone.
- The modelling of electrical conductivity in the nanocomposites is suggestive of complex morphology caused by the numbers of parameters including aggregation of carbon nanotubes, polymer-filler interaction, environment effects, etc.

- From the work mentioned in chapter 6, it is obvious that blending of a suitable thermoplastic, with a desired printable thermoset, not only improves rheology but provides a working window (print time) which is desired for the print process. The selection of a thermoplastic polymer and its concentration is critical in its nature as the selection of inappropriate thermoplastic polymer or excessive concentration lead to phase separation that leads to material clogging which disrupts the printing process. Moreover, if the concentration is less than critical concentration, the working window will decrease that will lead to print incomplete part.
- The epoxy-based printed nanocomposites samples are mechanically brittle. Brittleness is one of the key issues with epoxy-based systems. Since this work is not in the scope of the study and will be addressed in another study in which particular attention will be directed toward this issue. Addition of a long chain polymer, like siloxanes, is proposed to address this issue.

7.3 FUTURE PERSPECTIVE

- The hybrid material printing (layer by layer printing of thermoplastic and thermosets polymers together) is a future perspective.
- Printing of functional devices e.g. a solid-state battery.
- Control over the microstructure (e.g. crystallinity) right after printing using additive manufacturing technology.
- Controlling the brittleness issue in diglycidyl ether of bisphenol-A based epoxy system.

7.4 REFERENCES

- [1] V. Francis, and P.K. Jai, "Advances in nanocomposite materials for additive manufacturing," *Int. J. Rapid Manufacturing*, Vol. 5, Nos. 3/4, pp.215-233, 2015.
- [2] S. Hong, S. Lee and D. Kim, "Materials and Design Strategies of Stretchable Electrodes for Electronic Skin and its Applications," *Proceedings of the IEEE*, vol. 107, no. 10, 2185-2197, 2019.
- [3] Wei Wu, "Stretchable electronics: functional materials, fabrication strategies and applications," *Science and Technology of Advanced Materials*, vol. 20, Issue 1, pp. 187-224, 2019.
- [4] D.K. Chattopadhyay, and D. C.Webster, "Thermal stability and flame retardancy of polyurethanes," *Progress in Polymer Science*, vol.34, pp. 1068–1133, 2009.
- [5] H. Liu, X. Wang, and D. Wu, "Preparation, isothermal kinetics, and

performance of a novel epoxy thermosetting system based on a phosphazene-cyclomatrix network for halogen-free flame retardancy and high thermal stability", *Thermochimica Acta*, vol. 607, pp. 60–73, 2015.

- [6] A. Kausar, "Role of Thermosetting Polymer in Structural Composite," *American Journal of Polymer Science & Engineering*, vol.5, pp.1-12, 2017.
- [7] M. Biron, *Thermosets and Composites. Material Selection, Applications, Manufacturing and Cost Analysis*, 2nd ed. Oxford: Elsevier Ltd., 2014.
- [8] I. Hamerton, "Recent Developments in Epoxy Resins," *Rapra Technology Ltd.*, vol.8, Issue7, 1996.
- [9] V. Mittal, *Modeling and Prediction of Polymer Nanocomposite Properties*, Weinheim: Wiley-VCH, 2013.